DigitalCommons
@WayneState

Wayne State University

Wayne State University Dissertations

1-1-2013

How Atomic Level Interactions Drive Membrane Fusion: Insights From Molecular Dynamics Simulations

Navendu Bhatnagar
Wayne State University,

Follow this and additional works at: http://digitalcommons.wayne.edu/oa_dissertations

Recommended Citation

Bhatnagar, Navendu, "How Atomic Level Interactions Drive Membrane Fusion: Insights From Molecular Dynamics Simulations" (2013). *Wayne State University Dissertations.* Paper 637.

This Open Access Dissertation is brought to you for free and open access by DigitalCommons@WayneState. It has been accepted for inclusion in Wayne State University Dissertations by an authorized administrator of DigitalCommons@WayneState.

HOW ATOMIC LEVEL INTERACTIONS DRIVE MEMBRANE FUSION: INSIGHTS FROM MOLECULAR DYNAMICS SIMULATIONS

by

NAVENDU BHATNAGAR

DISSERTATION

Submitted to the Graduate School

of Wayne State University,

Detroit, Michigan

in partial fulfillment of the requirements

for the degree of

DOCTOR OF PHILOSOHPY

2013

MAJOR: CHEMICAL ENGINEERING

Approved by:

Advisor Date

DEDICATION

To my loving family and friends.

ACKNOWLEDGEMENT

This work would not have been possible without the help, support and advice of many individuals.

I sincerely want to thank my mentor and advisor, Dr. Jeffrey J Potoff who is a constant source of inspiration and diligence. His highly motivating words and constant guidance have been the central axis of this research. The way he efficiently manages his time despite an extremely hectic schedule day in and day out and still finds time to discuss research with students and provide them with valuable ideas is truly admirable. I have been lucky to work as a research student with him as my advisor which has resulted in my academic growth in the field of research.

I would like to thank my Department Chair and also my co-advisor, Dr. Charles W. Manke, who inspired me to pursue the Ph.D. course and contributed his valuable time and advice for this research. I would like to thank Dr. Guangzhao Mao and Dr. Howard Matthew for being a part of my research committee. I would like to thank Dr. Bhanu P. Jena, from the Department of Physiology for providing valuable ideas on membrane fusion and helping this research.

I would like to thank all my lab members who have helped me with valuable advices related to my research and made the working environment an amicable one.

I would like to thank my loving family members for their constant love, guidance and support.

TABLE OF CONTENTS

Dedication II

Acknowledgement III

List of Figures viii

List of Tables xv

CHAPTER 1: INTRODUCTION & OVERVIEW 1

LIPID BILAYER 1

MEMBRANE FUSION 6

OCTANOL-WATER PARTITION COEFFICIENTS 8

CHAPTER 2: SIMULATION METHODOLOGIES 11

MOLECULAR DYNAMICS 11

ADAPTIVE BIASING FORCE 14

CHAPTER 3: PREDICTION OF 1-OCTANOL/WATER PARTITION COEFFICIENT FOR N-ALKANES USING ADAPTIVE BIASING FORCE METHOD 20

BACKGROUND 20

SIMULATION DETAILS 23

RESULTS AND DISCUSSION 29

Free energy of hydration *29*

Free energy of solvation *33*

Partition coefficients *37*

Convergence and error analysis *47*

CONCLUSIONS 52

CHAPTER 4: COMPUTATIONAL PREDICTION OF IONIC LIQUID 1-OCTANOL/WATER PARTITION COEFFICIENT 55

BACKGROUND 55

SIMULATION DETAILS 57

RESULTS & DISCUSSION 59

Potential of mean force *59*

Partition Coefficients *60*

Sampling efficiency of ABF method *64*

CONCLUSION 65

CHAPTER 5: 1-OCTANOL-WATER AND AIR-WATER PARTITION COEFFICIENTS FOR NITRO-AROMATIC COMPOUNDS FROM MOLECULAR DYNAMICS SIMULATIONS. 66

BACKGROUND 66

FORCE FIELD 69

SIMULATION DETAILS 74

RESULTS AND DISCUSSION 77

Hydration free energy *77*

Solvation free energy *79*

Partition coefficient *80*

CONCLUSIONS 88

CHAPTER 6: CHEMICAL WARFARE AGENTS 90

INTRODUCTION 90

FORCE FIELD 93

SIMULATION DETAILS 95

RESULTS AND DISCUSSION 100

Hydration free energy 100

Henry's law constant 101

Solvation free energy 103

Partition coefficient 104

Impact of water saturation 106

ABF convergence 108

Bioaccumalation analysis 110

CONCLUSIONS 112

CHAPTER 7: BIOMOLECULAR SIMULATIONS WITH THE TRANSFERABLE POTENTIALS FOR PHASE EQUILIBRIA: EXTENSION TO PHOSPHOLIPIDS. 114

BACKGROUND 114

FORCE FIELD 119

SIMULATION DETAILS 125

Volume per Lipid 136

Bilayer Thickness 138

Electron Density 143

X-Ray Form Factors ... *151*

CHAPTER 8: EFFECT OF CA2+ ON THE INTERACTIONS BETWEEN SYNAPTOTAGMIN-1 PROTEIN WITH MEMBRANE BILAYERS ... **154**

BACKGROUND ... 154

SIMULATION DETAILS ... 157

RESULTS AND DISCUSSION ... 159

Effect of Calcium ions ... *159*

Effect of bilayer composition ... *165*

Protein docking ... *165*

Electrostatic potential of protein surface ... *169*

Interaction energy between SYT-1 and bilayer ... *171*

Force between SYT-1 and bilayer ... *173*

Potential of mean force ... *175*

ENERGETICS OF SNARE DISSOCIATION ... 177

Bibliography ... **182**

Abstract ... **234**

Autobiographical Statment ... **237**

LIST OF FIGURES

Figure 1: Lipid Bilayer Composed Of Popc Phospholipid. Headgroup Phosphorus Atoms Are shown As Golden Spheres And Nitrogen Atoms As Blue Spheres. Lipid Tails Are Colored in Cyan. 2

Figure 2: Popc Lipid Bilayer (Grey) Interacting With C2a Domain Of Protein Synaptotagmin (Syt). Membrane Penetrating Amino Acid Residues Are Shown In Red. 3

Figure 3: Chemical Structure Of Phospholipid Headgroups. 5

Figure 4: Schematic Of Membrane Fusion Of Two Vesicles. Two Vesicles In Close Contact (Left), Hemifusion Stage (Middle) And Fused Vesicles (Right). 7

Figure 5: Schematic Of 1-Octanol. Carbon Atoms Are Shown In Cyan, Hydrogen In White And Oxygen In Red. 10

Figure 6: Schematic Of The System Used For The Calculation Of Δg Via The Method Of Direct Transfer (System S3). The Solute N-Butane Was Placed Initially At The Center Of Water Box. During The Simulation, The Solute Diffused From The Water Rich Phase To The 1-Octanol Rich Phase. A, B, C, D, E, F, G, H, And I Correspond To The Midpoint Of The 9 Abf Windows Along The Reaction Coordinate. The Corresponding Average Free Energy For Each Of The 9 Windows Is Shown As Filled Circles On The Pmf Profile. Arrow Shows The Direction Of Solute Transfer From Water Into 1–Octanol 26

Figure 7: Hydration Free Energy Profile Generated With Abf-Md Method For N-Alkane Transfer From Water To Vacuum (System S1). Dashed Line Denotes The Location Of The Interface. Data Shown Are From Calculations Performed With A 14 Å Lj Cutoff. 30

Figure 8: Hydration Free Energy For N–Alkanes As Predicted By Adaptive Biasing Force Molecular Dynamics Simulations With An Lj Cut–Off Of 14.0 Å (Red Diamonds); Thermodynamic Integration (Green Squares); Experiment (Black Circles). 32

Figure 9: Solvation Free Energy Profile Generated With Abf Method For N-Alkane Transfer From 1–Octanol To Vacuum (System S2). Dashed Line Denotes The Location Of The Interface. Data Shown Are From Calculations Performed With A 14 Å Lj Cutoff. 34

Figure 10: Solvation Free Energy For Transfer Of N–Alkanes From Vacuum Into 1–Octanol Predicted By Adaptive Biasing Force Molecular Dynamics Using A Lennard-Jones

Cut Off Of 14 Å For The Trappe-Ua Force Field (Red Diamonds); Thermodynamic Integration Green Squares); Gemc (Blue Triangles); Experiment (Black Circles). ... 36

Figure 11: Octanol–Water Partition Coefficient For *N*–Alkanes Predicted By Adaptive Force Bias Molecular Dynamics Simulations Using A 14 Å Lj Cutoff: Direct Transfer For 30 Å (Red Diamond) And 100 Å (Orange Triangles) 1-Octanol Box; Indirect Transfer (Blue Triangles); Thermodynamic Integration (Green Squares); Experiment (Black Circles). 39

Figure 12: Density Profiles For System S3. The Density Has Been Normalized By Average Bulk Density Of Each Component: Water (Green), 1-Octanol Ch2 (Black), 1-Octanol Oxygen (Red). Dashed Blue Line Represents Position Of The Interface. 41

Figure 13: Free Energy Profile Generated With Abf Method For Ethane (Red), Butane (Orange), Hexane (Green) And Octane (Blue) Transfer In System S3 From Water To 1–Octanol (Dry) Phase. Data Shown Are From Calculations Performed With A 14 Å Lj Cutoff. Dashed Black Line Marks The Location Of The Interface. 42

Figure 14: Free Energy Profile Generated With Abf Method For N-Alkane Transfer From Water To 1–Octanol (Dry) Phase In System S4. Data Shown Are From Calculations Performed With A 14 Å Lj Cutoff. 44

Figure 15: Top Panel: Number Integrals For Interactions Between Ch_2 (Octane) And O (1-Octanol). Bottom Panel: Number Integrals For Interactions Between Ch_2(Octane) And Ch_2(1-Octanol). System S3 (Black Line), System S4 (Red Line). 46

Figure 16: Distribution Of Samples Along The Reaction Coordinate From 8 Ns Abf–Md Simulations For The Transfer Of *N*-Pentane From Water To Vacuum (Red) And From 1-Octanol To Vacuum (Black). Distribution Was Constructed By Combining Data From The 5 Individual Simulations. 48

Figure 17: Evolution Of Sampling Histogram From 0.02 Ns To 1.0 Ns During 1.0 Ns Abf-Md Simulation. 50

Figure 18: Evolution Of Max-Min Ratio During 1ns Abf Md Simulation. 51

Figure 19: Schematic Diagram For The “Indirect Transfer Method”. (A) 1-Octanol And (B) Water Boxes Containing [Bmim][Ntf_2] Solute Are Shown. Six Windows Of 5 Å Bin Width Each In The Z-Direction Were Used To Compute The Potential Of Mean Force Using Abf–Md Simulations. The Arrow Suggests The Direction Of Solute Transfer With A Force *F* Along The Z Reaction Coordinate. Right: Average Free Energy Of Solvation Profiles Generated With Abf–Md For Six Ils Transferred From A 1-Octanol-Rich Phase To Vacuum (Top) And From A Water-Rich Phase To Vacuum. 59

Figure 20: Comparison Between 1-Octanol/Water Partition Coefficients Determined For [Bmim][X] Ils Using Abf–Md Simulations And Eqn. 1 And Experimental Values For Various Anions. X = Anion. 61

Figure 21: Distribution Of Sampling Along The Reaction Coordinate Showing Results For [Bmim][Tfo] Transfer From Water To Vacuum (Red) And 1-Octanol To Vacuum (Black). B) Temporal Evolution Of The Maxmin Ratio. 63

Figure 22: Electrostatic Potential Energy Surfaces Mapped To The Total Electron Density For Nitrobenzene, 1,4-Dinitrobenzene And 1,3,5-Trinitrobenzene. 72

Figure 23: Potential Of Mean Force As A Function Of Reaction Coordinate For The Hydration Of Selected Nitro-Aromatic Compounds. Zero Of The Reaction Coordinate Represents The Location Of The Water-Vacuum Interface. 79

Figure 24: Potential Of Mean Force As A Function Of Reaction Coordinate For The Solvation Of Selected Nitro-Aromatic Compounds In 1-Octanol. Zero Of The X-Axis Corresponds To The Location Of The 1-Octanol-Vacuum Interface. 80

Figure 25: Log K_{ow} Predicted By The Trappe-Ua Force Field Vs. Experimental Data For The 11 Nitro-Aromatic Compounds Studied In This Work. Data Are Coded As Follows: Mononitro Compounds (Red Circles), Dinitro Compounds (Green Squares) And Trinitro Compounds (Blue Diamonds). 82

Figure 26: Log H Predicted By The Trappe-Ua Force Field Vs. Experimental Data For Six Nitro-Aromatic Compounds. Data Are Coded As Follows: Mononitro Compounds (Red Circles), Dinitro Compounds (Green Squares). 84

Figure 27: Radial Distribution Functions For Dnan (Black) And 4-Nan (Red) In Water (Left Panel) And 1-Octanol (Right Panel). Labels Denote Interaction Sites On The Solvent (Water Or 1-Octanol), Followed By Interaction Sites On The Solute. 86

Figure 28: Snapshots From Molecular Dynamics Simulations Illustrating The Formation Of 1-Octanol Cages Around Dnan. Images Are From The Same Molecular Configuration And Have Been Rotated To Provide Alternate Views Of The 1-Octanol Chains. Alkyl Tails Of 1-Octanol Have Been Shown In Licorice Mode For Clarity............. 87

Figure 29: Schematic Representation Of The Simulant (A) Dmmp And The Three Nerve Agents (B) Sarin, (C) Soman And (D) Vx. 92

Figure 30: Schematic Diagram For The “Indirect–Transfer Method” Of Solute From Condensed Phase To Vacuum. 5 Windows Of 5 Å Bin Width Each In The Z Direction Were Used To Compute The Potential Of Mean Force. 98

Figure 31: A) Average Free Energy Of Hydration Profile Generated With Abf–Md For Solute Transfer From Water Phase To Vacuum Phase. B) Average Free Energy Of Solvation Profile Generated With Abf–Md For Solute Transfer From 1-Octanol To Vacuum Phase. 103

Figure 32: 6 Left Panel: Radial Distribution Functions Of The Octanol (A) And Water (B) Interacting With The Oxygen O2 Of Dmmp (Black), Sarin (Red), Soman (Orange) And Vx (Green) At 298 K. Middle Panel: The Corresponding Number Integrals Respectively. Right Panel........ 107

Figure 33: A) Distribution Of Sampling Along The Reaction Coordinates. Results Are For The Case Of Vx Transfer From Water To Vacuum (Red) And 1–Octanol To Vacuum (Black). B) Evolution Of The Maxmin Ratio During 10 Ns Of Abf-Md Simulation. 110

Figure 34: Mobility And Multimedia Exposure Chart. Zone A Has Heavy Multimedia, Multispecies And Bioaccumulation Concerns. Zone B Has Heavy Concerns Regarding Bioaccumulation. Zone C Has Concerns Regarding Atmospheric Problems. Zone D Has Heavy Concern For Dire Direct Effects On Water Column. Zone E And Zone F Are Low Ecotoxicology Concern Due To Very Low Mobility. Filled Circles Are Simulation Predictions While Experiment Is Denoted By Filled Squares........ 112

Figure 35: Schematic Of Model Compounds Used In This Study For Torsion Fitting Is Shown. A) Choline, B) Dimethylphosphate (Dmp), C) 2-Hexene, D) Hexane, E) Esterified Glycerol-Phosphate Analogue ((M)Pgly) And F)) Esterified Glycerol Analogue ((M)Egly). 122

Figure 36: Energy Scans Of Torsions From Lipid Headgroup Predicted With Trappe Force Field (Red Circle) And Compared With C36 Parameter Set (Black). A) N-C12-C11-O12, B) C1-C2-C3-O31, C) O11-C1-C2-C3, D) Ct2-Ct2-Ct2-Ct3, E) O12-P-O11-C1, F) O21-C21-C22-C23, G) C28-C29=C210-C211 And H) O13-P-O11-C1. 124

Figure 37: Evolution Of Area Per Lipid (Black) With Simulation Run Time Lipids Studied In This Work. Average Value Of Apl Predicted By Trappe Is Shown (Green-Dotted) And Compared With Experiment (Red), C36 (Blue) And Gromacs (Orange) Data. 127

Figure 38: Area Per Lipid Predicted By The Trappe-Ua Force Field For Lipid Bilayers Composed Of Phosphatidylcholine (Red Circles), Phosphatidylethanolamine (Orange Squares), Phosphatidylserine (Blue Triangles) And Phosphatidylglycerol (Green Triangles). 128

Figure 39: Density Profile Along The Bilayer Normal For Water (Black) And Glycerol (Orange) Components. Solid And Dotted Lines Represent Spce And Tip3 Systems Respectively. 129

Figure 40: Radial Distribution Function For Interaction Of Water Oxygen Atoms With Oxygen Atoms Of Glycerol Region In Dppc Lipid Bilayer. 130

Figure 41: Radial Distribution Functions For Interaction Of Cations: Sodium (Black) And Potassium (Red) With Phosphate (O2l) And Glycerol (Obl) Oxygen Atoms Of Dlpg Lipid Bilayer. 131

Figure 42: Non Bonded Potential Energy As A Function Of Distance Between Sodium Ion And Phosphate Oxygen In Dlpg Lipid Bilayer. Profile With $Na^{+\ Charmm}$ [1] Parameters Is Shown In Black And One With $Na^{+\ Aqvist}$ [2]Parameters Is Shown On Red. 133

Figure 43: Radial Distribution Function Profile For Interaction Of Sodium Ion (Black: $Na^{+\ Charmm}$ [1]; Red: $Na^{+\ Aqvist}$ [2]) With O2l (Phosphate Oxygen), Oslp (Phosphate Oxygen), Obl (Glycerol Oxygen) And Pl (Phosphorus) 134

Figure 44: Evolution Of Area Per Lipid As A Function Of Simulation Run. Results Are Shown For Dlpg Lipid Bilayer With $Na^{+\ Charmm}$ [1] (Black) And $Na^{+\ Aqvist}$ [2] (Red) Parameters. 135

Figure 45: Volume Per Lipid Predicted By Trappe Force Field Compared To Experimental Data For Pc (Red Squares), Pg (Green Circles) And Ps (Blue Diamond) Lipid Bilayers. 137

Figure 46: Evolution Of Bilayer Thickness (Black) With Simulation Run Time Lipids Studied In This Work. Average Value Of Bilayer Thickness (D_{hh}) Predicted By Trappe Is Shown (Green-Dotted) And Compared With Experiment (Red), C36 (Blue) And Gromacs (Orange) Data. 142

Figure 47: Bilayer Thickness Predicted By Trappe Force Field And Compared To Experimental Data For Pc (Red), Pg (Green) And Ps (Blue) Lipid Bilayers. 143

Figure 48: [Top] Total Electron Density Profile For Dppc Bilayer Produced By Trappe Force Field. Experimental Data (Black), Simulation (Red). [Bottom]: Individual Component Density Profile For Dppc Bilayer Produced By Trappe Force Field. Simulation (Dotted) And Experiment (Solid) Are Shown For Components: Glycerol (Orange), Phosphate+Choline (Blue), Methylene (Red), Terminal Methyl (Green) And Water (Black). 145

Figure 49: Individual Component Density Profile For Bilayers Produced By Trappe Force Field Is Shown For Components: Glycerol (Orange), Phosphate+Choline (Blue), Methylene (Red), Terminal Methyl (Green) And Water (Black). 147

Figure 50: Deuterium Order Parameters As Predicted By Trappe Parameters Are Shown For Sn-1 (Open Square) And Sn-2 (Open Circle) For Dppc, Dmpc, Dlpc And Popc Bilayers And Compared With C36 (Green Circle) And Experimental Data (Red Triangle). 150

Figure 51: Form Factors Predicted By Npt Molecular Dynamics Simulations (Black Solid Line) For Dppc, Dmpc And Dlpc And Compared With Experimental Data For Unilamella Vesicles (Red Square) And Oriented Samples (Red Circles). 152

Figure 52: Form Factors Predicted By Npt Molecular Dynamics Simulations (Black Solid Line) For Dlpg, Dmpg And Dopg; Compared With Experimental (Red Circles) Data.... 153

Figure 53: Initial Configuration Showing Ca^{2+}-Bound C2a Domain Of Syt-1 Close To Anionic Lipid Bilayer (At T= 0 Ns). Nitrogen Atoms In Lipid Headgroup Are Shown As Blue Spheres. Residues Known To Penetrate The Bilayer (Shown In Red) Are Placed At A Distance Of 2.0 From The Bilayer Surface. Ca^{2+} Ions Are Shown As Green Spheres. 161

Figure 54: System Configuration After 10.0 Ns Showing Ca2+-Bound C2a Domain Of Syt-1 Close To Anionic Lipid Bilayer . Nitrogen Atoms In Lipid Headgroup Are Shown As Blue Spheres. Residues Known To Penetrate The Bilayer (Shown In Red) Have Practically Inserted Into The Bilayer. Ca^{2+} Ions Are Shown As Green Spheres..... 163

Figure 55: Initial Configuration Showing Ca^{2+}-Bound C2b Domain Of Syt-1 Close To Anionic Lipid Bilayer (At T= 0 Ns). Nitrogen Atoms In Lipid Headgroup Are Shown As Blue Spheres. Residues Known To Penetrate The Bilayer (Shown In Orange) Are Placed At A Distance Of 2.0 Å From The Bilayer Surface. Ca^{2+} Ions Are Shown As Green Spheres. 164

Figure 56: System Configuration After 10.0 Ns Showing Ca2+-Bound C2b Domain Of Syt-1 Close To Anionic Lipid Bilayer. Nitrogen Atoms In Lipid Headgroup Are Shown As Blue Spheres. Residues Known To Penetrate The Bilayer (Shown In Orange) Have Practically Inserted Into The Bilayer. Ca^{2+} Ions Are Shown As Green Spheres..... 164

Figure 57: Docked Syt-1 In Bilayer. Variation In Distance Between Ca2+ Ions And Syt-1 (Black) ; Bilayer And (Red) W.R.T. Run Time. 166

Figure 58: Applied Force Vs. Run Time For Pulling The C2b Domain Away From Acidic Bilayer. Profile For Bilayer Bound And Bilayer Free Syt-1 Is Shown In Red And Black Respectively. 167

Figure 59: Post Simulation Configuration Of C2b Domain After Removal Of Ca2+ Ions From The Designated Pockets. Residue 367 (Orange) Is Ejected From The Bilayer Surface. 169

Figure 60: Electrostatic Potential Maps Of Ca^{2+}-Bound (Left) And Ca^{2+}-Free (Right) C2a Domain. Red And Blue Colors Denoted Negatively And Positively Charged Surfaces Respectively. 171

Figure 61: Electrostatic Energy Vs. Distance Between Anionic Bilayer (Pc/Ps) And Approaching C2b Domain. Resulting Profile For System With Ca2+ - Free C2b Is Shown In Red And With Ca2+ - Bound C2b Is Shown In Blue Color. 172

Figure 62: : Force Required In Bringing C2a Domain Close To Anionic Bilayer (Pc/Ps) Surface Plotted As A Function Of Distance. Resulting Profile For System With Number Of Bound Ca2+ Ions Equal To 0 And 3 Are Shown In Black And Red Colors Respectively. 174

Figure 63: Force Required In Bringing C2b Domain Close To Anionic Bilayer (Pc/Ps) Surface Plotted As A Function Of Distance. Resulting Profile For System With Number Of Bound Ca2+ Ions Equal To 0, 1 And 2 Are Shown In Black, Red And Blue Colors Respectively. 175

Figure 64: Potential Of Mean Force Between Pc/Ps (65:35) Bilayer And C2a Domain Of Syt-1. Red Profile Is For The Ca2+ Free C2a Domain And Black Profile Is For The Ca2+ Bound C2a Domain. 177

Figure 65: Schematic Of A Snare Complex. Syntaxin1-A Is Shown In Red, Vamp-2 In Blue And The Two Coils Of Snap-25 In Orange And Green. 179

Figure 66: Smd Pulling Force Plotted Versus Distance Between Fixed And Smd Atom. Peaks Denote The Dissociation Of Residue Pares. Peak 6 Marks The Point Where Vamp-2 Completely Dissociates From The Complex. 180

Figure 67: Electrostatic Energy Between Vamp-2 And (T)-Snares Plotted Versus Distance Between Fixed And Smd Atom. Jumps In Energy Correspond To Peaks In Force Curve. Flat Region After Peak-6 Point Is Due To Complete Dissociation Of The Snare Complex. 181

LIST OF TABLES

Table 1: Hydration free energies δghyd for n–alkanes predicted by trappe-ua force field 31

Table 2: Comparison of log kow for n–alkanes predicted using spc/e and tip4p water models. data are shown for simulations using a 14.0 å lj cut–off.. 33

Table 3: Solvation free energies (δgsolv) for n–alkanes in 1–octanol predicted using trappe-ua force field.. 35

Table 4: Effect of water saturation of the octanol phase on the free energies of solvation and partition coefficients for *n*–alkanes. data shown are for simulations using a 14.0 å lj cut–off... 37

Table 5: Octanol–water partition coefficients (log kow) predicted by the trappe-ua force field for n–alkanes. 38

Table 6: Sampling efficiency and max-min ratio at the end of abf simulations. data shown are for the case of *n*-pentane transfer from 1–octanol to vacuum (system s1), *n*-pentane transfer from water to vacuum (system s2) and of *n*-pentane transfer from water to 1–octanol (system s3)... 52

Table 7: Predictions of the trappe-ua force field for free energies of hydration, solvation in 1-octanol, log k_{ow} and log h for nitro-aromatic compounds. 76

Table 8: Comparison of the free energy of hydration, 1-octanol/water partition coefficient and henry's law constant predicted using abf–md simulations at 298 k and experiment. .. 101

Table 9: Area per lipid (apl), volume per lipid (vpl) and bilayer thickness (d^{hh} and d^{b}) as predicted by trappe force field.. 139

Table 10: Systems studied in this work. 158

Table 11: Summary of results for c2a domain interacting with lipid bilayers........................... 160

Table 12: Summary of results for c2b domain interacting with lipid bilayers. 162

Chapter 1: Introduction & Overview

Lipid bilayer

Lipid bilayer is an essential and universally occurring component in living organisms as a part of cellular membranes. The role of a bilayer is critical as it provides a definite boundary to cell which acts as a barrier to various biological molecules from getting in and out of the cell without the use of proper regulatory factors. In a way lipid bilayer compartmentalizes various biological components, keeping them separate from each other owing to the impermeable membrane structure. Lipid bilayer is made of two distinct monolayers packed together as sheet which is around 4-5 nanometers in thickness and comprises of various lipids. Water and other ions can pass through the membrane with the help of certain facilitators in the form of membrane proteins which are embedded in the bilayers and are specific to the type of molecule that needs to permeate through. Lipid bilayers frequently interact with various proteins during the cell signaling process which is a constant area of study and research. Cytoplasmic proteins are recruited to various cellular membranes during cell signaling and membrane trafficking. These proteins are collectively known as peripheral proteins which contain one or more modular domains specialized in lipid binding [3].

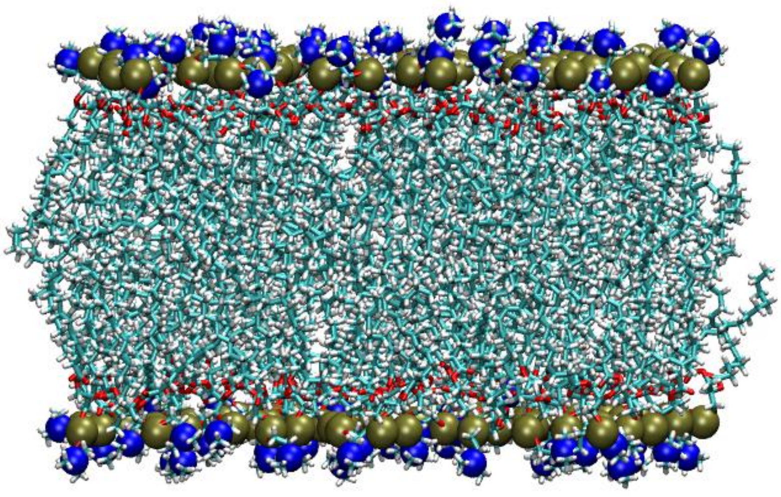

Figure 1: Lipid bilayer composed of POPC phospholipid. Headgroup phosphorus atoms are shown as golden spheres and nitrogen atoms as blue spheres. Lipid tails are colored in cyan.

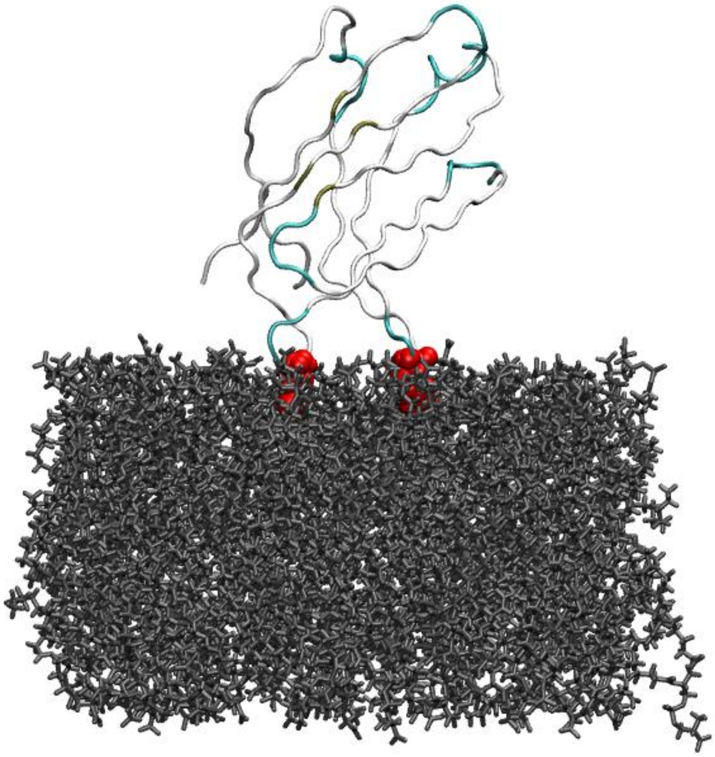

Figure 2: POPC lipid bilayer (grey) interacting with C2A domain of protein synaptotagmin (SYT). Membrane penetrating amino acid residues are shown in red.

Phospholipids are the building blocks lipid bilayer and are derived from fatty acids with the replacement of fatty acid by a phosphate group. They have a hydrophilic head on one end and a hydrophobic tail on the other which make phospholipids arrange in a bilayer like structure where the water-soluble phosphate ends on the outside and the carbon based hydrophobic tails on the inside. Depending on the lipid concentration and composition structures other than the bilayer can also be formed such as vesicles, micelles and lipid rafts. Phospholipids can be categorized into different types based on their headgroup and tail composition. Some common lipid head groups are phoasphatidylcholine (PC), phosphatidylserine (PS), phosphatidylethanolamine (PE) and phosphatidylglycerol (PG). Common fatty acid chains that make a phospholipid are palmitoyl, oleoyl, myristoyl and laureoyl varying on the basis of number of non-polar carbons and degree of saturation.

Chemical structures of three phospholipid head groups are shown below,

Phosphatidylcholine (PC)

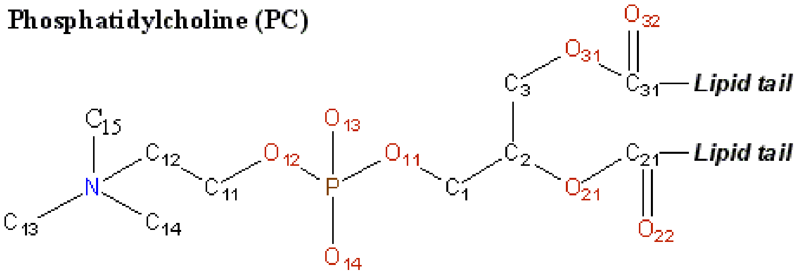
O32
O31
C3
C31
Lipid tail
C15
O13
C12
O12
O11
C2
C21
Lipid tail
N
P
C11
C1
O21
C13
C14
O22
O14

Phosphatidylethanolamine (PE)

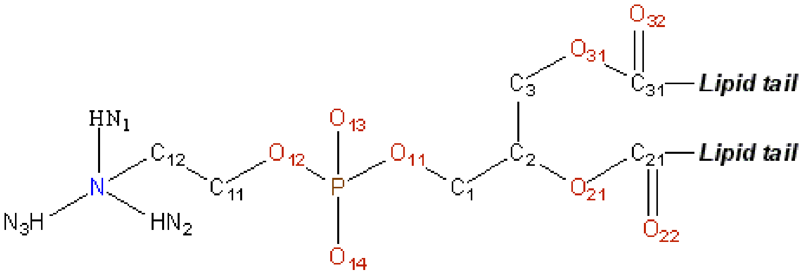
O32
O31
C3
C31
Lipid tail
HN1
O13
C12
O12
O11
C2
C21
Lipid tail
N
P
C11
C1
O21
N3H
HN2
O22
O14

Phosphatidylserine (PS)

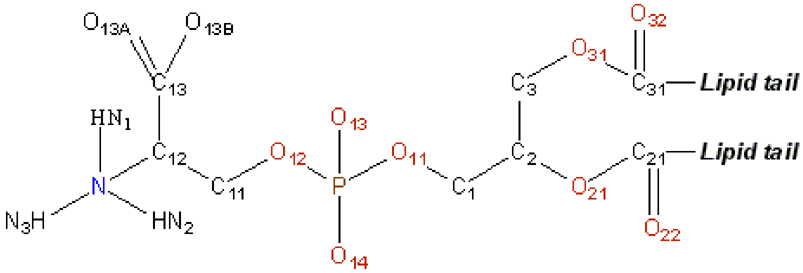
O13A
O13B
O32
O31
C13
C3
C31
Lipid tail
HN1
O13
C12
O12
O11
C2
C21
Lipid tail
N
P
C11
C1
O21
N3H
HN2
O22
O14

Figure 3: Chemical structure of phospholipid headgroups.

Membrane fusion

Membrane fusion of apposed bilayers is one of the most fundamental and frequently occurring biological phenomena in living organisms. It is an essential step in several cellular processes such as neuronal exocytosis, sperm fusion with oocytes and intracellular fusion of organelles to name a few. The process occurs at sub-millisecond time scale and involves the release of neurotransmitter from the synaptic vesicle into the pre-synaptic plasma membrane once the vesicle and target membrane merge and fuse with each other. All fusion reactions embody an elementary process that includes membrane contact, membrane merger, and the opening of an aqueous fusion pore[4]. Fusion can either be heterotypic which occurs when a membrane fuses with a dissimilar type of membrane body such as, a vesicle with a plasma membrane as in synaptic vesicle exocytosis or homotypic which involves similar compartments such as fusion of two vesicles in endosome–endosome fusion process [5]. Membrane fusion process is energetically unfavorable which means in thermodynamics terms that energy needs to be supplied through external factors in order to complete the process which is due to the existence of various high energy barriers. One of the main energy barriers is to bring the two membrane bodies in close contact with each other in order to provide a starting point for fusion process. This requires protein clearance where different proteins between the two membranes must be cleared also known as ‘sieving’ process followed by overcoming the electrostatic energy barriers formed by negative charge on the membrane surfaces which causes repulsion between the membranes. This is followed by the barriers related to curvature deformations during hemifusion-stalk and fusion-pore formation and expansion [6].

Various factors have been identified that lower these energy barriers thereby facilitating the fusion process [7, 8]. One such factor is the SNARE (soluble NSF attachment protein receptor) family of proteins. SNARE proteins are known to bring the vesicle and target membrane in a close proximity by forming a tight zipper like complex between the vesicle bound v-SNARE protein, synaptobrevin (VAMP) and target membrane bound t-SNARE proteins, syntaxin and SNAP-25 which is proposed to result in membrane fusion [9-12].

Ca^{2+} is known to regulate this event in a precise manner although the exact mechanism at the molecular level is still unknown. Another protein which has been identified to play a significant role in membrane fusion is synaptotagmin-1 (SYT-1). SYT-1 function is directly linked to the SNARE complex and has shown to have a direct effect on the kinetics of exocytosis [13].

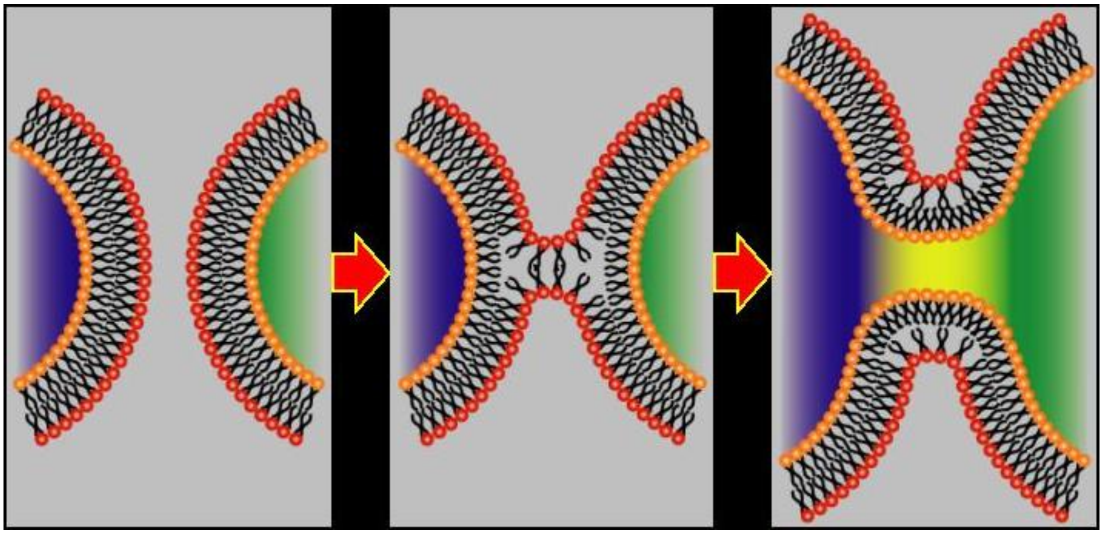

Figure 4: Schematic of membrane fusion of two vesicles. Two vesicles in close contact (left), hemifusion stage (middle) and fused vesicles (right).

Main objective of this research is to identify and understand the role of such factors in membrane fusion by studying the phenomena at the atomic detail with the use of molecular simulation. This study intends to provide a better understanding of the fusion process with applications in medical arena especially in the field of targeted drug delivery. Two major factors that have been identified and studied experimentally are the protein Synaptotagmin and SNAREs. In addition, Ca^{2+} is known to play a crucial role in this process, however the exact mechanism of action is still unknown. Role of Ca^{2+} in the interactions between SYT and bilayer membranes is also studied.

Octanol-water partition coefficients

Partition coefficient, in general, is defined as the ratio of solute concentration in two partially miscible solvents at equilibrium. This occurs when a compound has a tendency to distribute itself between two solvents which are immiscible with each other and are able to dissolve the solute to a partial extent. It provides a measure of difference of the compound solubility in two immiscible phases.

The two solvents to be chosen for calculation of partition coefficient strictly depends on the problem at hand. For example, in problems related to organic chemistry, it was found out that use of solvents with a big polarity difference facilitate the distribution and purification of desired products [14]. For biologically relevant problems, 1-octanol was chosen to be the most efficient solvent as it mimics the biological environment owing to the unique structure represented by a hydrophilic head and a hydrophobic tail. This structure resembles the lipid bilayers and cell membranes which are at the center of partitioning of biological molecules. In conjunction with water, the specific parameter is termed as 1-octanol water partition coefficient which is defined as the ratio of solute concentration in the 1-octanol phase to that in the water phase when the two solvents are at equilibrium.

Mathematically it is expressed as,

$$K_{OW} = \frac{C^{1-Oct}}{C^{Water}}$$

Equation 1

Where, K_{OW} is the octanol water partition coefficient, $C^{1\text{-Oct}}$ is the concentration of solute in 1-octanol phase and C^{Water} is the concentration of solute in water when the two phases are at equilibrium.

Solute that stays preferentially in water is termed as hydrophilic and if the concentration is higher in 1-octanol phase, then it is termed as hydrophobic.

The octanol–water partition coefficient, first introduced by Hansch and Fujita[15], is perhaps the most important quantity for the prediction of pharmacological and environmental properties for trace solutes[16]. K_{OW} has been used extensively for the prediction of a wide variety properties for drug molecules and trace pollutants; examples include bioactivity[17], bioaccumulation potential[18-20], skin permeability[21, 22] and soil–water partitioning[23, 24].

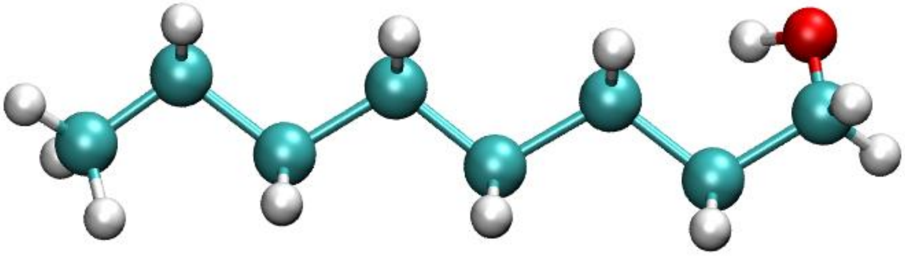

Figure 5: Schematic of 1-octanol. Carbon atoms are shown in cyan, hydrogen in white and oxygen in red.

This work describes the application of the adaptive force bias method, combined with molecular dynamics simulations (ABF-MD), for the direct calculation of 1–octanol–water partition coefficients. The ABF methodology [25-29] offers a number of potential advantages over existing methods for the calculation of free energies of transfer, perhaps the most important of which is that the ABF method eliminates the need for reference solutes and therefore provides a robust method for determination of the absolute free energies of transfer.

CHAPTER 2: Simulation Methodologies

Molecular dynamics

Molecular dynamics is a computational method used to simulate the system of interest and generate system properties at the microscopic level. The output is in the form of atomic level coordinates and velocities which is converted to macroscopic level properties such as pressure, energy etc. with the use of statistical mechanics.

Theoretically, this method is based on Newton's second law of motion which states that acceleration of an object is directly proportional to the force applied on the object in the direction of motion and inversely proportional to the mass of object. System under study may contain a given number of atoms and initial force on each atom from which the acceleration can be determined. Equations of motion are then integrated which yield information about the position, velocity and acceleration of each atom in the system as a function of time. This allows the system to evolve as a function of time and from this system trajectory, various properties can be determined.

Molecular dynamics simulations can be computationally expensive but with the significant advancements in the field of computational power it is getting easier to simulate a wide variety of systems. Molecular dynamics based simulations serve as an essential tool to understand the physical properties of biological macromolecules [30]. The first molecular dynamics simulation of a biologically relevant molecule was published in the year 1977 [31]. Increment in computational power can be understood from the fact that the original simulation was less than 10 picosecond in length compared to the current scale of 10-100 nanosecond which is around 1000 times faster but require 1/50th of the time for a particular system [30].

In this work, molecular dynamics simulations have been employed to study a range of biological as well as other systems by the generation of equilibrium properties. NAMD software engine has been employed throughout this study to run molecular dynamics simulations. VMD is employed for system and trajectory visualization followed by relevant analysis.

NAMD has been developed by Schulten and coworkers to enable high performance computing of large biomolecular systems. It is a parallel molecular dynamics code which has the capability to employ computers in parallel thereby increasing the computational efficiency [32].

Potential energy used to describe interactions between various atoms in the system forms the backbone of anu molecular dynamics simulation and defines the accuracy of the calculation. This potential energy function on a whole is termed as “force field”.

General force field potential function comprises of interactions of the bonded type and non-bonded type between atoms. Bonded interactions are further classified as bond, angle or dihedral interactions where the atoms are attached together by a covalent bond. Non-bonded interactions are of two types: one accounting for the electrostatic interactions between atoms and second for the van der Waal’s forces.

In NAMD, these interactions are described by the following functions,

Bonded Interactions

a) Bond : This term describes interactions between atom pairs which are separated by a covalent bond and is represented as a harmonic potential function,

$$U_{BOND} = \sum_{i} k_i^{bond} (r_i - r_0)^2$$

Equation 2

where, k^{bond} is the bond force constant, r_i and r_0 are the measured and equilibrium bond distance.

b) Angle : This terms defines interactions between three atoms connected by covalent bonds using the harmonic function,

$$U_{ANGLE} = \sum_{i} k_i^{angle} (\theta_i - \theta_0)^2$$

Equation 3

where, k^{angle} is the angle force constant, θ_i and θ_0 are the measured and equilibrium angle.

c) Dihedral : This term describes the interactions between two atoms separated by three covalent bonds using a cosine series,

$$U_{TOR} = \sum_i k_i^{dih} \left[1 + \cos(n_i \emptyset_i - \gamma_i)\right]$$

Equation 4

where φ is the dihedral angle and γ is the phase angle, n is the multiplicity of torsions.

Adaptive biasing force

Standard methodologies for the determination of free energy differences, such as free energy perturbation and thermodynamic integration, are based on perturbation theory, where the free energy difference between two systems A and B can be written as

$$A_A - A_B = -kT \ln < \exp[-\beta(U_A - U_B)] >$$

Equation 5

Since this average is slowly convergent for all but the smallest transformations, it is expedient to split a single large perturbation into a series of smaller perturbations where the overall interaction of the solute with the solvent is represented by

$$U = \lambda U_B + (1 - \lambda) U_A$$

Equation 6

where λ varies between 0 and 1, with 1 corresponding to state B and 0 to state A. This methodology was demonstrated in the seminal work of Jorgenson and Ravimohan where free energy of solvation of methanol relative to ethane was determined [33], and has been used extensively over the last 30 years with various modifications, for example to avoid "end–point catastrophe," for the determination of relative free energies of solvation for numerous low molecular weight compounds.

Despite the widespread use of free energy perturbation, it is not the ideal methodology for the calculation of partition coefficients. First and foremost is the fact that the calculated free energies are relative to a reference solute, which in turn produces a partition coefficient relative to that of the reference solute. To determine the absolute value of the partition coefficient requires knowledge of the experimental partition coefficient for the reference solute. Furthermore, an accurate molecular model or "force field" is required for both the reference solute and the solute of interest. In principle it is possible to perform a perturbation from a ghost (non–interacting) particle to a fully interacting one [34], but a large number of intermediate states may be required to achieve convergence. Another method for the calculation of absolute free energies of transfer and partition coefficients is Gibbs ensemble Monte Carlo (GEMC)[35],[36]. In GEMC, two condensed phases are simulated concurrently and attempts are made periodically to "swap" the solute of interest between phases. The free energy of transfer is determined simply as the ratio of the number density of the solute in each phase[37].

$$\Delta G = 2.303\, RT \log\left(\frac{\rho_{water}}{\rho_{octanol}}\right)$$

Equation 7

This method works well for small solutes where reasonable acceptance rates for the transfer of solute molecules between phases may be achieved, but becomes impractical for larger molecules as the acceptance rate for molecule exchange goes to 0.

The ABF methodology[25-29] offers a number of potential advantages over existing methods for the calculation of free energies of transfer, perhaps the most important of which is that the ABF method eliminates the need for reference solutes and therefore provides a robust method for determination of the absolute free energies of transfer. Non-equilibrium methods based on Jarzynski's equality [38, 39], sometimes referred to as "fast growth" methods, in principle could also be used to determine partition coefficients without the need for reference solutes. However, calculations of fluoro-methane transfer across a water-hexane interface have shown the fast growth method produces poor results for these types of calculations, with a systemic bias and large statistical uncertainty compared to ABF. For this particular calculation of solute transfer across a liquid-liquid interface, the fast growth method fails because of the difficultly in achieving adiabatic switching of the external force applied along the reaction coordinate.

Adaptive biasing force (ABF) method is a technique developed by Darve *et al.* [25],[26, 27]to calculate the free energy difference of certain chemical or biological processes along generalized reaction coordinates in the system of interest. This method is a combination of probability density and constraint force methods, and is based on the thermodynamic integration of average force acting on coordinates, which is unconstrained.[25] As a part of ABF algorithm, an external biasing force, estimated locally from the sampled conformations of the system, is applied at each step to facilitate the system in overcoming significant energy barriers along the reaction coordinate. This allows the system to evolve freely without constraints, enabling the simulation to visit multiple states separated by high free energy barriers and improving sampling long the reaction coordinate. The theoretical foundation of this method is based on Equation 5, which is a modified version of the expression proposed by Darve and Pohorille[25, 26] for the effective force (F^u) acting on the reaction coordinate (ξ),

$$\boldsymbol{F_{\xi}^{u} = m_{\xi}\frac{d^2\xi}{dt^2} + \frac{1}{\beta}\sum_{k=1}^{3M}\frac{1}{m_k}\frac{d\xi}{dx_k}\frac{dm_{\xi}}{dx_k}}$$

Equation 8

where m_k are generalized masses associated with generalized coordinates represented by $x_{k.}$

The average of this applied force is equal and opposite to the mean force acting on ξ and cancels the free energy derivative computed for small intervals of reaction coordinate ξ so that the system can evolve and overcome free energy barriers.

$$\langle\frac{\partial H}{\partial \xi}\rangle_{\xi} = -\langle F_{\xi}^{u}\rangle_{\xi}$$

Equation 9

The Helmholtz free energy $\boldsymbol{A}$ at constant temperature T, constant volume V and number of particles N is given by:

$$A\,(N,V,T) = -k_b\,T \log Z(N,V,T)$$

Equation 10

where $\boldsymbol{Z}$ is the canonical partition function and $\boldsymbol{k_b}$ is the Boltzmann's constant.

The free energy as a function of the reaction coordinate can be written as:

$$A\,(N,V,T,\xi) = -k_b\,T \log \frac{\int \exp[-\beta H(x,p)]\delta(\xi(x)-\xi_o)dx\,dp}{\Lambda^{3M}\,N!}$$

Equation 11

where Λ is the thermal de Broglie wavelength and p is the conjugate momenta of position coordinate x.

It is more convenient to compute the free energy difference $\Delta\,\boldsymbol{A_{a\rightarrow b}}$ between state A and B for a system. The states A and B are based on the reaction coordinate which is a function of the particle position.

$$\Delta\,A_{a\rightarrow b} = \int_{\xi_a}^{\xi_b} \frac{dA(\xi)}{d\xi}\,d\xi$$

Equation 12

The first derivative of the free energy is related to the partial derivative of the Hamiltonian of the system with the reaction coordinate and therefore based on Equation 12 can be related to the constraint force acting along the reaction coordinate

$$\Delta\,A_{a\rightarrow b} = \int_{\xi_a}^{\xi_b} \frac{dA(\xi)}{d\xi}\,d\xi = \int_{\xi_a}^{\xi_b} \langle\frac{dH(\xi)}{d\xi}\rangle_{\xi}\,d\xi = \int_{\xi_a}^{\xi_b} -\langle F_{\xi}^{u}\rangle_{\xi}\,d\xi$$

Equation 13

Further details of the ABF method and formulation including the implementation in NAMD [32] molecular dynamics package can be found in these publications [25-29] [40-42]. The Helmholtz free energy ***A*** obtained from *NVT* ensemble simulations is in close approximation to the Gibbs free energy ***G*** in condensed phase.[43] The Gibbs free energy difference is used to compute the free energy of hydration and partition function.

CHAPTER 3: Prediction Of 1-Octanol/Water Partition Coefficient For N-Alkanes Using Adaptive Biasing Force Method

*This work has been published in literature [44]

Background

The octanol–water partition coefficient, first introduced by Hansch and Fujita[15], is perhaps the most important quantity for the prediction of pharmacological and environmental properties for trace solutes[16]. Numerous experimental methods have been developed for the determination of log K_{ow}. These include the shake flask [14, 45-47], slow–stir [48], reverse phase high performance liquid chromatography (HPLC) [49-51], generator column [52] and voltammetry [53, 54]. The shake flask method is widely used due to its simplicity, however, this method is unreliable for solutes with poor water solubility (log K_{ow} >5) due to the formation of 1–octanol emulsions in the aqueous phase[16, 55]. Other methods, such as generator column and HPLC avoid the problem of octanol microemulsion formation, but are generally limited to neutral species and hydrophobic solutes[56]. More recently, voltametric methods have been developed for the determination of log K_{ow} for zwitterionic and charged species, such as drug molecules and surfactants, which due to their amphiphilic nature tend to partition at the octanol–water interface, making traditional shake–flask experiments unreliable [53],[57],[58].

Motivated by the acute need for octanol–water partition coefficients, which are required for the development of many consumer products, computational methods known as Quantitative

Structure Property Relationships (QSPR) have been developed in an attempt to relate known molecular properties, such as structure, functional groups, dipole moment, etc, with various physical properties, such as aqueous solubility, vapor pressure, and octanol–water partition coefficient[59-66]. There are numerous variants of QSPR, but in general, a large number of “descriptors” are fit to reproduce a specific physical property (vapor–pressure log K_{ow}, etc) for molecules in the “training set”. Training sets may contain anywhere from a few hundred to tens of thousands of molecules, and in general, the larger the training set, the better the predictive capability. Overall, most QSPR do an excellent job of predicting physical properties for molecules with similar molecular structure as those in the training set. However, for molecules that differ significantly from those used in the optimization of the QSPR, the predictions may be unreliable [67, 68]. In particular, the use of QSPR for energetic materials and molecules with amphiphilic character has been particularly problematic [69-73].

Computer simulations using atom–based potential functions provide another computational route to the prediction of octanol–water partition coefficients. Recognizing that the partition coefficient is related to the Gibbs free energy of transfer between 1-octanol and water phases

$$\log K_{OW} = \frac{\Delta G}{2.303RT}$$

Equation 14

it is possible to determine log K_{ow} directly as long as a suitable methodology exists for the determination of $\boldsymbol{\Delta G}$.

Despite the widespread use of free energy perturbation, it is not the ideal methodology for the calculation of partition coefficients. First and foremost is the fact that the calculated free energies are relative to a reference solute, which in turn produces a partition coefficient relative to that of the reference solute. To determine the absolute value of the partition coefficient requires knowledge of the experimental partition coefficient for the reference solute. Furthermore, an accurate molecular model or "force field" is required for both the reference solute and the solute of interest. In principle it is possible to perform a perturbation from a ghost (non–interacting) particle to a fully interacting one[34], but a large number of intermediate states may be required to achieve convergence. Another method for the calculation of absolute free energies of transfer and partition coefficients is Gibbs ensemble Monte Carlo (GEMC)[35],[36]. In GEMC, two condensed phases are simulated concurrently and attempts are made periodically to "swap" the solute of interest between phases. The free energy of transfer is determined simply as the ratio of the number density of the solute in each phase[37].

$$\Delta G = 2.303\ RT \log\left(\frac{\rho_{water}}{\rho_{octanol}}\right)$$

Equation 15

This method works well for small solutes where reasonable acceptance rates for the transfer of solute molecules between phases may be achieved, but becomes impractical for larger molecules as the acceptance rate for molecule exchange goes to 0.

This work describes the application of the adaptive force bias method, combined with molecular dynamics simulations (ABF-MD), for the direct calculation of 1–octanol–water partition coefficients. The ABF methodology[25-29] offers a number of potential advantages over existing methods for the calculation of free energies of transfer, perhaps the most important of which is that the ABF method eliminates the need for reference solutes and therefore provides a robust method for determination of the absolute free energies of transfer. Non-equilibrium methods based on Jarzynski's equality[38, 39], sometimes referred to as "fast growth" methods, in principle could also be used to determine partition coefficients without the need for reference solutes. However, calculations of fluoro-methane transfer across a water-hexane interface have shown the fast growth method produces poor results for these types of calculations, with a systemic bias and large statistical uncertainty compared to ABF. For this particular calculation of solute transfer across a liquid-liquid interface, the fast growth method fails because of the difficultly in achieving adiabatic switching of the external force applied along the reaction coordinate. As will be shown later in this work, the ABF method is able to provide accurate values of hydration and solvation free energies with a computational effort comparable to calculations performed with traditional thermodynamic integration. The methodology presented here will work for nearly any solute, and the predicted free energies are insensitive to the choice of simulation parameters.

Simulation Details

In this work the adaptive biasing force method was used to determine the free energies of solvation for *n*–alkane solutes from C_1 to C_8 (methane to octane) in 1–octanol and water, and these data were used to determine the octanol–water partition coefficient log K_{ow}. Adaptive biasing force (ABF) method is a technique developed by Darve *et al.* [25],[26, 27]to calculate the free energy difference of certain chemical or biological processes along generalized reaction coordinates in the system of interest. This method is a combination of probability density and constraint force methods, and is based on the thermodynamic integration of average force acting on coordinates, which is unconstrained. As a part of ABF algorithm, an external biasing force, estimated locally from the sampled conformations of the system, is applied at each step to facilitate the system in overcoming significant energy barriers along the reaction coordinate. This allows the system to evolve freely without constraints, enabling the simulation to visit multiple states separated by high free energy barriers and improving sampling long the reaction coordinate.

The TraPPE force field was used for *n*–alkanes[74] and 1–octanol[75], while the SPC/E[76] and TIP4P[77] force fields were used for water.

Two approaches for the calculation of 1–octanol–water partition coefficients were evaluated. The first, denoted as "indirect transfer," (IT) involved the calculation of the free energy of solvation for the water and octanol phases separately. These free energies were combined according to Equation (11)

$$\Delta \boldsymbol{G} = \Delta \boldsymbol{G}_{\boldsymbol{HYD}} - \Delta \boldsymbol{G}_{\boldsymbol{SOLV}}$$

Equation 16

where ΔG_{HYD} is the free energy of hydration in water and ΔG_{SOLV} is the free energy of solvation in 1–octanol for the considered solute, to provide the overall free energy of transfer from water to 1–octanol phase. In the second approach, termed "direct transfer," (DT) the free energy of transfer from water to octanol phases is determined directly in a simulation containing both a water and 1-octanol phase in contact. From the free energy of transfer, it is possible to determine the 1–octanol–water partition coefficient according to Equation 1.

Four different configurations were generated for the required calculations: separate water|vacuum (S1) and 1–octanol|vacuum (S2) systems for the indirect transfer (IT) approach , and two types of combined water/1–octanol systems for the direct transfer (DT) approach; one with an extended cell size in the z-direction (S3) compared to the other one (S4) For systems S1 and S2, a rectangular simulation cell was used, with dimensions 30 Å x 30 Å x 60 Å, with the condensed phase occupying a region approximately 30 Å x 30 Å x 30 Å. For system S3, a rectangular simulation cell was used with dimensions 30 Å x 30 Å x 200 Å , which included a 30 Å x 30 Å x 50 Å water phase, and a 30 Å x 30 Å x 100 Å 1-octanol phase. This cell was extended to 200 Å in the z–direction with a 50 Å vacuum region, which was necessary to prevent interactions of the solute with the condensed phases through periodic boundary conditions. System S4 consisted of a 30 Å x 30 Å x 30 Å water region in contact with a 30 Å x 30 Å x 30 Å 1-octanol phase. A schematic for the direct transfer approach is shown in **Figure 6** for the calculation of ΔG for the transfer of *n*-butane from water to 1-octanol.

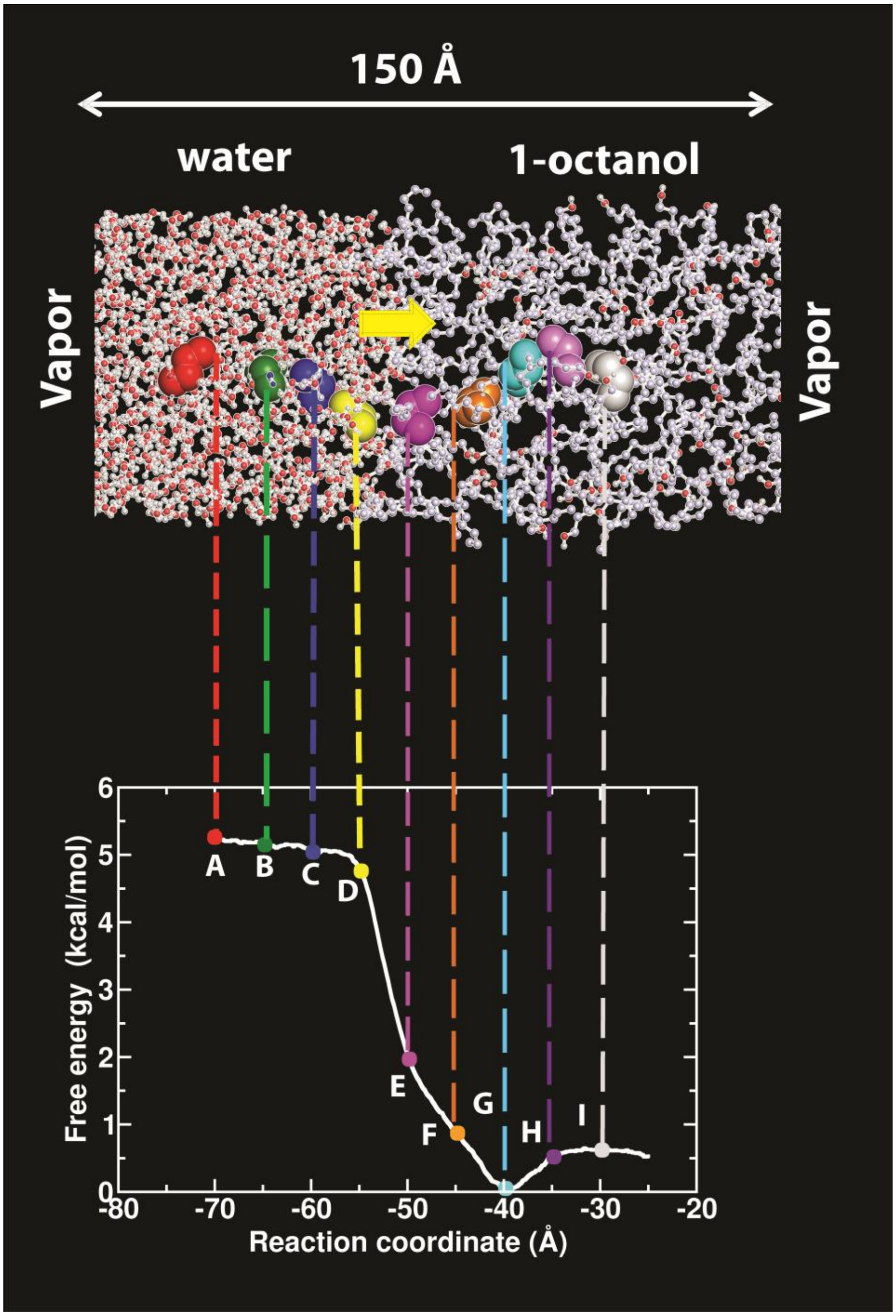

Figure 6: Schematic of the system used for the calculation of ΔG via the method of direct transfer (system S3). The solute n-butane was placed initially at the center of water box. During the simulation, the solute diffused from the water rich phase to the 1-octanol rich phase. A, B, C, D, E, F, G, H, and I correspond to the midpoint of the 9 ABF windows along the reaction coordinate. The corresponding average free energy for each of the 9 windows is shown as filled circles on the PMF profile. Arrow shows the direction of solute transfer from water into 1–octanol

The free energies corresponding to nine different locations (windows) along the reaction coordinate are shown to illustrate the relationship between the free energy profile and solute location. The number of molecules in each box was selected to reproduce the density of water or 1–octanol predicted by *NPT* simulations at 1 atm and 298 K for a specific potential truncation (10 or 14 Å). For calculations where Lennard–Jones interactions were truncated at 10 Å, 1–octanol and water systems S1, S2, S4 contained 99 and 893 molecules, respectively. For systems utilizing a 14 Å cut–off, 102 and 896 1-octanol and water molecules were used, respectively. System S4 contained 339 1-octanol and 1500 water molecules. It should be noted that the TraPPE force field was developed using an analytical tail correction for Lennard–Jones interactions, and therefore it is expected that the predictions of simulations using a truncated potential will differ slightly from the original parameterization. In this case, the predicted densities for 1–octanol at 298 K and 1 atm were 0.795 (r_{cut} = 10 Å) and 0.814 (r_{cut} = 14 Å), which are in reasonable agreement with the experimental value of 0.826, but slightly less than predicted by the TraPPE force field when used with analytical tail corrections for the Lennard–Jones interactions.

The reaction coordinate for the determination of free energy changes was defined as the distance between the center of mass of the solute (COMS) under study and center of mass of the condensed phase (COMCP). In the initial system setup, the COMS was placed at approximately the COMCP. Over the course of simulation, the reaction coordinate spanned a distance of 45.0 Å for system S3, 25.0 Å for systems S1, S2 and S4 from the center of mass of the condensed phase to the center of the vacuum region, or center of mass of the 1–octanol phase. To reduce the statistical error of the calculations, the reaction pathway was divided into five equally sized non–overlapping windows of 5.0 Å for systems S1, S2 and S4. For system S3, the reaction coordinate was split into 12 windows, where the 10 Å section through the interface was split into 5 windows 2 Å wide and remainder of the reaction coordinate was split into 7 windows, each 5.0 Å wide. Smaller windows were chosen for the interfacial region to enhance sampling and improve the statistical quality of the PMF, which changes rapidly in this section of the reaction coordinate. To generate the initial configurations for each window, a 15,000 ps steered molecular dynamics simulation was performed where the solute was pulled with a constant velocity of 0.005 Å/fs along the reaction coordinate. Coordinates from the trajectory of this simulation were saved periodically to generate the initial coordinate files for each window. For the ABF calculations, force statistics were stored in bins of width 0.2 Å. The biasing force was applied after 500 samples were collected in each bin. To keep the solute within the specified window, a harmonic force with a magnitude of 10.0 kcal/mol/Å was applied on the upper and lower boundary of the window along the z–axis of the simulation cell.

Molecular dynamics simulations were performed with NAMD version 2.7b3[78]. Initial configurations for each system were generated with Packmol [79]. Energy minimization was performed on all systems for 500 steps using the steepest decent technique. Systems were equilibrated over a time period of 2.0 ns in isobaric–isothermal ensemble at 1.0 atm and 298 K, followed by the ABF-MD calculation in *NVT* ensemble. For all calculations, the temperature was maintained at 298.0 K using Langevin dynamics. For initial *NPT* simulations, used to determine the density of each system, constant pressure was maintained at 1.0 atm using the

Nose–hoover algorithm[80],[81]. A timestep of 2.0 fs was used for the integration of Newton's equation of motion. Periodic boundary conditions were used in all the three spatial coordinates. Long range electrostatic interactions were calculated with particle–mesh Ewald algorithm[82, 83]. A switching function was applied for all Lennard–Jones interactions at 8.5 Å for the 10.0 Å cut–off and at 12.5 Å for 14.0 Å cut–off. Data were analyzed using visual molecular dynamics [84]. Statistical errors were estimated from the standard deviation of the predicted free energies generated from 5-10 unique sets of simulations.

Results and Discussion

Free energy of hydration

The free energy of hydration for *n*–alkanes has been studied extensively both experimentally[14] and with atom–based simulations.[33],[34],[85],[86] The wealth of data available makes this an ideal system for validation of the adaptive force bias methodology. Hydration free energies were determined for each solute at 298 K by transferring the solute from the center of the condensed water phase to a vacuum region. The potential of mean force (PMF) for each solute as a function of distance is plotted in **Figure 7.**

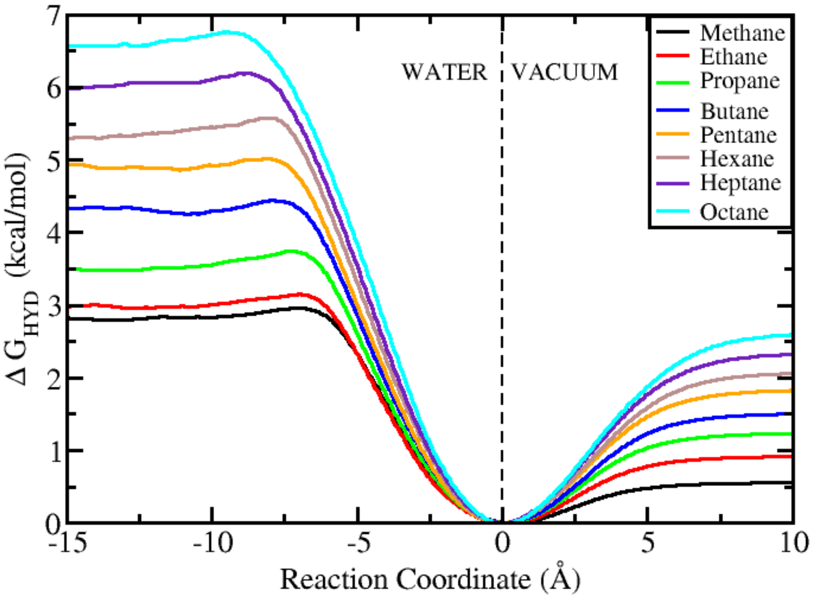

Figure 7: Hydration free energy profile generated with ABF-MD method for n-alkane transfer from water to vacuum (system S1). Dashed line denotes the location of the interface. Data shown are from calculations performed with a 14 Å LJ cutoff.

These data correspond to simulations of the TraPPE–UA force field for *n*–alkanes and the SPC/E force field for water. As the solute moves through the water region, the PMF is flat until the solute is within 5 Å of the interface, at which point the PMF drops rapidly to a minimum, and then increases as the solute moves from the water phase to the vacuum region. The free energy of transfer is determined from the difference in the measured PMF near the centers of each region. The fact that the PMF is invariant over 5 Å of the initial and final sections of the reaction coordinate suggests the simulation cell is large enough that the measured free energy of transfer was not affected by the proximity of the interface.

Table 1: Hydration free energies ΔGHYD for n–alkanes predicted by TraPPE-UA force field

Solute	ΔG_{HYD} (kcal/mol) 10.0 Å LJ cut–off	ΔG_{HYD} (kcal/mol) 14.0 Å LJ cut–off	TI–method [34]	Experiment [86, 87]
Methane	2.4 ± 0.2	2.3 ± 0.1	2.3 ± 0.1	1.98
Ethane	2.4 ± 0.1	2.1 ± 0.1	2.1 ± 0.1	1.81
Propane	2.6 ± 0.1	2.3 ± 0.1	2.4 ± 0.1	2.02
Butane	3.0 ± 0.1	2.8 ± 0.1	2.8 ± 0.1	2.18
Pentane	3.4 ± 0.1	3.1 ± 0.1	3.1 ± 0.1	2.36
Hexane	3.7 ± 0.2	3.3 ± 0.1	3.4 ± 0.1	2.58
Heptane	3.7 ± 0.1	3.7 ± 0.1	3.7 ± 0.1	2.65
Octane	3.9 ± 0.1	4.0 ± 0.2	4.2 ± 0.2	2.93

Values of the hydration free energy are presented in **Table 1** for *n*–alkanes C_1–C_8. Because the TraPPE force field was originally developed for use with analytical tail corrections for the Lennard–Jones potential, the effect of potential truncation on the free energies of solvation were also calculated. The data show that the difference between ΔG_{HYD} from truncation of the Lennard–Jones potential at 10 Å and 14 Å is within the statistical error of the calculation, which is 0.2–0.3 kcal/mol. While the choice of Lennard–Jones cut–off has a significant impact on the prediction of vapor–liquid coexistence, these data show that the free energy of hydration is relatively insensitive. For comparison, the recent calculations of Garrido *et al.*, who used thermodynamic integration to determine hydration free energies of alkanes[34], are included. The predictions of the ABF-MD calculations are in excellent agreement with prior thermodynamic integration calculations, as shown in **Figure 8**.

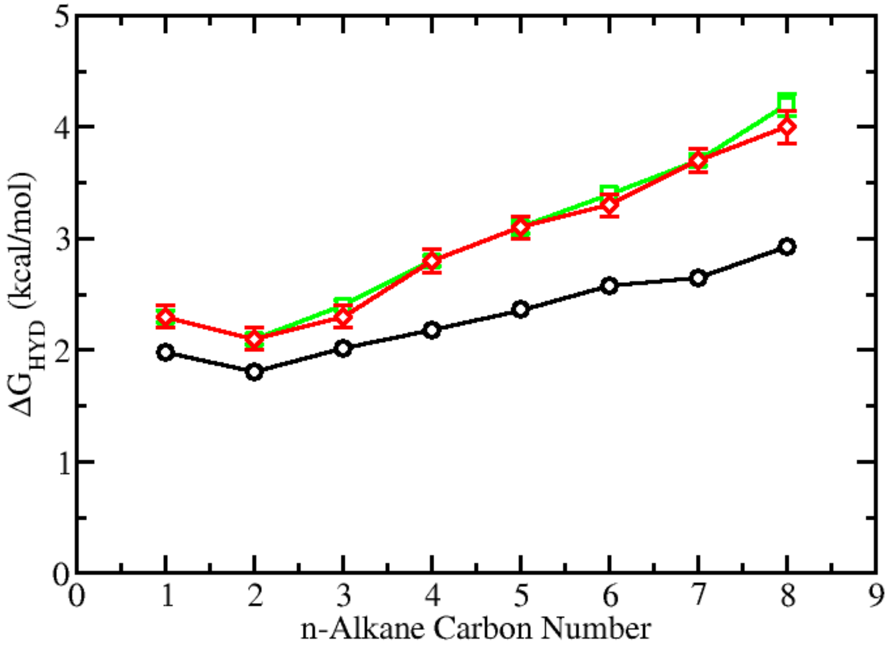

Figure 8: Hydration free energy for n–alkanes as predicted by adaptive biasing force molecular dynamics simulations with an LJ cut–off of 14.0 Å (red diamonds); thermodynamic integration (green squares); experiment (black circles).

The close agreement of the ΔG_{HYD} predicted by both studies is also of interest because Garrido *et al* used the MSPC/E water model [88], while the SPC/E force field was used for water in this work [76]. To further investigate the effect of water models on the predicted free energies of hydration, additional calculations were performed with the TIP4P force field[77]. The results of these calculations for ΔG_{HYD} are listed in **Table 2**, and show that the choice of water force field has no effect on the predicted hydration free energies for *n*–alkanes.

Table 2: Comparison of log Kow for n–alkanes predicted using SPC/E and TIP4P water models. Data are shown for simulations using a 14.0 Å LJ cut–off.

Solute	ΔG_{HYD} (kcal/mol)			Log K_{OW}		
	TIP4P	SPC/E	Experiment	TIP4P	SPC/E	Experiment[14]
Methane	2.4 ± 0.05	2.3 ± 0.1	1.98	1.2 ± 0.1	1.2 ± 0.2	1.1
Butane	2.6 ± 0.1	2.8 ± 0.1	2.18	3.0 ± 0.1	3.2 ± 0.2	3.9
Hexane	3.2 ± 0.15	3.3 ± 0.1	2.58	4.2 ± 0.15	4.4 ± 0.3	4.7
Octane	4.2 ± 0.25	4.0 ± 0.2	2.93	6.0 ± 0.1	5.9 ± 0.3	5.2

This is to be expected, since the sole interaction between water and *n*-alkanes in the chosen force fields is through Lennard-Jones interactions, and the Lennard-Jones parameters for SPC/E and TIP4P are nearly identical ($\square_{SPC/E}$ = 78.21 K, $\square_{TIP4P}$ = 78.12 K, $\square_{SPC/E}$ = 3.167 Å, $\square_{TIP4P}$=3.153 Å).

Free energy of solvation

The free energies of solvation for *n*–alkanes in 1–octanol were determined using a methodology similar to that used for the hydration free energy calculations. The potential of mean force for each solute as a function of distance along the reaction coordinate is presented in **Figure 9**.

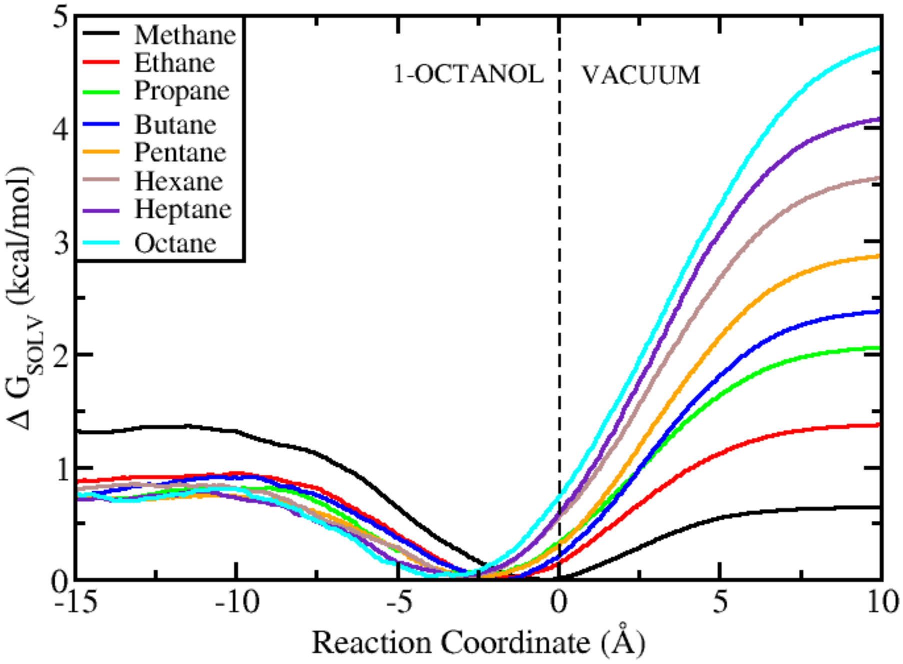

Figure 9: Solvation free energy profile generated with ABF method for n-alkane transfer from 1–octanol to vacuum (system S2). Dashed line denotes the location of the interface. Data shown are from calculations performed with a 14 Å LJ cutoff.

These data correspond to the TraPPE–UA force field for both the *n*–alkane solute and the 1–octanol solvent. From these data, the free energy of solvation was calculated for all solutes and is plotted as a function of chain length in **Figure 10**. For n–alkanes C_1–C_7, the data are in close agreement with previous calculations performed using thermodynamic integration, see **Table 3**. ΔG_{SOLV} for *n*–octane predicted from ABF–MD simulations is about 0.6 kcal/mol lower than prior calculations performed with thermodynamic integration[34], and shows improved agreement with experimental data[89]. The effect of Lennard–Jones cut–off was also determined from simulations using a 10 Å and 14 Å cut–off and these data are listed in **Table 4**.

Although Lennard–Jones interactions are more dominant in this system compared to calculations of hydration free energy, the effect of potential truncation is still within the error of the calculation, which is ~0.3 kcal/mol.

Table 3: Solvation free energies (ΔGSOLV) for n–alkanes in 1–octanol predicted using TraPPE-UA force field.

Solute	ΔG_{SOLV} (kcal/mol)		TI–method[34]	GEMC[36]	Experiment[89]
	10.0 Å LJ cut–off	14.0 Å LJ cut–off			
Methane	0.5 ± 0.05	0.7 ± 0.1	0.5 ± 0.1	0.44	0.5
Ethane	–0.4 ± 0.05	–0.5 ± 0.1	–0.4 ± 0.2	–0.54	–0.6
Propane	–0.9 ± 0.1	–1.2 ± 0.15	–1.0 ± 0.2	–1.18	–1.2
Butane	–1.7 ± 0.2	–1.6 ± 0.15	–1.4 ± 0.2	–1.82	–1.8
Pentane	–1.9 ± 0.1	–2.1 ± 0.15	–2.2 ± 0.2	–	–2.3
Hexane	–2.3 ± 0.05	–2.7 ± 0.1	–2.7 ± 0.2	–	–3.3
Heptane	–3.0 ± 0.1	–3.4 ± 0.2	–3.2 ± 0.2	–	–4.1
Octane	–3.4 ± 0.25	–4.0 ± 0.1	–3.4 ± 0.2	–	–4.6

Finally, the difference between the free energy of solvation in wet and dry octanol was determined. This is of particular interest for calculations of the partition coefficient since significant amounts of water are soluble in the 1–octanol phase. ΔG_{SOLV}□ was determined for a 1–octanol phase with the mole fraction of water of 0.255, which corresponds to the experimental value.

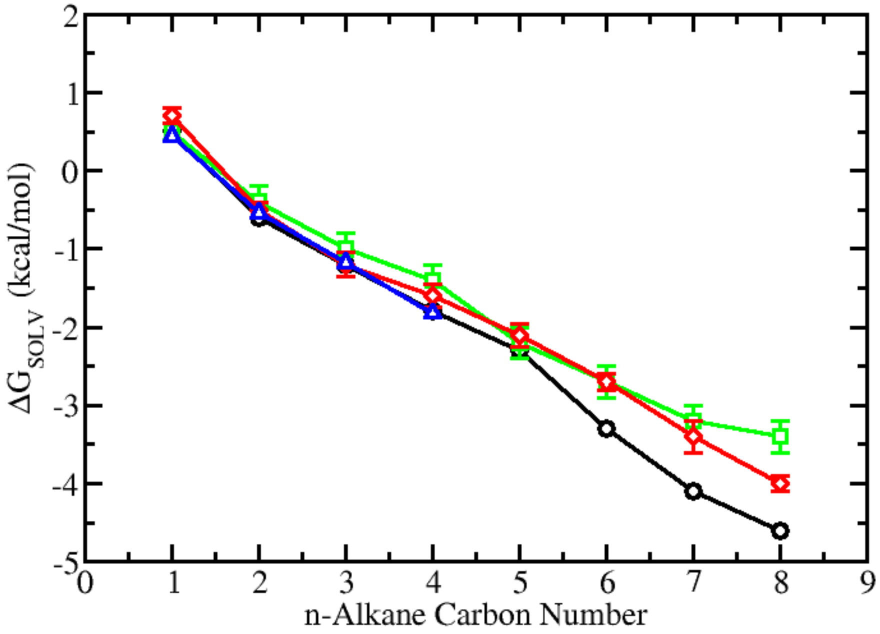

Figure 10: Solvation free energy for transfer of n–alkanes from vacuum into 1–octanol predicted by adaptive biasing force molecular dynamics using a Lennard-Jones cut off of 14 Å for the TraPPE-UA force field (red diamonds); thermodynamic integration green squares); GEMC (blue triangles); experiment (black circles).

We note that this value likely does not correspond to the equilibrium value that would be predicted from simulations[35], but is expected to provide an upper bound on the maximum difference in ΔG_{SOLV} between wet and dry 1-octanol. ΔG_{SOLV} predicted by ABF–MD calculations are listed in **Table 4**. The data show that the presence of water leads to a slight decrease in the predicted ΔG_{SOLV}□ of 0.2–0.3 kcal/mol, which is consistent with prior calculations [89, 90], and in this case is within the statistical error of the calculation. Therefore the use of dry octanol for the calculation of ΔG_{SOLV} and partition coefficients is justified, at least in the case of non–polar molecules, given the small change in ΔG_{SOLV} relative to the uncertainty of the calculation.

Table 4: Effect of water saturation of the octanol phase on the free energies of solvation and partition coefficients for *n*–alkanes. Data shown are for simulations using a 14.0 Å LJ cut–off.

Solute	ΔG_{SOLV} (kcal/mol)			Log K_{OW}		
	wet	dry	Experiment	wet	dry	Experiment[14]
Methane	0.8 ± 0.2	0.7 ± 0.1	0.5	1.1 ± 0.2	1.2 ± 0.2	1.1
Butane	–1.4 ± 0.2	–1.6 ± 0.2	–1.8	2.8 ± 0.2	3.2 ± 0.2	3.9
Hexane	–2.5 ± 0.3	–2.7 ± 0.3	–3.3	4.2 ± 0.3	4.4 ± 0.3	4.7
Octane	–3.6 ± 0.3	–4.0 ± 0.4	–4.6	5.7 ± 0.2	5.9 ± 0.3	5.2

Partition coefficients

From knowledge of ΔG_{SOLV} and ΔG_{HYD} it is possible to calculate the octanol–water partition coefficient log K_{ow} via Equation 1. 1-Octanol–water partition coefficients predicted by combining previously calculated free energy of solvation/hydration data are reported in **Table 5** and plotted in **Figure 11**. These data show close agreement with previous calculations performed with thermodynamic integration [34].

Table 5: Octanol–water partition coefficients (log KOW) predicted by the TraPPE-UA force field for n–alkanes.

Solute	Indirect Transfer		Direct Transfer (30 A box)		Direct Transfer (100 A box)	TI–method[34]	Experiment[14]
	10.0 Å LJ cut–off	14.0 Å LJ cut–off	10.0 Å LJ cut–off	14.0 Å LJ cut–off			
Methane	1.4 ± 0.3	1.2 ± 0.2	1.6 ± 0.3	1.4 ± 0.3	-	1.3	1.1
Ethane	2.1 ± 0.2	1.9 ± 0.2	1.9 ± 0.2	2.0 ± 0.2	2.0 ± 0.2	1.8	1.8
Propane	2.6 ± 0.3	2.5 ± 0.3	2.7 ± 0.3	2.8 ± 0.3	-	2.5	2.4
Butane	3.3 ± 0.3	3.2 ± 0.2	3.0 ± 0.2	3.5 ± 0.3	3.1 ± 0.1	3.1	2.9
Pentane	3.8 ± 0.2	3.8 ± 0.2	3.9 ± 0.2	4.1 ± 0.2	-	3.9	3.4
Hexane	4.5 ± 0.2	4.4 ± 0.3	4.6 ± 0.2	4.8 ± 0.2	4.4 ± 0.3	4.3	3.9
Heptane	4.9 ± 0.3	5.2 ± 0.3	5.3 ± 0.3	5.3 ± 0.3	-	5.1	4.7
Octane	5.4 ± 0.3	5.9 ± 0.3	5.8 ± 0.2	5.7 ± 0.2	5.8 ± 0.2	5.6	5.2

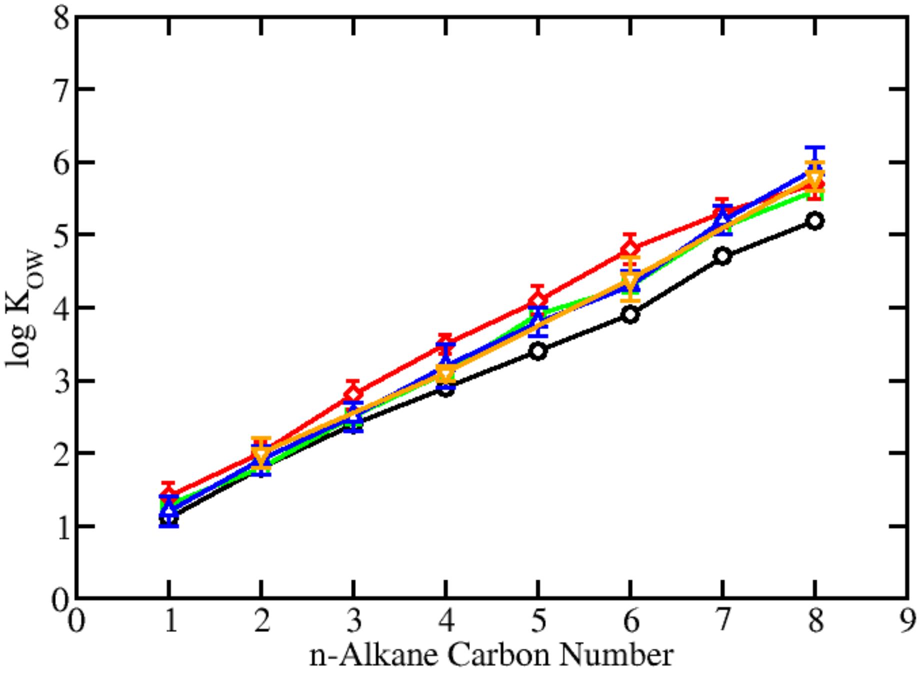

Figure 11: Octanol–water partition coefficient for *n*–alkanes predicted by adaptive force bias molecular dynamics simulations using a 14 Å LJ cutoff: direct transfer for 30 Å (red diamond) and 100 Å (orange triangles) 1-octanol box; indirect transfer (blue triangles); thermodynamic integration (green squares); experiment (black circles).

In addition to the indirect transfer method, log K_{ow} was determined by using the ABF methodology to transfer a solute directly from 1–octanol to water phase. Prior molecular dynamics simulations have shown the 1-octanol-water interface is approximately 25 Å wide, which is due to the amphiphilic nature of 1-octanol [91]. 1-Octanol molecules tend to align perpendicular to the interface, which allows their hydroxyl groups to form hydrogen bonds with water. The structure of 1-octanol in the interfacial region differs significantly from that of bulk

1-octanol, and it is not clear how the presence of the interface or the local microstructure affects the potential of mean force felt by the solute.

In order to answer these questions, a series of ABF-MD calculations were performed for the solutes ethane, n-butane, n-hexane and n-octane using a system containing water and 1-octanol phases of 30 Å x 30 Å x 50 Å and 30 Å x 30 Å x 100 Å, respectively. A 50 Å vacuum region was added to the simulation cell to eliminate interactions through periodic boundary conditions. These systems were large enough to ensure that the endpoints of the reaction coordinate were in regions where bulk conditions (density, local structure, etc) were observed. Initial calculations were performed with a 75 Å reaction coordinate, starting from the center of the 1-octanol phase and ending in the center of the water phase. From the density profiles shown in Figure 7, the final and initial states were clearly deep enough within each respective phase to be considered in bulk solution.

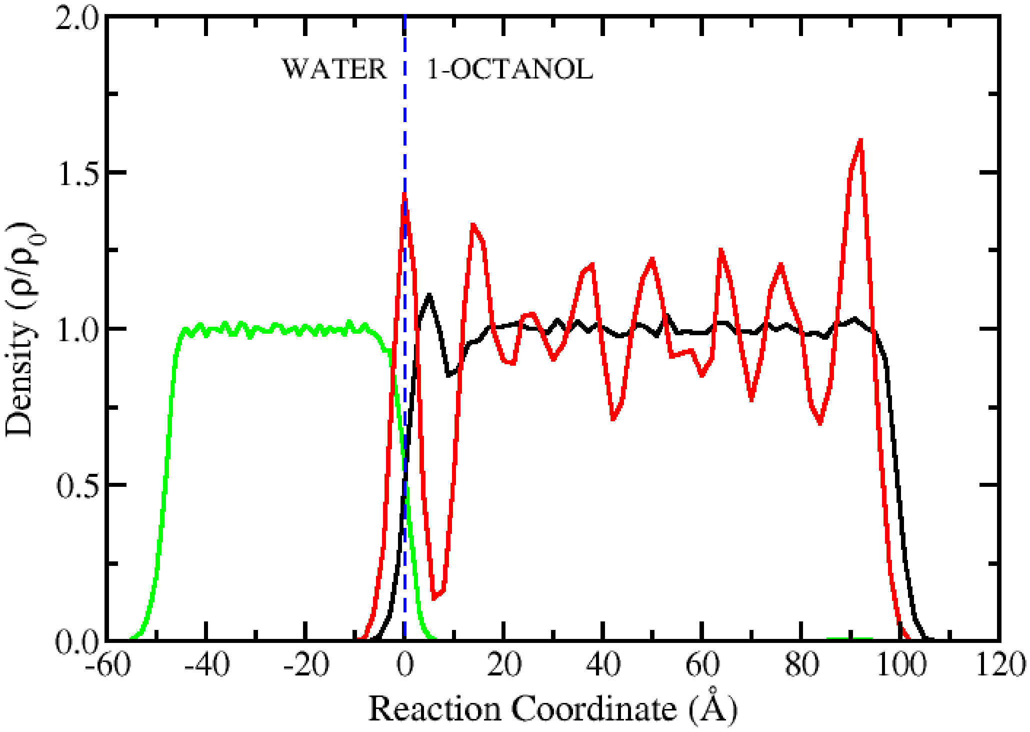

Figure 12: Density profiles for system S3. The density has been normalized by average bulk density of each component: water (green), 1-octanol CH2 (black), 1-octanol oxygen (red). Dashed blue line represents position of the interface.

From simulations of *n*-octane transfer, Figure 12, it was found that the PMF was invariant over the last 30 Å of the reaction coordinate (-30 to 0 Å in Figure 12), and subsequent calculations for ethane, butane and hexane were performed using a 45 Å reaction coordinate to reduce the computational expense of the calculation. It is important to note that while the local density of oxygen atoms in the 1-octanol phase varied significantly along the last 30 Å of the reaction coordinate, this had no effect on the calculated PMF. The PMF profiles for ethane, butane and hexane are plotted as a function of reaction coordinate in Figure **13**. For each solute, the free energies of the final and initial states were determined by averaging over the first and last 10 A of each PMF profile. The resulting log K_{ow} values are plotted in **Figure 11** and listed in Table **5**. These values agree within the statistical uncertainty of the calculation with results produced using the indirect transfer method, and data from the literature determined from thermodynamic integration [34].

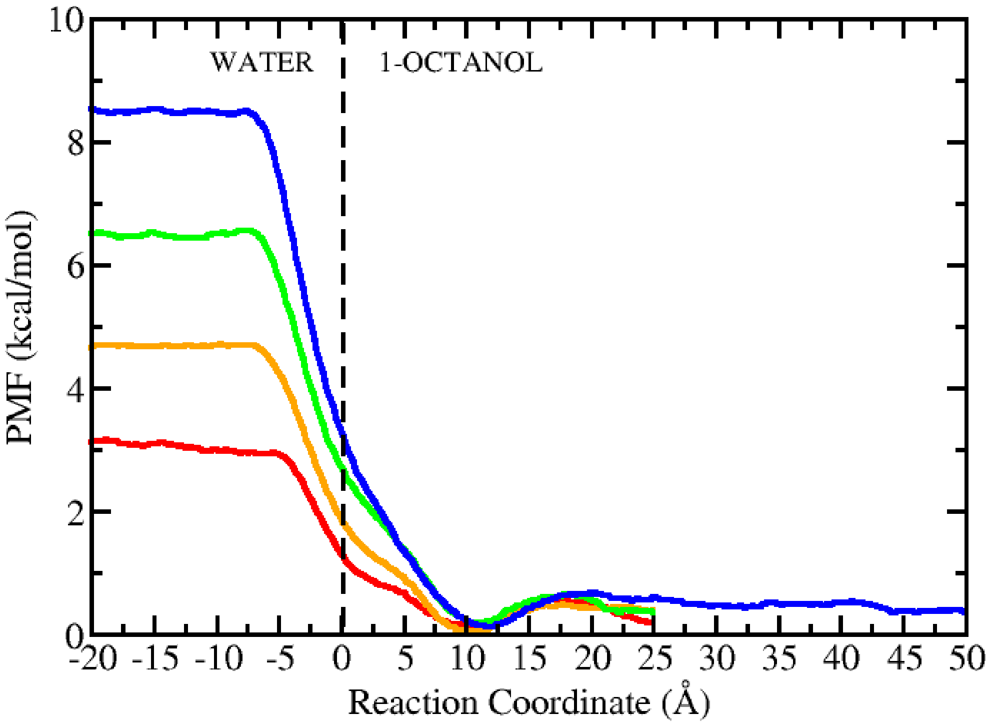

Figure 13: Free energy profile generated with ABF method for ethane (red), butane (orange), hexane (green) and octane (blue) transfer in system S3 from water to 1–octanol (dry) phase. Data shown are from calculations performed with a 14 Å LJ cutoff. Dashed black line marks the location of the interface.

To understand how the local solvation environment affects the observed PMF and optimize the computational time required to produce reliable free energies of transfer, calculations were repeated using an interfacial system where both the octanol and water phases were 30 Å x 30 Å x 30 Å. Each solute was transferred from the center of mass of the water phase to the center of mass of the 1-octanol phase. The PMF profiles for the solutes methane to octane are presented in Figure **14**. The predicted free energies of transfer are listed in Table **7** in comparison to the prior indirect transfer calculations, and direct transfer calculations for the large system (S3). In all cases, the agreement between the three methods, as well as prior calculations performed with thermodynamic integration is excellent [34]. This is despite the fact that the reaction coordinate is only slightly larger than the width of the interface, which raises a concern that the solute may not actually be in a "bulk" phase at the endpoints of the reaction coordinate.

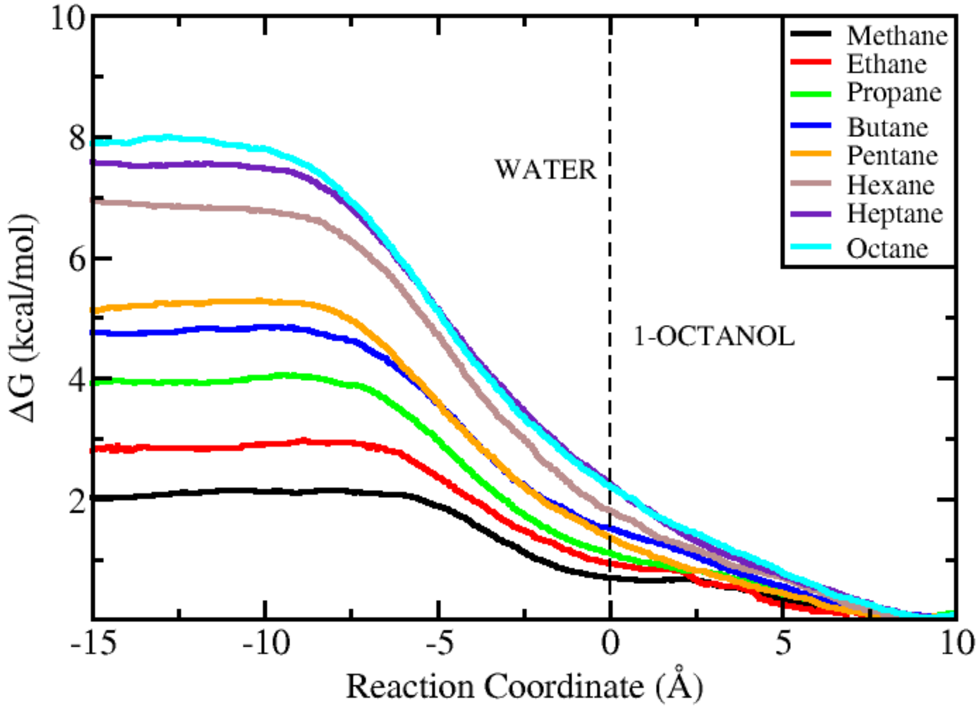

Figure 14: Free energy profile generated with ABF method for n-alkane transfer from water to 1–octanol (dry) phase in system S4. Data shown are from calculations performed with a 14 Å LJ cutoff.

Number integrals were calculated for CH_2 (octane)-CH_2(1-octanol) interactions and CH_2(octane)-O(1-octanol) interactions and used to analyze the effect of system size on the local solvation structure in the 1-octanol phase. Data for system S3 (100 Å 1-octanol phase) were determined from the first ABF window, which corresponds to the center of the 1-octanol phase. Data for system S4 (30 Å 1-octanol phase) were also determined from the first ABF window, which corresponds to the center of the 1-octanol phase, but is on the edge of the interfacial region where 1-octanol is aligned perpendicular to the interface. The CH_2(octane)-O(1-octanol) number integral is presented in Figure **15**, and shows only slight differences between the number of oxygen atoms interacting with the solute. The CH_2 (octane)-CH_2(1-octanol) number integrals for systems S3 and S4 are presented in Figure **15** and are indistinguishable.

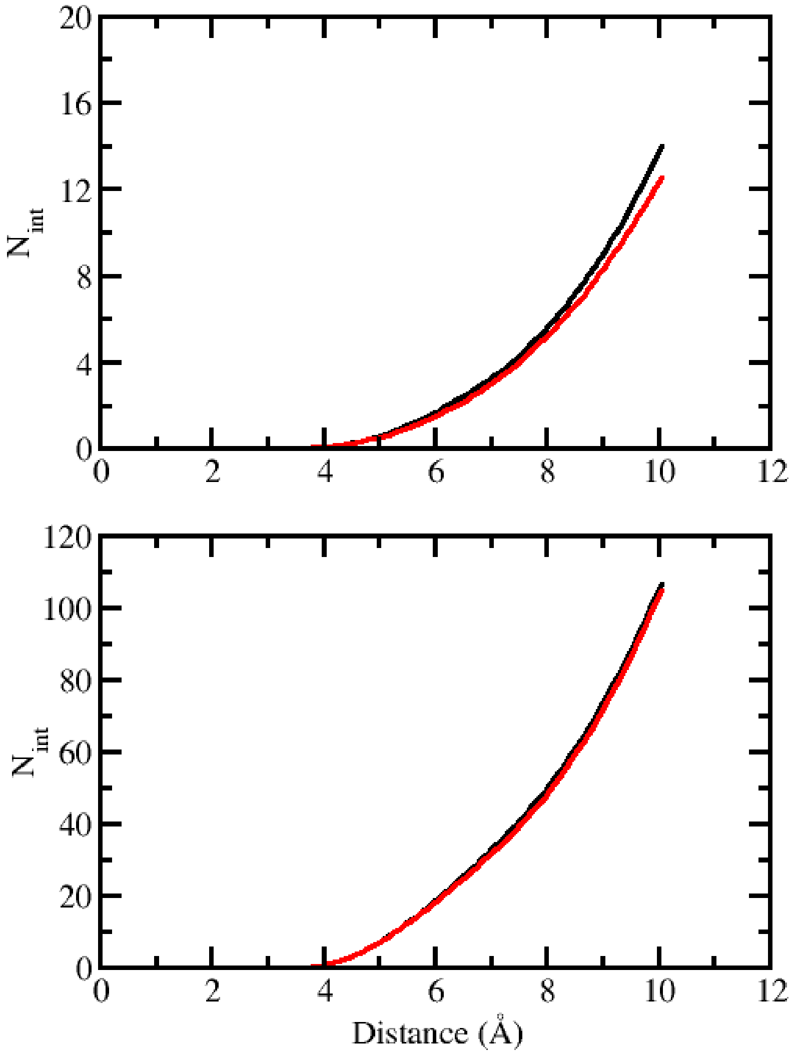

Figure 15: Top panel: Number integrals for interactions between CH_2 (octane) and O (1-octanol). Bottom panel: Number integrals for interactions between CH_2(octane) and CH_2(1-octanol). System S3 (black line), system S4 (red line).

These data show that although the microstructure of the 1-octanol phase in the S3 system may differ from that of bulk 1-octanol, the local solvation environment around the solute is indistinguishable from that of the bulk phase. Since the solute experiences the same local solvation environment in the small system S4 as it does in bulk 1-octanol, the PMF experienced by the solute must also be identical. These results are consistent with Gibbs ensemble Monte Carlo calculations that were used to investigate the effect of water saturation on the microstructure of 1-octanol and its effect on the free energy of transfer for non-polar and polar solutes[36]. While water saturation was found to have a significant impact on the microstructure of 1-octanol, the local solvation environment around non-polar solutes, such as *n*-alkanes, was unchanged compared to dry 1-octanol. Similarly, water saturation was not found to have a measurable effect on the free energy of solvation for *n*-alkanes C_1-C_4.

Convergence and error analysis

In this section, a detailed study is presented for n–pentane to determine the effect of various simulation parameters on the accuracy and precision of the ABF method. It is assumed that similar behavior will be observed for the other solutes studied in this work. The most basic measure of sampling quality is the number of times the solute visits are particular location along the reaction coordinate. A plot of the number of samples observed during the ABF-MD simulations at each point along the reaction coordinate is presented in **Figure 16** for the transfer of n–pentane from water to vacuum (system S1) and from 1–octanol to vacuum (system S2). This plot verifies that uniform sampling occurred along the complete reaction pathway for both systems S1 and S2.

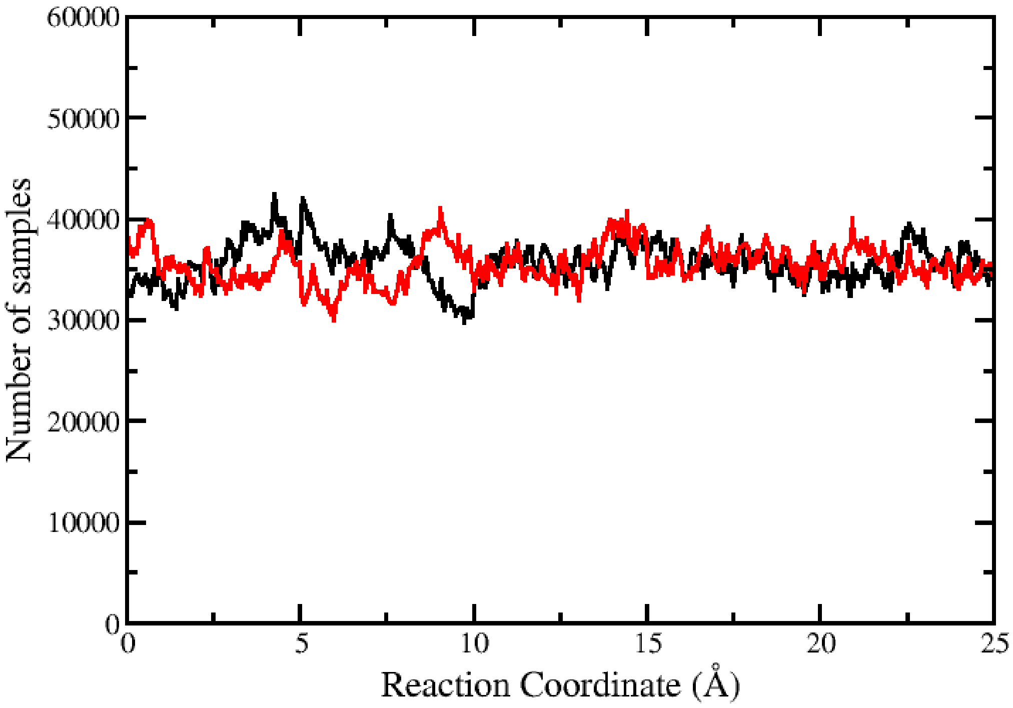

Figure 16: Distribution of samples along the reaction coordinate from 8 ns ABF–MD simulations for the transfer of *n*-pentane from water to vacuum (red) and from 1-octanol to vacuum (black). Distribution was constructed by combining data from the 5 individual simulations.

The evolution of sampling along the reaction coordinate was also studied for the n–pentane system for 0< t < 1.0 ns, and the resulting histograms are presented in **Figure 17**. At 0.02 ns, only a few locations along the reaction coordinate were sampled. As expected, though, the number of samples and the uniformity of sampling increased with increased runtime. By 0.3 ns, all locations along the reaction coordinate had be visited multiple times, although not uniformly. The uniformity of sampling may be quantified using the max-min ratio, which is defined as the largest number of samples observed for a particular location on the reaction coordinate, divided by the smallest number of samples observed. At 0.02 ns, the max-min ratio is ∞ since some locations have not yet been visited by the simulation. As shown in **Figure 18**, the max-min ratio drops rapidly from over 50 (at 0.10 ns) , to a value of approximately 1.35 after 1.0 ns, which suggests a uniform sampling of the reaction coordinate was achieved rapidly.

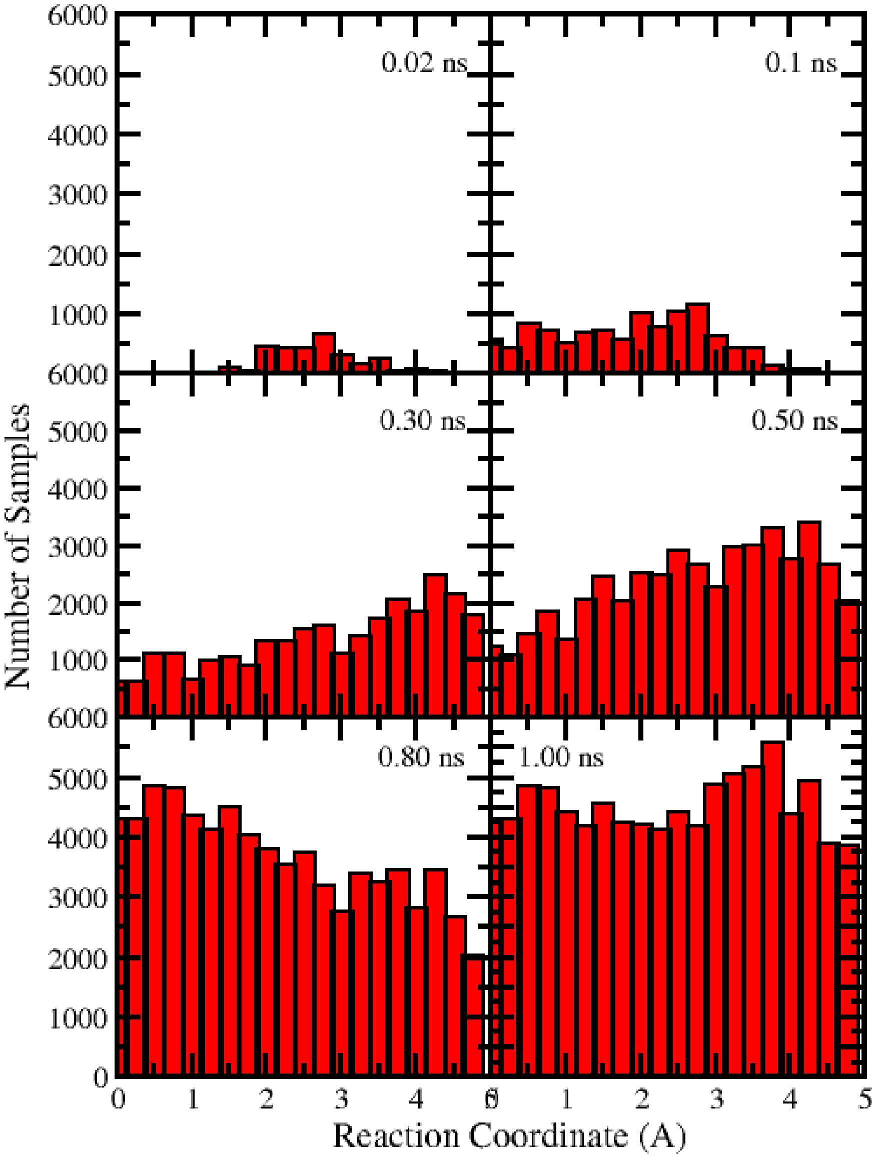

Figure 17: Evolution of sampling histogram from 0.02 ns to 1.0 ns during 1.0 ns ABF-MD simulation.

Sampling efficiency, defined as the ratio of total number of samples collected in a particular window to the total number of simulation steps, was evaluated and is tabulated for the n–pentane for all the three systems S1, S2 and S3 are in Table 6. The max-min ratio, is also presented for each window. The data shows that for all cases, a high sampling efficiency, between 88–90 %, was observed. Loss of samples occurs when the solute occasionally crosses the window barrier and during the simulation. For each window, the max-min ratio was between 1.18 and 1.52, illustrating convergence of the calculation.

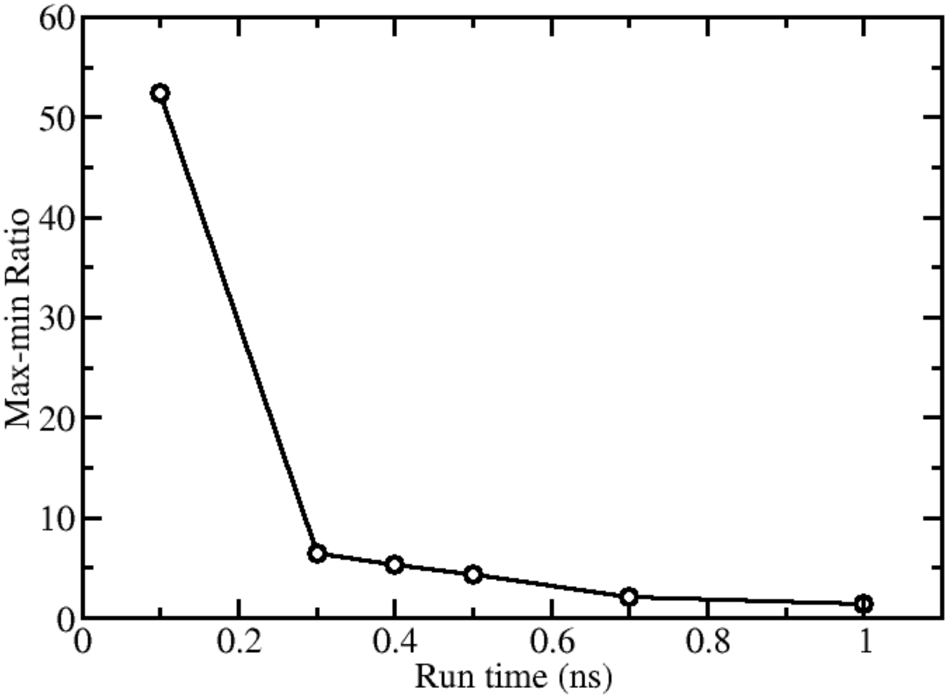

Figure 18: Evolution of max-min ratio during 1ns ABF MD simulation.

Table 6: Sampling efficiency and max-min ratio at the end of ABF simulations. Data shown are for the case of *n*-pentane transfer from 1–octanol to vacuum (system S1), *n*-pentane transfer from water to vacuum (system S2) and of *n*-pentane transfer from water to 1–octanol (system S3).

		System S1			System S2			System S3		
Window	Range (Å)	Total Samples accrued	Sampling Efficiency (%)	MaxMin Ratio	Total Samples accrued/ $4*10^6$	Sampling Efficiency (%)	MaxMin Ratio	Total Samples accrued/ $6*10^6$	Sampling Efficiency (%)	Max Min Ratio
1	0 – 5	3579870	89.50	1.36	3539980	88.50	1.24	5301322	88.36	1.52
2	5 – 10	3563272	89.08	1.41	3464591	86.61	1.37	5339307	88.99	1.45
3	10 – 15	3586021	89.65	1.18	3602301	90.06	1.28	5350243	89.17	1.48
4	15 – 20	3572167	89.30	1.19	3591461	89.79	1.20	5409373	90.16	1.43
5	20 – 25	3543811	88.60	1.22	3556602	88.92	1.21	5355089	89.25	1.50

Conclusions

This work illustrates the application of the adaptive force bias methodology, originally developed for determination the potential of mean force in biological systems, to the direct calculation of absolute free energies of hydration, solvation, and 1-octanol-water partition coefficients. Two different approaches were used to calculate the free energy difference for the transfer of a solute from water to 1–octanol phase; one where the 1–octanol and water phases do not interact with each other (IT method) and the other where the 1-octanol and water phases are in direct contact (DT Method). Calculations were performed with two different values of LJ cut–off (10.0 Å and 14.00 Å) for all the systems. ΔG and log K_{ow} values generated through ABF method using both DT and IT approach were consistent with each other and with prior calculations performed with traditional thermodynamic integration[34] and Gibbs ensemble Monte Carlo (GEMC)[36]. Direct transfer calculations performed on large systems were used to further validate the proposed methodology, and illustrated how the potential of mean force felt by the solute, at least for *n*-alkanes, were remarkably insensitive to the structure of the solvent. Investigation of the local microstructure around the solute provides an explanation for this: regardless of the solution microstructure, identical local solvation environments were observed around solutes both near the interface and in the bulk region.

In this particular application, the ABF method displayed rapid convergence, with the max-min ratio approaching an ideal value of 1 after only 1 ns of simulation. While still computationally more expensive for a given statistical uncertainty than GEMC, the ABF-MD method is more effective than GEMC for the calculation of log K_{ow} for larger solutes that cannot be transferred easily between condensed phases using configurational-bias Monte Carlo. Of the two methods described in this work, indirect transfer, although requiring two separate systems, is more robust than the direct transfer method for the calculation of partition coefficients. The air-water interface in each of the indirect transfer calculations is approximately half the width of the octanol-water interface, which reduces the sensitivity of the calculation to system size. Additionally, half of the reaction coordinate in the indirect transfer calculations is in the vacuum region, ensuring excellent sampling of phase space, and providing opportunities for further optimization. Direct transfer calculations require a system that is large enough that the solute is able to achieve a local solvation environment that is the same is it would in a bulk 1-octanol phase. For *n*-alkanes this can be done in a system as small as 30 Å in length, but for polar molecules, such as alcohols, a significantly larger simulation cell would be required to ensure the presence of the interface did not affect the solvation structure around the solute at each endpoint of the reaction coordinate. Like all free energy methods, the optimal simulation parameters, such as system size, length of the reaction coordinate, windows size, etc, are expected to vary depending on the solute of interest.

CHAPTER 4: Computational Prediction Of Ionic Liquid 1-Octanol/Water Partition Coefficient

*This work has been published in literature [92]

Background

Ionic liquids (ILs) are being touted as “panacea” solvents with recognized applications extending from cellulosic dissolution to overcome recalcitrance problems in biomass processing,[93] to liquid-phase exfoliation of grapheme [94], carbon capture[95] and battery electrolytes [96]. Salient features for the superlative behaviour exhibited by this class of fluid include non-volatility and high thermal stability. The multitude of cations and anions which can generate ILs provides seemingly infinite permutations for developing designer or task-specific ILs. And while ILs are often associated with negligible vapour pressures and so should not contribute to atmospheric pollution, they certainly do raise serious eco-toxicological concerns. Of course, the potential pathways defining the environmental fate of any compound include volatility, sorption, hydrolysis, and degradation. The aspects involved in this process include the complexity of water systems, soils, and various organisms. A classic, fundamental, and quantifiable index describing solute hydrophobicity related to partition behaviour is the 1-octanol/water partition coefficient (K_{ow}), the ratio of the concentration of the solute in the 1-octanol phase to that in a juxtaposed aqueous phase at equilibrium. Besides playing a role in understanding the environmental fate of a compound, the relative magnitude of K_{ow} serves as a rough guideline for predicting "enzyme compatible" media for non-aqueous biocatalysis[97]. Experimentally, this quantity may be determined using the shake flask (or tube) method followed by concentration determination using UV–vis spectroscopy or high-performance liquid chromatography (HPLC). Often, these techniques report a combined partition coefficient based on the presence of dissociated/un-dissociated ions. To date, the determination of K_{ow} among ILs has been limited to imidazolium-based ILs due to the ability to detect the imidazolium ring by UV–vis.[98]

Theoretically, linear free energy relation correlations (LFER) based on Abraham's general solvation model[99] and COSMO–RS[100] have been used to predict partition coefficients of ILs. A major disadvantage of these methods is the requirement of an extensive training set of experimentally-determined K_{ow} to parameterize the coefficients for solvation free energy correlation. Partition coefficients are computed based on the difference in Gibbs free energy of solute transfer between two phases. To this effect, free energy computations such as free energy perturbation (FEP) theory[101] and thermodynamic integration[102] (TI) have been employed.

The free energy calculations using FEP are dependent on the creation of a thermodynamic cycle involving a reference solute. In principle, it is possible to perform a perturbation from a ghost (non-interacting) particle to a fully-interacting one, but a large number of intermediate states may be required to achieve convergence. Another method for the calculation of absolute free energies of transfer and partition coefficients is Gibbs ensemble Monte Carlo (GEMC). In GEMC, two condensed phases are simulated concurrently and attempts are made periodically to "swap" the solute of interest between the phases. However, this too suffers, in this case from low acceptance rates for large molecules exchanging phases. This work furthers the adaptive bias force method (ABF) of Darve *et al*. [103-105] to calculate the free energy difference of chemical/biological process along a reaction coordinate. This method has been used previously to accurately predict the free energies of solvation and partition coefficients of homologous alkane series.[106] An advantage of the ABF method is that no reference solute is needed. Non–equilibrium methods based on Jarzynski's equality, sometimes referred to as "fast growth" methods, can in principle be applied to determine partition coefficients without the need for reference solutes. However, calculations of fluoromethane transfer across a water/hexane interface have shown the fast growth method produces poor results for these types of calculations, with a systemic bias and large statistical uncertainty compared to ABF.[27] Another significant feature of the ABF method is the use of unconstrained reaction coordinates thereby assisting in unbiased and uniform sampling of the defined region. Building off these advantages, the current work represents the first study using ABF–MD for directly calculating 1-octanol/water partition coefficients for imidazolium-based ILs.

Simulation Details

The heart of any FEP or TI using Monte Carlo or MD is the intermolecular potential used to describe the pairwise interactions. In this work, an all-atom force field developed by Lopes *et al*. was used to model the imidazolium cation and anion interactions.[107] The TraPPE–UA model for alcohols[108] was used in turn to model 1-octanol. The SPC/E model was used to model water explicitly.[109] The ABF method[110] adopted in NAMD[111] was used to determine the free energies of solvation for imidazolium ILs in 1-octanol and water, and these data used to determine log K_{ow} values. As part of the ABF algorithm, an external biasing force (F^U), estimated locally from the sampled conformations of the system and updated continuously, was applied at each step to facilitate the system in overcoming significant energy barriers that may be present along the reaction coordinate. This force was applied to a (cation + anion) pair of the ionic liquid "solute" as shown in Fig. 1. This allows the system to evolve freely without any constraints, enabling the simulation to visit multiple states separated by high energy barriers, resulting in an improved sampling of the reaction coordinate. Two different configurations were generated for the required calculations; an individual water/vacuum system (S1), 1-octanol/vacuum system (S2) for the indirect transfer (IT) approach as seen in Fig. 1a,b. For systems S1 and S2, a rectangular simulation cell was used, with dimensions of 30 × 30 × 60 Å, with the condensed phase occupying a region 30 × 30 × 30 Å. The number of molecules in each box was selected to reproduce the density of water or 1-octanol predicted by isothermal–isobaric NPT simulations at 1 atm and 298 K for a specific potential truncation (14 Å). For systems utilizing a 14 Å cut-off, 102 1-octanol and 896 water molecules were used, respectively.

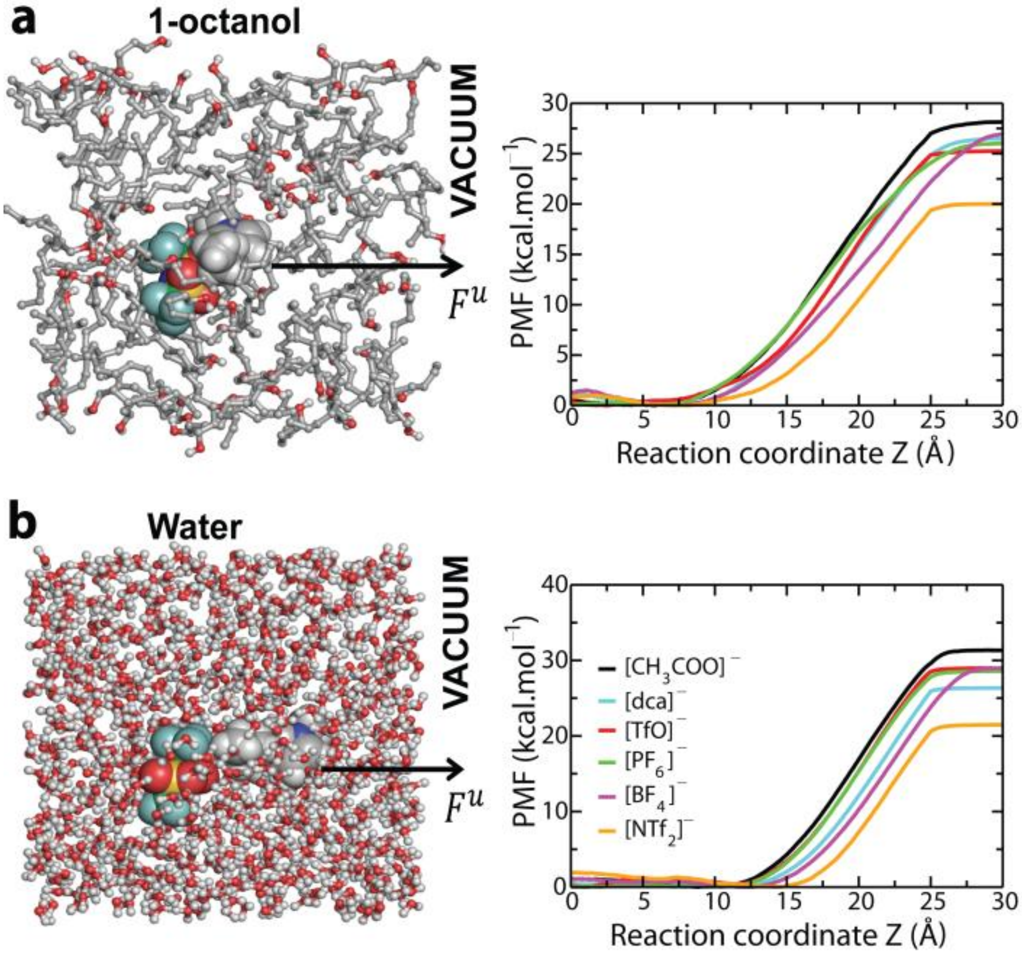

Figure 19: Schematic diagram for the "indirect transfer method". (a) 1-Octanol and (b) water boxes containing [bmim][NTf$_2$] solute are shown. Six windows of 5 Å bin width each in the Z-direction were used to compute the potential of mean force using ABF–MD simulations. The arrow suggests the direction of solute transfer with a force *F* along the Z reaction coordinate. Right: Average free energy of solvation profiles generated with ABF–MD for six ILs transferred from a 1-octanol-rich phase to vacuum (top) and from a water-rich phase to vacuum.

Results & Discussion

Potential of mean force

The profiles of the potential of mean force (PMF) for each solute in 1-octanol and water as a function of distance along the reaction coordinate are presented in panels (a) and (b) of **Figure 19**, respectively. The PMF for each solute shown is based on an average profile obtained from three to five independent simulations. Unlike in the case for alkanes, the PMF profiles are flat at the interface which is attributed to the balance between the entropic factor and the solute solvent interactions. ILs comprising six different anions paired with the 1-butyl-3-methylimidazolium ($[\text{bmim}]^+$) cation were studied in this work. The free energy of hydration/solvation was computed based on the difference in the free energy of the first window (solute in water-rich phase) and the last window (solute in vacuum phase). The rank order for the ILs based on the free energies of hydration ranging from maximum to minimum affinity towards water was found to be $[CH_3COO]^- > [BF4]^- \geq [TfO]^- \geq [PF_6]^- > [dca]^- > [NTf_2]^-$. This ranking can be loosely correlated with the order of the association strength[112] of the anions reflected in the ability of the anion to interact with its solvated cation partner.

Partition Coefficients

The partition coefficients of several imidazolium ILs have been reported over the past decade, however.[98, 100] Theoretically, K_{ow} can be computed using,

$$\log K_{ow} = \frac{\Delta G_{\text{hyd}} - \Delta G_{\text{solv}}}{2.303\text{RT}}$$

Equation 17

Figure 20 presents computed log K_{ow} values alongside experimental ones. For $[CH_3COO]^-$, the predictions are in excellent accord with experimental data. For $[TfO]^-$ and $[PF_6]^-$, the ABF method appears to over-predict the IL hydrophilicity by *ca.* 0.80 and 0.2 log units, respectively. In the case of $[NTf_2]^-$, the predictions lie within the experimentally observed range.

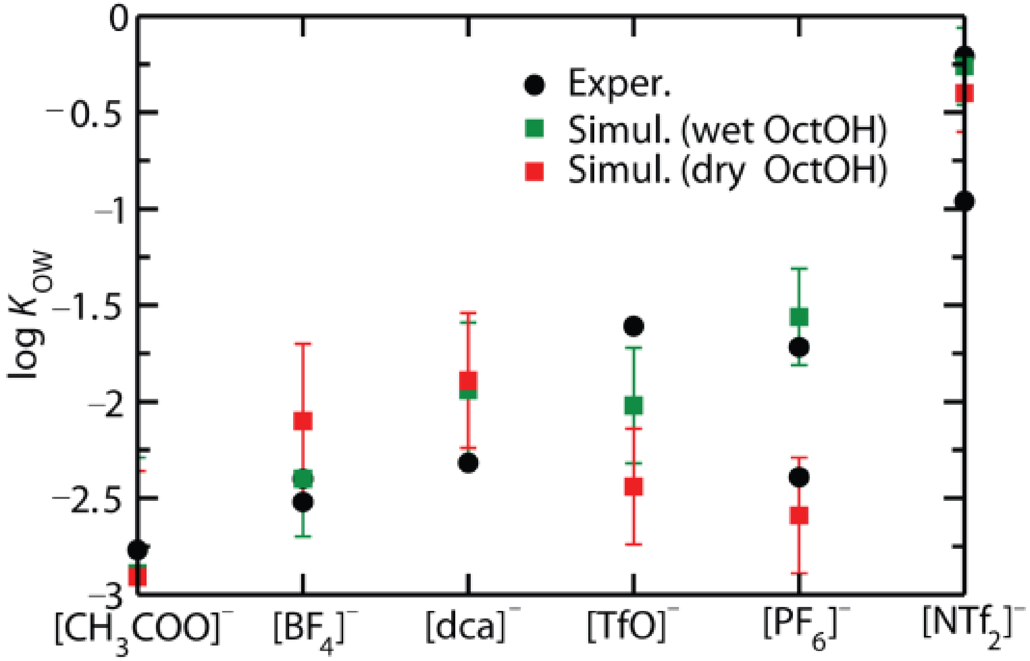

Figure 20: Comparison between 1-octanol/water partition coefficients determined for [bmim][X] ILs using ABF–MD simulations and eqn. 1 and experimental values for various anions. X = anion.

Overall, ABF–MD simulation predictions suggest a slightly more hydrophilic nature than experimental observations, with the exception of $[CH_3COO]^-$, $[BF_4]^-$, and $[dca]^-$, in which case the experimental log K_{ow} can be considered to fall within computational uncertainty. The deviation from experiment for the remaining three ILs may arise in part from the united-atom model being used for 1-octanol and the choice of the water model. It must be stated, however, that there are relatively few experimental data and considerable scatter in cases where log K_{ow} has been determined by multiple groups for a given IL [98, 113]. Computational studies have shown that a water saturated 1-octanol phase (i.e., “wet” octanol) is a more favourable phase for computing partition coefficients of polar solutes [36, 114], a logical consideration given that this reflects how K_{ow} is actually determined experimentally.

With this in mind, we performed additional simulations in a box consisting of 35 waters and 102 1-octanol molecules, based on the reported water saturation in 1-octanol of 20–29 mol%.[115] The corresponding log K_{ow} determined using wet octanol is given in **Figure 20**. The ΔG_{solv} for wet octanol is greater in magnitude than ΔG_{solv} for dry octanol in the case of these polar solutes. The presence of additional hydrogen bonding sites in the form of water molecules in wet 1-octanol provides a larger energy barrier for the solute to transverse from the condensed phase region into vacuum. The increased ΔG_{solv} magnitude in the case of wet 1-octanol results in a reduction in log K_{ow}, bringing the values more in line with experiment.

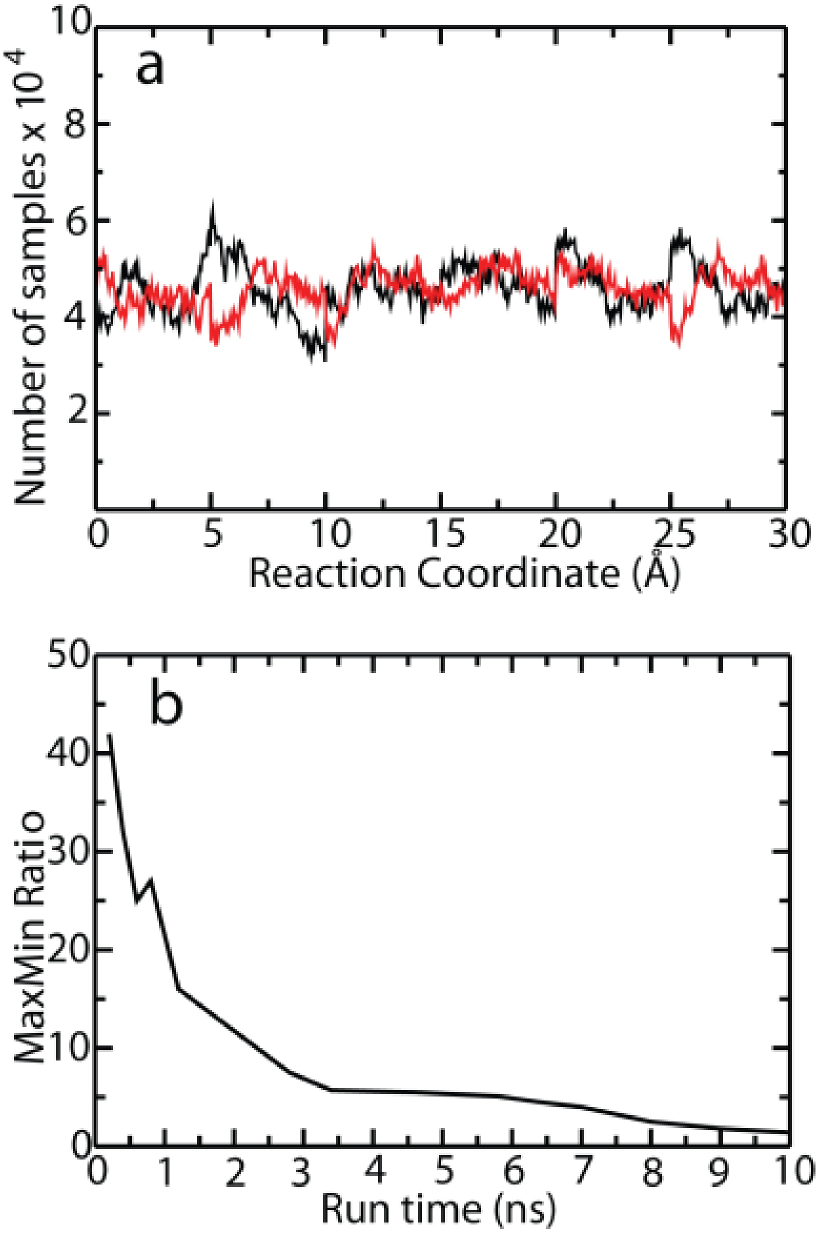

Figure 21: Distribution of sampling along the reaction coordinate showing results for [bmim][TfO] transfer from water to vacuum (red) and 1-octanol to vacuum (black). b) Temporal evolution of the MaxMin ratio.

Sampling efficiency of ABF method

A hallmark of the ABF method is that sampling of the phase space along a chosen reaction coordinate occurs in a uniform and homogenous manner irrespective of high-energy barriers present along the pathway. To validate the sampling behaviour in these ABF simulations, a test case of [bmim][TfO] was chosen for which the number of samples accumulated at the end of the simulation were plotted as a function of the reaction coordinate. The resulting plot shows the transfer of [bmim][TfO] from water to vacuum and from 1-octanol to vacuum (**Figure 21**). In both cases, uniform sampling is observed along the complete reaction pathway. The evolution in sampling was also studied for [bmim][TfO] transfer from 1-octanol and water to vacuum phase. Histograms collected during the course of simulation as a function of the reaction coordinate indicated that the sampling became uniform around 8 ns, indicating the convergence of ABF run. The MaxMin ratio is another parameter commonly used to determine the convergence of ABF simulations. It is defined as the ratio of the maximum-to-minimum number of samples collected in a specific region along the reaction coordinate. This ratio is infinite at the start of the simulation but attains a measurable value as the simulation progresses and all locations are sampled at least once. In this case, the MaxMin value eventually decays to near unity after 8 ns of runtime, suggesting that all the locations have been equally visited and marking the convergence of the ABF run. In the case of alkanes, the convergence was achieved faster as the maxmin ratio reached unity in one nanosecond [106].

Conclusion

In summary, ABF–MD simulations were used to expediently predict 1-octanol/water partition coefficients for imidazolium- based ILs for which measurable K_{ow} values are known. The use of wet 1-octanol in the simulations gives a more realistic estimate for ΔG_{solv}, providing more satisfactory estimates for log K_{ow}. This computational strategy is as powerful as it is general, suggesting its extension to ILs for which K_{ow} is not known or is difficult to measure experimentally due to lack of a reliable chromophore (e.g., ammonium, pyrrolidinium, or phosphonium ILs). These encouraging results suggest prospects for this computational tool in the *a priori* prediction of log K_{ow} values of ionic liquids broadly with possible screening implications as well (e.g., prediction of CO_2-philic ionic liquids).

CHAPTER 5: 1-Octanol-Water and Air-Water Partition Coefficients for Nitro-Aromatic Compounds from Molecular Dynamics Simulations.

*This work has been accepted and is currently under publication in Physical Chemistry Chemical Physics (PCCP) journal

Background

The prediction of environmental fate of energetic materials requires knowledge of physical property data, such as vapor pressures, aqueous solubility, 1-octanol-water partition coefficients and Henry's law constants. Common energetic materials such as trinitrotoluene (TNT), cyclotrimethylenetrinitramine (RDX) and sym-cyclotetramethylene-tetramitramine (HMX) have been studied extensively and numerous physical property data are available. For TNT, 1-octanol-water partition coefficients[116], Henry's law constants, vapor pressures and aqueous solubility have all been determined experimentally by a number of groups[117-121]. Vapor pressures have also been determined for RDX and HMX. In cases where multiple data sets exist, however, significant differences have been observed between some of the data sets. For example, reported values of the aqueous solubility for TNT may vary by as much as a factor of 2[122]. For new formulations, physical property data are sparse. In the case of two materials of interest in this work, 2,4-dinitroanisole (DNAN) and N-methyl-p-nitroaniline (MNA), experimental aqueous solubility, octanol-water partition coefficients and Henry's law constants have only recently been published[123, 124]. For emerging energetic materials the crystal structures and melting points are usually known, but little else is known about thermodynamic or transport properties.

The lack of consistent physical property, and the acute need for such data that may be used to provide some prediction of the environmental fate of a particular compound, drives the development of methodologies for the prediction of relevant physicochemical properties. The most common of these methods is Quantitative Structure Property Relationship (QSPR)[65, 125-130]. There are numerous variants of QSPR, but in essence, a large number of “descriptors” are fit to reproduce a specific physical property (vapor-pressure log K_{ow}, etc) for molecules in the training set. Training sets may contain anywhere from a few hundred to tens of thousands of molecules, and in general, the larger the training set, the better the predictive capability. Overall, most QSPR do an excellent job of predicting physical properties for molecules with similar molecular structure as those in the training set. However, for molecules that differ significantly from those used in the optimization of the QSPR there is a concern that the predictions of QSPR may not be representative of experimental data[67, 131]. In particular, the use of QSPR for energetic materials has been particularly problematic[73].

Computer simulations using atom–based potential functions provide another computational route to the prediction of partition coefficients (air-water, 1-octanol-water), albeit at significantly greater computational cost that QSPR. Recognizing that the partition coefficient (log K_{ow}) is related to the Gibbs free energy of transfer between 1-octanol and water phases,

$$\log K_{OW} = \frac{\Delta G}{2.303RT}$$

Equation 18

it is possible to determine log K_{ow} directly as long as a suitable methodology exists for the determination of ΔG.

Indeed, a variety of methods have been used to determine the free energy of transfer for a solute between octanol and water from computer simulation. Garrido *et al*, have used molecular dynamics simulations combined with thermodynamic integration to determine partition coefficients for a wide variety of compounds, including alkanes, alcohols, aromatics, ketones and chlorobenzenes[34, 132, 133], and have shown that calculations of hydration free energies may be used to optimize force field parameters[134]. Expanded ensemble techniques have been used to determine partition coefficients for a number of compounds, including the energetic material N-methyl-p-nitroaniline[135]. Chen and Siepmann used Gibbs ensemble Monte Carlo to determine free energies of transfer for short alkanes and alcohols[35]. Finally, our group has used adaptive biasing force molecular dynamics (ABF-MD) simulations to determine log K_{ow} for n-alkanes[136], as well as a number of ionic liquids[92].

In this work, united-atom force fields, based on the Transferable Potentials for Phase Equilibria (TraPPE-UA), are developed for eleven nitro-aromatic compounds, which include 2,4-dinitrotoluene (24-DNT), 2,6-dinitrotoluene (2,6-DNT), 3-nitrotoluene(3-NT), 4-nitrotoluene(4-NT), 1,3-dinitrobenzene (1,3-DNB), 1,4-dinitrobenzene (1,4-DNB), 2,4-dinitroanisole (DNAN), 1,3,5-trinitrobenzene (TNB), 2-nitroanisole (2-NAN), 4-nitroanisole (4-NAN) and n-methyl-p-nitroaniline (MNA). 1-octanol-water and air-water partition coefficients are predicted for the optimized TraPPE-UA force field with adaptive biasing force molecular dynamics simulations, and compared to available experimental data. Two additional models are presented for energetic materials with five membered rings for which no experimental data are available in the open literature: 3,5-dinitropyrazole (DNP) and 3-nitro-1,2,4-triazole-5-one (NTO).

The development of reliable models has been challenging for molecules containing nitro functional groups. Calculations performed with the Optimized Potentials for Liquid Simulations all-atom (OPLS-AA) force field suggest that *ab initio* methods tend to produce partial charges that are too large, leading to large over-predictions of hydration free energies[137, 138]. Similar problems were observed in this work for dinitro and trinitro aromatic compounds, which necessitated the empirical optimization of partial charges to reproduce 1-octanol-water partition coefficients. The charge optimization procedure and other relevant details of the optimized force fields are discussed in detail in the next section.

Force Field

In the TraPPE-UA force field, non-bonded interactions between sites are described by pairwise-additive Lennard-Jones potentials and point charges:

$$U(r_{ij}) = 4\varepsilon_{ij}\left[\left(\frac{\sigma_{ij}}{r_{ij}}\right)^{12} - \left(\frac{\sigma_{ij}}{r_{ij}}\right)^{6}\right] + \frac{q_i q_j}{4\pi\varepsilon_0 r_{ij}}$$

Equation 19

where r_{ij}, ε_{ij}, σ_{ij}, and q_i, are the separation, LJ well depth, LJ collision diameter, and partial charges, respectively, for the pair of interaction sites i and j. ε_0 is the permittivity of vacuum. Non-polar hydrogen atoms, i.e. hydrogen atoms bonded to carbon atoms, were combined with carbon to form a single united-atom interaction site. Interaction sites were placed on the nuclei of their respective atoms. Lennard-Jones parameters for various functional groups were taken from analogous compounds in the TraPPE force field[74, 139-141], and are listed in the supplementary information. Interactions between unlike atoms were determined using Lorentz-Berthelot combining rules:

$$\sigma_{ij} = \frac{\sigma_i + \sigma_j}{2}$$

Equation 20

$$\varepsilon_{ij} = \sqrt{\varepsilon_i \varepsilon_j}$$

Equation 21

Initial estimates of partial charge distributions were determined from a CHELPG analysis of electrostatic potential energy surfaces derived from *ab initio* calculations at the HF/6-31+G(d,p) level of theory and basis set. All electronic structure calculations were performed with Gaussian 09[142]. Compounds were optimized in the gas phase from numerous initial conformations to ensure a global minimum had been reached. Partial charges predicted by *ab initio* calculations for atoms in certain functional groups, e.g. –NO_2, -OCH_3, -$NHCH_3$, varied slightly (0.02-0.4 e) from molecule to molecule. To simplify the models, the partial charges for these functional groups were averaged from the results produced by *ab initio* calculations for DNAN and MNA. Partial charges for the alpha carbons were set so that the functional group plus alpha carbon formed a neutral charge group. This methodology of using neutral charge groups was chosen to allow one to potentially construct models for new compounds without having to perform additional *ab initio* calculations. Calculation of air-water and 1-octanol-water partition coefficients revealed that partial charges predicted by a single combination of theory level and basis set did not produce uniformly accurate results for all nitro-aromatic compounds, necessitating an empirical optimization approach. For mono-nitro compounds, reliable results were obtained with partial charges determined directly from the aforementioned *ab initio* calculations. Using these charges for dinitro compounds, however, produced 1-octanol-water partition coefficients that were approximately 1.0 log unit too low, suggesting the model was too hydrophilic. From simulations of 1,3-dinitrobenzene, it was determined that a scaling factor of 0.9 should be applied to partial charges derived from *ab initio* data for all dinitro compounds. For trinitro compounds, the *ab initio* derived charges produced log K_{ow} values that were 7 log units too low (too hydrophilic). To obtain good agreement with experimental data for trinitrobenzene, partial charges determined from HF/6-31+G(d,p) *ab initio* calculations had to be scaled by a factor of 0.5.

Similar empirical scaling factors have been applied to partial charge distributions by others to improve the agreement of simulation with experiment for the prediction of 1-octanol-water partition coefficients and/or hydration free energies. Garrido *et al* have recently proposed a modification of the TraPPE-UA force field for substituted alky-aromatics by scaling partial charges determined from a natural population analysis applied to density functional calculations by a factor of 0.5 [134]. This factor was determined through calculations of the hydration free energy for benzene and was found to produce hydration free energies that were within 0.2 kcal/mol of experimental values. This strategy was also applied successfully to determine hexane-water and octanol-water partition coefficients for polychlorinated biphenyls[132].

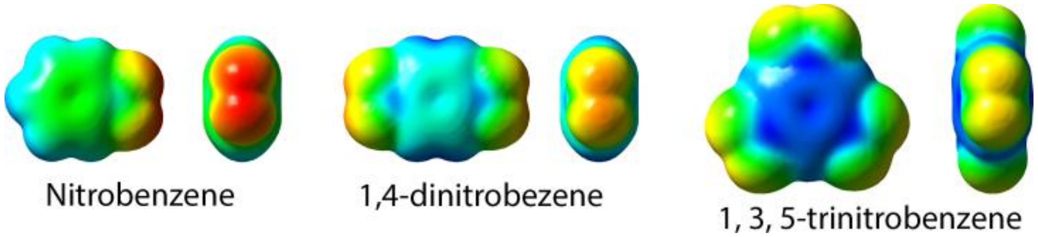

Figure 22: Electrostatic potential energy surfaces mapped to the total electron density for nitrobenzene, 1,4-dinitrobenzene and 1,3,5-trinitrobenzene.

Ab initio HF/6-31+G(d,p) calculations verify qualitatively trends in the partial charges determined through the empirical optimization process. A CHELPG analysis of the *ab initio* calculations predicts partial charges for oxygen in the nitro group of -0.48 (mononitro), -0.46 (dinitro) and -0.43 (trinitro) compared to the optimized empirical partial charges of -0.48 (mononitro), -0.432 (dinitro) and -0.24 (trinitro). The electrostatic potential energy surface mapped to the total electron density, shown in **Figure 22**, for nitrobenzene, 1,4-dinitrobezene and 1,3,5-trinitrobenzene illustrates this phenomena. The addition of nitro groups around the aromatic ring leads to increased delocalization of charge. A similar phenomenon was observed for the OPLS-AA force field for fluorobenzenes, where the magnitude of the partial charge on fluorine atoms was reduced as the number of fluorine-hydrogen substitutions increased [143].

While the TraPPE-UA force field typically uses rigid bond lengths, molecules were treated as fully flexible to simplify their implementation in molecular dynamics codes. Bond stretching and bond angle bending were both controlled by a harmonic potential

$$U_{Bend} = \frac{k_\theta}{2}(\theta - \theta_O)^2$$

Equation 22

where k_θ is the force constant that describes the stiffness of the angle (or bond), θ is the bond angle (or bond length) at a specific instant in time and θ_0 is the equilibrium bond angle (or bond length). The force constant k_θ was determined by fitting above equation to a scan of the potential energy surface, determined from *ab initio* calculations, with respect to bond angle (or length). Relaxed potential energy scans, using Hartree-Fock theory with the 6-31+G(d,p) basis set[144, 145], were performed by varying the bond length or angle of interest and reoptimizing all remaining degrees of freedom.

Interactions between atoms that are three bond lengths apart were governed by a torsional potential in the form of a cosine series

$$U_{TORS} = \sum_{i=1}^{n} c_i\big(1 + cos(i\varphi - \delta)\big)$$

Equation 23

where φ is the dihedral angle, δ is the phase angle and c_i are constants fit to reproduce *ab initio* derived potential energy surfaces. Rotational barriers for each dihedral of interest were determined from relaxed potential energy scans performed with Hartree-Fock theory and the 6-31+G(d,p) basis set.

Simulation Details

The adaptive biasing force method [25, 26, 28, 146, 147] was used to determine the free energies of hydration and solvation (in 1-octanol) for each of the solutes of interest. The hydration and solvation free energies were calculated from two independent simulations, where the solute was transferred from the water or 1-octanol phase to a vacuum phase. The resulting free energies were combined according to Equation 7 to provide the net free energy of transfer from water to 1-octanol

$$\Delta G = \Delta G_{HYD} - \Delta G_{SOLV}$$

Equation 24

where ΔG_{HYD} is the free energy of hydration in water and ΔG_{SOLV} is the free energy of solvation in 1–octanol for the solute of interest. With knowledge of the free energy of transfer from water to 1-octanol phases, log K_{ow} was calculated via:

$$\log K_{OW} = \frac{\Delta G}{2.303RT}$$

Equation 25

For free energy of hydration calculations, a rectangular simulation cell was constructed with dimensions 30 Ǻ x 30 Ǻ x 100 Ǻ, where the condensed water phase occupied a region approximately 30 Ǻ x 30 Ǻ x 50 Ǻ. For the solvation free energy, the condensed 1-octanol phase occupied a region approximately 30 Ǻ x 30 Ǻ x 100 $Ǻ^3$ and an overall box size of 30 Ǻ x 30 Ǻ x 150 Ǻ The large vacuum region on the end of the simulation cell was used to prevent the solute from interacting with the solvent through periodic boundary conditions. The TraPPE-UA force field was used for 1-octanol[75] while water was modeled with the SPC/E[76] force field.

Reaction coordinate for the determination of free energy changes was defined as the distance between the center of mass of the solute (COMS) under study and center of mass of the condensed phase (COMCP). Over the course of simulation, the reaction coordinate spanned a distance of 45.0 Ǻ from approximately 25 Ǻ deep into the condensed phase. Prior calculations have shown this is deep enough into the condensed phase that the structure of the solvent around the solute is not affected by the presence of an interface[136]. To reduce the statistical error of the calculations, the reaction coordinate was divided into nine equally sized non–overlapping windows of 5.0 Ǻ. To generate the initial configurations for each window, a single steered molecular dynamics (SMD) simulation was performed were the solute was pulled along the reaction pathway from 0.0 Ǻ to 45.0 Ǻ. Coordinates from the trajectory of this simulation were saved at suitable intervals to generate initial coordinate files for each of the nine windows. Windows were sub–divided into bins with a width of 0.05 Ǻ to collect the force statistics and the biasing force was applied after 500 samples were collected in each bin. To keep the solute within the specified window, a harmonic force with a magnitude of 10.0 kcal $mol^{-1}Å^{-1}$ was applied on the upper and lower boundary of the window.

Table 7: Predictions of the TraPPE-UA force field for free energies of hydration, solvation in 1-octanol, log K_{ow} and log H for nitro-aromatic compounds.

Compound	ΔG_{HYD} (kcal/mol)	ΔG_{SOLV} (kcal/mol)	Log K_{ow}	Log H	Log Kow (expt)[123, 124, 148, 149]	Log H (expt)[123, 124, 150]
3-nitrotoluene	-3.50 ±0.3	-6.50±0.3	2.22±0.4	-2.57±0.2	2.45	-3.42
4-nitrotoluene	-3.74±0.2	-6.67±0.3	2.15±0.2	-2.60±0.1	2.42	-3.64
2-nitroanisole	-4.72±0.2	-7.35±0.2	1.93±0.3	-3.46±0.2	1.80	NA
4-nitroanisole	-4.59±0.2	-7.35±0.2	2.03±0.1	-3.37±0.1	2.03	NA
N-methyl-p-nitroaniline	-4.51±0.2	-7.72±0.4	2.35±0.3	-3.31±0.2	2.10	-3.61
2,4-dinitroanisole	-8.21±0.1	-10.4±0.1	1.60±0.1	-6.02±0.1	1.61	-3.26
1,3-dinitrobenzene	-7.65±0.2	-9.60±0.4	1.44±0.3	-5.61±0.1	1.49	-5.70
1,4-dinitrobenzene	-7.84±0.2	-9.19±0.3	1.23±0.3	-5.75±0.1	1.45	NA
2,4-dinitrotoluene	-7.46±0.2	-10.54±0.2	2.26±0.2	-5.47±0.2	1.98	-5.66
2,6-dinitrotoluene	-7.41±0.2	-10.08±0.2	1.95±0.2	-5.44±0.2	2.02	NA
1,3,5-trinitrobenzene	-3.05±0.2	-4.77±0.2	1.26±0.3	-2.24±0.2	1.18	NA
3-nitro-1,2,4-triazole-5-	-15.37±0.2	-15.6±0.4	0.21±0.4	-11.26±0.2	NA	NA
3,5-dinitropyrozole	-12.34±0.2	-13.2±0.3	0.63±0.3	-9.05±0.2	NA	NA

Molecular dynamics simulations were performed with NAMD version 2.9[32]. Initial configurations for the water and octanol phases were generated with Packmol [79]. These systems were minimized, and equilibrated for 10 ns in isobaric–isothermal ensemble at 1.0 atm and 298 K. The equilibrated condensed phases were used for ABF-MD calculations, which were performed in the NVT ensemble. For all calculations, the temperature was maintained at 298.0 K using Langevin dynamics; for simulations in the NPT ensemble, the pressure was maintained at 1.01 bar using the Nose–Hoover algorithm[80]. Each window was simulated for 8 ns using a 2.0 fs time step. Periodic boundary conditions were used in all the three spatial coordinates. Long-range electrostatic interactions were calculated with particle–mesh Ewald algorithm[82]. Lennard-Jones interactions were truncated at 14 Ǻ and a switching function was applied at 12.5 Ǻ. Although the Lennard-Jones parameters for the TraPPE force field were developed using analytical tail corrections, prior free energy calculations by our group have shown the potential truncation has a negligible effect on predicted free energies of transfer[136]. Data were analyzed using VMD [151]. Statistical uncertainties were estimated from the standard deviation of the free energies predicted from 5-10 unique sets simulations, where a simulation set consisted of the 9 simulations required to determine a single free energy of transfer for a particular solute.

Results and Discussion

Hydration free energy

Hydration free energies were determined for each solute at 298 K by transferring the solute from the vacuum region to approximately 25 Ǻ deep into the water phase. The potential of mean force (PMF) as a function of solute position is presented for representative solutes in **Figure 23**. Additional PMF data for the remaining solutes may be found in the supplementary information. A minimum in the PMF was observed at the location of the water-air interface, indicating favorable interactions between the water and the solute, while a barrier of 3 kcal/mol for mono-nitro compounds and 2 kcal/mol for di-nitro compounds, was observed for the transfer of the solute from the interface to the bulk solvent. This barrier is related to the increased solvent density away from the interface, and the free energy of cavity formation, which requires the disruption of water hydrogen bonds. The PMF was invariant with position when the solute was greater than 10 Ǻ from the interface, verifying the water box was large enough and the reaction coordinate long enough to ensure reliable free energies of transfer could be calculated. This invariance of the PMF with respect to location suggests that for positions on the reaction coordinate from -10 to -20 Ǻ that the solvent structure around the solute is the same as what would be expected for a solute in a bulk water, i.e. the presence of the interface did not affect local solvent structure around the solute. The free energy of hydration was determined by taking the difference between the average value of the PMF in the water phase from -20 to -10 Ǻ and the vacuum region from 10-20 Ǻ along the reaction coordinate. These data are listed in **Table 7**.

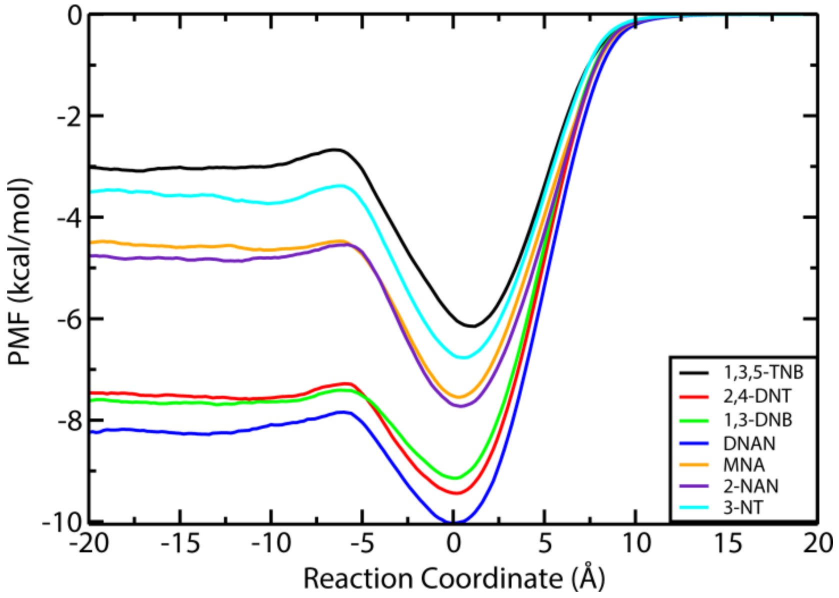

Figure 23: Potential of mean force as a function of reaction coordinate for the hydration of selected nitro-aromatic compounds. Zero of the reaction coordinate represents the location of the water-vacuum interface.

Solvation free energy

The free energies of solvation in 1-octanol at 298 K for the twelve energetic materials of interest were determined with a methodology similar to that used for the hydration free energy calculations. The potential of mean force for representative solutes as a function of distance along the reaction coordinate is presented in Figure 3. Free energies of solvation were calculated by taking the difference between the average values of the PMF in the vacuum and condensed phase regions. These data are listed in **Table 7**. For each solute, the PMF drops monotonically to a minimum value at the interface, and remains constant as the solute moves from the 1-octanol-air interface into the bulk 1-octanol phase. Prior calculations have shown for n-alkanes that the free energy barrier for the transfer of a solute from the interface to bulk solvent phase is approximately 1 kcal/mol[136]. This suggests the free energy of cavity formation is balanced by favorable electrostatic interactions between 1-octanol and the solute.

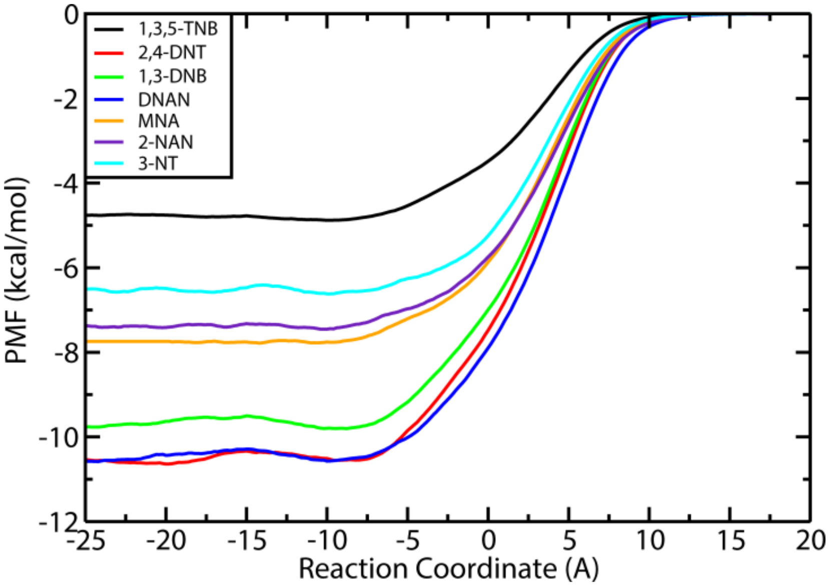

Figure 24: Potential of mean force as a function of reaction coordinate for the solvation of selected nitro-aromatic compounds in 1-octanol. Zero of the x-axis corresponds to the location of the 1-octanol-vacuum interface.

Partition coefficient

The free energies of hydration and solvation were combined to determine the free energy of transfer for each solute from water to 1-octanol phase, which is directly related to log K_{ow} via Equation 8. The predicted partition coefficients are listed in **Table 7**, and plotted vs. experimental data in Figure 25. Overall, excellent agreement with experimental data is observed; an average absolute deviation between simulation and experiment of 0.19 log units was observed for the eleven nitro-aromatic compounds. The TraPPE-UA force field produced consistent results within a particular class of compounds, such as mono-nitro, di-nitro, etc., validating the approach used for optimization of partial charge distributions. For DNP and NTO, no experimental data were available for comparison. Previous COSMO-RS calculations predict a log K_{ow} for DNP of 0.371[152], which is in reasonable agreement with log K_{ow} = 0.63±0.2 predicted by the TraPPE-UA force field. A larger difference is observed between simulation and COSMO-RS predictions for NTO. The TraPPE-UA force field predicts log K_{ow} = 0.21±0.4, while COSMO-RS predicts log K_{ow} -1.19[152]. The predictions of the TraPPE-UA force field are improved, compared to prior COSMO-RS calculations for DNAN and MNA. TraPPE-UA predicts log K_{ow} for DNAN and MNA to within 0.1 and 0.3 log units of experimental data, respectively, while the predictions of COSMO-RS are 0.3 log units too large for DNAN and 1.3 log units too low for MNA[152]

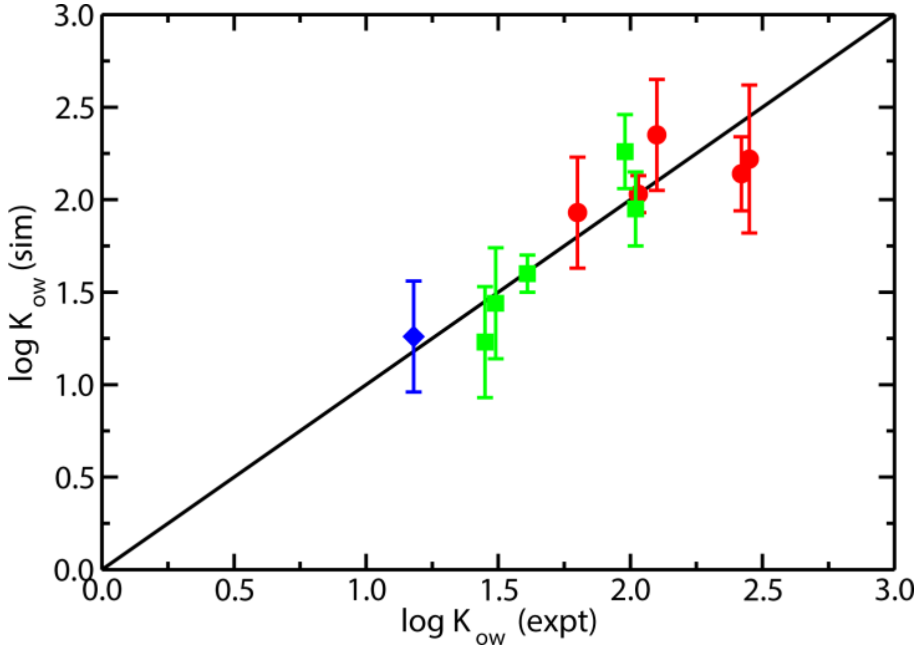

Figure 25: Log K_{ow} predicted by the TraPPE-UA force field vs. experimental data for the 11 nitro-aromatic compounds studied in this work. Data are coded as follows: mononitro compounds (red circles), dinitro compounds (green squares) and trinitro compounds (blue diamonds).

Dimensionless Henry's law constants can be related to the free energy of hydration via

$$\log H = \frac{\Delta G_{HYD}}{2.303RT}$$

Equation 26

where R =1.986×10^{-3} kcal/mol is the universal gas constant, and T = 298 K is the temperature. Henry's law constants are plotted against experimental data in **Figure 26** for six nitro-aromatic compounds for which reliable experimental data could be located.

Henry's law constants are available for some of the other compounds, but the data are not peer reviewed, and in many cases are actually predictions from QSPR tools, such as SPARC[65, 129, 130], masquerading as experimental data. The predictions of simulation for log H were in close agreement with experiment for 5 of the 6 compounds, with an average absolute deviation of 0.5 log units. However, significant discrepancies were observed for DNAN with respect to the experimental Henry's law constants[123]. For DNAN, the predictions of simulation were consistent with other dinitro compounds; the hydration free energies for 1,3-DNB, 1,4-DNB, 2,4-DNT, 2,6-DNT and DNAN were all predicted to be between -5.4 and -6.0 kcal/mol. DNAN contains a methoxy group which is expected to enhance interactions with water compared to dinitro-benzenes and dinitro-toluenes. Indeed, the predicted free energy of hydration for DNAN is -6.02 vs. -5.47 kcal/mol for 2,4-DNT. In comparison to experimental data for other dinitro compounds, such as 1,3-DNB (log H = -5.7) and 2,4-DNT (log H = -5.66), the experimental value for DNAN (log H = -3.26) is low by approximately by 2.4 log units. Therefore it is unclear if the source of the error is a failure of the model, or an inconsistency in the experimental data.

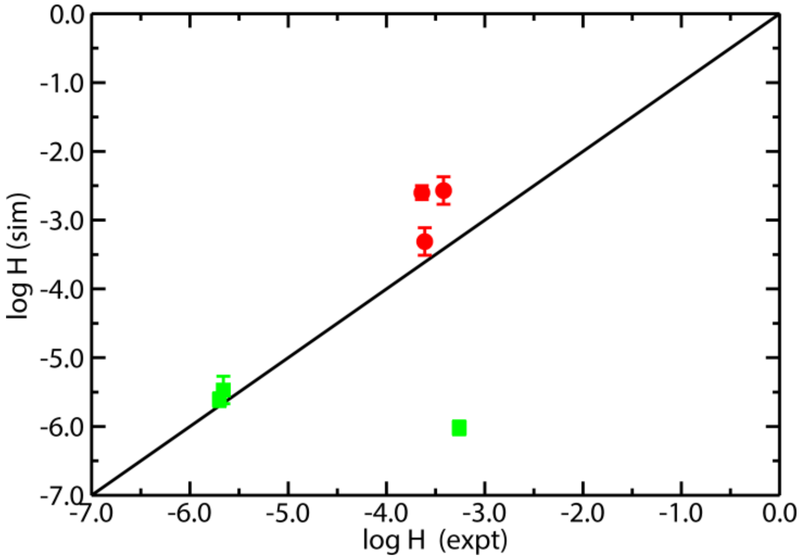

Figure 26: Log H predicted by the TraPPE-UA force field vs. experimental data for six nitro-aromatic compounds. Data are coded as follows: mononitro compounds (red circles), dinitro compounds (green squares).

Radial distribution functions were calculated for DNAN and 4-NAN in water and 1-octanol to highlight differences in the local solvent structure around mono and dinitro compounds. These data are presented in **Figure 27**. Both DNAN and 4-NAN display weak, non-specific interactions with water. Minimal hydrogen bonding was observed between water and nitro group oxygens for both DNAN and 4-NAN. For DNAN, the presence of the ortho nitro group blocks water access to the methoxy group, while for 4-NAN, a small amount of hydrogen bonding was observed between water and the methoxy group.

In 1-octanol, greater local solvent structure was observed. The radial distribution function for hydrogen atoms (in the hydroxyl group) interacting with nitro group oxygen atoms displays a peak at 1.8 Ǻ for both DNAN and 4-NAN. The peak height for 4-NAN is approximately twice that of DNAN due to the 10% larger partial charges on the nitro group. In water, the presence of the ortho nitro group in DNAN blocks solvent access to the methoxy oxygen; however, in 1-octanol the ortho nitro group enhances interactions of the methoxy oxygen with the solvent. This is due to the increased strength of hydrogen bond interactions between 1-octanol hydroxyl groups and nitro oxygens compared to the corresponding water interactions.

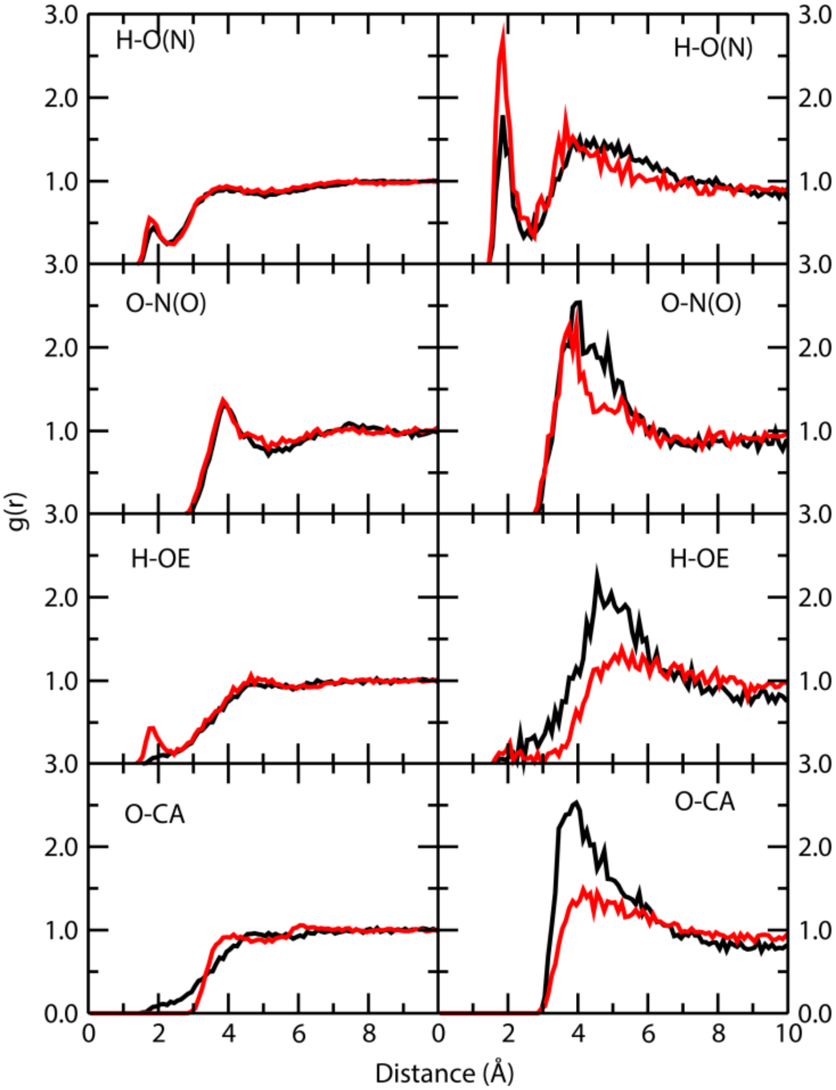

Figure 27: Radial distribution functions for DNAN (black) and 4-NAN (red) in water (left panel) and 1-octanol (right panel). Labels denote interaction sites on the solvent (water or 1-octanol), followed by interaction sites on the solute.

While participating in hydrogen bonding with the ortho nitro group, the 1-octanol hydroxyl group is also in close proximity to the methoxy group oxygen, which accounts for the peak observed at approximately 4 Ǻ.

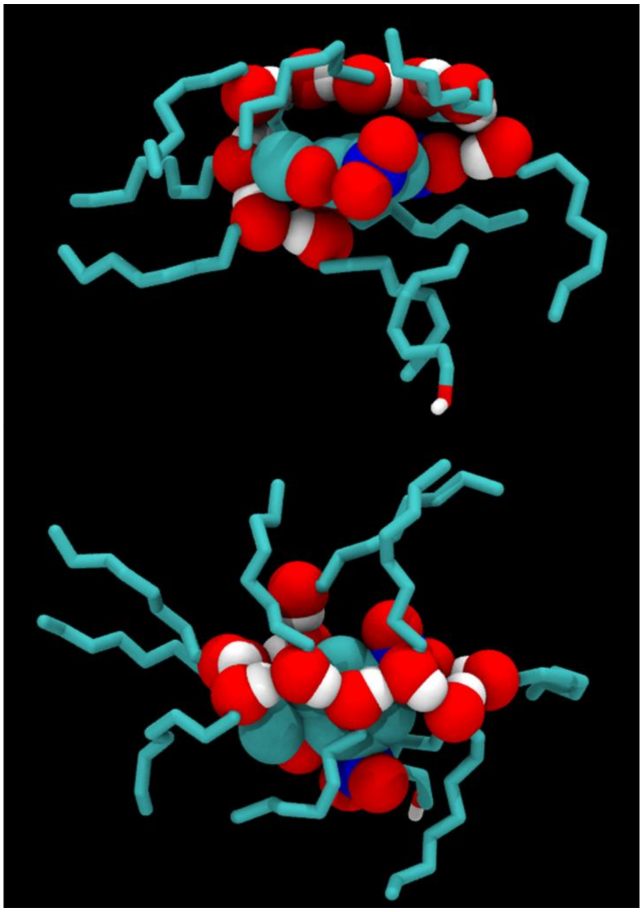

Figure 28: Snapshots from molecular dynamics simulations illustrating the formation of 1-octanol cages around DNAN. Images are from the same molecular configuration and have been rotated to provide alternate views of the 1-octanol chains. Alkyl tails of 1-octanol have been shown in licorice mode for clarity.

Strong 1-octanol hydroxyl interactions with the nitro group also influence the local solvation structure around DNAN and 4-NAN. Through a combination of hydrogen bond interactions between the nitro group (oxygen) and 1-octanol (hydrogen), and electrostatic interactions between nitrogen and 1-octanol (oxygen), 1-octanol is able to form hydrogen bonded cages around DNAN, examples of which are shown in Figure 28. The peak observed at 4 Å for the RDF corresponding to the hydroxyl group interacting with the aromatic carbons of DNAN is not due to any specific interactions between them, but is instead a by-product of the solvent reorganization to accommodate the solute. 1-octanol assumes a slightly different structure around 4-NAN. Hydrogen bonded 1-octanol chains tend to wrap around parts of the aromatic ring, but no structures spanning the entire aromatic ring were observed during the simulations.

Conclusions

A force field based on the TraPPE-UA parameter set was developed for eleven nitro aromatic compounds, as well as two energetic materials based on five membered rings. Compounds containing the nitro functional group are known to be a particularly difficult case regarding the prediction of accurate free energies of hydration[137]. The difficulty in accurately estimating the free energies of hydration in nitro aromatic compounds is increased due to the increased delocalization of charge as nitro groups are added to the molecule. During the force field optimization process, it was determined that a single model chemistry or level of quantum theory and basis set would not work for all nitro aromatic compounds. While quantum chemistry correctly predicts an increased delocalization of charge as nitro groups are added, the magnitude of the predicted charges was too large, which resulted in an over prediction of the free energies of hydration for dinitro compounds. Scaling factors of 0.9 for dinitro compounds and 0.5 for trinitro compounds were found to produce uniformly accurate results for molecules within a particular class of compounds.

These optimized potentials were used to predict free energies of hydration, solvation and transfer from 1-octanol to water for nitro aromatics. From the free energies of transfer, log K_{ow} and log H were predicted for each compound. Log K_{ow} values were reproduced to within 0.19 log units (AAD) of experimental data. Log H values were more varied, with an AAD of 0.5 log units. With respect to the prediction of Henry's law constants, data for 5 of the 6 compounds were in close agreement with experimental data, with DNAN showing significant deviations from experiment. Experimentally, DNAN exhibits an anomalously low free energy of hydration that is inconsistent with values published for other dinitro compounds. Resolving this perplexing situation will likely require additional experiments and simulations.

In addition to free energies of transfer, structural data was extracted from the simulation to show differences between the interactions of mono-nitro and dinitro compounds with the solvent. For both DNAN and 4-NAN in water, the radial distribution functions were unremarkable, suggesting weak interactions with the solvent. Much stronger interactions were observed for DNAN and 4-NAN in 1-octanol. The nitro group was able to participate in hydrogen bonding with the hydroxyl group of 1-octanol. For dinitro compounds, 1-octanol was able to interact with both nitro groups to form chains around the aromatic rings. For mono-nitro compounds, extensive chain and ring formation was observed between 1-octanol molecules, but these chains tended to cover only 1/3 to 1/2 of the aromatic ring.

CHAPTER 6: Chemical Warfare Agents

Introduction

Nerve agents are a subset of a broad group of compounds known as “chemical warfare agents,” a term that generally refers to any chemical that may be used to kill or seriously injure humans. Nerve agents are based on organo-phosphate chemistry and were discovered during research on synthetic insecticides in the 1930’s at I.G. Farbenindustrie (Germany). The compounds *N,N*-dimethylphosphor-amidocyanidate (tabun) and isopropylmethylphosphonofluoridate (sarin) were first synthesized at this time, while the third of the G-agents, Pinacolyl methylphosphonofluoridate (soman) was synthesized independently in 1944 by the Nobel laureate Richard Kuhn[153]. Research on organo-phosphate based pesticides continued through the 1950’s in England, Germany and Sweden, and in the process the extremely toxic ethyl ((2-[bis(propan-2-yl)amino]ethyl)sulfanyl) (methyl)phosphinate (VX) was discovered[154].

Nerve agents have been called the “poor man’s nuclear bomb,” capable inflicting mass casualties, while being relatively cheap easy to manufacture using equipment and raw materials designed for civilian applications. A variety of chemical warfare agents, including mustard gas and tabun, where used by Iraq with varying degrees of effectiveness during the 8 year war with Iran[155]. While of limited utility as a battlefield weapon, concern is increasing regarding the potential use of nerve agents by terrorist organizations. These concerns have lead to significant research efforts focused on development of improved materials (metal oxides[156-159], nano–

materials [160-167] and biosensors [168, 169]) for detection and filtration of chemical warfare agents (CWA), as well as understanding the environmental fate of such compounds.

The toxic nature of nerve agents makes them ideal candidates for study using computational methods, such as quantum chemical calculations or molecular dynamics simulations. *Ab initio* calculations have been used to determine the lowest energy conformers for trimethyl phosphate (TMP)[170], DMMP[171-173], sarin[174], soman[174] and tabun[175]. The interactions of organophosphorous compounds with metal oxides[176-178] and clays[179] have been studied extensively using both density functional theory and quantum mechanics calculations. In addition to ab initio calculations, atom-based force fields have been developed for DMMP[180, 181], DIFP[182] (diisopropyl fluorophosphate) sarin[181], soman[181]. These models have been used in molecular dynamics simulations to determine the liquid phase structure of concentrated solutions of DMMP and sarin in water and have shown that both DMMP and DIFP provide a reasonable approximation of sarin's interactions with water[183]. Molecular dynamics simulations have also provided important insight into the interactions between DMMP and polyelectrolyte membranes [184, 185], which have potential applications as proactive barriers from nerve agents.

In general, the partitioning of trace solutes in the environment is governed by the 1-octanol/water partition coefficient (log K_{ow}) and Henry's Law constant (log H)[16]. Ideally, such data would be collected experimentally, however, in the case of highly toxic materials, e.g. nerve agents, experiments are difficult to perform and costly. As a result, experimental data for these compounds are scarce and in some cases contradictory when multiple data sets exist. The G and

V agents hydrolyze readily, which further complicates the accurate determination of partition coefficients from experiment[186].

In this work, adaptive biasing force molecular dynamics simulations (ABF-MD)[25, 105, 146] are used in conjunction with the **Tra**nsferable **P**otentials for **P**hase **E**quilibria (TraPPE) force fields for DMMP[181], sarin[181], soman[181] and VX, shown in **Figure 29**, to predict their Henry's Law constant and 1–octanol/water partition coefficients. ABF-MD eliminates the need for reference solutes, which are required in free energy perturbation, since the entire solute is transferred intact from condensed phase to vacuum, providing the absolute free energy of hydration/solvation[44, 92]. A new united-atom force field for VX is developed that is consistent with the TraPPE force field. Molecular dynamics simulations are used to determine the local structure of water around each agent, and these data are used to explain observed trends in Log K_{ow} and the Henry's constant.

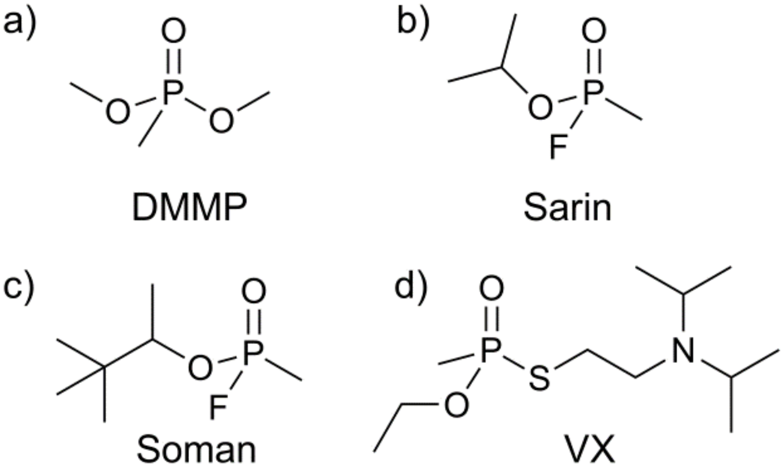

Figure 29: Schematic representation of the simulant (a) DMMP and the three nerve agents (b) Sarin, (c) Soman and (d) VX.

Force Field

Lennard-Jones parameters and partial charges for the DMMP, sarin and soman were taken from TraPPE united–atom (UA) force field[181]. The TraPPE–UA force field for alcohols[108] was used to model the 1-octanol and the SPC/E force field was used for water[187]. The combination of force fields has been shown in previous calculations to provide reliable estimates of partition coefficients for *n*-alkanes[44].

A similar united–atom approach was used for VX; hydrogen atoms bonded to carbon atoms were combined to form a single interaction site (pseudo–atom)[37]. Hydrogen atoms for polar interaction sites that carried a partial charge were modelled explicitly. Lennard–Jones parameters for the various interaction sites in VX were taken from previously parametrized compounds that contained analogous functional groups. For instance, Lennard–Jones parameters for the methyl carbons were obtained from methyl groups in alkanes[37], phosphorous and oxygen parameters were transferred from DMMP[188], the nitrogen parameter from the tertiary amine force field[189], and finally parameters for sulphur were taken from the LJ parameters of sulphides[190]. Point charges were determined for the lowest energy conformer from a CHELPG population analysis of HF/6-31g+(d,p) quantum calculations performed using GAUSSIAN 09[191]. For all molecules, interactions between the atoms of different types were determined with the Lorentz–Berthelot combining rules[192]. Bond stretching and bond angle bending were controlled with a harmonic potential. The dihedral angle rotation was governed by a cosine series functional form. The total energy of the molecule *U(r)* is given by the summation of all these individual contributions as shown in Equation 1.

$$U(r) = \sum_{bonds} k_b (b - b_o)^2 + \sum_{angle} k_\theta (\theta - \theta_o)^2 + \sum_{dihedrals} k_\chi (1 + \cos(n\chi - \delta)) + \sum_{nonbonded} \varepsilon_{ij} \left[\left(\frac{R_{\min ij}}{r_{ij}} \right)^{12} - 2 \left(\frac{R_{\min ij}}{r_{ij}} \right)^{6} \right] + \frac{q_i q_j}{\varepsilon_o r_{ij}}$$

Equation 27

Parameters governing the rotation around various dihedral angles were optimized to reproduce rotational barriers predicted by HF/6-31+g(d,p) quantum mechanics calculations. Potential energy scans were performed in intervals of 20° for each dihedral of interest with GAUSSIAN 09. In the TraPPE force field, 1-4 interactions are not usually included in the calculation of rotational barriers, i.e. the total dihedral potential is accounted for by the cosine series. However, to ensure compatibility with typical molecular dynamics software, the optimized dihedral parameters for the cosine series in this work follow the CHARMM methodology and include contributions from 1-4 Lennard-Jones and Coulombic interactions.

The rotational barriers predicted by QM and MM calculations for DMMP show close agreement for DMMP and sarin. For VX, the locations of the global minima predicted by QM and MM calculations are in agreement, but it was not possible to simultaneously reproduce all of the local minima predicted by QM calculations. These discrepancies arise from the inability of the cosine series to simultaneously reproduce the multidimensional potential energy surface (seven dihedral angles for VX). Increasing force constants in the cosine series beyond 3 kcal mol^{-1} made the molecule rigid. The periodicity *n* was truncated at 3 to reflect the three–fold nature of the potential energy surface for the rotation of two sp^3 hybridized centres. In the fitting process, more emphasis was placed on the reproduction of the global and local minima, while lesser importance was given towards reproduction of geometries whose energetics were greater than 10 *kT,* since it is unlikely such structures would ever be observed during simulations below the normal boiling point of these compounds. Changing the magnitude of force constants and increasing *n*–fold terms of the cosine series functional form was found to improve the energetics of a certain dihedral angle while worsening the energetics of another. Therefore the optimized dihedral parameters represent a compromise to provide the best overall reproduction of the conformational behaviour for each molecule.

Simulation Details

The adaptive biasing force (ABF) method is a technique developed by Darve *et al.*[103, 104, 193] for the calculation of free energy differences of certain chemical or biological processes along generalized reaction coordinates in the system of interest. This method is a combination of probability density and constraint force methods, and is based on the thermodynamic integration of average force acting on coordinates, which is unconstrained.[103] As a part of ABF algorithm, an external biasing force, estimated locally from configurations sampled by the simulation, is applied at each step to facilitate the system in overcoming energy barriers that may be present along the reaction coordinate. This allows the system to evolve freely, without constraints, and enables the simulation to visit states separated by large free energy barriers.

In this work the adaptive force bias method as implemented in adopted in NAMD[111] version 2.7b3 was used to determine the free energies of solvation for a simulant (DMMP) and three chemical warfare agents (sarin, soman and VX) in 1-octanol and water; these data were used to determine the 1-octanol/water partition coefficient log K_{ow}. An “indirect transfer,” process is used where the free energy of transfer from water to 1-octanol is determined from two separate calculations; transfer of the solute from 1-octanol to vacuum ($\Delta \boldsymbol{G}^{\boldsymbol{SOLV}}$**)** and transfer from water to vacuum ($\Delta \boldsymbol{G}^{\boldsymbol{HYD}}$**)**. The free energies of hydration and solvation were combined according to Equation (8)

$$\Delta \boldsymbol{G} = \Delta \boldsymbol{G}^{\boldsymbol{HYD}} - \Delta \boldsymbol{G}^{\boldsymbol{SOLV}}$$

Equation 28

where ΔG^{HYD} is the free energy of hydration in water and ΔG^{SOLV} is the free energy of solvation in 1–octanol for the considered solute, to provide the overall free energy of transfer from water to 1–octanol phase. From the free energy of transfer, it is possible to determine the 1-octanol/water partition coefficient according to

$$\log \mathrm{K}_{\mathrm{OW}} = \frac{\Delta G}{2.303RT}$$

Equation 29

Two different configurations were generated for the required calculations; a water/vacuum system (S1) and 1-octanol/vacuum system (S2) as shown in Figure 2. For calculations involving DMMP, sarin and soman, a rectangular simulation cell was used, with dimensions 30 Å x 30 Å x 90 Å, with the condensed phase occupying a region 30 Å x 30 Å x 30 Å. For VX, the dimensions of the simulation cell were 40 Å x 40 Å x 100 Å, with the condensed phase occupying a region 40 Å x 40 Å x 40 Å. The vacuum region is necessary to prevent interactions of the solute with the condensed phases through periodic boundary conditions.

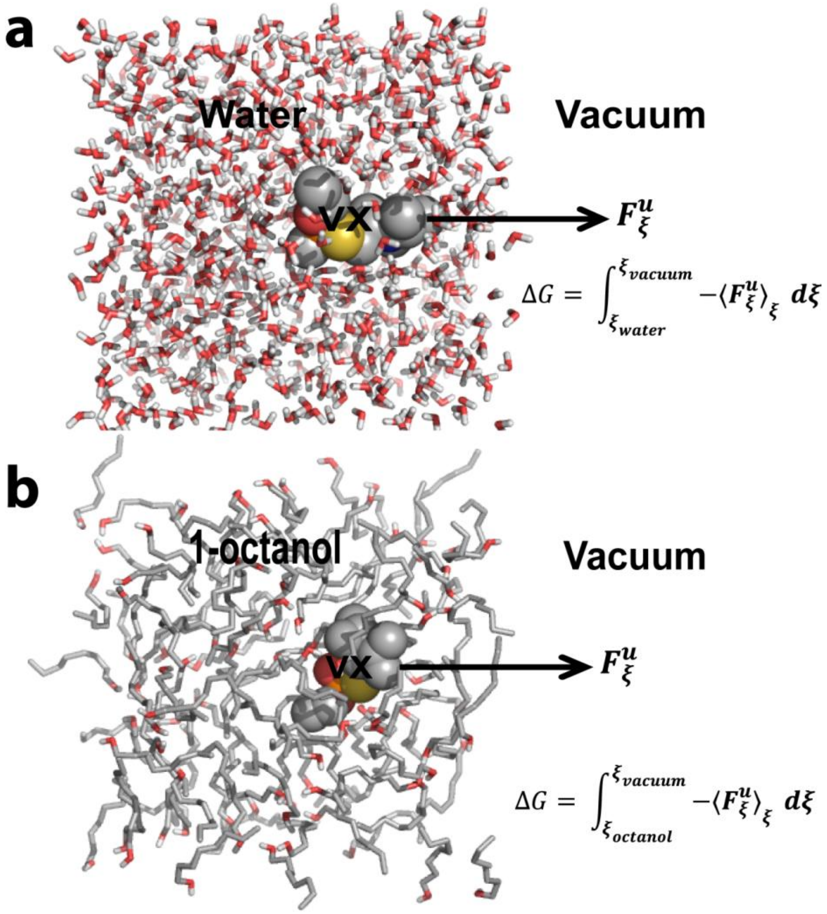
a
Water
Vacuum
VX
F_{ξ}^{u}
$\Delta G = \int_{\xi_{water}}^{\xi_{vacuum}} -\langle F_{\xi}^{u} \rangle_{\xi}\, d\xi$
b
1-octanol
Vacuum
VX
F_{ξ}^{u}
$\Delta G = \int_{\xi_{octanol}}^{\xi_{vacuum}} -\langle F_{\xi}^{u} \rangle_{\xi}\, d\xi$

Figure 30: Schematic diagram for the "Indirect–transfer method" of solute from condensed phase to vacuum. 5 windows of 5 Å bin width each in the z direction were used to compute the potential of mean force.

The reaction coordinate for the determination of free energy changes was defined as the distance between the center of mass of the solute (COMS) and center of mass of the condensed phase (COMCP). This reaction coordinate is the same as ξ in equations (3) to (7). In the initial system setup, the COMS are placed approximately at the COMCP. For DMMP, sarin and soman, the reaction coordinate spanned a distance of 30.0 Å from the center of mass of the condensed phase to the center of the vacuum region. For VX, the reaction coordinate was extended to 40 Å. To reduce the statistical uncertainty of the calculations, the reaction pathway was divided into five equally sized non–overlapping windows 5.0 Å wide. To generate the initial configurations for each window, a single 5 ns ABF run was performed spanning the complete reaction pathway from 0.0 Å to 30.0 Å. Coordinates from the trajectory of this simulation were saved at suitable intervals to provide an initial configuration for each window. Windows were sub–divided into bins with width of 0.05 Å for the collection of force statistics. The biasing force applied after 500 samples were collected in each bin. To keep the solute within the specified window, a harmonic potential with a magnitude of 10.0 kcal $mol^{-1}Å^{-1}$ was applied on the upper and lower boundary of the window along the *z*–axis.

Molecular dynamics simulations were performed with NAMD version 2.7b3. Initial configurations for each system were generated with Packmol[79]. Energy minimization was performed on all systems for 500 steps using the steepest decent technique. Systems were equilibrated over a time period of 2.0 ns in isobaric–isothermal ensemble at 1.0 atm and 298 K, followed by the ABF calculation in NVT ensemble. For all calculations, the temperature was maintained at 298.0 K using Langevin dynamics. A timestep of 2.0 fs was used for the integration of Newton's equation of motion. Periodic boundary conditions were used in all the three spatial coordinates. Long range electrostatic interactions were calculated with particle–mesh Ewald algorithm[82]. Lennard-Jones interactions were truncated at 14 Å and a switching function was applied at 12.5 Å. Data visualization and analysis was performed with VMD[151]. Statistical errors were estimated from the standard deviation of the predicted free energies generated from three to five unique sets of simulations. Initial validation of the VX force field was performed with NPT molecular dynamics simulations performed for 5 ns on a 128 molecule system. The predicted densities at 298, 308 and 323 K were 1044.67 kg/m^3, 1035.89 kg/m^3 and 1022.73 kg/m^3, which were within 3.5% of experimental data.

Results and Discussion

Hydration free energy

The profiles for the potential of mean force for each solute in water as a function of distance along the reaction coordinate are presented in **Figure 30**. Profiles are flat in the bulk water phase and drop to zero at 13-14 Å as the water-vacuum interface reached. This minimum is a result of reduced density at the interface compared to the bulk water phase, which reduces the free energy cost of accommodating the solute. However, apart from entropic reasons, another factor that has an effect on the profile is the interactions between water and solute. These interactions are more favourable compared to those in the vacuum phase, hence the profile rises to a maximum after crossing the interface and reaching the bulk vacuum region. For the case of solvation free energy profile, shown in **Figure 30**, there is a balance between the entropic factor and the interactions between the solute and 1-octanol resulting in a flat profile for the free energy of solvation at the interface.

The free energy of hydration was computed based on the difference in the free energy of the first window (solute in water rich phase) and the last window (solute in vacuum phase). These free energy differences are listed in Table 1 for DMMP, sarin, soman and VX. For all solutes, with the exception of DMMP, the free energy of hydration was within 1 kcal mol^{-1} of experiment.

Henry's law constant

The dimensionless Henry's law constant was determined using the relative free energy difference of moving the solute from the water rich phase to the vacuum phase.

Table 8: Comparison of the free energy of hydration, 1-octanol/water partition coefficient and Henry's law constant predicted using ABF–MD simulations at 298 K and experiment.

	ΔG^{HYD} (kcal mol^{-1}) Expt.	**ΔG^{HYD} (kcal mol^{-1}) Sim.**	**ΔG^{SOLV} (kcal mol^{-1}) Sim.**	**log H Expt.**	**log H Sim.**	**log K_{ow} Expt.**	**log K_{ow} (dry octanol) Sim.**	**log K_{ow} (wet octanol) Sim.**
DMMP	–5.82[194] –7.67[195]	–7.63 ± 0.3	–7.51 ± 0.3	–4.27[194, 196] –5.63[195]	–5.57	–0.61[186] –1.30[195]	–0.07 ± 0.3	–0.27± 0.3
Sarin	–4.67	–5.58 ± 0.2	–6.68 ± 0.2	–3.42[197] –4.63[194, 196]	–4.03	0.30[194, 198] 0.72[196] 0.45[198] 0.299[186] 0.15[199, 200]	0.85 ± 0.2	1.20± 0.2
Soman	–5.07 –5.29	–4.75 ± 0.2	–8.15 ± 0.3	–3.72[194] –3.88[201]	–3.48	1.02[199, 200] 1.78[194, 196] 1.824[186]	2.49 ± 0.4	2.70± 0.4
VX	–9.34	–9.45 ± 0.3	–14.45 ±0.2	–6.85[194] –4.05[201]	–6.96	0.675[186] 2.09[194] 1.992[202] 2.22 2.36[199, 200]	3.66 ± 0.4	3.80± 0.4 -

The predicted Henry's law constant of –6.96 for VX is in excellent agreement with experimental value of –6.85[194], highlighting the transferability of the TraPPE force field. For DMMP, the predicted Henry's law constant of –5.57 is in excellent agreement with the value determined using vapour pressure and water solubility as described in the DMMP consortium report[195]. However, other measurements of the Henry's law constant give log H = –4.27. Given the disagreement between experimental data sources, it is difficult to rigorously evaluate the quality of the force field. The data of Ref [194, 196]suggest that the free energy of hydration is over-predicted slightly by the TraPPE DMMP force field. Improved free energies of hydration could be achieved through a slight reduction in the partial charges, but this would lead to errors in the predictions of other thermodynamic properties, such as liquid densities, heats of vaporization or the normal boiling point, which were used in the original optimization of the model[181]. In the case of sarin, the predicted Henry's law constant of -4.03 lies in between the experimentally reported range of –3.42 and –4.63. For soman, the free energy of hydration is slightly under–predicted in comparison to experiment, –3.48 (simulation) vs. –3.72[194] to –3.88[201] (experiment).

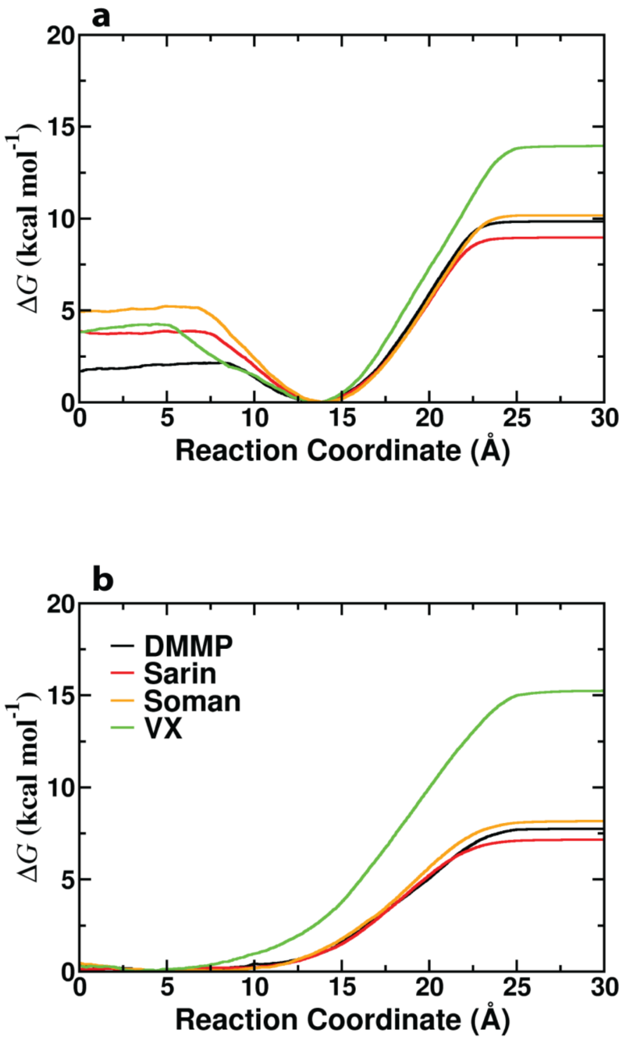

Figure 31: a) Average free energy of hydration profile generated with ABF–MD for solute transfer from water phase to vacuum phase. b) Average free energy of solvation profile generated with ABF–MD for solute transfer from 1-octanol to vacuum phase.

Solvation free energy

The free energy of solvation was computed similar to the free energy of hydration and are shown in Table 1. Singer *et al*. computed the octanol–air partition coefficient (K_{oa})[196] using the following equation

$$K_{\mathrm{OA}} = \frac{1000RTK_{\mathrm{ow}}}{K_H}$$

Equation 30

The experimental free energy of solvation can be determined for comparison to the simulation data. For sarin, simulations predict ΔG^{SOLV} =–6.68 kcal mol^{-1}, which is within 10% of the experimental value of 7.29 kcal/mol estimated from reference [46] using Equation 11. In the case of soman, the value of –8.15 kcal mol^{-1} predicted by simulation is within 5% of experiment. For DMMP, however, the free energy of solvation is over-estimated by approximately 2.5 kcal/mol. No experimental data was found for VX.

Partition coefficient

From knowledge of G^{SOLV} and G^{HYD}, it is possible to calculate the log K_{ow}. Table 8 lists the computed log K_{ow} for the simulant and three nerve agents. For VX, although the Henry's law constant was in good agreement with experiment, the log K_{ow} is over-predicted by 2.0 log units. There is, however, significant scatter in the experimental data, with some data compilations reporting a number of 0.675[203] while others suggesting a value of 2.09[194]. For sarin, the predicted partition coefficient is within 0.12 log units of experiment. A negative value for the log

K_{ow} of DMMP suggests this compound prefers the water phase over 1-octanol. In this case, the model predicts correctly a negative value for log Kow, but there are quantitative differences of 0.5 to 1.2 log units between simulation and experiment. Given the large scatter in the experimental data, the agreement between simulation and experiment is reasonable. The negative enthalpy of mixing for DMMP in water[182] further corroborates the hydrophilic nature of DMMP.

The interaction of DMMP with water has been studied extensively using matrix–isolation IR spectroscopy with *ab initio* computation[204], molecular dynamicss[182, 205] and NMR[206]. In the vapor phase, *ab initio* calculations have predicted a strong hydrogen bond of –7.7 kcal mol^{-1} between water and oxygen O=(P) of DMMP. In the aqueous phase, two water molecules bind to the sp^2 hybridized oxygen of DMMP at higher water concentrations. Vishnyakov *et al*. have used molecular simulation to study the interactions of DMMP with water. These calculations show significant clustering of DMMP for low water concentrations, suggesting a dominance of hydrophobic interactions with low life times of the DMMP-water complex. This could also account for the lower value of the 1-octanol/water coefficient predicted for DMMP in comparison to experiment. In the case of soman, log K_{ow} was over-predicted by 0.8 log units. This over-prediction of the partition coefficient using the TraPPE force field was observed for all solutes, which given the close agreement between simulation and experiment for the free energy of hydration suggests the force fields are over-predicting the free energy of solvation.

Impact of water saturation

In experiments for the determination of octanol-water partition coefficients, the octanol phase is typically saturated with water. While the use of a wet octanol phase has a negligible effect on the partition coefficients predicted by simulation for non-polar molecules[36, 114, 207], water saturation may have a significant impact on predicted log K_{ow} values for polar molecules[208]. To investigate this, additional simulations were performed for wet octanol, where the simulation box 1-octanol phase contained 25.5 mole% water. In general, the addition of water slightly increased log K_{ow} for each solute, except for DMMP, where log K_{ow} was reduced from -0.1 to -0.27. In each case, log Kow values predicted with wet octanol were withing the statistical uncertainty of the corresponding calculations performed with dry octanol, showing that the presence of water in 1-octanol was a limited effect on the partitioning of these solutes.

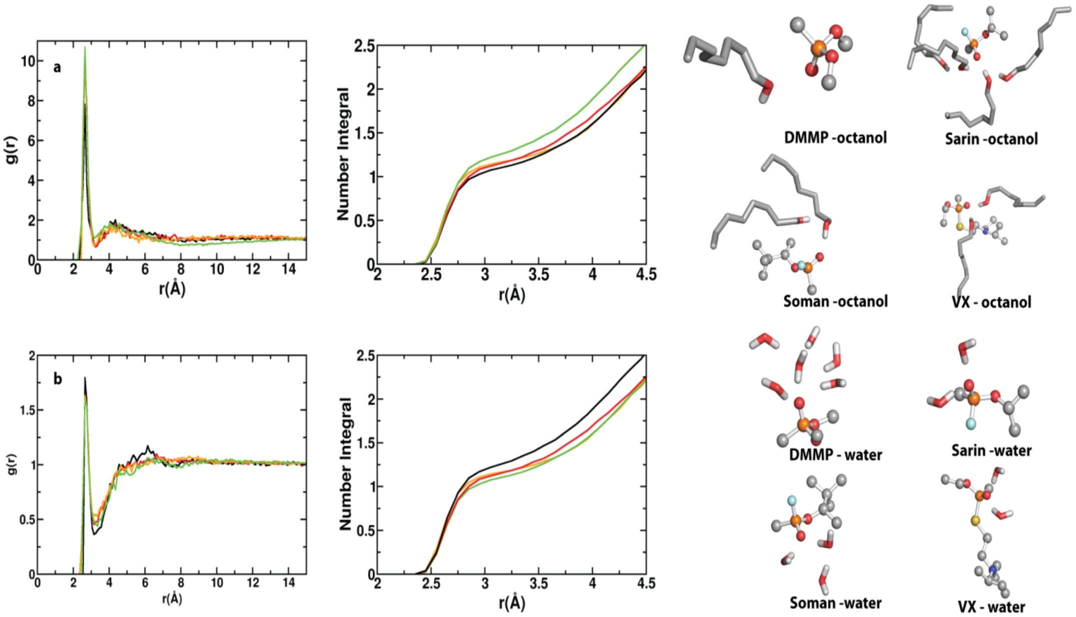

Figure 32: 6 Left Panel: Radial Distribution functions of the octanol (a) and water (b) interacting with the oxygen O2 of DMMP (black), Sarin (red), Soman (orange) and VX (green) at 298 K. Middle Panel: The corresponding number integrals respectively. Right Panel

The microstructure of the chemical warfare agents interacting with water and 1-octanol was investigated using the pair-wise radial distribution functions. For each of the compounds investigated in the present study, there is an oxygen (O_2) doubly bonded to phosphorous and an oxygen singly bound to phosphorous and carbon. The oxygen O_2 (double bonded to the phosphorous atom) interacts strongly with the hydroxyl oxygen of 1-octanol. A peak at 2.7 Å for the O_2 interaction with oxygen of the 1-octanol suggests strong hydrogen bonding interactions between the 1-octanol hydrogen and O_2 of the chemical warfare agent. However, the magnitude of this peak decreases as one goes from VX to DMMP, providing certain insights into the hydrophobic nature of VX in comparison to DMMP. Looking at the number integrals, at 3 Å, the average number of hydrogen bonding interactions drop from 2 for VX to 1.3 for DMMP, see middle panel of Figure 32. This suggests that in comparison to VX, sarin and soman dmmp is less solvated by 1-octanol. Although, one would attribute the hydrophobic nature of any compound to the carbon-carbon interactions of the alkyl groups in cwa and 1-octanol, here it's the relative increased affinity of VX for the polar group (hydroxyl group) of the 1-octanol that maybe responsible for its hydrophobic nature. A similar instance is seen for the polar affinity of the other two nerve agents with 1-octanol. This affinity for the hydroxyl group of 1-octanol is reduced in the case of DMMP. While other polar groups exist in the nerve agents, O_2 interactions with 1-octanol is are the most pronounced. A similar scenario is present in the case of the cwa interacting with water. DMMP O_2 interacts more strongly with water in comparison to sarin, soman and VX, indicating the more hydrophilic nature of DMMP, see Figure 32 (left panel). The magnitude of the peak at 2.7 Å decreases from 1.7 to 1.5 for DMMP to VX, suggesting that this subtle difference in magnitude would provide clues to the hydrophilic nature of DMMP in comparison to the hydrophobic nature of the other three nerve agents. As seen from the snapshot, Figure 4b, right panel, the O_2 of DMMP has more water molecules interacting than the other three nerve agents.

ABF convergence

ABF method embodies a prominent feature of sampling the phase space along the chosen reaction coordinate in a uniform and homogenous manner irrespective of the high energy barriers present along the pathway. To check the sampling behaviour of ABF simulations for systems used in this study, a test case of VX was chosen for which, number of samples accumulated at the end of simulation were plotted as a function of reaction coordinate. The resulting plot is shown in **Figure 31** for the transfer of VX from water to vacuum and from 1-octanol to vacuum. Uniform sampling is observed along the complete reaction pathway for both the cases.

Evolution of sampling was also studied for the test case of VX transfer from 1-octanol to vacuum phase to check the convergence of ABF method. Sampling histograms were generated at various intervals during the course of simulation as a function of the reaction coordinate. In the early stages of simulation (0.02 ns), only a few locations have been sampled while the others remain unvisited. As time proceeds, the sampling becomes uniform and attains uniformity around 6.0 ns indicating the convergence of ABF run. Maxmin ratio is another parameter that is used to mark the convergence of ABF based simulation. It is defined as the ratio of maximum number of samples to minimum number of samples collected in a specific region along the reaction coordinate. This ratio is equal to ∞ for the VX test case at a point when simulation has run for 0.02 ns as the minimum number of samples count to zero. Evolution of maxmin ratio with time is shown in **Figure 33**. Ratio attains a measurable value as simulation progresses and all the locations are visited at least once. Maxmin value eventually drops down and comes close to 1.0 after 8 ns of runtime which means that all the locations have been visited for almost equal number of times marking the convergence of ABF run.

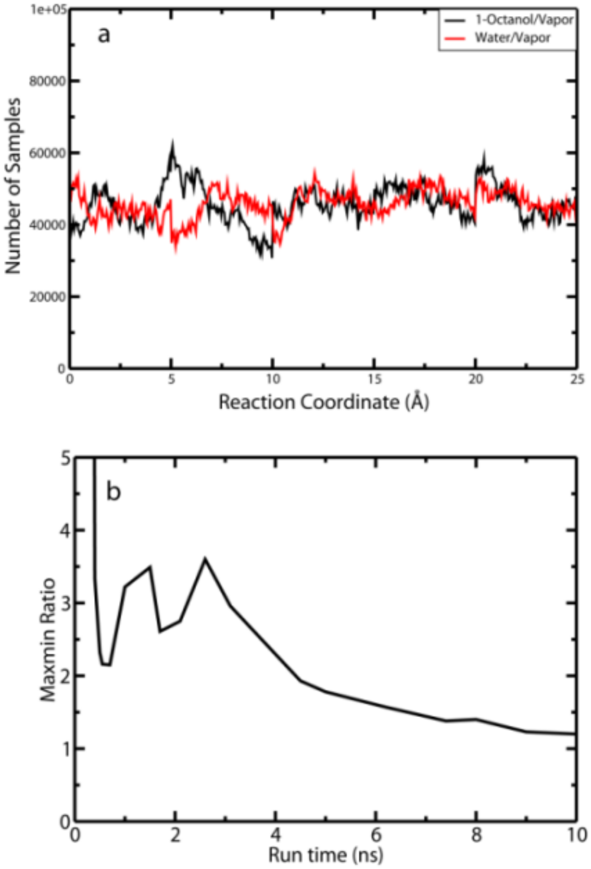

Figure 33: a) Distribution of sampling along the reaction coordinates. Results are for the case of VX transfer from water to vacuum (red) and 1–octanol to vacuum (black). b) Evolution of the maxmin ratio during 10 ns of ABF-MD simulation.

Bioaccumalation analysis

The 1-octanol/water partition coefficients for the solutes suggest that the three nerve agents are neither hydrophobic (log $K_{ow} > 6$) nor hydrophilic (log $K_{ow} < 0$). However the simulant DMMP is hydrophilic in nature with log $K_{ow} = –0.1$. This raises certain questions towards the choice of

DMMP as a simulant as it is hydrophilic in comparison to all the nerve agents which tend to be hydrophobic. Figure 34 is mobility and multimedia chart[209][209] designed by Gillett in 1983 to characterize compounds based on their comparative mobility due to volatilization. As seen in this figure 5, DMMP falls in the same zone D as that of the other nerve agents. In terms of predicting the environmental fate of the nerve agents, DMMP is able to mimic the behaviours of nerve agents. The simulant DMMP and the three nerve agent's fall in the zone D which is characterized by direct effects to the water column, leading to leaching, plant uptake and drinking water toxicologic effects. Although the partition coefficient and Henry's law constant predictions by our models are in fair agreement, the model predictions also fall in the zone D. VX on the other hand falls on the border of Zone D and B as predicted by our model. However quantity A which is measure of the sum of Henry's law constant and log K_{ow} and determines the tendency of the solute to the leave the aqueous phase equals to –3.26 and is < -1 for VX, still making this compound a concern for contamination of the water column and bioaccumulation. Soman being on the boundary of zone D and B provides additional concerns of bioaccumulation.

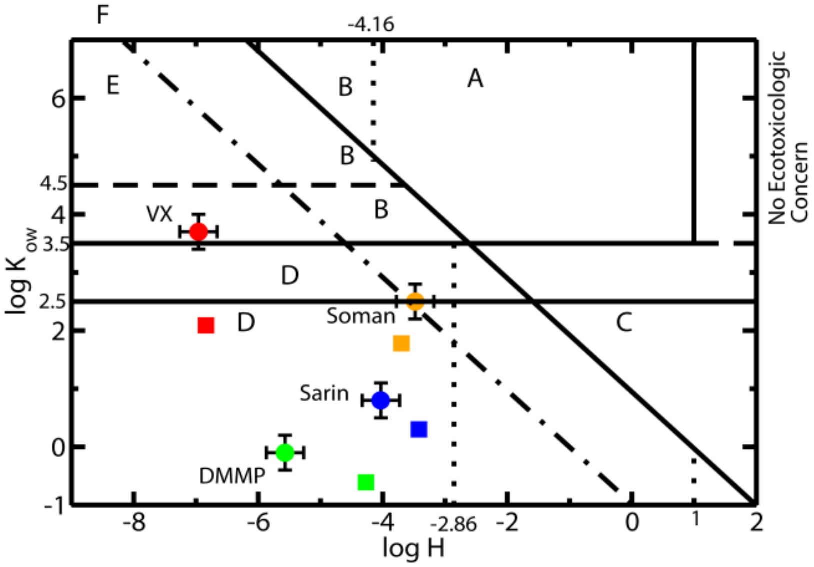

Figure 34: Mobility and multimedia exposure chart. Zone A has heavy multimedia, multispecies and bioaccumulation concerns. Zone B has heavy concerns regarding bioaccumulation. Zone C has concerns regarding atmospheric problems. Zone D has heavy concern for dire direct effects on water column. Zone E and Zone F are low ecotoxicology concern due to very low mobility. Filled circles are simulation predictions while experiment is denoted by filled squares.

Conclusions

Adaptive Biasing Force–Molecular Dynamics simulations have been used to predict the 1-octanol/water partition coefficient and Henry's law constant for nerve gas agents using the TraPPE force field. New dihedral parameters consistent with molecular dynamics simulation engines, such as CHARMM and NAMD are introduced, as is a new force field for VX. In general, the TraPPE force field provides reasonable estimates of Log H and Log K_{ow} for each compound. Although the free energy of solvation and hydration for DMMP are over-predicted by the present model, the predicted partition coefficient has the correct sign and is within 0.5 log units of experiment. The liquid density predictions for VX at three different temperatures were within 3.5% of experiment. Finally analysis of the microstructure suggests that the relative difference in the degree of solvation of these chemical warfare agents in 1-octanol and water may be responsible for hydrophilic or-phobic nature.

CHAPTER 7: Biomolecular Simulations with the Transferable Potentials for Phase Equilibria: Extension to Phospholipids.

Background

At the heart of any molecular simulation is the force field used to describe interaction between atoms in molecules. A central question regarding force fields is that of transferability, i.e. what is the predictive capability of a force field when used to calculate properties at temperatures and pressures far removed from those used in the original parameterization? Is it possible to optimize parameters to a particular set of target data and obtain reliable results for other properties that were not used in the optimization process? This idea of transferability may be carried even further; to what extent may parameterized functional groups or atoms be reused in other molecules and still provide accurate results?

Traditional approaches to the parameterization of non-bonded interactions for biomolecular force fields involve the optimization of parameters to reproduce condensed phase properties, such as liquid densities and heats of vaporization at ambient conditions[210-213]. Additional input from quantum mechanical calculations, such as binding energies with water [212, 214] or rare gas atoms [215, 216] may be used to further optimize partial charge distributions and Lennard-Jones parameters. Free energies of solvation in water and other solvents, such as hexane, cyclohexane or 1-octanol, have also been used as a target parameters in the optimization process [134, 213, 217].

On the other end of the spectrum are force fields for the prediction of vapor-liquid equilibria [74, 218-221]. These force fields typically make use of quantum chemical calculations for the determination of partial charge distributions, while Lennard-Jones parameters are optimized to reproduce complete vapor liquid coexistence curves from the normal boiling point to the critical point. Additional data, such as vapor pressures [222, 223] or mixture phase equilibria may also be used in the optimization process [224, 225]. By optimizing non-bonded parameters over a broad range of temperatures and pressures, these force fields are capable of making reliable predictions for fluid physical properties over a broad range of temperatures, pressures, phases (gas, liquid and solid), for pure fluids and complex mixtures.

In recent years generalized versions of biomolecular force fields have been published[226, 227], and these have been used to provide valuable insight for a broad array of chemical in addition to biological systems. On the other hand, there has been little cross-over for force fields developed for the prediction of vapor-liquid equilibria into the realm of biomolecular computation. In the past this was due to limitations of the parameter sets, however, in recent years parameter sets have expanded to the point where the simulation of biological systems is now a possibility.

Lipid bilayers composed of phospholipids are crucial to sustaining life; forming the boundaries of cells and acting as scaffolds to support a variety of proteins. Because of their central importance in understanding life processes, lipid bilayers have been studied extensively, both through experiments and computer simulations. Early attempts to simulate lipid bilayers relied on “ad-hoc” force fields, with parameters derived from analogous compounds and combined to form the lipids of interest. An example of this is the well-known “Berger” force field for phosphatidylcholine, which was derived by combining bonded interactions from GROMOS with non-bonded interactions from the OPLS-UA (united-atom) force field[228] and partial charges from the work of Chiu *et al*.[229]. This model included new parameters for the alkyl tail, which were optimized to reproduce the heat of vaporization of pentadecane. Additional united-atom force fields for phoshatidylcholine lipids have appeared in the literature based on the GROMOS force field, of which there are numerous variants. Chiu *et al.* combined partial charge distributions from a prior work[229], with Lennard-Jones parameters optimized by fitting to reproduce liquid densities and heats of vaporization of model compounds to produce the 43A1-S3 parameter set for lipids [230]. While providing a good reproduction of bilayer properties, such as area per lipid, the 43A1-S3 force field introduced subtle inconsistencies in the non-bonded parameters used for lipids and other compounds. A self-consistent GROMOS lipid force field for DPPC based on the G53A6 parameter set, referred to as G53A6$_L$, appeared shortly thereafter[231]. Additional models have been proposed for phosphatidylglycerol (PG) lipids by Kukol[232], who combined the G53A6 Lennard-Jones parameters with partial charges from Zhao *et al.* [233].

Development of lipid force fields based on the AMBER parameter set followed a path similar to GROMOS. Parameters from the Generalized Amber Force Field (GAFF) were combined with RESP derived partial charges[234] to produce a model for POPC. However, simulations in the tensionless NPT ensemble led to bilayer condensation, with area per lipid values approximately 20% below experiment. For this parameter set, an applied surface tension of 30 mN/m was required to reproduce the experimental area per lipid[235]. LIPID11 uses a modular approach, analogous to proteins, to build lipid force fields from GAFF, although the resulting models require simulation using constant area, or with a non-zero surface tension to prevent condensation above the gel phase transition temperature[236]. The tendency for bilayer condensation was eliminated by refitting of the Lennard-Jones parameters for carbon and hydrogen atoms in the alkyl tails to reproduce the heat of vaporization and liquid density for pentadecane[237]. This parameterization is known as GAFFlipid.

Like GAFF, CHARMM is an all atom force field for the simulation of nucleic acids, proteins, carbohydrates, and lipids. The CHARMM lipid force field has a long history and has undergone continuous revision as computer hardware advances have provided access to larger systems and longer run times. While lipid bilayer simulations were performed with the C22 parameters set for approximately 1 ns[238, 239], the latest C36 parameter set was validated with simulations of over 100 ns[240]. For simulations of DPPC with the C22 parameters, NPT simulations of approximately 1 ns showed good agreement with experimental area per lipid values. However, later simulations of DPPC bilayers in the NPγT ensemble revealed that for γ=0 the C22 parameter set produced area per lipid values that were approximately 14% lower that experimental values[241]. The C27 parameterization involved the optimization of Lennard-Jones parameters for the alkyl tails, and torsional potentials for the phosphate head group[242]. Despite these improvements, the C27 parameter set still exhibited a tendency towards condensation at temperatures above the gel phase transition temperature when used in tensionless NPT simulations[243]. Through reoptimization of the partial charges for the phospholipid head group using the RESP method, Sonne *et al.* produced a variant of the C27 force field was capable of predicting an area per lipid for DPPC within 6% of experimental values when run in the NPT ensemble[244]. The C36 parameter set included significant reparameterization of torsional potentials, partial charge distributions and Lennard-Jones parameters for both the lipid head group and the alkyl tails. Extensive NPT simulations have shown that this latest parameterization reproduces closely a broad range of experimental data, including area per lipid[240]. The C36 parameter set also provides the foundation for another lipid force field known as Slipids (Stockholm Lipids)[245, 246].

Given the extensive data that exist in the literature, phospholipid bilayers are the ideal system to assess the reliability of intermolecular potentials developed for vapor-liquid equilibria calculations when used in biological systems. In this work, the Transferable Potentials for Phase Equilibra (TraPPE) [74, 75, 139-141, 247-250] are extended to phospholipids that contain phosphatidylcholine (PC), phosphatidylethanolamine (PE), phosphatidylserine (PS) and phosphatidlglycerol (PG) functionalities. To highlight the transferable nature of the TraPPE force field, Lennard-Jones parameters developed for the prediction of low molecular weight organic molecule vapor-liquid equilibria are used without modification. Partial charges are determined from a CHELPG analysis of HF/6-31+G(d,p) *ab inito* calculations, while torsional parameters are refit to match the rotational barriers predicted by the CHARMM C36 lipid force field. A variety of quantities, including the area per lipid, volume per lipid, bilayer thickness, electron density and x-ray form factors are calculated from molecular dynamics simulations in the tensionless NPT ensemble and are shown to be in close agreement with experimental data.

Force Field

Non-bonded interactions in the TraPPE force field are described by the pairwise-additive 12-6 Lennard-Jones potentials and Coulombic interactions of partial charges

$$U_{ij} = 4\varepsilon_{ij}\left[\left(\frac{\sigma_{ij}}{r_{ij}}\right)^{12} - \left(\frac{\sigma_{ij}}{r_{ij}}\right)^{6}\right] + \frac{q_i q_j}{4\pi\epsilon_o r_{ij}}$$

Equation 31

where r_{ij} , □$_{ij}$, □$_{ij}$, q_i, and q_j are the separation, LJ well depth, pseudo-atom diameter and partial charges, respectively, for the pair of interaction sites *i* and *j* and ϵ_o is the permittivity of vacuum. A united-atom representation is used for all CH*x* groups; *i.e.* hydrogen atoms bonded to carbon atoms are not represented explicitly and are instead combined with the carbon atoms to form a single interaction action site or “pseudo-atom”. Lennard-Jones parameters for each interaction site were taken from previous TraPPE publications and used without modification.

Partial charges were determined from *ab inito* calculations performed on complete head groups, but without the hydrocarbon tails. Previous calculations have shown splitting of the head group into fragments may result in partial charge distributions that lead to area per lipid values that are significantly lower than experimental values. Consistent with the TraPPE force field, CH_X groups in the hydrocarbon tail were given a partial charge of 0. For zwitterionic lipids (PC, PE), structures were optimized using Hartree-Fock theory with the 6-31G(d,p) basis set, while for charged lipids (PS, PG) the 6-31+G(d,p) basis set was used. Partial charges were extracted from the electrostatic potential energy surfaces using the CHELPG (charges from electrostatic potentials using a grid based method) methodology. Charges on symmetrical or identical interaction sites were averaged to simplify the model. All quantum calculations were performed with Gaussian 09.

Each phospholipid was modeled as a fully flexible molecule, with conformational behavior controlled by a combination of harmonic potentials for bond stretching and angle bending

$$U = k(x - x_0)^2$$

Equation 32

where U corresponds to the bond stretching or bending energy, and x and x_{o} and the instantaneous (bond length or angle) and equilibrium (bond length or angle), respectively. Traditionally, the TraPPE force field uses fixed bond lengths; however, in this work flexible bonds were used to simplify the implementation of the force field in molecular dynamics. Values of the bond stretching constants were taken from the CHARMM C36 force field.

Rotations around dihedral angles are described with a cosine series

$$U_{tors} = \sum_{i=1}^{n} k_i [1 + \cos(i\varphi + \delta)]$$

Equation 33

where k_i are force constants, i is the periodicity or multiplicity, φ is the dihedral angle and δ the phase shift.

In prior implementations of the TraPPE force field, 1-4 Lennard-Jones and electrostatic interactions were not calculated explicitly. Instead, the cosine series was used to represent to total energy for barriers to rotation. This strategy was also used in the original OPLS united-atom force field. However, this poses problems for the use of TraPPE in most molecular dynamics simulation engines, which follow the conventions of biomolecular force fields, such as CHARMM and AMBER and explicitly include 1-4 Lennard-Jones and electrostatic interactions as part of the calculation of rotational barriers. Naively combining the CHARMM torsional potentials with the TraPPE Lennard-Jones and partial charges produced rotational barriers with significant errors compared to quantum chemical calculations. For example, the combing the CHARMM dihedral potential for the n-alkane tail with the TraPPE non-bonded parameters resulted in a significant over-prediction of *trans* relative to *cis* conformations.

Resolving this issue required the optimization of new parameters for the dihedral potential that took into account explicit 1-4 Lennard-Jones and Coulombic interactions. Lipid molecules were split into a series of model compounds, which are shown in **Figure 35**. Choline and dimethylphosphate were used to parameterize the torsions in lipid head group; ethylacetate for glycerol linker; hexane and hexene for the tail region. Dihedral parameters derived from these compounds were further optimized in calculations of rotational barriers in (M)EGLY and (M)PGLY. The use of larger model compounds for the optimization of dihedral parameters was found to be crucial to reproducing experimental order parameter data, including the phenomena of order parameter splitting near the head group. The branched region in (M)EGLY formed by atoms C1-C2-C3-O31 and C1-C2-O21-C21 contains multiple redundant dihedrals, the parameters for which were fit simultaneously. For each dihedral of interest, rotational barriers were determined from relaxed potential energy scans performed with the CHARMM software, version 34. For the lipids containing the phosphatidylcholine head group, parameters were optimized to reproduce rotational barriers given by the CHARMM 36 force field [240]. The CHARMM C36 force field was selected as the target data over quantum calculations since these parameters have already been optimized to reproduce QM data, and represent the current ``state of the art" for all atom lipid simulations. Additional rotational barriers found in phosphatidylserine and phosphatidylglycerol were optimized to reproduce data extracted from relaxed potential energy scans from MP2/6-31+G(d,p) quantum chemical calculations.

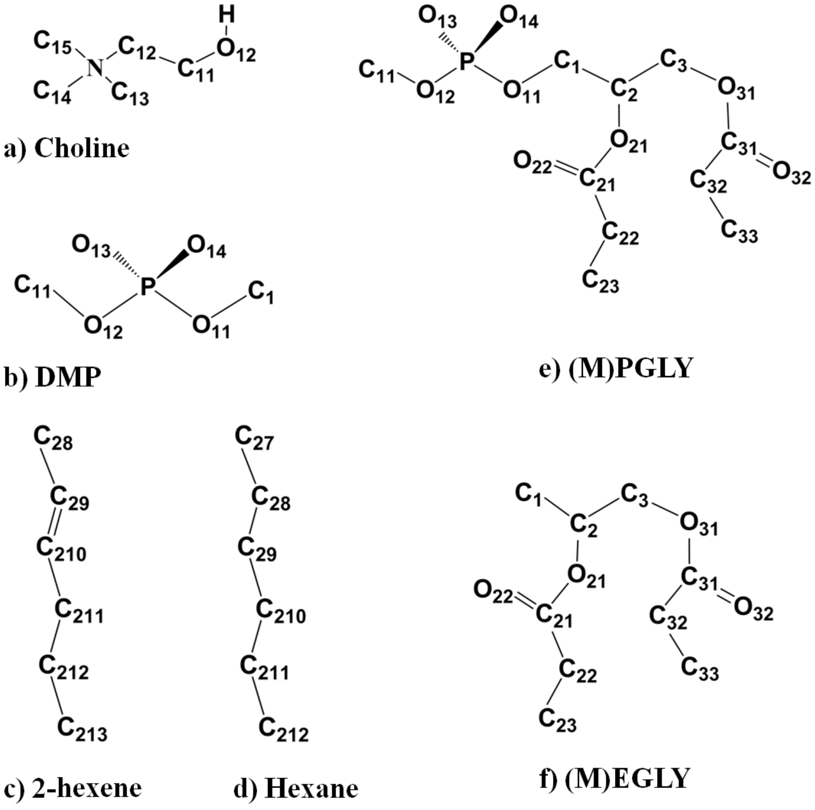

a) Choline

b) DMP

c) 2-hexene **d) Hexane**

e) (M)PGLY

f) (M)EGLY

Figure 35: Schematic of model compounds used in this study for torsion fitting is shown. a) Choline, b) dimethylphosphate (DMP), c) 2-hexene, d) hexane, e) esterified glycerol-phosphate analogue ((M)PGLY) and f)) esterified glycerol analogue ((M)EGLY).

In **Figure 36**, a comparison between selected rotational barriers predicted with the optimized TraPPE parameters and the CHARMM C36 force field is presented. Overall, the data show close agreement with predictions of the C36 parameter set. Subtle differences were observed for some of the rotational barriers in (M)EGLY and (M)PGLY. For the O12-C21-C22-C23 dihedral in (M)EGLY, the TraPPE force field over-predicts the magnitude of the barrier at 90 degrees by approximately 0.8 kcal/mol, while for the C1-C2-C3-O31 dihedral, the locations of minima are shifted by 2-3 degrees compared to the C36 parameter set. These small differences arise due to limitations in the united-atom representation, which does not provide as much fine-grained control over 1-4 Lennard-Jones interactions as an all-atom representation.

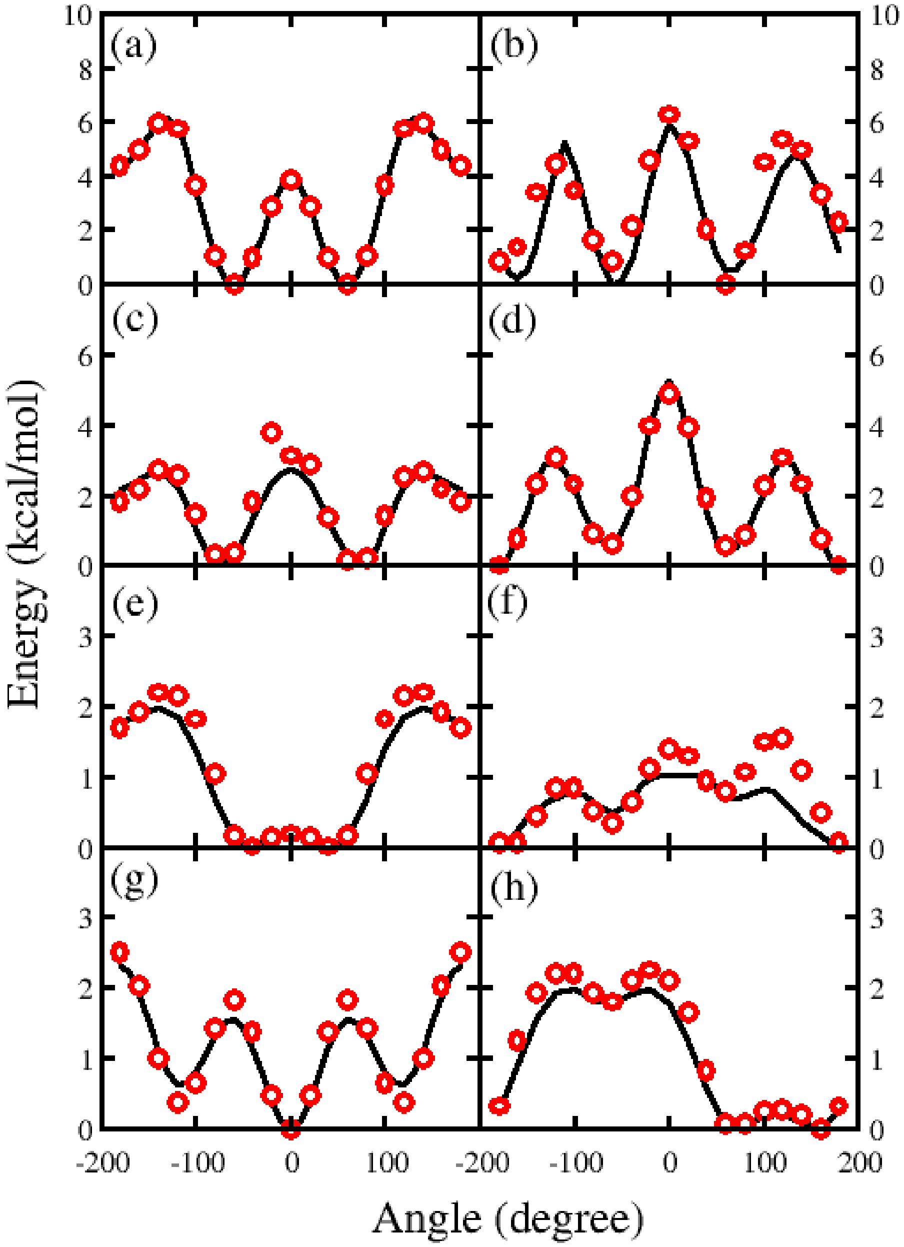

Figure 36: Energy scans of torsions from lipid headgroup predicted with TraPPE force field (red circle) and compared with C36 parameter set (black). a) N-C12-C11-O12, b) C1-C2-C3-O31, c) O11-C1-C2-C3, d) CT2-CT2-CT2-CT3, e) O12-P-O11-C1, f) O21-C21-C22-C23, g) C28-C29=C210-C211 and h) O13-P-O11-C1.

Simulation Details

The TraPPE force field was developed for nine lipids (DPPC, DMPC, DLPC, DOPC, DLPE, DOPS, DLPG, DMPG and DOPG), covering four different head groups and four different acyl chains. Calculations were performed on bilayers containing 128 lipids, solvated by approximately 50 water per lipid for zwitter ionic lipids, and 90 waters per lipid for charged lipids. Additional waters were included for charged lipids to provide sufficient hydration of ions used for charge neutralization, and minimize the interactions of the bilayer with itself through periodic boundary conditions. 128 Na^+ were added to the PS and PG systems to maintain charge neutrality. Interactions between water molecules were governed by the SPC/E force field. Simulations were performed with NAMD 2.9 in the isothermal-isobaric ensemble. Lennard-Jones interactions were truncated at 12 A, with a smooth switching function starting at 10 A. Electrostatic interactions were calculated using the Particle Mesh Ewald (PME). Temperature was controlled using Langevin dynamics with a damping coefficient of 5.0 ps^{-1}. The pressure was maintained at 1 atm with the Nose-Hoover Langevin piston, with an oscillation period of 100 fs and piston decay period of 50 fs. The cell volume was allowed to fluctuate independently in the x-y plane and the z coordinate access.

All the systems were initially minimized to the lowest energy state, followed by slow heating to a temperature of 323 K for DPPC, 308 K for DLPE and 303 K for all other lipids. All the temperatures were chosen to be above the gel phase transition temperatures of the respective lipids. Systems were simulated for 100 ns, using a time step of 2.0 fs.

Results and Discussion

Area per lipid

The area per lipid is a key structural property of lipid bilayers and is governed by a complex interplay of interactions between lipids and water. Of particular importance are interactions between water and oxygen atoms in the glycerol linker region. If these interactions are too weak, bilayers exhibit a tendency in tensionless NPT simulations to condense to area per lipid values indicative of the gel phase. This was illustrated clearly in simulations of DPPC bilayers using the GROMOS 53A6 parameter set with two sets of charges, GROMOS96, and those taken from Chiu et al[229, 231]. Simulations using the GROMOS96 charge set produced an area per lipid of 42.6 A^2, while those using the Chiu charges produced an area per lipid of 63.1 A^2. The CHARMM C27 force field for DPPC also displayed a propensity to condense at temperatures above the gel-phase transition temperature. Application of new partial charges determined from a RESP fit of RHF/6-31G(d) ab initio data to the C27 parameter set produced a model capable of reproducing the experimental area per lipid[244]. For both the GROMOS and CHARMM C27

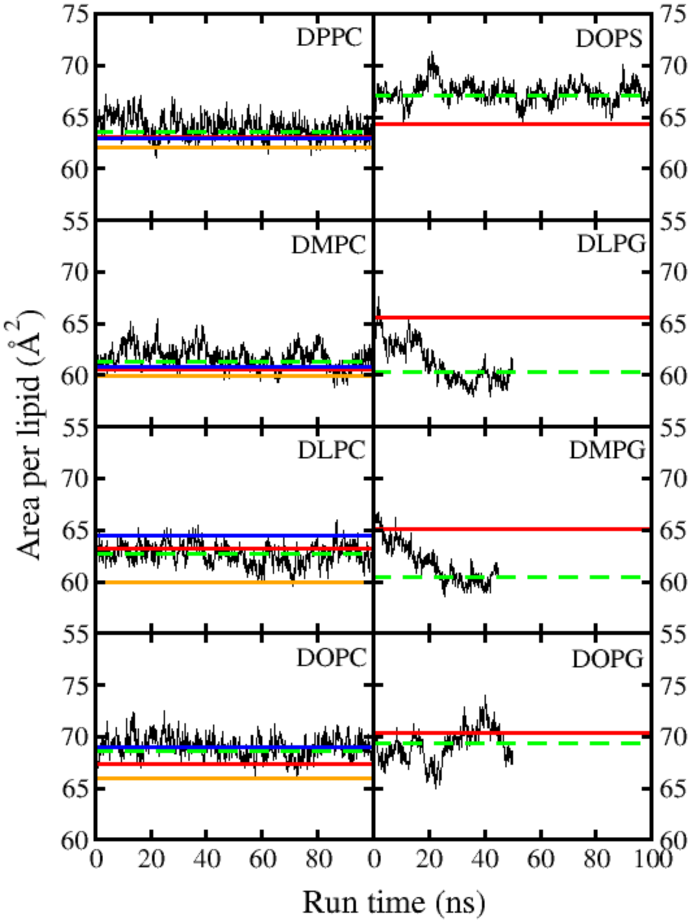

Figure 37: Evolution of area per lipid (black) with simulation run time lipids studied in this work. Average value of APL predicted by TraPPE is shown (green-dotted) and compared with experiment (red), C36 (blue) and GROMACS (orange) data.

force fields, the revised partial charge distributions feature significant increases in the magnitude of the partial charges for oxygen atoms in the fatty acid section of the lipid tails[231, 244, 251].

Because of the importance of water interactions with the lipid-head group, the choice of water model can have a significant impact on the predicted values of the area per lipid. Care must be taken to ensure the derived partial charge distribution for the lipids of interest is compatible with the chosen water model. In this work, partial charges were derived from a CHELPG analysis of HF/6-31G(d,p) and HF/6-31+G(d,p) ab initio calculations, which has been found by our group to produce accurate free energies of hydration for solutes modeled by the TraPPE-UA force field in SPC/E water. Evolution of area per lipid is plotted as a function of simulation run time and shown in Figure 37. Area per lipid values predicted by the TraPPE-UA force field are plotted vs. experiment in **Figure 38**, and numerical data are listed in **Table 9**.

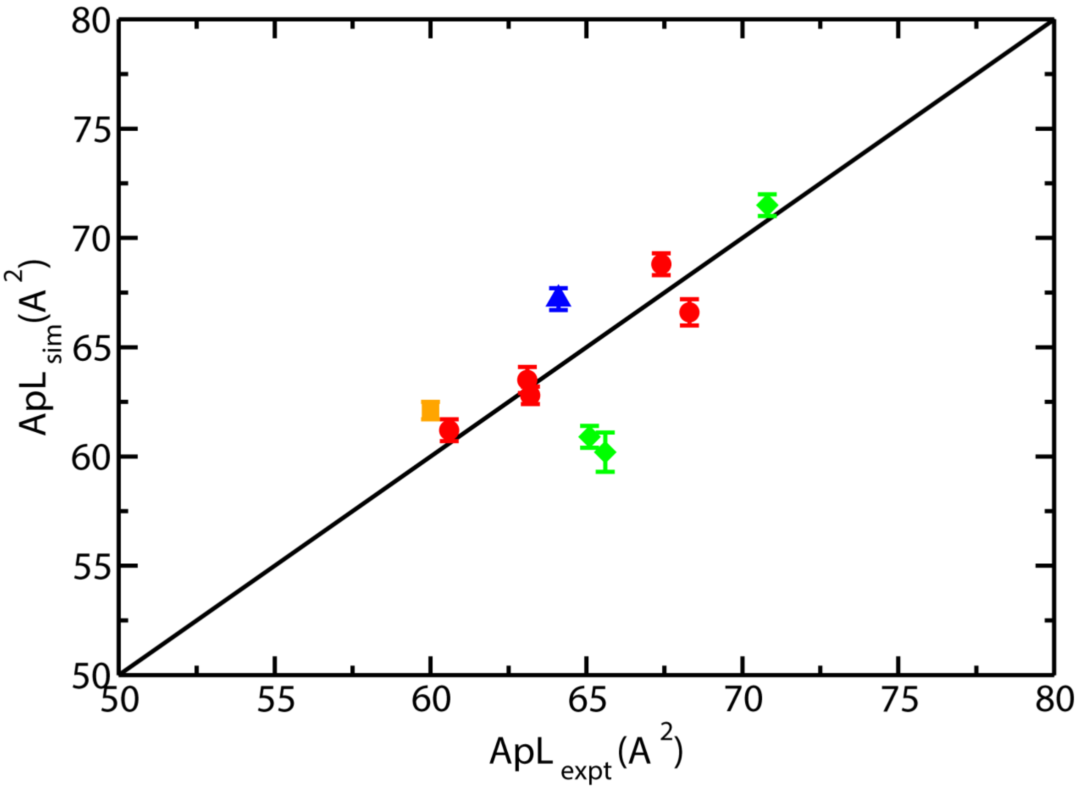

Figure 38: Area per lipid predicted by the TraPPE-UA force field for lipid bilayers composed of phosphatidylcholine (red circles), phosphatidylethanolamine (orange squares), phosphatidylserine (blue triangles) and phosphatidylglycerol (green triangles).

For lipids that contain the phosphatidylcholine head group (DPPC, DMPC, DLPC, DOPC, POPC), the TraPPE-UA force field predicted area per lipid values with an absolute average deviation of 1.02 A^2, which is of similar accuracy as the most accurate all atom force fields, CHARMM C36[240], and SLipids[245]. For POPE, TraPPE predicts an area per lipid of 62.3 A^2, which compares favorably to the experimental value of 59-60 A^2.

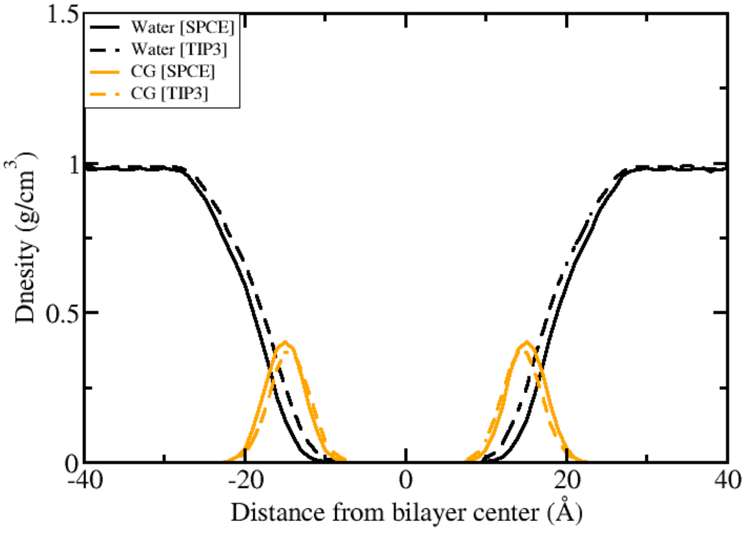

Figure 39: Density profile along the bilayer normal for water (black) and glycerol (orange) components. Solid and dotted lines represent SPCE and TIP3 systems respectively.

To understand the effect of water model on the predicted area per lipid, additional calculations were performed for DPPC using the TIP3P force field. The use of TIP3P produced a slight increase in the predicted area per lipid to 68.3 A^2, compared to 63.6 A^2 for simulations using SPC/E. Density profiles (**Figure 39**) show slightly deeper penetration of TIP3P water into the lipid bilayer compared to SPC/E. Radial distribution functions for water interacting with oxygens in the fatty acid group of the lipid tails (**Figure 40**) show a measureable increase in the first peak for TIP3P water compared to

SPC/E, illustrating how stronger water-lipid interactions lead to an increase in hydration of the phospholipid head group and greater area per lipid.

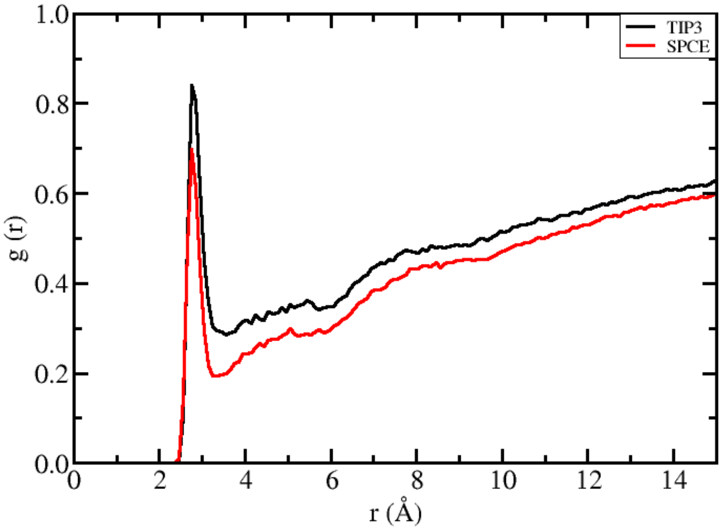

Figure 40: Radial distribution function for interaction of water oxygen atoms with oxygen atoms of glycerol region in DPPC lipid bilayer.

Simulation of systems containing charged lipids, such as those containing phosphatidylserine or phosphatidylglycerol is even more complex, since they require a neutralizing cation, such as Na^+ or K^+. Numerous simulations have shown that cations may bind to phospholipid head groups of zwitterionic lipids, leading to significant reductions in the predicted area per lipid. For example, simulations of POPC or DPPC showed that the addition of Na^+ or K^+ caused a reduction in the area per lipid by 10-15%[252-254]. Therefore, like in the case of water, it is important that the parameterization of the cations be consistent with the phospholipid model. Calculations were performed on phosphatidylserine (PS) and phosphatidylglycerol (PG) containing lipids with either 128 Na^+ or K^+ added as counter ions. In addition, two sets of force field parameters were evaluated for Na^+ (CHARMM [1] and Aqvist [2]). Simulations were initially performed with Na^+ ions. After 100 ns of equilibration, Na^+ was replaced with K^+ and an additional 20 ns of simulation was performed. Simulations performed for PG lipids using Na^+ with the CHARMM parameters produced area per lipid values that were

4-5 A^2 lower than experimental values. Replacing Na^+ with K^+ ion lead to immediate expansion of the bilayer, with area per lipid values in close agreement with experimental data. One of the prime reasons for this shift in area per lipid values is the larger size to charge ratio of potassium ion compared to sodium. This increase in size weakens the interactions between cation and lipid oxygens (in phosphate and glycerol regions) which may cause the lipid bilayer expansion. Radial distribution functions for cations interacting with O2L (phosphate oxygen) and OBL (glycerol oxygen) show that potassium ion has a weaker interaction with oxygen atoms compared to sodium ion (**Figure 41**).

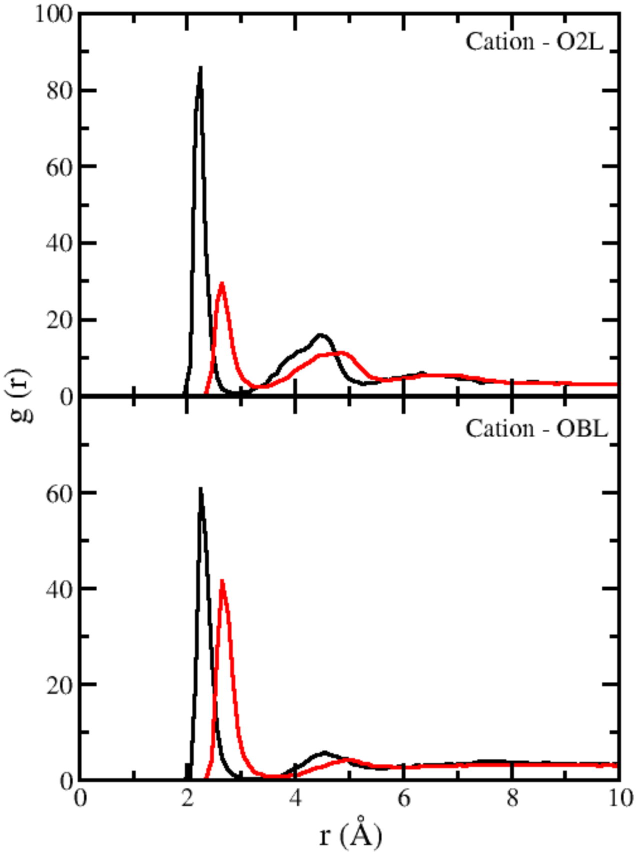

Figure 41: Radial distribution functions for interaction of cations: sodium (black) and potassium (red) with phosphate (O2L) and glycerol (OBL) oxygen atoms of DLPG lipid bilayer.

Additional calculations performed using the Na^+ parameters from Aqvist [2] ($Na^{+\ AQVIST}$) also produced improved values of the area per lipid compared to the CHARMM parameters ($Na^{+\ CHARMM}$). Sodium parameters from Aqvist have a larger sigma and a lower epsilon value which may potentially lead to weakened interactions between the ion and phosphate oxygen atom of lipid. To check this, non-bonded potential energy comprising of Lennard Jones and electrostatic contributions was plotted as a function of separation distance between sodium ion and phosphate oxygen atom (shown in **Figure 42**).

The depth of the Lennard Jones potential well is a measure of how strongly the two particles attract each other. Comparison shows that $Na^{+\ CHARMM}$ has a more favorable interaction with the lipid oxygen atoms compared to $Na^{+\ AQVIST}$. Radial distribution function for interactions between $Na^{+\ CHARMM}$ / $Na^{+\ AQVIST}$ ions and oxygen atoms of DLPG lipid (shown in **Figure 43**) show that $Na^{+\ CHARMM}$ interacts more strongly with lipid atoms compared to $Na^{+\ AQVIST}$ which may well result in a lower area per lipid value when working with CHARMM parameters.

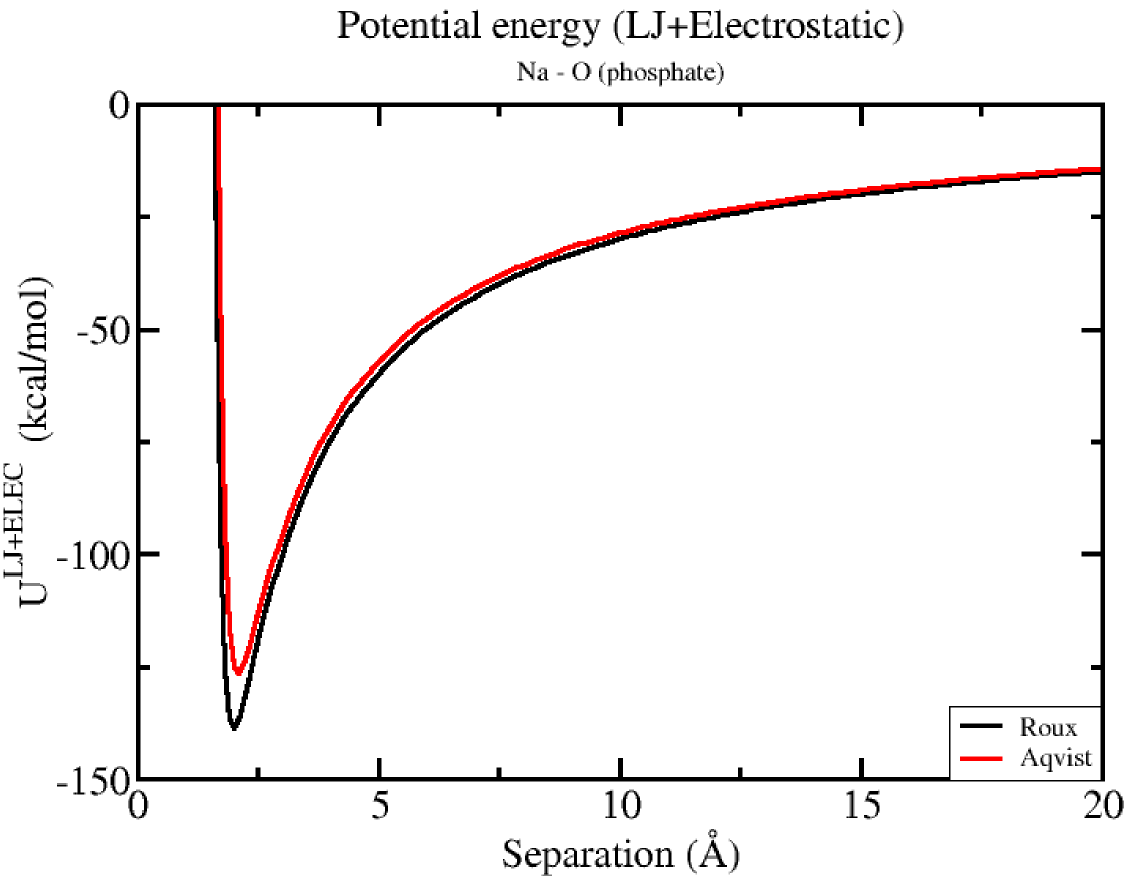

Figure 42: Non bonded potential energy as a function of distance between sodium ion and phosphate oxygen in DLPG lipid bilayer. Profile with $Na^{+\ CHARMM}$ [1] parameters is shown in black and one with $Na^{+\ AQVIST}$ [2]parameters is shown on red.

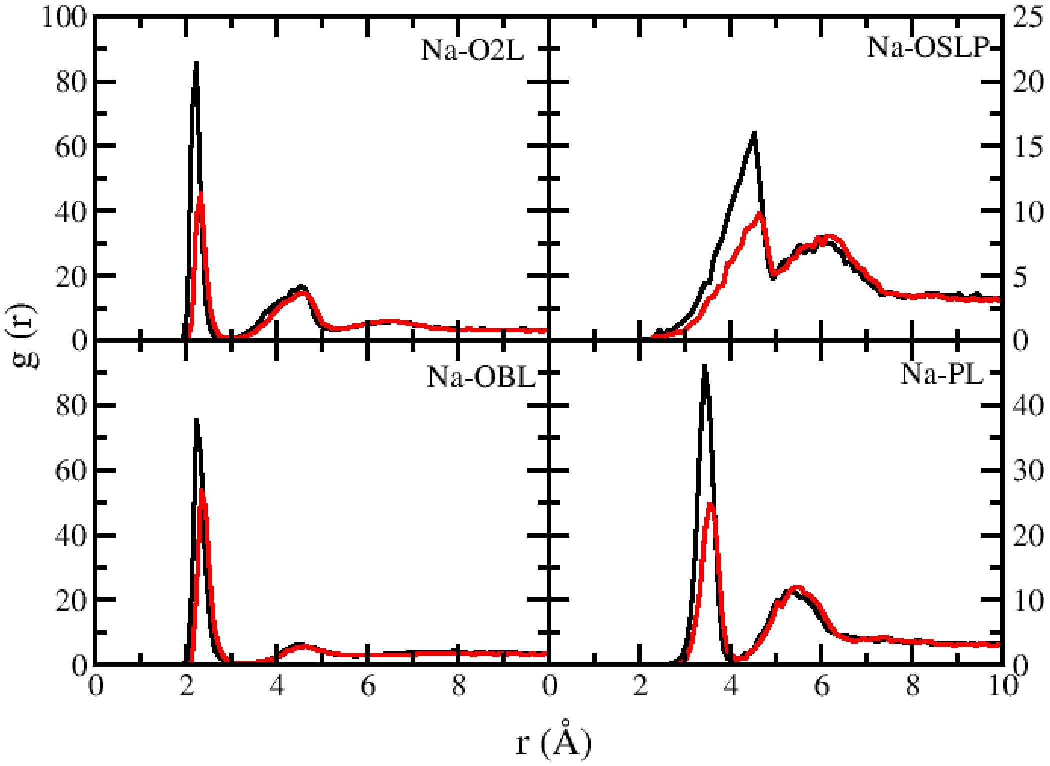

Figure 43: Radial distribution function profile for interaction of sodium ion (black: Na^{+}_{CHARMM} [1]; red: $Na^{+\ AQVIST}$ [2]) with O2L (phosphate oxygen), OSLP (phosphate oxygen), OBL (glycerol oxygen) and PL (phosphorus)

Evolution of area per lipid for simulation of DLPG lipid bilayer with $Na^{+\ CHARMM}$ and $Na^{+\ AQVIST}$ is shown in **Figure 44**. Profile shows that for $Na^{+\ AQVIST}$ area per lipid is increased by 2-3 A^2 compared to $Na^{+\ CHARMM}$ case illustrating how ion parameters may play a significant role in correct prediction of physical properties of anionic phospholipid bilayers.

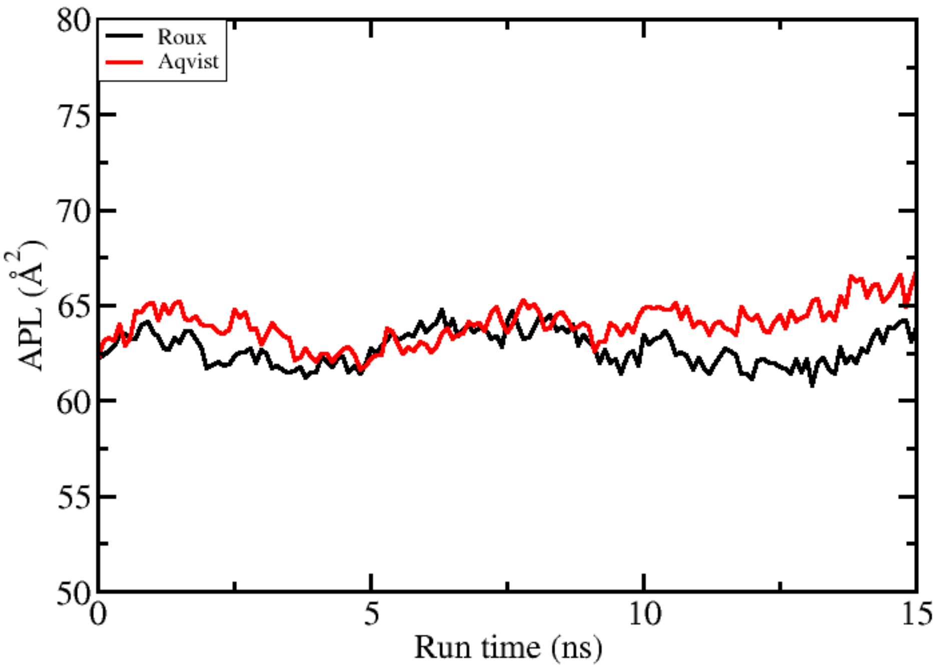

Figure 44: Evolution of area per lipid as a function of simulation run. Results are shown for DLPG lipid bilayer with $Na^{+\ CHARMM}$ [1] (black) and $Na^{+\ AQVIST}$ [2] (red) parameters.

Volume per Lipid

As discussed by Anezo et al. [255], area per lipid is highly sensitive to a force field model and other simulation parameters such as the treatment of long range electrostatics and therefore cannot be considered a good metric of force field quality. Another parameter that is frequently used an an alternate to area per lipid for the analysis of bilayer structure is the volume per lipid (VPL), useful for relating the lateral structure of the bilayer to transverse structure [256].

VPL is less sensitive to methodological changes [255] and also exhibits faster convergence when compared to APL, making it a desirable target parameter when running simulations for short time period. Unlike area per lipid, the volume per lipid is well-defined experimentally [256, 257] because of which a more concrete comparison can be made with the simulation output. In a simulation set up, VPL can calculated with the following relation,

$$V_{Total} = N_{Lipid} \times V_{Lipid} + N_{Water} \times V_{Water}$$

Equation 34

The total volume of the simulation box was calculated by multiplying the length of box in the x, y and z direction averaged over time. Volume occupied by one water molecule was then determined. Since SPCE water model is used in this study, 892 SPCE water molecules were packed in a simulation box with a density of 0.99 g/cc and system was simulated for 12.0 ns at two different temperatures of 323.0 K and 303.0 K at a constant pressure of 1.013 bar. The volume per lipid for DPPC was equal to 1230.4 Å^3 which compares well with the experimental value of 1229 Å^3 [256]. VPL values for all the other lipids are in excellent agreement with the experimental data and are listed in **Table 9**. VPL for DOPS was found to be 1251 Å^3, which is 1% higher than the experimental value [258]. VPL values for PG headgroup based lipid bilayers are within 1% of the experimental data as well. Values of volume per lipid as predicted by TraPPE parameters are plotted with the experimental data and shown in **Figure 45**.

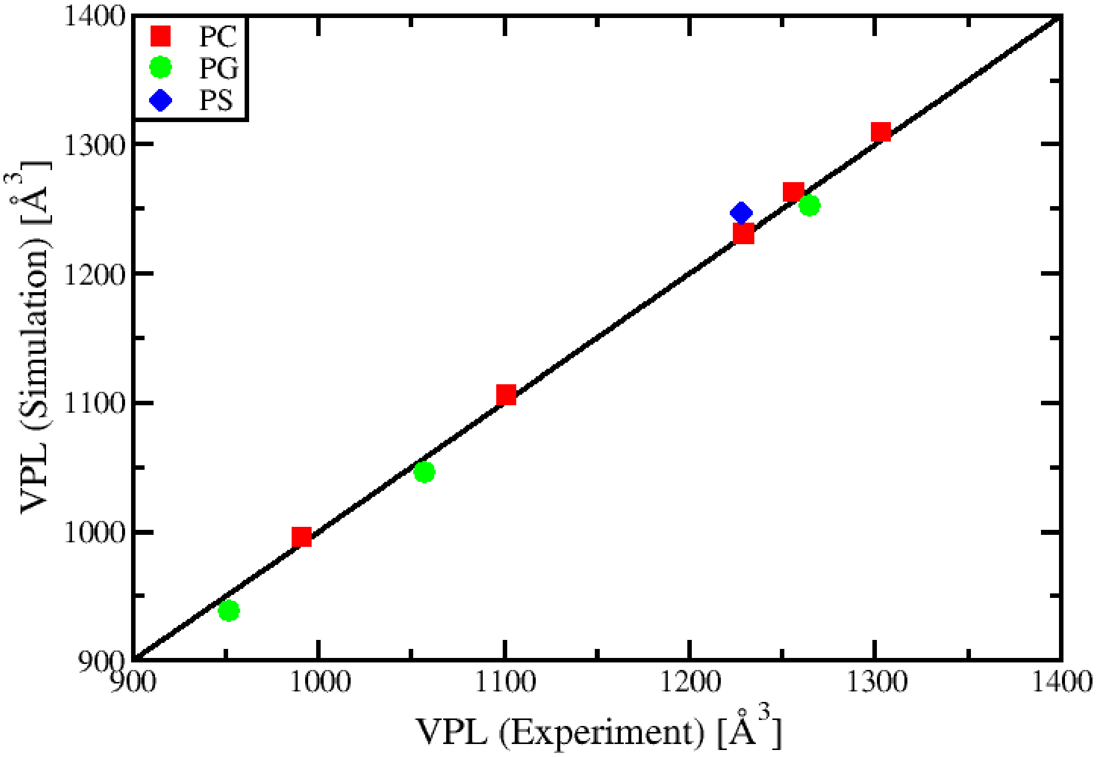

Figure 45: Volume per lipid predicted by TraPPE force field compared to experimental data for PC (red squares), PG (green circles) and PS (blue diamond) lipid bilayers.

Bilayer Thickness

Bilayer thickness is another parameter, used to quantify the membrane structure; membrane simulations are known to converge when the membrane thickness becomes stable and fluctuates around an average value [251]. Nagle et al. [256] have defined several types of bilayer thickness, such as head to head bilayer thickness (D_{HH}) hydrophobic thickness (D_C), partial headgroup thickness (D_{H1}) and others. The above three parameters are related to each other through the following equation,

$$D_{HH} = (2 \times D_C) + (2 \times D_{H1})$$

Equation 35

Full thickness of the bilayer region, also known as Luzzati thickness (D_B) [256] is defined as

$$D_B = 2 \times \left(V_{Lipid}/A_{Lipid}\right)$$

Equation 36

The calculated values of D_{HH} and D_B are listed in **Table 9** for all the lipids with their respective experimental values where available. D_{HH} values predicted by TraPPE for DPPC, DMPC, DLPC and DOPC are in excellent agreement with the experimental data with a 1-3 % deviation. For PG and PS lipid bilayers, an over-prediction of 6-8 % from experimental data is observed which

Table 9: Area per lipid, volume per lipid, and bilayer thickness as predicted by TraPPE-UA force field.

	Area Per Lipid (A_{LIPID}) Å^2	**Volume Per Lipid (V_{LIPID}) Å^3**	**Bilayer Thickness (D_{HH}) Å**	**Luzzati Thickness (D_B) Å**	**Area Compressibilty Modulus (Ka) mN/m**
			DPPC		
Experiment	63.1	1229	38.0	39.0	231 ± 20
TraPPE	63.6 ± 0.6	1231 ± 0.8	37.5 ± 0.2	38.7 ± 0.3	371 ± 40
CHARMM36 [240]	62.9	-	-	-	-
GAFFlipid [237]	61.2	1265.4	37.6	-	274 ± 22
SLipids [245]	62.4	1201	37.7		238 ± 35
GROMOS 54A7 [259]	64.8	-	35.1	38.0	414
Berger [228]	65.5	1226	34.7	37.3	-
43A1-S3 [230]	63.7	1209	35.7	38.0	-
			DMPC		
Experiment	60.6	1101	35.3	36.3	234 ± 23
TraPPE	61.4 ± 0.5	1106 ± 0.6	34.5 ± 0.1	36.0 ± 0.2	383 ± 20
CHARMM36 [240]	60.8	-	-	-	-
GAFFlipid [237]	59.9	1117.8	33.6	-	299 ± 75
SLipids [245]	60.8	1060	34.5	-	250 ± 29
GROMOS 53A6 [260]	61.6	1077	32.7	34.9	475
Berger [228]	62.6	1112	32.3	35.5	-
43A1-S3 [230]	62.1	1086	32.6	35.0	-
			DLPC		
Experiment	63.2	991	30.8	31.4	-
TraPPE	62.8 ± 0.4	996 ± 0.9	30.5 ± 0.3	31.7 ± 0.2	468 ± 86
CHARMM36 [240]	64.4	-	-	-	-
GAFFlipid [237]	59.9	1008.8	31.6	-	291 ± 64
SLipids [245]	62.4	951	30.1	-	268 ± 24
GROMOS 53A6 [260]	63.2	969	28.5	30.7	461
Berger [228]	65.4	1013	27.8	31.0	-
43A1-S3 [230]	63.0	977	28.5	31.0	-

	Area Per Lipid (A_{LIPID}) Å^2	**Volume Per Lipid (V_{LIPID}) Å^3**	**Bilayer Thickness (D_{HH}) Å**	**Luzzati Thickness (D_B) Å**	**Area Compressibilty Modulus (Ka) mN/m**
			DOPC		
Experiment	67.4	1303	36.7	38.7	254
TraPPE	68.8 ± 0.5	1310 ± 0.7	37.1 ± 0.1	38.1 ± 0.3	406 ± 27
CHARMM36 [240]	69.0	-	-	-	-
GAFFlipid [237]	66.8	1327.4	37.6	-	314 ± 39
SLipids [245]	68.0	1262	36.6	-	256 ± 29
GROMOS 53A6 [260]	64.9	1284	36.3	38.9	389
Berger [228]	66.3	1343	37.2	40.4	-
43A1-S3 [230]	66.0	1291	36.6	39.1	-
			POPC		
Experiment	68.3	1256	37	39.1	180-330
TraPPE	66.3 ± 0.6	1264 ± 1.0	37.1 ± 0.3	38.1 ± 0.2	300 ± 16
CHARMM36 [240]	64.7	-	-	-	-
GAFFlipid [237]	63.7	1277	37.6	-	391 ± 81
SLipids [245]	64.6	1213	36.5	38.5	298 ± 30
GROMOS 53A6 [260]	63.8	1232	34.6	38.7	404
			POPE		
Experiment	59 – 60	1180	39.5	-	233
TraPPE	62.3 ± 0.4	1228 ± 0.9	37.0 ± 0.1	39.5 ± 0.3	264 ± 24
CHARMM36 [240]	59.2	-	-	-	-
GAFFlipid [237]	55.6	1185	43.4	-	484 ± 34
SLipids [245]	56.3	1153	41.1	41.6	282 ± 29
			DOPS		
Experiment	64.1	1228	39.0	38.3	-
TraPPE	67.2 ± 0.5	1251 ± 1.1	38.0 ± 0.2	37.8 ± 0.2	378 ± 56
SLipids[261]	64.1	1222	38.1	38.5	261 ± 27

	Area Per Lipid (A_{LIPID}) Å^2	**Volume Per Lipid (V_{LIPID}) Å^3**	**Bilayer Thickness (D_{HH}) Å**	**Luzzati Thickness (D_B) Å**	**Area Compressibilty Modulus (Ka) mN/m**
DLPG					
Experiment [262]	65.6	953.6	29.1	29.1	-
TraPPE(Na^+_{CHARMM})	60.2 ± 0.9	938.4 ± 1.2	30.8 ± 0.2	31.1 ± 0.2	121 ± 20
TraPPE(Na^+_{AQVIST})	64.5 ± 0.4	-	-	-	-
TraPPE(K^+_{CHARMM})	66.3 ± 0.5	-	-	-	-
SLipids[261]	64.2	922	27.0	29.0	165 ± 30
DMPG					
Experiment [262]	65.1	1057.4	32.5	32.5	-
TraPPE(Na^+_{CHARMM})	60.8 ± 0.5	1045.9 ± 1.3	34.5 ± 0.1	34.4 ± 0.2	103 ± 15
TraPPE(Na^+_{AQVIST})	64.6 ± 0.3	-	-	-	-
TraPPE(K^+_{CHARMM})	66.1 ± 0.4	-	-	-	-
SLipids[261]	63.3	1030	31.8	32.4	161 ± 35
CHARMM [263]	58.5	-	-	-	-
DOPG					
Experiment [262]	70.8	1265	35.7	35.7	-
TraPPE(Na^+_{CHARMM})	69.3 ± 0.5	1252.5 ± 1.1	35.9 ± 0.2	34.9 ± 0.1	200 ± 37
TraPPE(Na^+_{AQVIST})	71.5 ± 0.3	-	-	-	-
TraPPE(K^+_{CHARMM})	72.1 ± 0.4	-	-	-	-
SLipids[261]	70.8	1232	34.5	35.0	241 ± 36

may possibly be due to higher ordering of the lipid tails and lower area per lipid values. Evolution of bilayer thickness (D_{HH}) with simulation is shown for all the lipids studied in this work in **Figure 46**. Values of bilayer thickness as predicted by TraPPE parameters are plotted with the experimental data and shown in **Figure 47**.

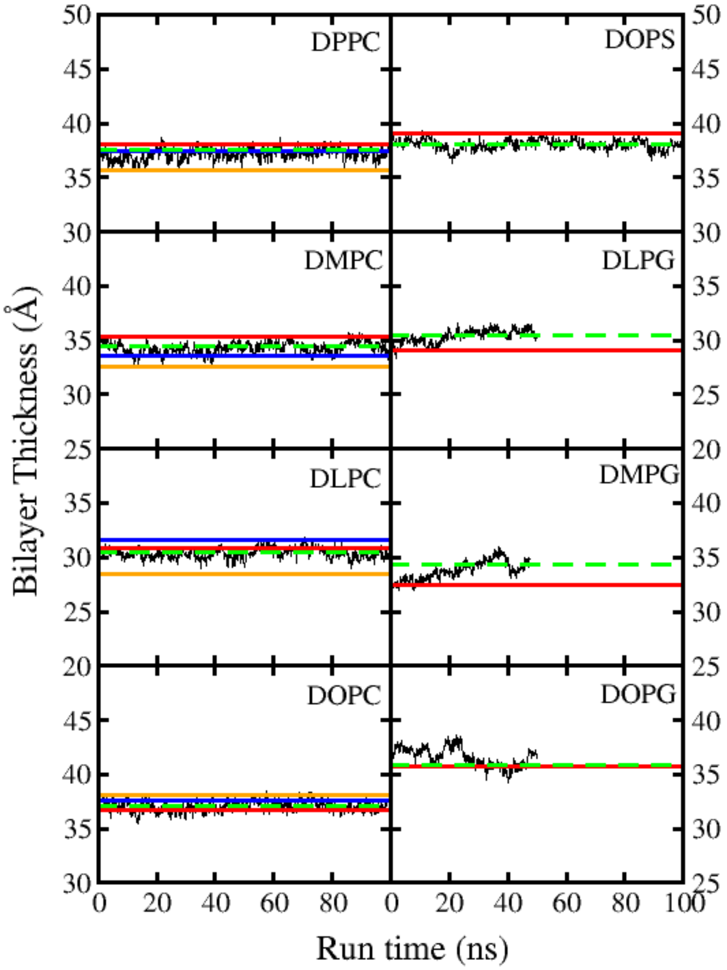

Figure 46: Evolution of bilayer thickness (black) with simulation run time lipids studied in this work. Average value of bilayer thickness (D_{HH}) predicted by TraPPE is shown (green-dotted) and compared with experiment (red), C36 (blue) and GROMACS (orange) data.

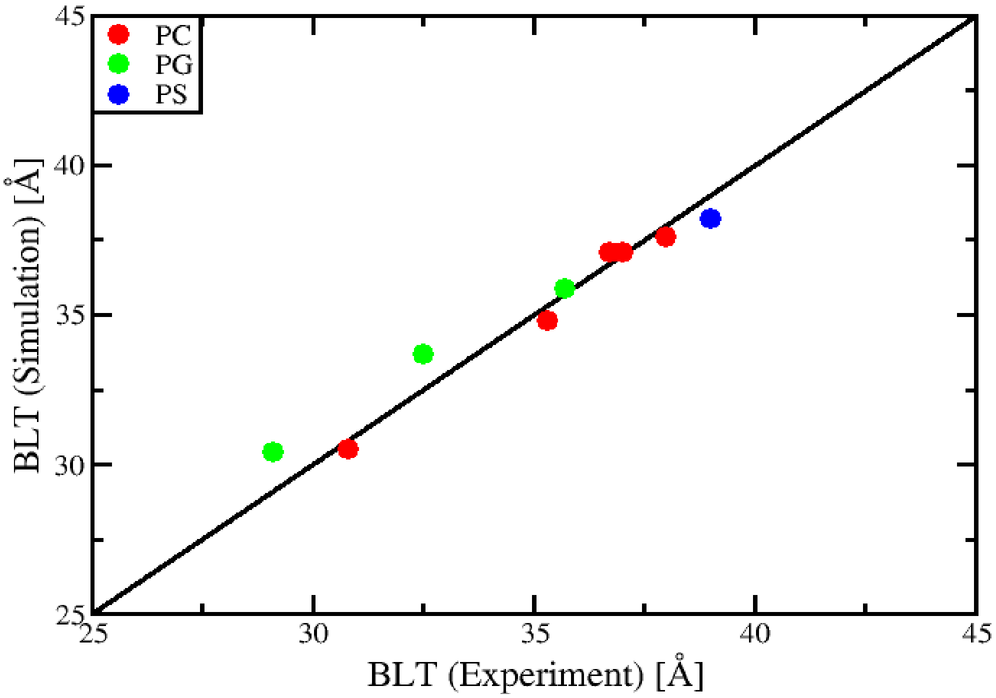

Figure 47: Bilayer thickness predicted by TraPPE force field and compared to experimental data for PC (red), PG (green) and PS (blue) lipid bilayers.

Electron Density

Apart from order parameter, the electron density profile is another quantity that provides qualitative structural information about the lipid bilayer and can be used to distinguish between bilayer fluid and gel phases [264, 265]. Sharp peaks in the headgroup region, contributed by the phosphate moiety, and a narrow deep trough in the central region of bilayer is indicative of bilayer in gel-phase. On the other hand, broad peaks and shallow trough indicative of a fluid phase. The electron density in this work was calculated by following the binning procedure which involves division of simulation box into small 1.0 Å, bins along the bilayer normal followed by calculating the number of electrons in each bin and then dividing it by the total volume of that bin. This procedure is averaged over the total number of frames considered. It is however important to note that for simulations running in the constant temperature-pressure (NPT) ensemble with periodic boundary conditions, it is common for the bilayer center to move and fluctuate in the direction of bilayer normal, a feature which results in artificial broadening of real space profiles [266]. To avoid this occurrence, lipid bilayer was re-centered in each frame before averaging over all frames and calculation of electron density data. In **Figure 48**, total electron density and individual component density for DPPC bilayer is plotted along the bilayer normal and compared to the experimental data. Individual component densities for the all the studied lipid bilayers is shown in **Figure 49**. Components of interest are the glycerol region (CG), phosphate region (PCN) and CH2 + CH3 groups in lipid tails. An good agreement with the

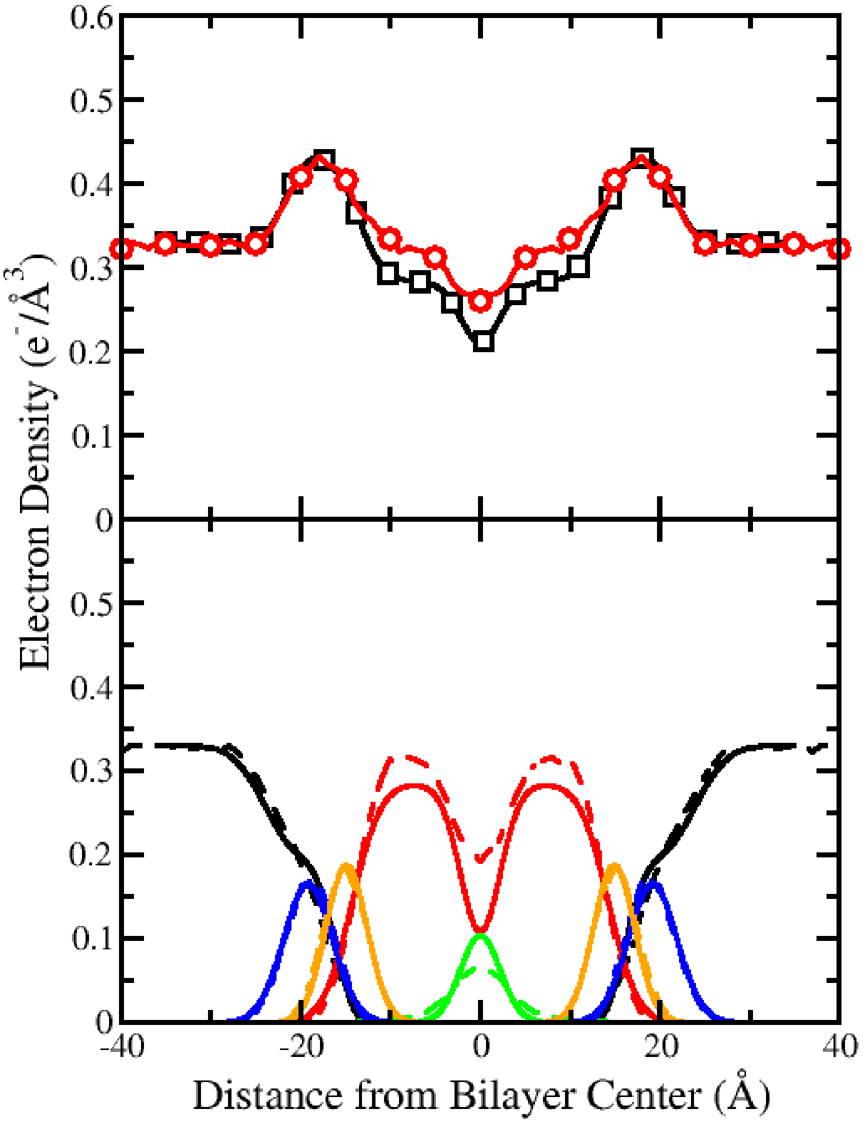

Figure 48: [TOP] Total electron density profile for DPPC bilayer produced by TraPPE force field. Experimental data (black), simulation (red). [BOTTOM]: Individual component density profile for DPPC bilayer produced by TraPPE force field. Simulation (dotted) and experiment (solid) are shown for components: glycerol (orange), phosphate+choline (blue), methylene (red), terminal methyl (green) and water (black).

experimental data is observed for PCN, CG and water groups of DPPC bilayer. CH2 and CH3 profiles in the component density plot for DPPC are broader with a higher electron density compared to experiment near the bilayer center. This observation can be attributed to a more fluidic nature of the lipid tails possibly due to the lack of hydrogen atoms. The peaks in the total electron density profile are due to the phosphate region in both the upper and lower leaflet; the lowest point in the profile (trough region) signifies the center of the bilayer. In addition to qualitative information, electron density provides a useful quantitative parameter, the head-to-head bilayer thickness (D_{HH}) The head-to-head bilayer thickness was already calculated in the previous section using a different method, but can also be evaluated using the electron density profile by measuring the distance between the phosphorus peaks in the upper and lower leaflet. D_{HH} value for DPPC measured by this method is equal to 38.2 Å, and agrees well with the experimental as well as previously calculated values listed in **Table 9** .

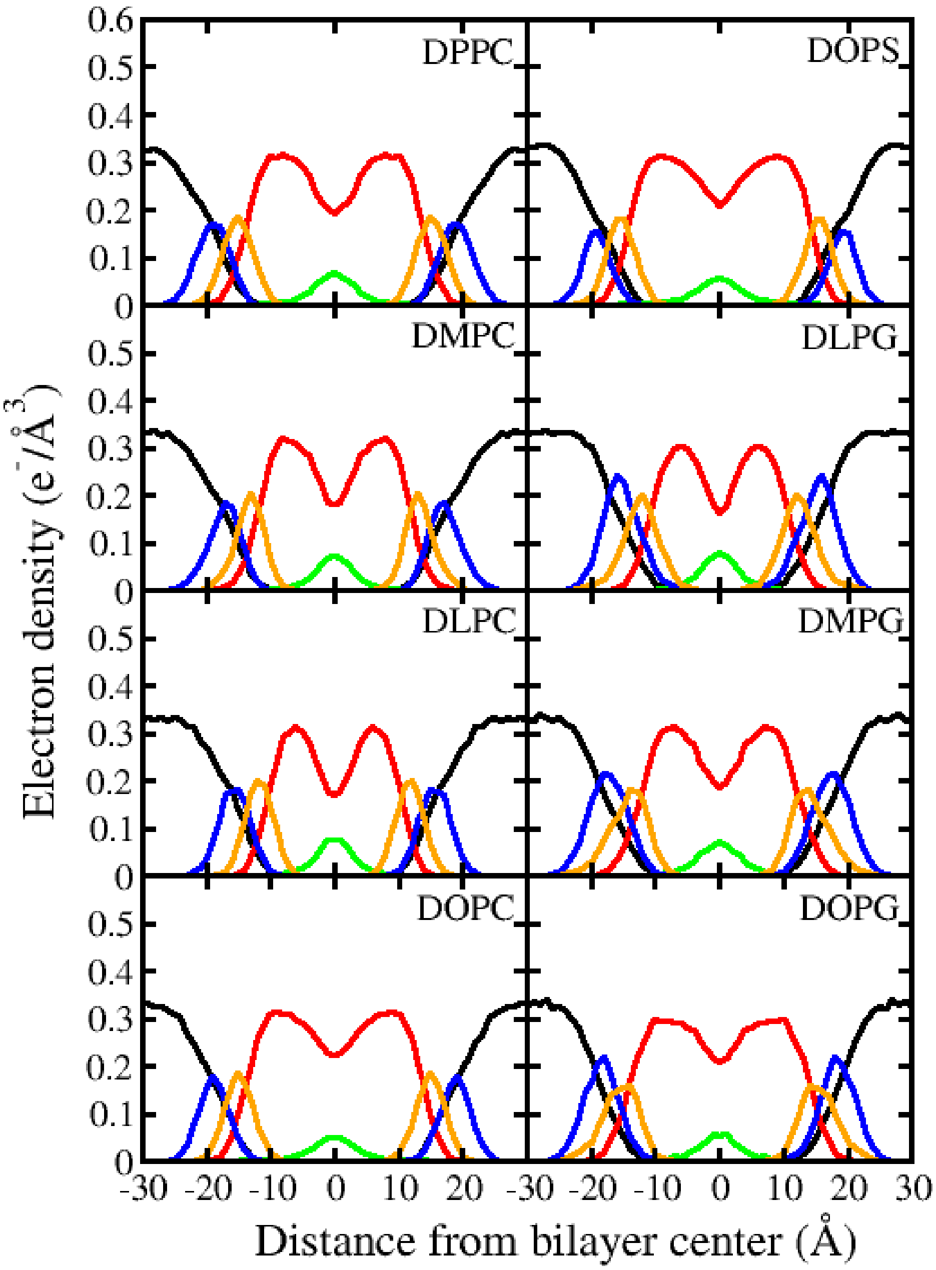

Figure 49: Individual component density profile for bilayers produced by TraPPE force field is shown for components: glycerol (orange), phosphate+choline (blue), methylene (red), terminal methyl (green) and water (black).

Order Parameter

The deuterium order parameter provides a means to quantify ordering of the acyl tails, measuring the orientation of the deuterium-carbon (C-D) bonds with respect to the bilayer normal. Order parameters are of particular interest for validation of molecular mechanics force fields because they can be measured directly from deuterium NMR experiments [267, 268], and unlike quantities such as area per lipid[269], the experimental data do not require models for interpretation[267].

In molecular dynamics simulations, the order parameter is calculated via

$$S_{CD} = \langle \frac{3\cos^2\theta - 1}{2} \rangle$$

Equation 37

where θ is the angle formed by the C-D vector and the bilayer normal, and the angular brackets denote an ensemble average [270]. United-atom force fields, such as the ones developed in this work, lack hydrogen atoms to form the required C_i-H_i vectors. Therefore hydrogen atoms were added to the lipid tails post-simulation assuming ideal tetrahedral geometry. For saturated lipids, such as DPPC, equivalent results for the order parameter may be determined by using the vector joining C_{i-1} – C_{i+1} carbons [270, 271]; the determination of order parameters for unsaturated lipid tails, however, requires the generation of pseudo-hydrogen atoms.

Calculated values of order parameter are plotted as a function of the carbon number with their respective experimental values [267, 272] in **Figure 50** for DPPC, DMPC and DLPC and POPC. For DPPC and POPC, data from the CHARMM C36 force field are provided for comparison [240]. Overall, close agreement was observed between the predictions of the TraPPE force field and experimental data, with the TraPPE force field correctly reproducing all major features of the order parameter, such as the location of the kink in the sn-2 chain of POPC and C2 splitting in the sn-2 chain. Compared to experimental data and the C36 force field, TraPPE predicts a slightly less ordering, which may be due to limitations in the united-atom representation.

Order parameter splitting at C2 position of sn-2 chain is a known feature for both saturated and unsaturated lipids. While not observed in older lipid force fields, such as the CHARMM c27 parameter set[240], nearly all modern all-atom force fields now show evidence of this phenomena [240, 245, 273]. Reproduction of experimentally observed C2 splitting is the result of optimization of the torsional potentials governing dihedral rotations in the glycerol region. Similar splitting was observed for all PC containing lipids. For DLPC, DMPC and DPPC, the lower splitting value was in excellent agreement with the experimental data, while the higher value is under-predicted by the TraPPE force field. For POPC, both values of split order parameter are an exact match to experimental data. To the best of our knowledge, this is the first united atom force field that is able to reproduce C2 splitting of the order parameter in the sn-2 chain. Experimentally, the S_{CD} value for sn-1 at C2 must be higher than that for the sn-2 chain [268]. These results are also reproduced by the TraPPE-UA force field. Order parameters for both sn-1 and sn-2 chains were calculated for DLPG, DMPG, DOPC, DOPS and were included in supplementary information since no experimental data were available for comparison.

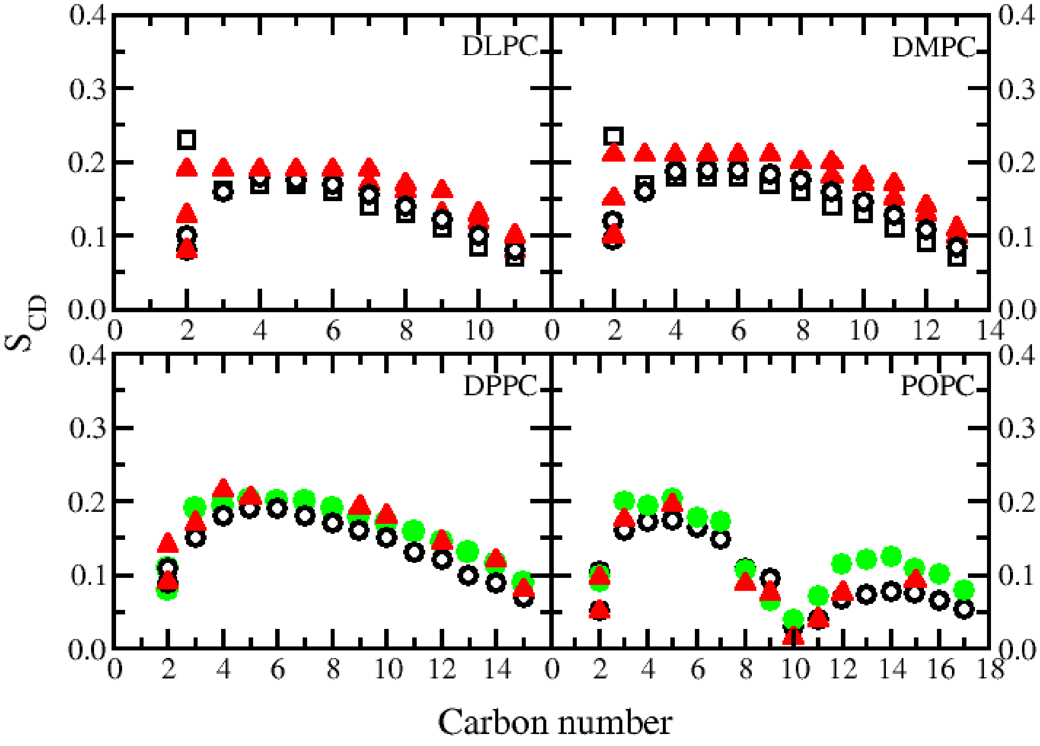

Figure 50: Deuterium order parameters as predicted by TraPPE parameters are shown for sn-1 (open square) and sn-2 (open circle) for DPPC, DMPC, DLPC and POPC bilayers and compared with C36 (green circle) and experimental data (red triangle).

X-Ray Form Factors

Electron density profiles can be easily extracted from molecular dynamics simulations but comparing them with the experimental data may not be such a good idea as experimental electron density profiles are generated based on certain assumptions and models which may likely result in an inaccurate comparison to simulation data [245, 274]. Order parameters also are a good measure order within the bilayer but do not shed light on the overall bilayer structure. One of the most rigorous methods for validation of simulation results is to compare with experimentally determined x-ray structure or form Factors [275]. They provide a direct comparison to the experimental data and is a much more robust way of comparison than with electron density. Mathematically, X-Ray form factor is the Fourier transform of the electron density profile in Z-direction.

In this work, structure factor for all the lipids was determined with SIMtoEXP package [266] by initially generating the number density data along the bilayer normal followed by calculation of structure factors. Experimentally determined form factors are obtained on a relative scale while simulation based form factors are generated on an absolute scale. This fact makes it important to scale the experimental data using a scaling factor in order to make it comparable with the simulation output. Experimental structure factor values were scaled by a factor between 0.8-1.0 in order to fit the simulated F(q), a procedure adapted in other lipid force field studies as well [244]. Form factors predicted by simulation for DMPC, DPPC, POPC and DLPC are shown in **Figure 51** and are found to be in excellent agreement with available experimental data [258, 276]. The location where form factor is zero matches well with the experimental data and peak magnitudes is also in good agreement indicating the correct reproduction of bilayer structure by simulation with this force field.

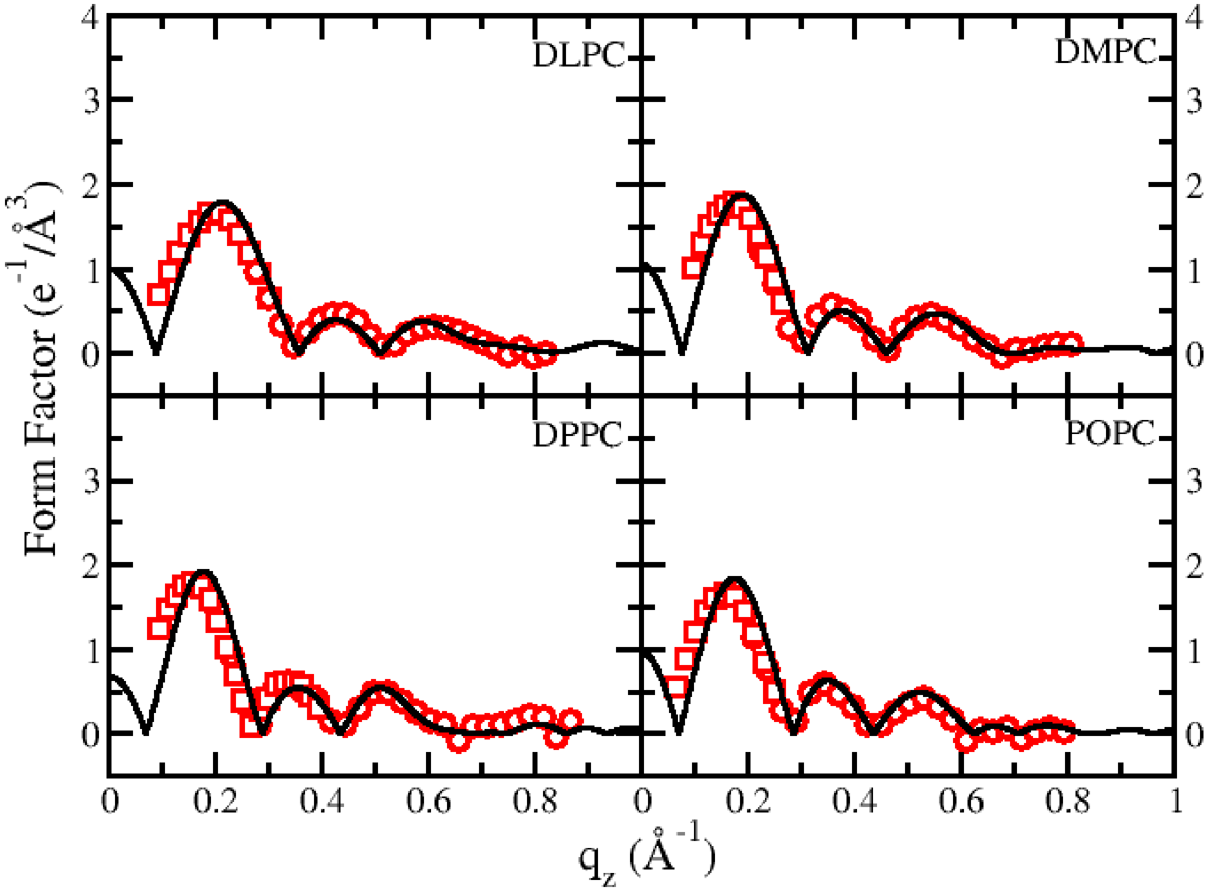

Figure 51: Form factors predicted by NPT molecular dynamics simulations (black solid line) for DPPC, DMPC and DLPC and compared with experimental data for unilamella vesicles (red square) and oriented samples (red circles).

Form factor plots for anionic PG lipids are shown in **Figure 52**. Location of peak heights and minima predicted by TraPPE force field is in good agreement with experimental data illustrating the correct structure of bilayer in a direction parallel to bilayer normal.

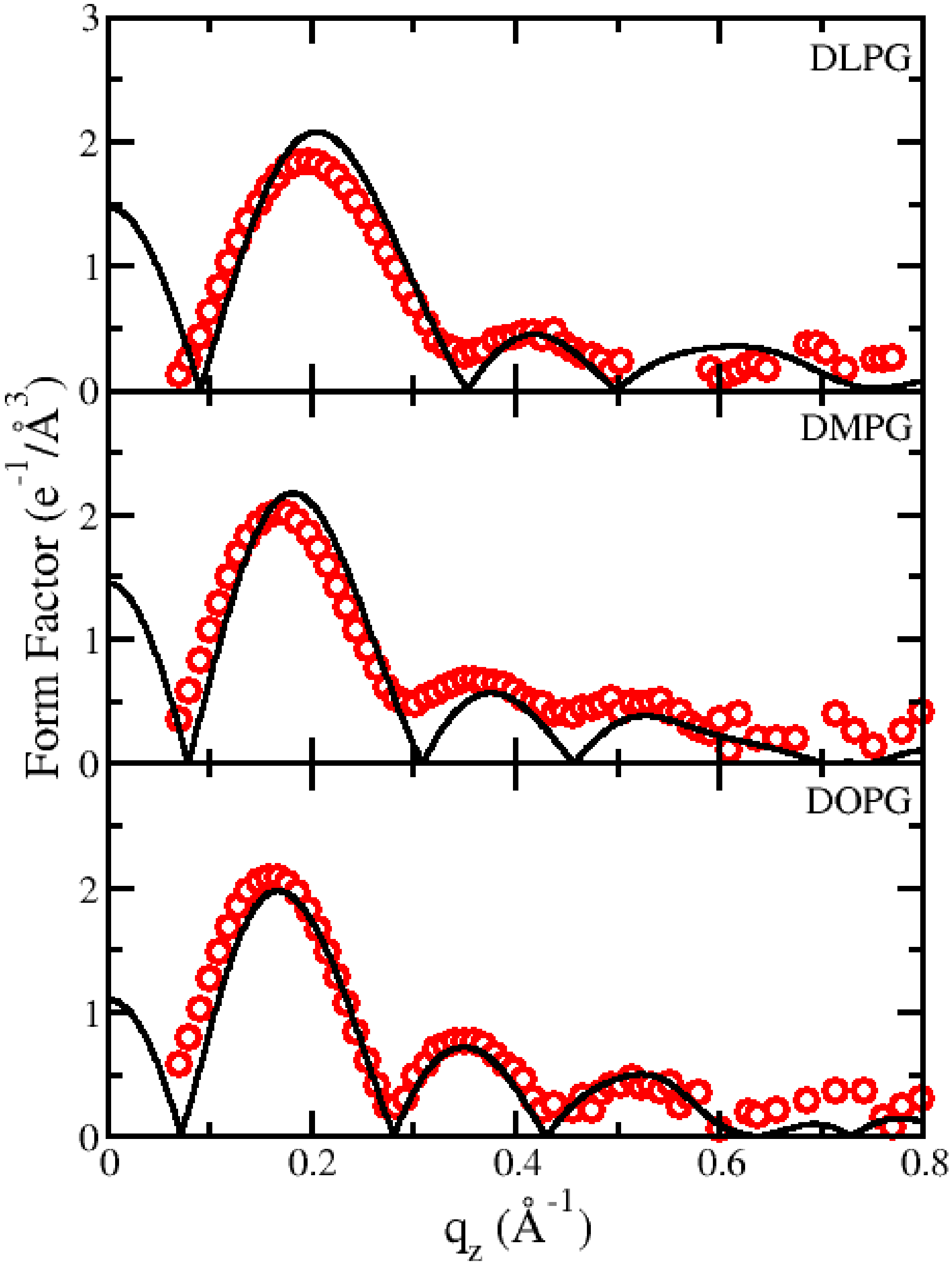

Figure 52: Form factors predicted by NPT molecular dynamics simulations (black solid line) for DLPG, DMPG and DOPG; compared with experimental (red circles) data.

CHAPTER 8: Effect Of Ca2+ On The Interactions Between Synaptotagmin-1 Protein With Membrane Bilayers

Background

Membrane fusion of apposed bilayers is one of the most fundamental and frequently occurring biological phenomena in living organisms. It is an essential step in several cellular processes such as neuronal exocytosis, sperm fusion with oocytes and intracellular fusion of organelles to name a few. Of these, neuronal exocytosis holds critical significance pertaining to its role in interneuronal communication. The process occurs at sub-millisecond time scale and involves the release of neurotransmitter from the synaptic vesicle into the pre-synaptic plasma membrane once the vesicle and target membrane merge and fuse with each other [277-279]. Ca^{2+} is known to regulate this event in a precise manner although the exact mechanism at the molecular level is still unknown. In addition to Ca^{2+}, several proteins like SNAREs and Synaptotagmin-1(SYT-1) are thought to play a key role in the neurotransmitter release machinery. SNARE proteins are known to bring the vesicle and target membrane in a close proximity by forming a tight zipper like complex between the vesicle bound v-SNARE protein, synaptobrevin (VAMP) and target membrane bound t-SNARE proteins, syntaxin and SNAP-25 which is proposed to result in membrane fusion [9-12]. SYT-1 is a synaptic vesicle localized protein and acts as a Ca^{2+} sensor for this process [280-283].

Synaptotagmin-1 protein is composed of N-terminal single membrane spanning domain, a small intraluminal domain and two tandem C-terminal domains, C2A and C2B [284, 285] which are connected by a linker. C2A and C2B adopt similar eight-stranded beta-sandwich structures connected by three flexible loops [286-288]. Both C2A and C2B domains possess Ca^{2+} binding pockets comprising of conserved aspartic acid residues and capable of binding three and two Ca^{2+} ions, respectively [286-290]. Post Ca^{2+} binding, SYT-1 is known to regulate membrane fusion, however, the mechanism is not clear, as yet.

Several theories have been proposed over the years on the pathway that SYT-1 follows upon binding of Ca^{2+} leading to fusion. The tandem C2 domains can interact and bind to the SNARE complex and also to individual proteins syntaxin-1 and SNAP-25 once Ca^{2+} ions are bound in their respective pockets [291-294]. These SYT-1-SNARE interactions have been identified as a requirement for Ca^{2+} to regulate the fusion process [295]. In addition to SNAREs, SYT-1 binds bilayer membranes composed of anionic phospholipids by partially inserting the hydrophobic residues located at the tip of C2 [296, 297]. Insertion has been attributed to changes in electrostatic potential on the surface of SYT-1 upon binding of Ca^{2+} which changes the negative potential on calcium binding loops into a positive potential [298]. This electrostatic switch promotes the interaction of SYT-1 with acidic phospholipid headgroups [299].

A proposed model, by Martens et al. [300] on SYT-1's role in membrane fusion is based on the penetration of SYT-1 into the plasma membrane resulting in induction of localized positive curvature on the initially flat membrane surface. This curvature reduces the distance between the plasma membrane and the synaptic vesicle and also lowers the energy barrier required for fusion process [300]. Another theory states that either individual or tandem C2 domains attach to both plasma membrane as well as the vesicle and drive them close to each other thereby facilitating in the fusion [301, 302]. Tremendous experimental work has been done over the past decade to understand the exact role of SYT-1 in membrane fusion with a focus on the way it interacts with the lipid bilayer. However, one of the major constraints *in vitro* processes is the inability to track the process in real time at the atomic level.

In this work, molecular dynamics simulations were performed to study the interactions between the SYT-1 and lipid bilayers. Simulations were used to determine the role of Ca^{2+} and acidic lipids on the insertion of SYT-1 into the bilayer. Experimentally, interaction of two C2 domains of SYT-1, C2A and C2B, with the lipid bilayers have been studied, both in tandem as well as individually [288, 291]. To reduce system size and complexity, the two domains were studied individually in this work. To understand the significance of electrostatics in SYT-1 - bilayer interactions, analysis of interaction energies was performed. Results show that both C2A and C2B domains when bound to Ca^{2+}, insert into lipid bilayers composed of anionic phospholipids. However, no insertion was observed for cases where either the domain is Ca^{2+} - free or the bilayer is carrying a neutral charge. Electrostatic energy plotted as a function of separation indicates presence of repulsive forces between the bilayer and approaching SYT-1 domain surface in the absence of Ca^{2+}. Electrostatic potential(ESP) maps of Ca^{2+}-bound and Ca^{2+}-free C2A and C2B domains were generated using Adaptive Poisson Boltzmann Solver(APBS) [303]. Results indicate that Ca^{2+} binding to SYT-1 causes a significant alteration in ESP near the Ca^{2+} binding pocket. Potential of mean force was calculated to understand the effect of Ca^{2+} on the interactions between SYT-1 and lipid bilayers.

Simulation Details

Lipid bilayer structures, both homogeneous and heterogeneous, were generated using CHARMM-GUI [304]. Homogeneous bilayers contain pure POPC lipid. The heterogeneous bilayer were composed of POPS and POPC lipid in a 35:65 ratio. All the bilayers were approximately 68 X 68 X 60 Ǻ in size and contained a total of 120 lipids with 60 lipids each in the upper and lower leaflet.. The initial structures have Ca^{2+} ions bound in their designated pockets. To work with C2A and C2B domain lacking bound calcium, Ca^{2+} ions were removed from the original PDB file. Hydrogen atoms were added to the initial protein structure using PSFGEN in VMD (Visual molecular dynamics) [151]. Systems S1 to S8 (**Table 10**) were prepared to check the insertion capability of the C2A and C2B domain in the bilayer and were built by aligning the bilayer perpendicular to the z-axis followed by placing the protein tip at a distance of approximately 2.0 Ǻ from the bilayer surface. The protein was aligned in such a way that the tip residues known to penetrate the bilayer (173, 234 in C2A and 304, 367 in C2B) were facing the bilayer surface. For interaction force and energy calculations, the protein was placed in a similar alignment as systems S1 to S8 but at an initial distance of 40.0 Ǻ from the bilayer.

Protein and bilayer systems were packed together and aligned using the PACKMOL [79] package. System was solvated with water using VMD. A 20.0 Å layer of water was added in the z-direction to prevent the interaction of top surface of protein with the bilayer through periodic boundaries.. System was then neutralized for charge by adding Na^+ and Cl^- ions using VMD.

Table 10: Systems studied in this work.

			Bilayer composition		
System	SYT-1 Domain	Bound Ca^{2+}	%PC	%PS	# of water molecules
S1	C2B	2	65	35	6735
S2	C2A	3	65	35	7650
S3	C2B	0	65	35	7833
S4	C2A	0	65	35	7928
S5	C2B	2	100	0	7463
S6	C2A	3	100	0	7850
S7	C2B	0	100	0	6468
S8	C2A	0	100	0	6908

Simulations were performed with NAMD 2.6 [32] using CHARMM27 force field [305]. CHARMM32 was also used specifically for building and simulation of POPS lipid. The TIP3P model [77] was used for water modeling. Isobaric-Isothermal (NPT) ensemble was used for all simulations. System was minimized for energy followed by heating the system to 300 K. Constant pressure was maintained by using the Langevin piston Nose-Hoover method [80, 306]. Temperature was controlled using Langevin dynamics with a damping coefficient of 1.0 ps^{-1}. Electrostatic forces were calculated using particle mesh Ewald (PME) method [82]. Lennard jones interactions were truncated at 12.0 Å. Steered molecular dynamics simulations were performed using the SMD plugin in NAMD. Data analysis and visualization was done with VMD [151]. Potential of mean force calculations were done using adaptive biasing force technique [25, 26, 146, 307], a method based on unconstrained molecular dynamics. Distance between centers of mass of the inserting residues (M173/F234) and the phosphorus atoms in upper bilayer leaflet was chosen as the reaction coordinate (RC). RC spanned a distance of 21.0 Å and was divided into seven equal windows of 3.0 Å each to improve the sampling of phase space. Simulations in each window were carried out for 4.0 ns. Average force were collected in 0.1 Å wide bins and the adaptive force was applied after 0.02 ns of runtime.

Results and Discussion

Effect of Calcium ions

Experimental studies on the SYT-1 protein have emphasized on its role of being a Ca^{2+} sensor [288, 290, 308] and that upon binding calcium, the two domains (C2A and C2B) insert or penetrate into the surface of lipid bilayer composed of anionic phospholipids. The first step in understanding this phenomena and the importance of Calcium in this process is to verify if Ca^{2+} bound protein (SYT-1) inserts itself in the lipid bilayer. To reduce computational expense and to avoid the complexity of inter-domain interactions, the two C2 domains of SYT-1, C2A and C2B were studied individually.

Table 11: Summary of results for C2A domain interacting with lipid bilayers.

			Distance from bilayer surface			
	Bilayer Composition		Residue M173		Residue F234	
Bound Ca^{2+}	% PC	% PS	Initial	Final	Initial	Final
0	100	0	+ 3.714	+ 5.636	+ 2.283	+ 3.369
2	100	0	+ 4.262	+2.352	+ 2.793	+ 1.129
0	65	35	+3.292	+ 4.576	+ 3.245	+ 4.465
2	65	35	+ 4.164	+ 2.690	- 2.042	-1.912

The first simulation system (S1) contained of all the factors thought to be necessary for protein insertion into the lipid bilayer i.e individual C2B domain with bound Ca^{2+} ions at their respective pockets and the anionic bilayer with 35% PS (phosphatidylserine) and 65% PC (phosphatidylcholine) headgroup lipids. C2B was placed close to the bilayer in a way so that the basic residues, 304 and 367, which are known to be the ones to penetrate the bilayer, are at a distance of ~ 3.0 Angstrom from the bilayer surface (**Figure 53**). After 10.0 ns, the two residues (304 and 367) were observed to penetrate into the bilayer surface to a depth of 3.0 Ǻ (**Figure 54**). Comparison of initial and final system shows that in 10.0 ns the C2B domain had moved ~ 4.0 Ǻ towards the bilayer. Similar calculation was performed with the C2A domain bound to three Ca^{2+} ions. Simulations show that after 10.0 ns, the two tip residues had inserted into the bilayer (**Figure 55**, **Figure 56**). Data for systems S1 and S2 show that both C2A and C2B domains are capable of inserting into the lipid bilayer when bound to Ca^{2+} and the bilayer carries a significant anionic charge.

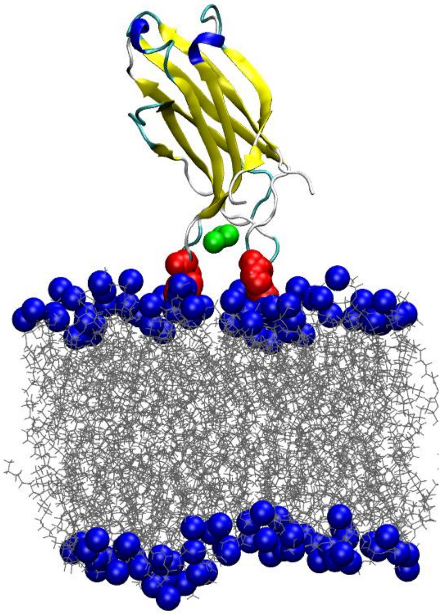

Figure 53: Initial configuration showing Ca^{2+}-bound C2A domain of SYT-1 close to anionic lipid bilayer (at t= 0 ns). Nitrogen atoms in lipid headgroup are shown as Blue spheres. Residues known to penetrate the bilayer (shown in Red) are placed at a distance of 2.0 from the bilayer surface. Ca^{2+} ions are shown as green spheres.

Having shown that SYT-1 was able to insert into the bilayer, the next step was to understand the role of Ca^{2+} in this process. For this study, systems S3 and S4 were constructed which resembled systems S1 and S2 except that the bound Ca^{2+} ions were removed from their designated pockets in the C2A and C2B domains.

Table 12: Summary of results for C2B domain interacting with lipid bilayers.

			Distance from bilayer surface			
	Bilayer Composition		Residue V304		Residue I367	
Bound Ca^{2+}	% PC	% PS	Initial	Final	Initial	Final
0	100	0	+ 5.107	+ 4.472	+ 1.593	+ 2.443
3	100	0	+ 3.827	+2.942	+ 3.457	+ 2.624
0	65	35	+2.091	+ 3.971	+ 3.172	+ 3.486
3	65	35	+ 3.123	+ 2.588	+ 3.123	-3.071

After 4.0 ns of production run it was observed that none of the identified residues (173 / 234 in C2A and 304 / 367 in C2B) penetrated the bilayer surface. The initial and final distance between the residues and bilayer surface are tabulated in **Table 11**and **Table 12**.

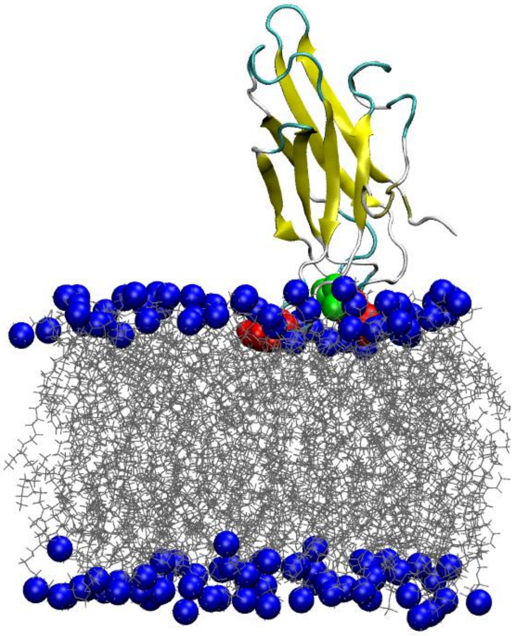

Figure 54: System configuration after 10.0 ns showing Ca2+-bound C2A domain of SYT-1 close to anionic lipid bilayer . Nitrogen atoms in lipid headgroup are shown as Blue spheres. Residues known to penetrate the bilayer (shown in Red) have practically inserted into the bilayer. Ca^{2+} ions are shown as green spheres.

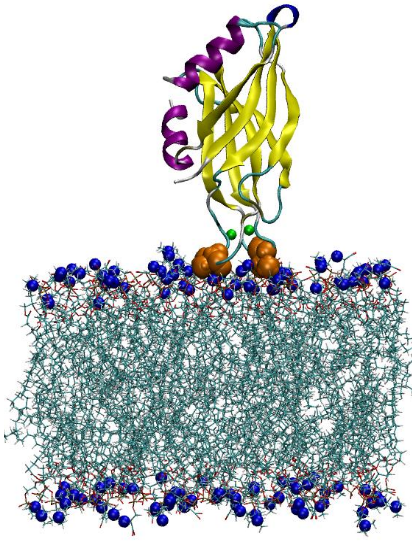

Figure 55: Initial configuration showing Ca^{2+}-bound C2B domain of SYT-1 close to anionic lipid bilayer (at t= 0 ns). Nitrogen atoms in lipid headgroup are shown as Blue spheres. Residues known to penetrate the bilayer (shown in Orange) are placed at a distance of 2.0 Ǻ from the bilayer surface. Ca^{2+} ions are shown as green spheres.

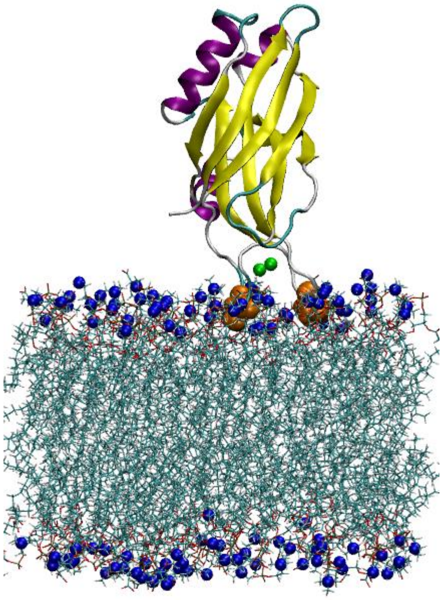

Figure 56: System configuration after 10.0 ns showing Ca2+-bound C2B domain of SYT-1 close to anionic lipid bilayer. Nitrogen atoms in lipid headgroup are shown as Blue spheres. Residues known to penetrate the bilayer (shown in Orange) have practically inserted into the bilayer. Ca^{2+} ions are shown as green spheres.

Effect of bilayer composition

To understand the significance of anionic phospholipids in the SYT-Bilayer insertion process, four new systems (S5-S8) were generated (**Table 10**) similar to S1-S4 in every aspect except that the bilayer was composed of pure POPC lipids. For both Ca^{2+} bound and Ca^{2+} free cases, C2A and C2B were unable to insert in the neutral lipid bilayer lacking anionic phospholipids. The result did not change for the case when Ca^{2+} was bound to the protein. These set of results underline the idea that both C2A and C2B domains of SYT-1 are capable of insertion into the lipid bilayer but require bound Ca^{2+} at their respective sites as well as the presence of anionic phospholipids in the bilayer. Failing to meet any of these criterions disables the insertion of protein SYT-1 into the bilayer. The need for Ca^{2+} ions in protein and anionic lipids in bilayer for insertion step suggests that electrostatic interactions are the dominating factor in this process.

Protein docking

Stability of SYT-1 – bilayer complex was studied by docking the Ca^{2+} bound C2B domain into the lipid bilayer and simulating the system for 15.0 ns. C2B was docked in a manner such that the distance between center of mass of inserting residues (V304, I367) and phosphorus atoms in the upper leaflet is ~ -6.0 Ǻ (negative sign means that residues are located below the bilayer surface plane). After 15.0 ns of simulation, the distance between Ca^{2+} ions and bilayer surface was measured and plotted as a function of run time as shown in**Error! Reference source not found.** In addition, distance between the center of mass of protein and bilayer surface was measured and plotted. Resulting profiles show that the distance does not change significantly with run time suggesting that Ca^{2+} ions and the whole C2B domain remain stable and in complex with respect to the bilayer.

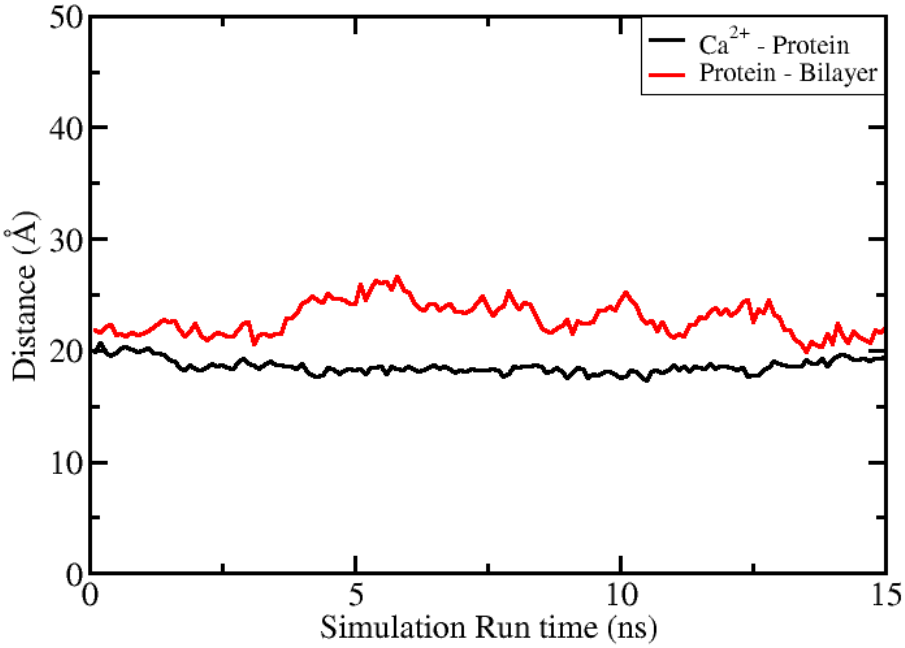

Figure 57: Docked SYT-1 in bilayer. Variation in distance between Ca2+ ions and SYT-1 (black) ; bilayer and (red) w.r.t. run time.

Steered Molecular Dynamics (SMD) was used to quantify the interactions between SYT-1 nad lipids and the effect of Ca^{2+} on these interactions. Using SMD, the inserted protein was pulled away from the lipid bilayer with a constant velocity and the force required for this pull was plotted as a function of timestep. Similar calculation was performed for the initial configuration case where SYT-1 is next to the bilayer but has not yet inserted into the bilayer. The force curves for these two simulations were plotted together for comparison. As can be seen from **Figure 58**, force required to pull the inserted protein out of the bilayer, denoted by the peak in each curve, is significantly higher than that required to pull the bilayer-free protein. This makes sense as favorable interactions between the protein and lipid headgroup increase once SYT-1 inserts itself into the bilayer.

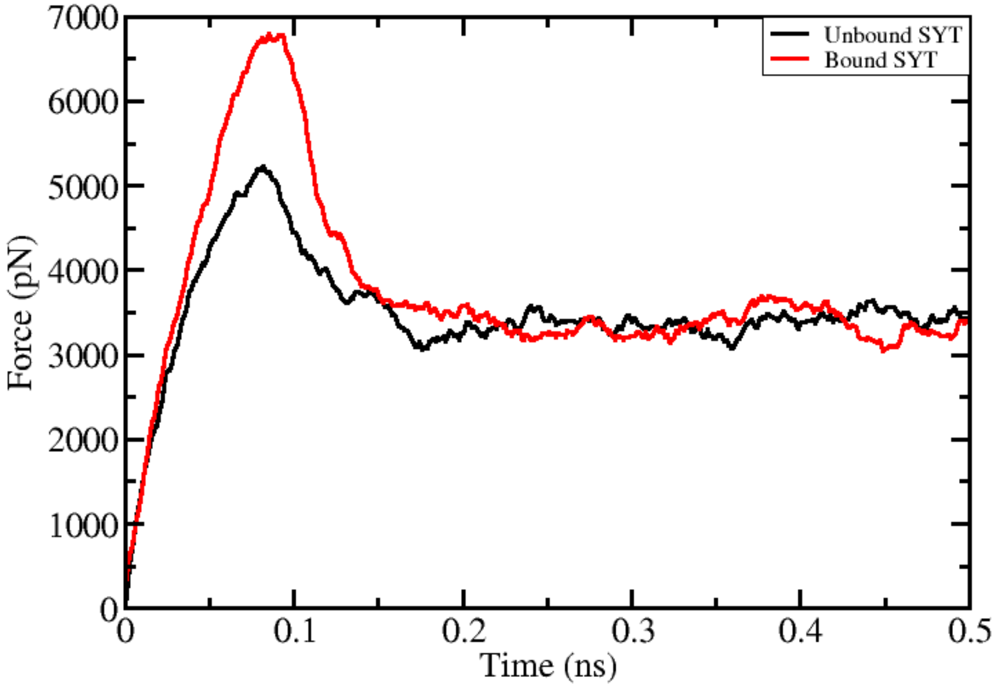

Figure 58: Applied force vs. run time for pulling the C2B domain away from acidic bilayer. Profile for bilayer bound and bilayer free SYT-1 is shown in red and black respectively.

To understand the importance of bound Ca^{2+} to SYT-1 protein, another experiment was carried out where the aim was to look at the behavior of inserted SYT-1 after Ca^{2+} is removed from the binding site. Initial configuration chosen for this experiment was that of inserted Ca^{2+}-bound C2B domain in the anionic lipid bilayer. Both the Ca^{2+} ions were removed from their respective pockets in this initial configuration without disturbing any other atom in the system. 4 Sodium ions were added to maintain overall charge neutrality of the system. After 6 ns of simulation, the inserted residues (304 and 367) pop out of the bilayer (**Figure 59**) from their respective inserted positions. Distance before and after the start of simulation is also shown. This result shows that Ca^{2+} ions are necessary to keep the C2B domain inserted in lipid bilayer. An explanation to this is that once Ca^{2+} is removed, the electrostatics of the system changes and repulsion between the negatively charged bilayer and interacting protein surface causes the protein to move away.

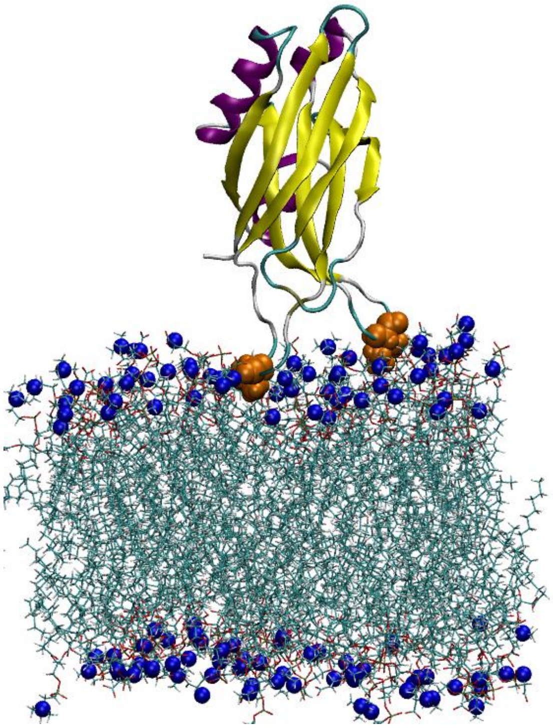

Figure 59: Post simulation configuration of C2B domain after removal of Ca2+ ions from the designated pockets. Residue 367 (Orange) is ejected from the bilayer surface.

Electrostatic potential of protein surface

The role of Ca^{2+} in imparting a positive electrostatic potential (ESP) to both C2A and C2B domains has been well documented in the literature [287, 298]. As proposed by Zheng et al. [299], one of the major driving forces for the association of SYT-1 protein to anionic lipid bilayers is the favorable electrostatic energy which arises due to binding of Calcium to SYT-1's C2A and C2B domain. Ca^{2+} binding increases the electrostatic potential locally around the binding site thereby attracting the negatively charged surface of anionic bilayers. Electrostatic maps of both Ca^{2+}-bound and Ca^{2+}-free C2A and C2B domains were generated to analyze the overall electrostatic effect (**Figure 60**). Maps were generated using the Adaptive Poisson Boltzman Solver software [303] incorporated in VMD which uses Finite element method to solve Poisson-Boltzmann equation numerically. Input file for APBS calculation was generated using PDB2PQR software [309, 310] which coverts system coordinate file in PDB format to PQR format as required by the APBS software. Circled region in Figure encloses the Ca^{2+} -ion pocket and this is where major changes in electrostatics occur upon Ca^{2+} binding. It can be seen that this region carries a high negative charge when Ca^{2+} ions are not bound but changes into a positively charges region upon Ca^{2+} binding. Negative charge in the Ca^{2+} binding pocket is due to the presence of Aspartic acid residues (also shown in Figure) in both C2A and C2B domains. Negative electrostatic potential (before Ca^{2+} binding) repels this protein region from the acidic bilayer thereby increasing the free energy barrier. However, post Ca^{2+} binding, resulting in a negative to positive shift in ESP, the energy barrier is lowered due to the attraction between this positive region of protein and negative region of bilayer surface which may result in SYT-1 association with bilayer. This calculation, although qualitative in nature, suggests the importance of electrostatic interactions in SYT-1 association with anionic bilayer.

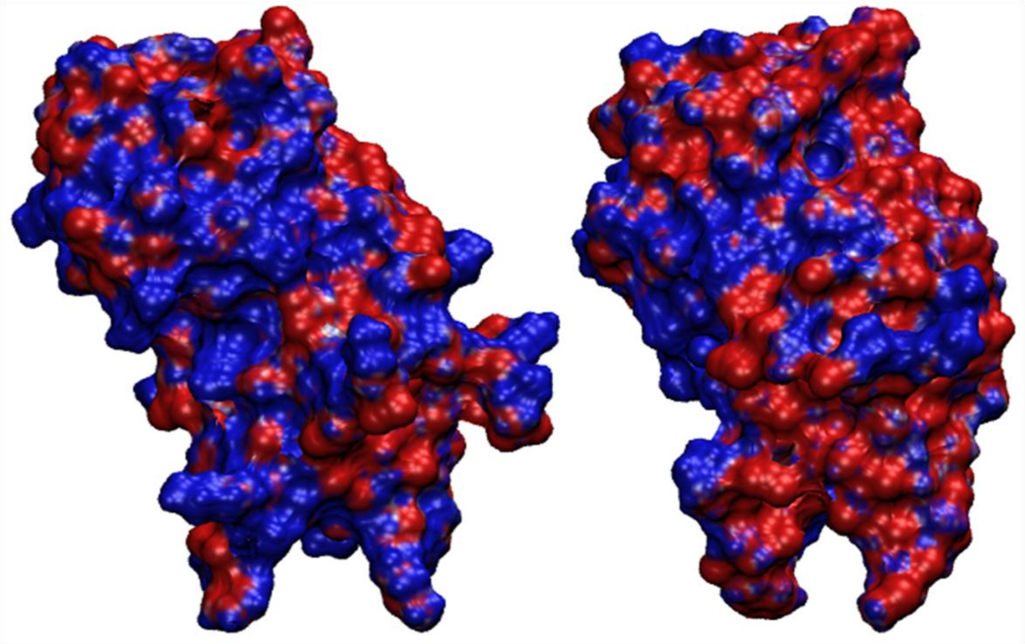

Figure 60: Electrostatic potential maps of Ca^{2+}-bound (left) and Ca^{2+}-free (right) C2A domain. Red and blue colors denoted negatively and positively charged surfaces respectively.

Interaction energy between SYT-1 and bilayer

Interaction energy between both C2A/C2B domains of SYT-1 and lipid bilayer was evaluated to further study the role of electrostatics in this insertion process. Steered molecular dynamics was applied for this calculation. Bilayer was fixed in space and the protein SYT-1, initially at a distance of 40.0 Ǻ from the bilayer surface, was moved towards the bilayer with a constant velocity and varying force to cover a distance of 40.0 Ǻ so that protein just touches the bilayer surface. Electrostatic energy was computed with the analysis tools in NAMD and plotted with the distance between the approaching protein and bilayer.

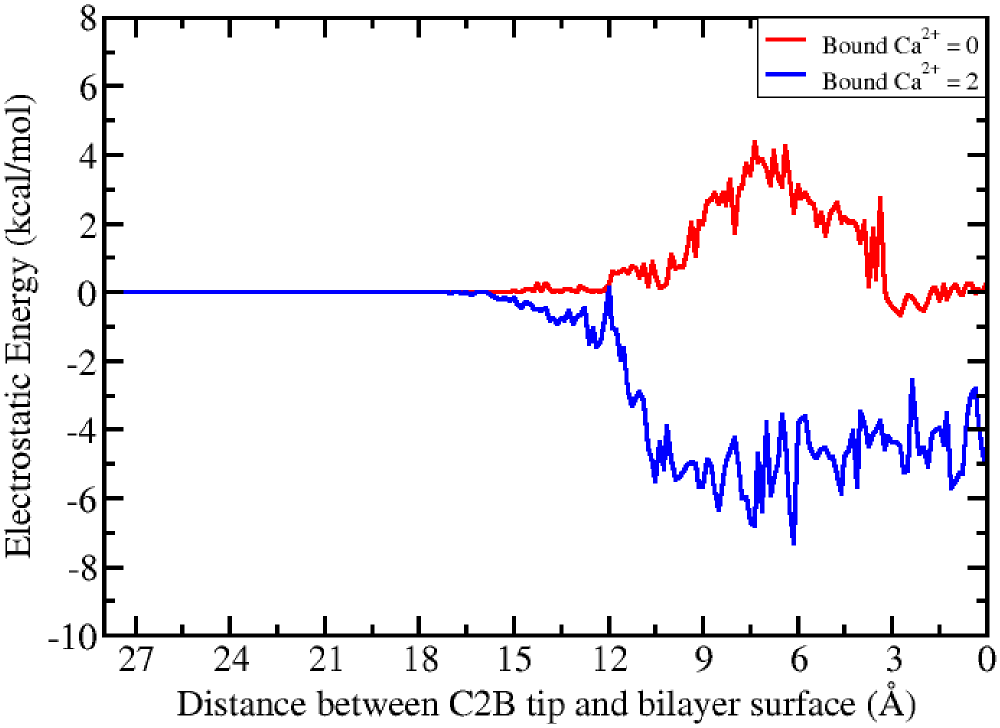

Figure 61: Electrostatic energy vs. distance between anionic bilayer (PC/PS) and approaching C2B domain. Resulting profile for system with Ca2+ - free C2B is shown in red and with Ca2+ - bound C2B is shown in blue color.

As can be seen from **Figure 61**, electrostatic energy between the protein and bilayer remains constant to a distance of 12.0 Ǻ suggesting that electrostatic interactions develop only when SYT-1 at a minimum distance of ~ 14.0 Ǻ from the bilayer surface. When Ca^{2+} ions are bound to the protein (C2A or C2B), the electrostatic energy lowers down from 0.0 kcal/mol to a value of -15.0 kcal/mol for C2A domain and to -8.0 kcal/mol for the C2B domain marking a favorable interaction between SYT-1 and bilayer. Contrasting to this result, when the two domains are Ca^{2+} free, and are moved towards the bilayer, there is a sharp rise in the electrostatic energy from

0.0 kcal/mol to 5.0 kcal/mol for both C2A and C2B. This profile suggests the repulsive behaviour between the protein and bilayer in the absence of Ca^{2+}. It should be noted that the electrostatic interactions in this case start developing around same point as observed for the case when Ca^{2+} ions were bound to the protein thereby strengthening the result that in this configuration SYT-1 starts interacting with the bilayer from a distance of ~ 14.0 Ǻ. The results are qualitative in nature and indicate that binding of Ca^{2+} to both C2A and C2B domains changes the electrostatics of system and the protein interactions with the bilayer are turned from unfavorable to favorable.

Force between SYT-1 and bilayer

Total number of bound Ca^{2+} ions can have an effect on the SYT-1-bilayer interactions. To measure this, SMD calculations with constant velocity and variable force were run for both C2A and C2B domain. Applied force was plotted against distance which provides a qualitative analysis on the attraction and repulsion behavior of the two interacting species. Calculations were done for three systems where the first had zero Ca^{2+} ions attached to C2B, second system had 1 bound Ca^{2+} ion and the third system had both Ca^{2+} ions bound at their designated sites.

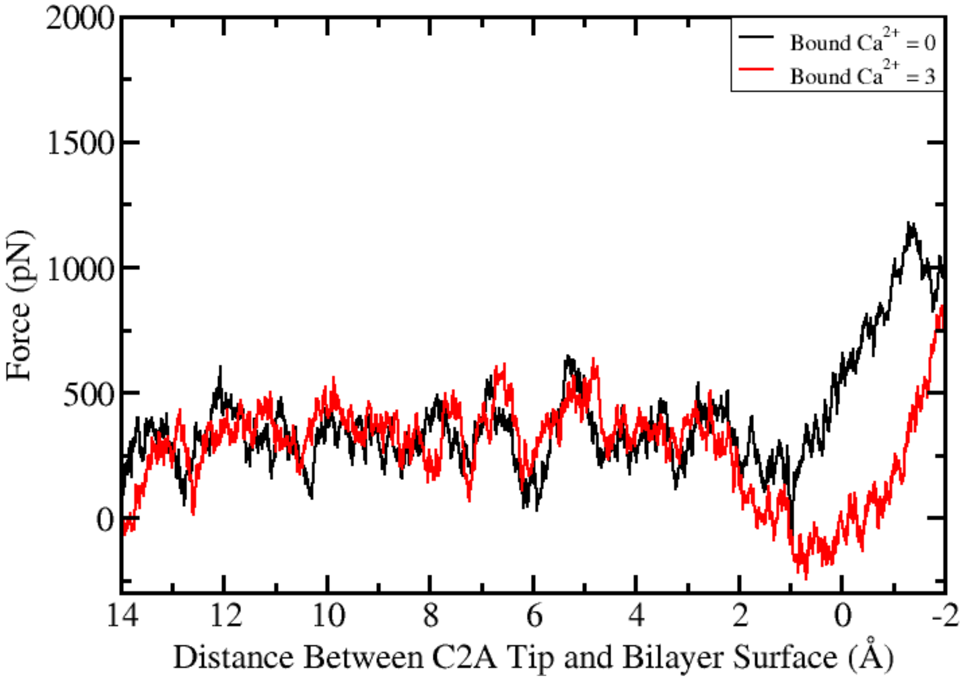

Figure 62: : Force required in bringing C2A domain close to anionic bilayer (PC/PS) surface plotted as a function of distance. Resulting profile for system with number of bound Ca2+ ions equal to 0 and 3 are shown in black and red colors respectively.

The three systems were pulled towards the bilayer with same velocities and force constant values. Plot between the applied force and distance between the approaching protein and bilayer is shown in **Figure 62**. There is a clear distinction between the magnitude of applied force for the three cases as the force required to pull the third system with 2 bound Ca^{2+} ions was lowest as compared to the other two cases and increased as the number of bound Ca^{2+} ions decreased. Results for C2A domain are shown in **Figure 63**. Force required for the case when Ca^{2+} is bound

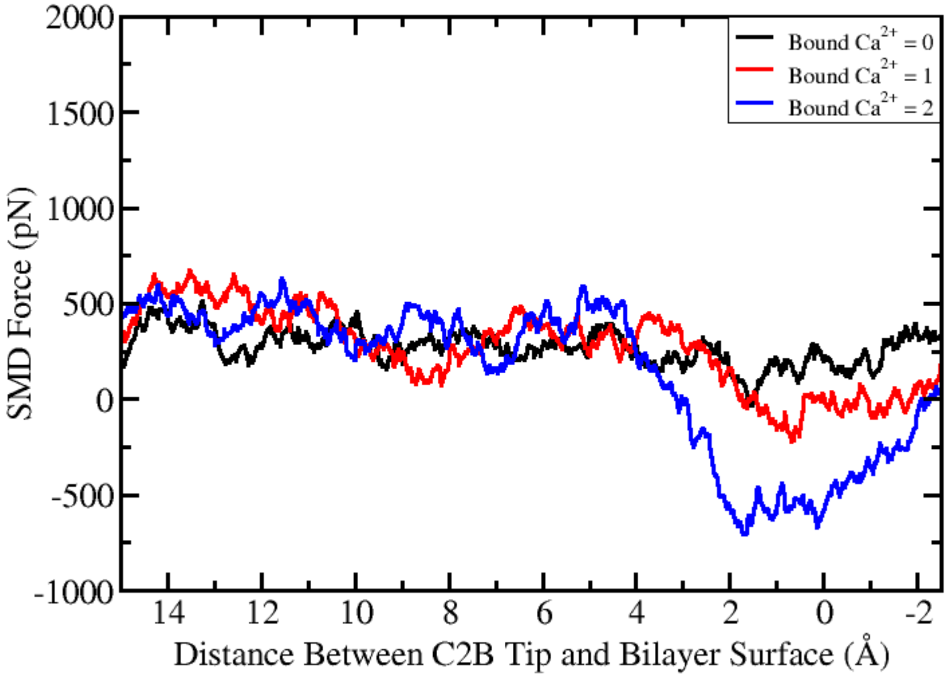

Figure 63: Force required in bringing C2B domain close to anionic bilayer (PC/PS) surface plotted as a function of distance. Resulting profile for system with number of bound Ca2+ ions equal to 0, 1 and 2 are shown in black, red and blue colors respectively.

to C2A is lower than when the domain is Ca^{2+} free. This result again provides a qualitative picture on the role of Ca^{2+} ions on increasing the favorable interactions between SYT-1 protein and the lipid bilayer.

Potential of mean force

Potential of mean force calculations with C2A domain were performed to understand the effect of Ca^{2+} on the binding affinity of SYT-1 to the lipid bilayer. PMF calculations were done using the adaptive biasing force (ABF) method. Distance between center of masses of the two penetrating residues (M173 and F234) and the upper leaflet of lipid bilayer was chosen as the reaction coordinate. PMF profiles for the Ca^{2+} free and Ca^{2+} bound C2A systems are displayed in **Figure 64** with red and black color scheme respectively. Profile for Ca^{2+} bound case shows a clear minimum at around 4.0 Ǻ, a stage where the protein tips just touch the bilayer surface, followed by a rise as C2A moves away from the bilayer into the bulk water phase. In contrast to this, Ca^{2+} free C2A domain profile attains a maximum when it is close to the bilayer surface and drops down to a minimum when moved into the water phase. Free energy difference between the two state points (C2A in contact with bilayer and in bulk water phase) for Ca^{2+} bound case is negative (-2.90 kcal/mol) suggesting a favorable interaction between C2A and bilayer in the presence of Ca^{2+}. For Ca^{2+} free case, this difference is positive (+1.5 kcal/mol) which means that bringing C2A domain (with no bound Ca^{2+}) close to the bilayer from bulk water phase is energetically unfavorable. These results highlight the role of Ca^{2+} in altering the interactions between SYT-1 and bilayer.

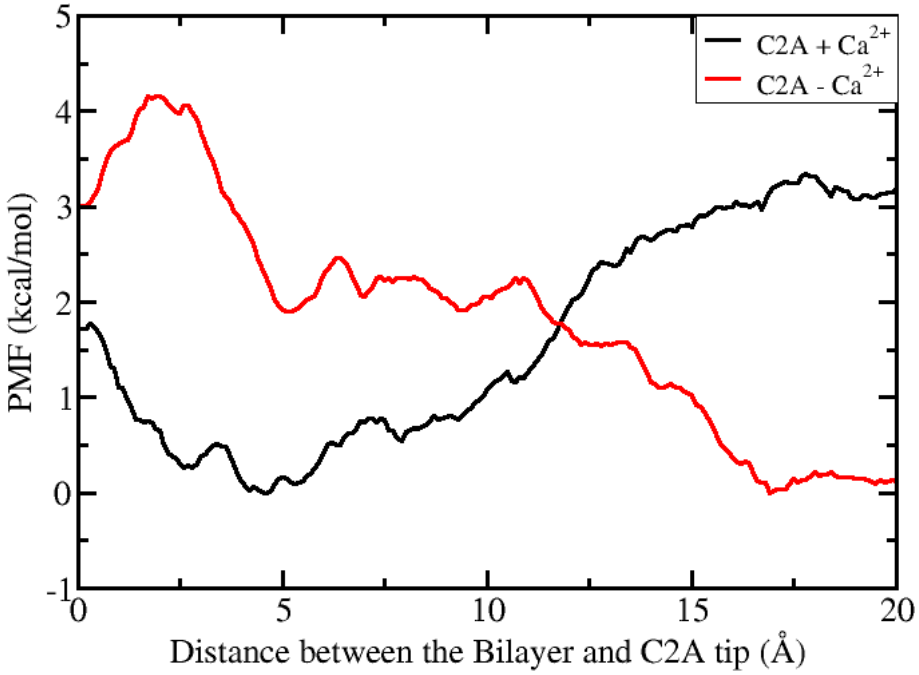

Figure 64: Potential of mean force between PC/PS (65:35) bilayer and C2A domain of SYT-1. Red profile is for the Ca2+ free C2A domain and black profile is for the Ca2+ bound C2A domain.

Energetics of SNARE dissociation

SNAREs (soluble N-ethylmalemide-sensitive factor attachment protein receptor) are a set of proteins which are known to facilitate the membrane fusion process by pulling the two membranes in close apposition to provide a contact point for fusion which is otherwise a thermodynamically unfavorable event [311]. This happens when SNAP-25 and Syntaxin-1A proteins (part of the target plasma membrane) start interacting with VAMP-2 (part of the synaptic vesicle) protein and form a tight complex in a zipper like fashion thereby bringing the two membrane bodies close to each other and the energy released in this complex formation process helps in crossing the energetic barrier. In this study, the stability and energetics of SNARE complex was investigated in order to understand the factors that hold the three proteins together in a favorable wound state.

Steered molecular dynamics (SMD) simulations were carried out to dissociate the SNARE complex (**Figure 65**) and forces and energy associated were measured.

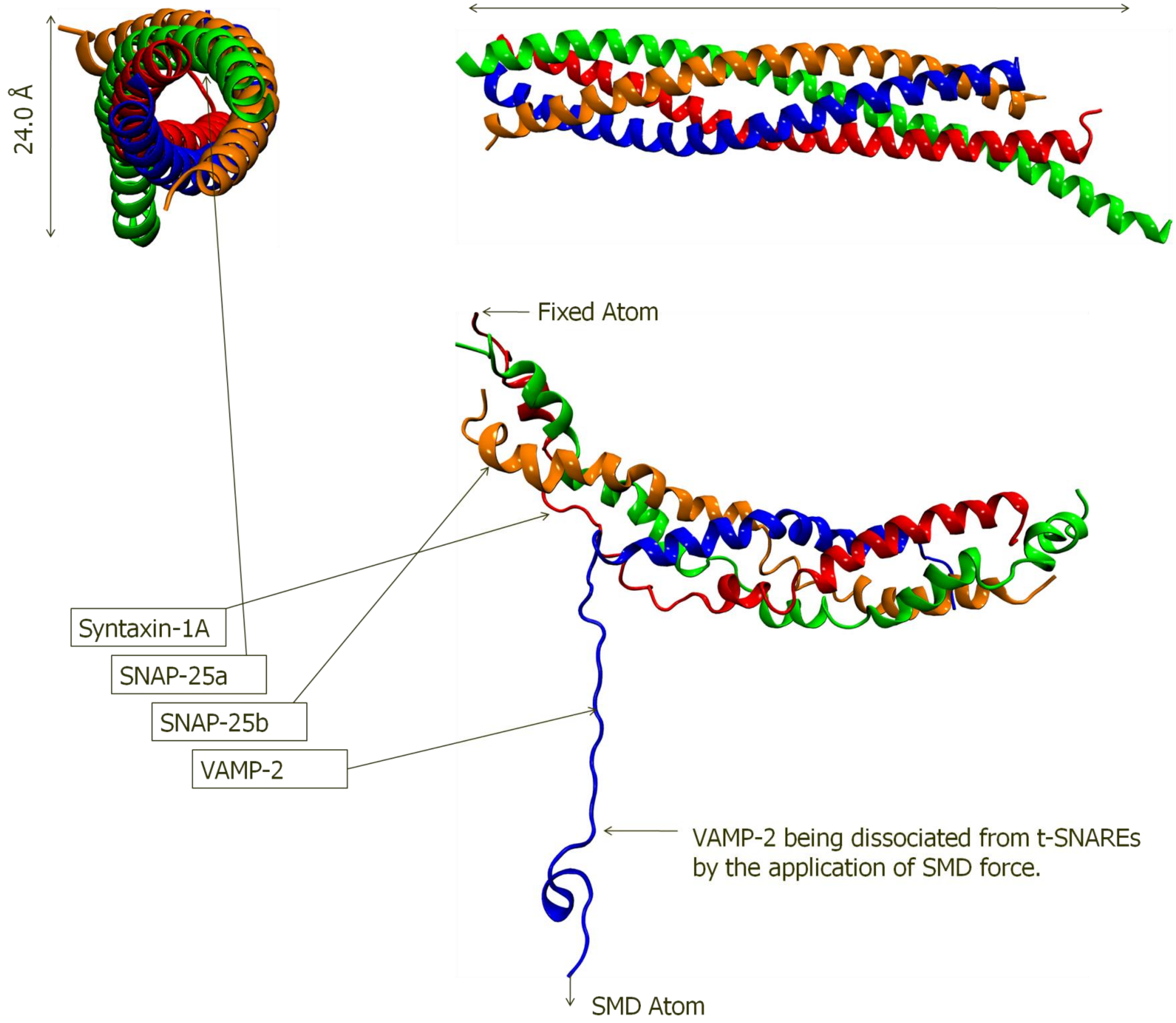
24.0 Å
Fixed Atom
Syntaxin-1A
SNAP-25a
SNAP-25b
VAMP-2
VAMP-2 being dissociated from t-SNAREs
by the application of SMD force.
SMD Atom

Figure 65: Schematic of a SNARE complex. Syntaxin1-A is shown in red, VAMP-2 in blue and the two coils of SNAP-25 in orange and green.

The first carbon atom of Syntaxin-1A and SNAP-25 on the N-termini was fixed while that of VAMP-25 was moved with a constant velocity of 12.0 Å/ns away from the fixed atoms in the negative z-direction thereby dissociating the complex. Variable forces and energy were then measured for this process and plotted as a function of distance between the fixed and moving atom to provide an estimate of energy stored in the complex. The force curve as a function of separation distance is plotted and shown in **Figure 66**.

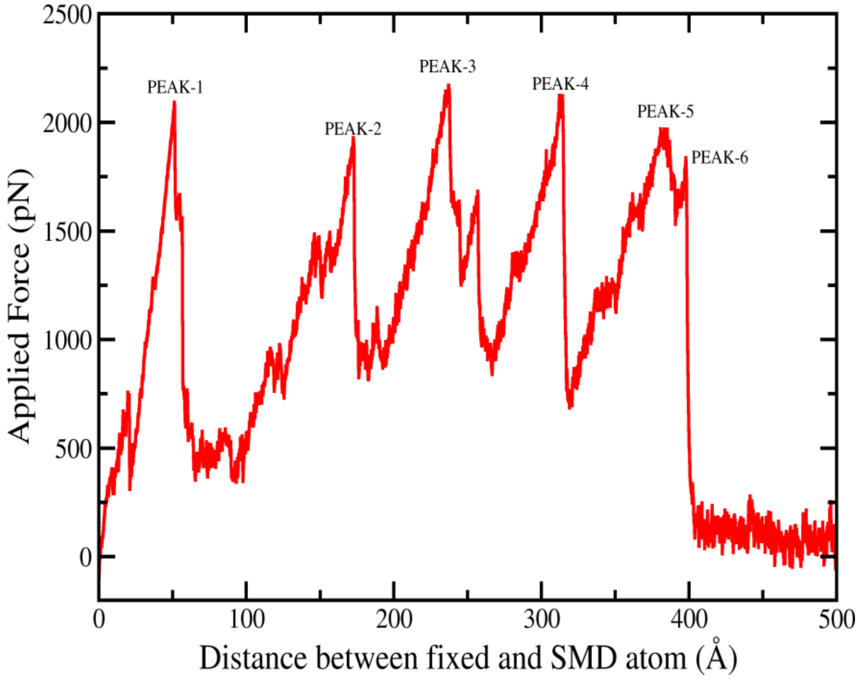

Figure 66: SMD pulling force plotted versus distance between fixed and SMD atom. Peaks denote the dissociation of residue pares. Peak 6 marks the point where VAMP-2 completely dissociates from the complex.

Distinctive peaks can be seen in the figure marking the point where the complex dissociates and a bond is broken. For the same run, electrostatic energy of the system was calculated and plotted (**Figure 67**).

Amino acid residues in the SNARE proteins that play a factor in stability of the complex were identified. Free energy of dissociation is plotted as a function of the reaction coordinate.

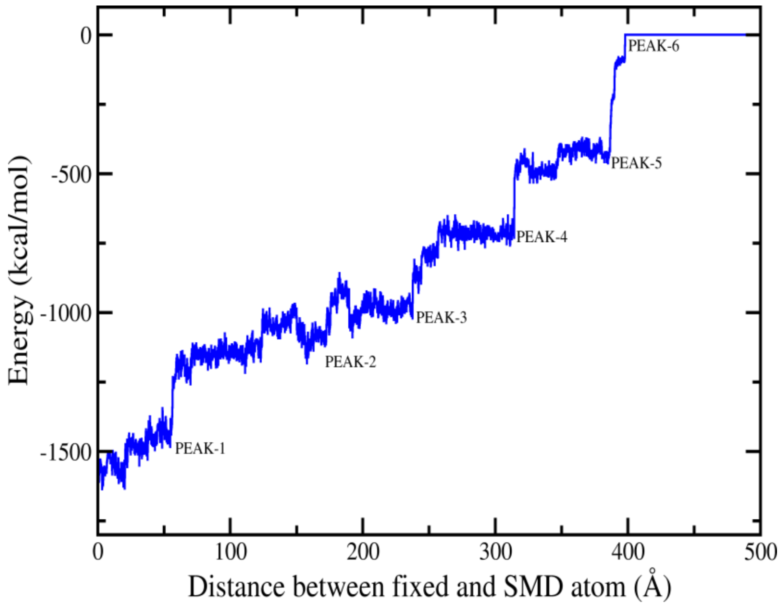

Figure 67: Electrostatic energy between VAMP-2 and (t)-SNAREs plotted versus distance between fixed and SMD atom. Jumps in energy correspond to peaks in force curve. Flat region after Peak-6 point is due to complete dissociation of the SNARE complex.

BIBLIOGRAPHY

1. Beglov, D. and B. Roux, *Finite Representation of an Infinite Bulk System - Solvent Boundary Potential for Computer-Simulations.* Journal of Chemical Physics, 1994. 100(12): p. 9050-9063.

2. Aqvist, J., *Ion Water Interaction Potentials Derived from Free-Energy Perturbation Simulations.* Journal of Physical Chemistry, 1990. 94(21): p. 8021-8024.

3. Cho, W.H. and R.V. Stahelin, *Membrane-protein interactions in cell signaling and membrane trafficking.* Annual Review of Biophysics and Biomolecular Structure, 2005. 34: p. 119-151.

4. Jahn, R., T. Lang, and T.C. Sudhof, *Membrane fusion.* Cell, 2003. 112(4): p. 519-533.

5. Martens, S. and H.T. McMahon, *Mechanisms of membrane fusion: disparate players and common principles.* Nature Reviews Molecular Cell Biology, 2008. 9(7): p. 543-556.

6. Cohen, F.S. and G.B. Melikyan, *The energetics of membrane fusion from binding, through hemifusion, pore formation, and pore enlargement.* Journal of Membrane Biology, 2004. 199(1): p. 1-14.

7. Cho, W.J., et al., *Membrane-directed molecular assembly of the neuronal SNARE complex.* Journal of Cellular and Molecular Medicine, 2011. 15(1): p. 31-37.

8. Jeremic, A., et al., *Energy-dependent disassembly of self-assembled SNARE complex: Observation at nanometer resolution using atomic force microscopy.* Journal of the American Chemical Society, 2006. 128(1): p. 26-27.

9. Hanson, P.I., et al., *Structure and conformational changes in NSF and its membrane receptor complexes visualized by quick-freeze/deep-etch electron microscopy.* Cell, 1997. 90(3): p. 523-535.

10. Lin, R.C. and R.H. Scheller, *Structural organization of the synaptic exocytosis core complex.* Neuron, 1997. 19(5): p. 1087-1094.

11. Poirier, M.A., et al., *The synaptic SNARE complex: A parallel four-stranded helical bundle.* Molecular Biology of the Cell, 1998. 9: p. 84a-84a.

12. Sutton, R.B., et al., *Crystal structure of a SNARE complex involved in synaptic exocytosis at 2.4 angstrom resolution.* Nature, 1998. 395(6700): p. 347-353.

13. Sorensen, J.B., et al., *Sequential N- to C-terminal SNARE complex assembly drives priming and fusion of secretory vesicles.* Embo Journal, 2006. 25(5): p. 955-966.

14. Sangster, J., *Octanol-Water Partition-Coefficients of Simple Organic-Compounds.* Journal of Physical and Chemical Reference Data, 1989. 18(3): p. 1111-1229.

15. Hansch, C. and T. Fujita, *r-s-p Analysis. A Method for the Correlation of Biological Activity and Chemical Structure.* J. Am. Chem. Soc., 1964. 86(8): p. 1616-1626.

16. Leo, A., C. Hansch, and D. Elkins, *Partition Coefficients and Their Uses.* Chemical Reviews, 1971. 71(6): p. 525-+.

17. Kerns, E.H., *High throughput physicochemical profiling for drug discovery.* Journal of Pharmaceutical Sciences, 2001. 90(11): p. 1838-1858.

18. Boethling, R.S., et al., *Improved method for estimating bioconcentration/bioaccumulation factor from octanol/water partition coefficient.* Environmental Toxicology and Chemistry, 1999. 18(4): p. 664-672.

19. Neely, W.B., Branson, D. R., Blau, G. E., *Partition coefficient to measure bioconcentration potential of organic chemicals in fish.* Environ. Sci. Technol., 1974. 8: p. 1113-1115.

20. Devillers, J., S. Bintein, and D. Domine, *Comparison of BCF models based on log P.* Chemosphere, 1996. 33(6): p. 1047-1065.

21. Potts, R.O. and R.H. Guy, *Predicting Skin Permeability.* Pharmaceutical Research, 1992. 9(5): p. 663-669.

22. Geinoz, S., et al., *Quantitative structure-permeation relationships (QSPeRs) to predict skin permeation: A critical evaluation.* Pharmaceutical Research, 2004. 21(1): p. 83-92.

23. Karickhoff, S.W., D.S. Brown, and T.A. Scott, *Sorption of Hydrophobic Pollutants on Natural Sediments.* Water Research, 1979. 13(3): p. 241-248.

24. Briggs, G.G., *Theoretical and Experimental Relationships between Soil Adsorption, Octanol-Water Partition-Coefficients, Water Solubilities, Bioconcentration Factors, and the Parachor.* Journal of Agricultural and Food Chemistry, 1981. 29(5): p. 1050-1059.

25. Darve, E. and A. Pohorille, *Calculating free energies using average force.* Journal of Chemical Physics, 2001. 115(20): p. 9169-9183.

26. Darve, E., M.A. Wilson, and A. Pohorille, *Calculating free energies using a scaled-force molecular dynamics algorithm.* Molecular Simulation, 2002. 28(1-2): p. 113-144.

27. Rodriguez-Gomez, D., E. Darve, and A. Pohorille, *Assessing the efficiency of free energy calculation methods.* Journal of Chemical Physics, 2004. 120: p. 3563.

28. Henin, J. and C. Chipot, *Overcoming free energy barriers using unconstrained molecular dynamics simulations.* Journal of Chemical Physics, 2004. 121(7): p. 2904-2914.

29. J. Henin, et al., *Exploring multidimensional free energy landscapes using time-dependent biases on collective variables.* J. Chem. Theor. Comput., 2010. 6: p. 35-47.

30. Karplus, M. and J.A. McCammon, *Molecular dynamics simulations of biomolecules.* Nature Structural Biology, 2002. 9(9): p. 646-652.

31. Mccammon, J.A., B.R. Gelin, and M. Karplus, *Dynamics of Folded Proteins.* Nature, 1977. 267(5612): p. 585-590.

32. Phillips, J.C., et al., *Scalable molecular dynamics with NAMD.* Journal of Computational Chemistry, 2005. 26(16): p. 1781-1802.

33. Jorgensen, W.L. and C. Ravimohan, *Monte-Carlo Simulation of Differences in Free-Energies of Hydration.* Journal of Chemical Physics, 1985. 83(6): p. 3050-3054.

34. Garrido, N.M., et al., *1-Octanol/Water Partition Coefficients of n-Alkanes from Molecular Simulations of Absolute Solvation Free Energies.* Journal of Chemical Theory and Computation, 2009. 5(9): p. 2436-2446.

35. Chen, B. and J.I. Siepmann, *Partitioning of alkane and alcohol solutes between water and (Dry or wet) 1-Octanol.* Journal of the American Chemical Society, 2000. 122(27): p. 6464-6467.

36. Chen, B. and J.I. Siepmann, *Microscopic structure and solvation in dry and wet octanol.* Journal of Physical Chemistry B, 2006. 110(8): p. 3555-3563.

37. Martin, M.G. and J.I. Siepmann, *Calculating Gibbs free energies of transfer from Gibbs ensemble Monte Carlo simulations.* Theoretical Chemistry Accounts, 1998. 99(5): p. 347-350.

38. Jarzynski, C., *Equilibrium free-energy differences from nonequilibrium measurements: A master-equation approach.* Physical Review E, 1997. 56(5): p. 5018-5035.

39. Jarzynski, C., *Nonequilibrium equality for free energy differences.* Physical Review Letters, 1997. 78(14): p. 2690-2693.

40. E. Darve, D. R. Gomez, and A. Pohorille, *Adaptive biasing force method for scalar and vector free energy calculations.* J. Chem. Phys., 2008. 128: p. 144120.

41. C. Chipot and J. Henin, *Exploring the free-energy landscape of a short peptide using an average force.* J. Chem. Phys., 2005. 123(24): p. 244906-244911.

42. C. Chipot and A. Pohorille, *Free Energy Calculations*. Theory and Applications in Chemistry and Biology2007, Berlin: Springer.

43. Buhl, M. and G. Wipff, *Insights into Uranyl Chemistry from Molecular Dynamics Simulations.* Chemphyschem, 2011. 12: p. 3095-3105.

44. Bhatnagar, N., et al., *Direct prediction of 1-octanol-water partition coefficients from adaptive biasing force molecular dynamics simulations.* Journal of Chemical Physics, 2012. in press.

45. Lodge, K.B., *Octanol-water partition coefficients of cyclic C-7 hydrocarbons and selected derivatives.* J. Chem Eng. Data, 1999. 44(6): p. 1321-1324.

46. J. Tolls, et al., *Slow-stirring method for determining the n-octanol/water partition coefficient (pow) for highly hydrophobic chemicals: Performance evaluation in a ring test.* Envir. Toxicol. Chem., 2003. 22(5): p. 1051-1057.

47. TakacsNovak, K. and A. Avdeef, *Interlaboratory study of log P determination by shake-flask and potentiometric methods.* Journal of Pharmaceutical and Biomedical Analysis, 1996. 14(11): p. 1405-1413.

48. Edelbach, D.J. and K.B. Lodge, *Insights into the measurement of the octanol-water partition coefficient from experiments with acrylate esters.* Physical Chemistry Chemical Physics, 2000. 2(8): p. 1763-1771.

49. Burkhard, L.P. and D.W. Kuehl, *N-Octanol Water Partition-Coefficients by Reverse Phase Liquid-Chromatography Mass-Spectrometry for 8 Tetrachlorinated Planar Molecules.* Chemosphere, 1986. 15(2): p. 163-167.

50. Burkhard, L.P., D.W. Kuehl, and G.D. Veith, *Evaluation of Reverse Phase Liquid-Chromatography Mass-Spectrometry for Estimation of N-Octanol Water Partition-Coefficients for Organic-Chemicals.* Chemosphere, 1985. 14(10): p. 1551-1560.

51. Mcduffie, B., *Estimation of Octanol-Water Partition-Coefficients for Organic Pollutants Using Reverse-Phase Hplc.* Chemosphere, 1981. 10(1): p. 73-83.

52. Woodburn, K.B., W.J. Doucette, and A.W. Andren, *Generator Column Determination of Octanol Water Partition-Coefficients for Selected Polychlorinated Biphenyl Congeners.* Environmental Science & Technology, 1984. 18(6): p. 457-459.

53. Carrupt, P.A., et al., *Standard partition coefficients of anionic drugs in the n-octanol/water system determined by voltammetry at three-phase electrodes.* Physical Chemistry Chemical Physics, 2003. 5(17): p. 3748-3751.

54. Scholz, F., R. Gulaboski, and V. Mirceski, *An electrochemical method for determination of the standard Gibbs energy of anion transfer between water and n-octanol.* Electrochemistry Communications, 2002. 4(4): p. 277-283.

55. Danielsson, L.G. and Y.H. Zhang, *Methods for determining n-octanol-water partition constants.* Trac-Trends in Analytical Chemistry, 1996. 15(4): p. 188-196.

56. Garst, J.E., *Accurate, Wide-Range, Automated, High-Performance Liquid-Chromatographic Method for the Estimation of Octanol Water Partition-Coefficients .2. Equilibrium in Partition-Coefficient Measurements, Additivity of Substituent Constants, and Correlation of Biological Dat.* Journal of Pharmaceutical Sciences, 1984. 73(11): p. 1623-1629.

57. Liu, X.L., et al., *Partition coefficients of ionizable compounds in o-nitrophenyl octyl ether/water measured by the potentiometric method.* Analytical Chemistry, 2003. 75(24): p. 7036-7039.

58. Ulmeanu, S.M., et al., *Water-oil partition profiling of ionized drug molecules using cyclic voltammetry and a 96-well microfilter plate system.* Pharmaceutical Research, 2003. 20(8): p. 1317-1322.

59. Beck, B., A. Breindl, and T. Clark, *QM/NN QSPR models with error estimation: Vapor pressure and LogP*. Journal of Chemical Information and Computer Sciences, 2000. 40(4): p. 1046-1051.

60. Duchowicz, P.R., et al., *QSPR MODELING OF THE OCTANOL/WATER PARTITION COEFFICIENT OF ALCOHOLS BY MEANS OF OPTIMIZATION OF CORRELATION WEIGHTS OF LOCAL GRAPH INVARIANTS.* The Journal of the Argentine Chemical Society, 2004. 92: p. 29-42.

61. Duchowicz, P.R., et al., *QSPR modeling the aqueous solubility of alcohols by optimization of correlation weights of local graph invariants.* Molecular Diversity, 2004. 8: p. 325-330.

62. Gonzalez, M.P., et al., *QSPR calculation of normal boiling points of organic molecules based on the use of correlation weighting of atomic orbitals with extended connectivity of zero- and first-order graphs of atomic orbitals.* Molecules, 2004. 9(12): p. 1019-1033.

63. J. D. Dyekjaer, K. Ramsussen, and S.O. Jonsdottir, J. Mol. Model, 2002. 8: p. 277-289.

64. Eros, D., et al., *Comparison of predictive ability of water solubility QSPR models generated by MLR, PLS and ANN methods.* Mini-Reviews in Medicinal Chemistry, 2004. 4(2): p. 167-177.

65. Hilal, S.H., et al., *Calculating physical properties of organic compounds for environmental modeling from molecular structure.* Journal of Computer-Aided Molecular Design, 2007. 21(12): p. 693-708.

66. Hilal, S.H., Karickhoff, S. A, Carreira, L. A., *Prediction of Chemical Reactivity Parameters and Physical Properties of Organic Compounds from Molecular Structure using SPARC (EPA/600/R-03/030).* EPA/600/R-03/030, 2003.

67. Doweyko, A.M., *3D-QSAR illusions.* Journal of Computer-Aided Molecular Design, 2004. 18(7-9): p. 587-596.

68. Hughes, L.D., et al., *Why are some properties more difficult to predict than others? A study of QSPR models of solubility, melting point, and Log P.* Journal of Chemical Information and Modeling, 2008. 48(1): p. 220-232.

69. Arp, H.P.H., C. Niederer, and K.U. Goss, *Predicting the partitioning behavior of various highly fluorinated compounds.* Environmental Science & Technology, 2006. 40(23): p. 7298-7304.

70. Armitage, J.M., M. MacLeod, and I.T. Cousins, *Response to Comment on "Comparative Assessment of the Global Fate and Transport Pathways of Long-Chain Perfluorocarboxylic Acids (PFCAs) and Perfluorocarboxylates (PFCs) Emitted from Direct Sources"*. Environmental Science & Technology, 2009. 43(18): p. 7153-7154.

71. Armitage, J.M., M. MacLeod, and I.T. Cousins, *Comparative Assessment of the Global Fate and Transport Pathways of Long-Chain Perfluorocarboxylic Acids (PFCAs) and Perfluorocarboxylates (PFCs) Emitted from Direct Sources.* Environmental Science & Technology, 2009. 43(15): p. 5830-5836.

72. Rayne, S. and K. Forest, *Comment on "Comparative Assessment of the Global Fate and Transport Pathways of Long-Chain Perfluorocarboxylic Acids (PFCAs) and Perfluorocarboxylates (PFCs) Emitted from Direct Sources"*. Environmental Science & Technology, 2009. 43(18): p. 7155-7156.

73. Chakka, S., Costales-Nieves, C., Boddu, V., Damavarapu, R., *Physical Properties of Munitions Compounds -- Chinalake (CL-20), Diamino-Dinitroethylene (DADE), Cyclotetramethylenetetranitramine (HMX) and Cyclotrimethylenetrinitramine (RDX)*, in *AICHE Annual Meeting*2011: Minneapolis, MN.

74. Martin, M.G. and J.I. Siepmann, *Transferable potentials for phase equilibria. 1. United-atom description of n-alkanes.* Journal of Physical Chemistry B, 1998. 102(14): p. 2569-2577.

75. Chen, B., J.J. Potoff, and J.I. Siepmann, *Monte Carlo calculations for alcohols and their mixtures with alkanes. Transferable potentials for phase equilibria. 5. United-atom description of primary, secondary, and tertiary alcohols.* Journal of Physical Chemistry B, 2001. 105(15): p. 3093-3104.

76. Berendsen, H.J.C., J.R. Grigera, and T.P. Straatsma, *The Missing Term in Effective Pair Potentials.* Journal of Physical Chemistry, 1987. 91(24): p. 6269-6271.

77. Jorgensen, W.L., et al., *Comparison of Simple Potential Functions for Simulating Liquid Water.* Journal of Chemical Physics, 1983. 79(2): p. 926-935.

78. Phillips, J.C., et al., *Scalable molecular dynamics with NAMD.* Journal of Computational Chemistry, 2005. 26: p. 1781-1802.

79. Martinez, L., et al., *PACKMOL: A Package for Building Initial Configurations for Molecular Dynamics Simulations.* Journal of Computational Chemistry, 2009. 30(13): p. 2157-2164.

80. Feller, S.E., et al., *Constant-Pressure Molecular-Dynamics Simulation - the Langevin Piston Method.* Journal of Chemical Physics, 1995. 103(11): p. 4613-4621.

81. Martyna, G.J., D.J. Tobias, and M.L. Klein, J. Chem . Phys., 1994. 101: p. 4177.

82. Darden, T., D. York, and L. Pedersen, *Particle Mesh Ewald - an N.Log(N) Method for Ewald Sums in Large Systems.* Journal of Chemical Physics, 1993. 98(12): p. 10089-10092.

83. Essmann, U., et al., *A Smooth Particle Mesh Ewald Method.* Journal of Chemical Physics, 1995. 103(19): p. 8577-8593.

84. Humphrey, W., A. Dalke, and K. Schulten, *VMD: Visual molecular dynamics.* Journal of Molecular Graphics, 1996. 14(1): p. 33-38.

85. D. L. Mobley, et al., *Comparison of charge models for fixed-charge force fields: small-molecule hydration free energies in explicit solvent.* J. Phys. Chem. B, 2007. 111: p. 2242-2254.

86. Wolfenden, R., et al., *Affinities of Amino-Acid Side-Chains for Solvent Water.* Biochemistry, 1981. 20(4): p. 849-855.

87. Cabani, S., et al., *Group Contributions to the Thermodynamic Properties of Non-Ionic Organic Solutes in Dilute Aqueous-Solution.* Journal of Solution Chemistry, 1981. 10(8): p. 563-595.

88. Bouloougouris, G.C., I.G. Economou, and D.N. Theodorou, *Engineering a molecular model for water phase equilibrium over a wide temperature range.* Journal of Physical Chemistry B, 1998. 102(6): p. 1029-1035.

89. Curutchet, C., M. Orozco, and F.J. Luque, *Solvation in octanol: Parametrization of the continuum MST model.* Journal of Computational Chemistry, 2001. 22(11): p. 1180-1193.

90. Bernazzani, L., et al., *Thermodynamic Study of the Partitioning of Organic-Compounds between Water and Octan-1-Ol.* Journal of the Chemical Society-Faraday Transactions, 1995. 91(4): p. 649-655.

91. Napoleon, R.L. and P.B. Moore, *Structural characterization of interfacial n-octanol and 3-octanol using molecular dynamic simulations.* Journal of Physical Chemistry B, 2006. 110(8): p. 3666-3673.

92. Kamath, G., et al., *Computational prediction of ionic liquid 1-octanol/water partition coefficients.* Physical Chemistry Chemical Physics, 2012. 14(13): p. 4339-4342.

93. H. Zhao, et al., *Regenerating cellulose from ionic liquids for an accelerated enzymatic hydrolysis.* J. of Biotechnol., 2009. 139: p. 47-54.

94. X. Wang, et al., *Direct exfoliation of natural graphite into micrometre size few layers graphene sheets using ionic liquids* Chem. Commun., 2010. 46: p. 4487-4489.

95. Bates, E.D., et al., *CO2 Capture by a Task-Specific Ionic Liquid.* JACS Commun., 2001. 124(6): p. 926-927.

96. M. M. Shaijumon, et al., *Flexible energy storage devices based on nanocomposite paper.* Proc. Natl. Acad. Sci. , 2007. 104: p. 13574-13577.

97. Kragl, U., M. Eckstein, and N. Kaftzik, *Enzyme catalysis in ionic liquids.* Curr. Opin. Biotechnol., 2002. 13: p. 565-571.

98. Ropel, L., et al., *Octanol–water partition coefficients of imidazolium-based ionic liquids.* Green Chem., 2005. 7: p. 83-90.

99. Abraham, M.H., et al., *Some Novel Liquid Partitioning Systems: Water−Ionic Liquids and Aqueous Biphasic Systems.* Ind. Eng. Chem. Res, 2003. 42: p. 413-418.

100. Cho, C.-W., et al., *Ionic Liquids: Predicitions of Physicochemical Properties with Experimental and/or DFT-Calculated LFER Parameters To Understand Molecular Interactions in Solution.* J. Phys. Chem. B, 2011. 115: p. 6040-6050.

101. Merz, K.M., S.A. Best, and C.H. Reynolds, *Free energy perturbation study of octanol/water partition coefficients: Comparison with continuum GB/SA calculations.* J. Phys. Chem. B, 1999. 103(4): p. 714-726.

102. Jorgensen, W.L., J.M. Briggs, and M.L. Contreras, *Relative Partition-Coefficients for Organic Solutes from Fluid Simulations.* J. Phys. Chem., 1990. 94(4): p. 1683-1686.

103. Darve, E. and A. Pohorille, *Calculating free energies using average force.* J. Chem. Phys., 2001. 115(20): p. 9169-9183.

104. Darve, E., M.A. Wilson, and A. Pohorille, *Calculating free energies using a scaled-force molecular dynamics algorithm.* Mol. Sim., 2002. 28(1-2): p. 113-144.

105. Darve, E., David Rodríguez-Gómez, and A. Pohorille, *Adaptive biasing force method for scalar and vector free energy calculations* Journal of Chemical Physics, 2008. 128: p. 144120.

106. N. Bhatnagar, et al., *Direct Calculation of Octanol–Water Partition Coefficients from Adaptive Bias Force Molecular Dynamics Simulations.* J. Chem. Phys. , 2011. submitted.

107. Lopes, J., J. Deschamps, and A. Padua, *Modeling ionic liquids using a systematic all-atom force field* J. Phys. Chem. B, 2004. 108: p. 2038-2047.

108. Chen, B., J.J. Potoff, and J.I. Siepmann, J. Phys. Chem. B 2001. 105: p. 3093.

109. Berendsen, H.J.C., J.R. Grigera, and T.P. Straatsma, *The Missing Term in Effective Pair Potentials.* J. Phys. Chem., 1987. 91: p. 6269-6271.

110. J. Henin, et al., *Exploring Multidimensional Free Energy Landscapes Using Time-Dependent Biases on Collective Variables.* J. Chem. Theo.Comput., 2010. 6: p. 35-47.

111. Phillips, J.C., et al., *Scalable molecular dynamics with NAMD.* J. Comp. Chem., 2005. 26: p. 1781-1802.

112. H. Zhao, et al., *Effect of ionic liquid properties on lipase stabilization under microwave irradiation.* J. Mol. Catal., 2009. 57: p. 149-157.

113. Kaar, J.L., et al., J. Am. Chem. Soc., 2003. 125: p. 4125-4131.

114. Chen, B. and J.I. Siepmann, *Partitioning of alkane and alcohol solutes between water and (Dry or wet) 1-Octanol.* J. Am. Chem. Soc., 2000. 122(27): p. 6464-6467.

115. Sangster, J., *Octanol-Water Partitioning Coefficients: Fundamentals and Physical Chemistry;* 1997, U.K.: John Wiley & Sons.

116. Sangster, J., *Octanol-Water Partition Coefficients: Fundamentals and Physical Chemistry. Vol. 2 of Wiley Series in Solution Chemistry*1997: John Wiley & Sons Ltd.

117. Leggett, D.C., *Vapor pressure of 2,4,6-trinitrotoluene by a gas chromatographic headspace technique.* Journal of Chromatography A, 1977. 133(1): p. 83-90.

118. Pella, P.A., *Measurement of the vapor pressures of image, 2,4-image, 2,6-image, and image.* The Journal of Chemical Thermodynamics, 1977. 9(4): p. 301-305.

119. Dionne, B.C., et al., *Vapor pressure of explosives.* Journal of Energetic Materials, 1986. 4: p. 447-472.

120. Cundall, R.B., T.F. Palmer, and C.E.C. Wood, *Vapor pressure measurements of some organic high explosives.* J. Chem. Soc., Faraday Trans., 1978. 71(1): p. 1339-1345.

121. Lenchitz, C. and R.W. Velicky, *Vapor Pressure and Heat of Sublimation of 3 Nitrotoluenes*. Journal of Chemical and Engineering Data, 1970. 15(3): p. 401-&.

122. Ro, K.S., et al., *Solubility of 2,4,6-trinitrotoluene (TNT) in water*. Journal of Chemical and Engineering Data, 1996. 41(4): p. 758-761.

123. Boddu, V.M., et al., *Thermophysical properties of an insensitive munitions compound, 2,4-dinitroanisole*. Journal of Chemical and Engineering Data, 2008. 53(5): p. 1120-1125.

124. Boddu, V.M., et al., *Physicochemical properties of an insensitive munitions compound, N-methyl-4-nitroaniline (MNA)*. Journal of Hazardous Materials, 2008. 155(1-2): p. 288-294.

125. Beck, B., A. Breindl, and T. Clark, *QM/NN QSPR models with error estimation: vapor pressure and logP*. J Chem Inf Comput Sci, 2000. 40(4): p. 1046-51.

126. Duchowicz, P.R., et al., *QSPR modeling the aqueous solubility of alcohols by optimization of correlation weights of local graph invariants*. Mol Divers, 2004. 8(4): p. 325-30.

127. Dyekjaer, J., K. Rasmussen, and S. Jonsdottir, *QSPR models based on molecular mechanics and quantum chemical calculations. 1. Construction of Boltzmann-averaged descriptors for alkanes, alcohols, diols, ethers and cyclic compounds.* Journal of Molecular Modeling, 2002. 8(9): p. 277-89.

128. Eros, D., et al., *Comparison of predictive ability of water solubility QSPR models generated by MLR, PLS and ANN methods.* Mini Rev Med Chem, 2004. 4(2): p. 167-77.

129. Hilal, S.H. and S.W. Karickhoff, *Prediction of Chemical Reactivity Parameters and Physical Properties of Organic Compounds from Molecular Structure using SPARC (EPA/600/R-03/030 March 2003)*, 2003, National Exposure Research Laboratory, Office of Research and Development, US Environmental Protection Agency: Research Triangle Park.

130. Hilal, S.H., L.A. Carreira, and S.W. Karickhoff, *Sparc - a Computer-Program for Estimation of Physicochemical Properties.* Abstracts of Papers of the American Chemical Society, 1994. 208: p. 189-COMP.

131. Hughes, L.D., et al., *Why are some properties more difficult to predict than others? A study of QSPR models of solubility, melting point, and Log P.* J Chem Inf Model, 2008. 48(1): p. 220-32.

132. Garrido, N.M., et al., *Prediction of the n-hexane/water and 1-octanol/water partition coefficients for environmentally relevant compounds using molecular simulation.* Aiche Journal, 2012. 58(6): p. 1929-1938.

133. Garrido, N.M., et al., *Using molecular simulation to predict solute solvation and partition coefficients in solvents of different polarity.* Physical Chemistry Chemical Physics, 2011. 13(20): p. 9155-9164.

134. Garrido, N.M., et al., *Predicting hydration Gibbs energies of alkyl-aromatics using molecular simulation: a comparison of current force fields and the development of a new parameter set for accurate solvation data.* Physical Chemistry Chemical Physics, 2011. 13(38): p. 17384-17394.

135. Ahmed, A. and S.I. Sandler, *Solvation free energies and hydration structure of N-methyl-p-nitroaniline.* Journal of Chemical Physics, 2012. 136(15).

136. Bhatnagar, N., et al., *Direct calculation of 1-octanol-water partition coefficients from adaptive biasing force molecular dynamics simulations.* Journal of Chemical Physics, 2012. 137(1).

137. Jorgensen, W.L., J.P. Ulmschneider, and J. Tirado-Rives, *Free energies of hydration from a generalized Born model and an ALL-atom force field.* Journal of Physical Chemistry B, 2004. 108(41): p. 16264-16270.

138. Udier-Blagovic, M., et al., *Accuracy of free energies of hydration using CM1 and CM3 atomic charges.* Journal of Computational Chemistry, 2004. 25(11): p. 1322-1332.

139. Wick, C.D., M.G. Martin, and J.I. Siepmann, *Transferable potentials for phase equilibria. 4. United-atom description of linear and branched alkenes and alkylbenzenes.* Journal of Physical Chemistry B, 2000. 104(33): p. 8008-8016.

140. Wick, C.D., et al., *Transferable potentials for phase equilibria. 7. Primary, secondary, and tertiary amines, nitroalkanes and nitrobenzene, nitriles, amides, pyridine, and pyrimidine.* Journal of Physical Chemistry B, 2005. 109(40): p. 18974-18982.

141. Stubbs, J.M., J.J. Potoff, and J.I. Siepmann, *Transferable potentials for phase equilibria. 6. United-atom description for ethers, glycols, ketones, and aldehydes.* Journal of Physical Chemistry B, 2004. 108(45): p. 17596-17605.

142. Frisch, M.J., et al., *Gaussian 09, Revision A.02*, 2009, Gaussian Inc: Wallingford, CT.

143. Price, D.J. and C.L. Brooks, *Detailed considerations for a balanced and broadly applicable force field: A study of substituted benzenes modeled with OPLS-AA.* Journal of Computational Chemistry, 2005. 26(14): p. 1529-1541.

144. Pietro, W.J., et al., *Self-Consistent Molecular-Orbital Methods .24. Supplemented Small Split-Valence Basis-Sets for 2nd-Row Elements.* Journal of the American Chemical Society, 1982. 104(19): p. 5039-5048.

145. Francl, M.M., et al., *Self-Consistent Molecular-Orbital Methods .23. A Polarization-Type Basis Set for 2nd-Row Elements.* Journal of Chemical Physics, 1982. 77(7): p. 3654-3665.

146. Rodriguez-Gomez, D., E. Darve, and A. Pohorille, *Assessing the efficiency of free energy calculation methods.* Journal of Chemical Physics, 2004. 120(8): p. 3563-3578.

147. Henin, J., et al., *Exploring Multidimensional Free Energy Landscapes Using Time-Dependent Biases on Collective Variables.* Journal of Chemical Theory and Computation, 2010. 6(1): p. 35-47.

148. Leggett, D.C., P.H. Miyares, and T.F. Jenkins, *Apparent Donor-Acceptor Interaction between Nitroaromatics and Acetonitrile.* Journal of Solution Chemistry, 1992. 21(1): p. 105-108.

149. Zhao, Y.H., et al., *Quantitative structure-activity relationships of nitroaromatic compounds to four aquatic organisms.* Chemosphere, 1997. 34(8): p. 1837-1844.

150. Altschuh, J., et al., *Henry's law constants for a diverse set of organic chemicals: Experimental determination and comparison of estimation methods.* Chemosphere, 1999. 39(11): p. 1871-1887.

151. Humphrey, W., A. Dalke, and K. Schulten, *VMD: Visual molecular dynamics.* Journal of Molecular Graphics, 1996. 14(1): p. 33-&.

152. Toghiani, R.K., et al., *Prediction of physicochemical properties of energetic materials.* Fluid Phase Equilibria, 2008. 264(1-2): p. 86-92.

153. Szinicz, L., *History of chemical and biological warfare agents.* Toxicology, 2005. 214(3): p. 167-181.

154. Langford, R.E., *Introduction to Weapons of Mass Destruction*2004, Hoboken, NJ: John Wiley & Sons Inc. 394.

155. Bai, J.H. and E.R. Chapman, *The C2 domains of synaptotagmin - partners in exocytosis.* Trends in Biochemical Sciences, 2004. 29(3): p. 143-151.

156. Tomchenko, A.A., G.P. Harmer, and B.T. Marquis, *Detection of chemical warfare agents using nanostructured metal oxide sensors.* Sensors and Actuators B-Chemical, 2005. 108(1-2): p. 41-55.

157. Brunol, E., et al., *Detection of dimethyl methylphosphonate (DMMP) by tin dioxide-based gas sensor: Response curve and understanding of the reactional mechanism.* Sensors and Actuators B-Chemical, 2006. 120(1): p. 35-41.

158. Kanan, S.M. and C.P. Tripp, *An infrared study of adsorbed organophosphonates on silica: A prefiltering strategy for the detection of nerve agents on metal oxide sensors.* Langmuir, 2001. 17(7): p. 2213-2218.

159. Kanan, S.M. and C.P. Tripp, *Prefiltering strategies for metal oxide based sensors: The use of chemical displacers to selectively cleave adsorbed organophosphonates from silica surfaces.* Abstracts of Papers of the American Chemical Society, 2002. 223: p. A84-A84.

160. Periasamy, A.P., Y. Umasankar, and S.-M. Chen, *Nanomaterials - Acetylcholinesterase Enzyme Matrices for Organophosphorus Pesticides Electrochemical Sensors: A Review.* Sensors, 2009. 9: p. 4034-4055.

161. Kong, L., et al., *Novel pyrenehexafluoroisopropanol derivative-decorated single-walled carbon nanotubes for detection of nerve agents by strong hydrogen-bonding interaction.* Analyst, 2010. 135: p. 368-374.

162. Gordon, W.O., B.M. Tissue, and J.R. Morris, *Adsorption and Decomposition of Dimethyl Methylphosphonate on Y2O3 Nanoparticles.* J. Phys. Chem. C, 2007. 111: p. 3233-3240.

163. Kim, K., et al., *Destruction and Detection of Chemical Warfare Agents.* Chem. Rev., 2011. 111: p. 5345-5403.

164. Potyrailo, R.A., et al., *Materials and Transducers Toward Selective Wireless Gas Sensing.* Chem. Rev., 2011. ASAP.

165. Lee, J.S., et al., *Fabrication of Ultrafine Metal-Oxide-Decorated Carbon Nanofibers for DMMP Sensor Application.* ACS Nano, 2011. ASAP.

166. Li, X. and P.K. Dutta, *Interaction of Dimethylmethylphosphonate with Zeolite Y: Impedance-Based Sensor for Detecting Nerve Agent Simulants.* J. Phys. Chem. C, 2010. 114: p. 7986–7994.

167. Choi, B.G., et al., *Solution Chemistry of Self-Assembled Graphene Nanohybrids for High-Performance Flexible Biosensors.* ACS Nano, 2010. 4: p. 2910–2918.

168. Wanekaya, A.K., W. ChenA, and A. Mulchandani, *Recent biosensing developments in environmental security*. J. Environ. Monit., 2008. 10: p. 703-712.

169. Wolfbeis, O.S., *Fiber-Optic Chemical Sensors and Biosensors.* Anal. Chem., 2006. 78: p. 3859-3874.

170. George, L., K.S. Viswanathan, and S. Singh, *Ab initio study of trimethyl phosphate: Conformational analysis, dipole moments, vibrational frequencies, and barriers for conformer interconversion.* Journal of Physical Chemistry A, 1997. 101(13): p. 2459-2464.

171. Ault, B.S., et al., *Matrix isolation infrared spectroscopic and theoretical study of the interaction of water with dimethyl methylphosphonate.* Journal of Physical Chemistry A, 2004. 108(46): p. 10094-10098.

172. Cuisset, A., et al., *Gas-phase vibrational spectroscopy and ab initio study of organophosphorous compounds: Discrimination between species and conformers.* Journal of Physical Chemistry B, 2008. 112(39): p. 12516-12525.

173. Suenram, R.D., et al., *Fourier transform microwave spectrum and ab initio study of dimethyl methylphosphonate.* Journal of Molecular Spectroscopy, 2002. 211(1): p. 110-118.

174. Kaczmarek, A., et al., *Sarin and soman: Structure and properties.* Structural Chemistry, 2004. 15(5): p. 517-525.

175. Paukku, Y., et al., *Investigation on the low energy conformational surface of tabun to probe the role of its different conformers on biological activity.* Chemical Physics Letters, 2006. 422(4-6): p. 317-322.

176. Michalkova, A., et al., *Theoretical study of the adsorption and decomposition of sarin on magnesium oxide.* Journal of Physical Chemistry B, 2004. 108(17): p. 5294-5303.

177. Michalkova, A., et al., *Theoretical study of adsorption of tabun on calcium oxide clusters.* Chemical Physics Letters, 2007. 438(1-3): p. 72-77.

178. Bermudez, V.M., *Computational Study of Environmental Effects in the Adsorption of DMMP, Sarin, and VX on gamma-Al2O3: Photolysis and Surface Hydroxylation.* Journal of Physical Chemistry C, 2009. 113(5): p. 1917-1930.

179. Michalkova, A., et al., *Theoretical study of adsorption of Sarin and Soman on tetrahedral edge clay mineral fragments.* Journal of Physical Chemistry B, 2006. 110(42): p. 21175-21183.

180. Vishnyakov, A. and A.V. Neimark, *Molecular model of dimethylmethylphosphonate and its interactions with water.* Journal of Physical Chemistry A, 2004. 108(8): p. 1435-1439.

181. Sokkalingam, N., et al., *Extension of the transferable potentials for phase equilibria force field to dimethylmethyl phosphonate, sarin, and soman.* J Phys Chem B, 2009. 113(30): p. 10292-7.

182. Vishnyakov, A., et al., *Molecular Modeling of Organophosphorous Agents and their Aqueous Solutions.* J. Phys. Chem. A, 2011. 115: p. 5201-5209.

183. Vishnyakov, A., et al., *Molecular Modeling of Organophosphorous Agents and Their Aqueous Solutions.* Journal of Physical Chemistry A, 2011. 115(20): p. 5201-5209.

184. Vishnyakov, A. and A.V. Neimark, *Molecular Dynamics Simulation of Nanoscale Distribution and Mobility of Water and Dimethylmethylphosphonate in Sulfonated Polystyrene.* Journal of Physical Chemistry B, 2008. 112(47): p. 14905-14910.

185. Vishnyakov, A. and A.V. Neimark, *Specifics of solvation of sulfonated polyelectrolytes in water, dimethylmethylphosphonate, and their mixture: A molecular simulation study.* Journal of Chemical Physics, 2008. 128(16).

186. Steven E. Czerwinski, et al., J. Biochem. Mol. Toxicology, 2006. 20: p. 5.

187. Berendsen, H.J.C., J.R. Grigera, and T.P. Straatsma., *The Missing Term in Effective Pair Potentials.* J. Phys. Chem., 1987. 91: p. 6269-6271.

188. Sokkalingam, N., et al., *Extension of the Transferable Potentials for Phase Equilibria Force Field to Dimethymethyl Phosphonate, Sarin and Soman.* J. Phys. Chem. B, 2009. 113: p. 10292.

189. Wick, C.D., et al., *Transferable potentials for phase equilibria. 7. United-atom description for nitrogen, amines, amides, nitriles, pyridine and pyrimidine.* J. Phys. Chem. B, 2005. 109: p. 18974-18982.

190. Lubna, N., et al., *Transferable potentials for phase equilibria. 8. United-atom description for thiols, sulfides, disulfides, and thiophene.* J. Phys. Chem. B, 2005. 109: p. 24100-24107.

191. Gaussian 09, R.A., M. J. Frisch, G. W. Trucks, H. B. Schlegel, G. E. Scuseria, M. A. Robb, J. R. Cheeseman, G. Scalmani, V. Barone, B. Mennucci, G. A. Petersson, H. Nakatsuji, M. Caricato, X. Li, H. P. Hratchian, A. F. Izmaylov, J. Bloino, G. Zheng, J. L. Sonnenberg, M. Hada, M. Ehara, K. Toyota, R. Fukuda, J. Hasegawa, M. Ishida, T. Nakajima, Y. Honda, O. Kitao, H. Nakai, T. Vreven, J. A. Montgomery, Jr., J. E. Peralta, F. Ogliaro, M. Bearpark, J. J. Heyd, E. Brothers, K. N. Kudin, V. N. Staroverov, R. Kobayashi, J. Normand, K. Raghavachari, A. Rendell, J. C. Burant, S. S. Iyengar, J. Tomasi, M. Cossi, N. Rega, J. M. Millam, M. Klene, J. E. Knox, J. B. Cross, V. Bakken, C. Adamo, J. Jaramillo, R. Gomperts, R. E. Stratmann, O. Yazyev, A. J. Austin, R. Cammi, C. Pomelli, J. W. Ochterski, R. L. Martin, K. Morokuma, V. G. Zakrzewski, G. A. Voth, P. Salvador, J. J. Dannenberg, S. Dapprich, A. D. Daniels, Ö. Farkas, J. B. Foresman, J. V. Ortiz, J. Cioslowski, and D. J. Fox., *Gaussian, Inc., Wallingford CT, 2009.*, 2009.

192. Berthelot, M. and E. Jungfleish, Ann. Chim. Phys. (4th Ser.), 1872. 26: p. 11.

193. Rodriguez-Gomeza, D., E. Darveb, and A. Pohorille, *Assessing the efficiency of free energy calculation methods.* Journal of Chemical Physics, 2004. 120: p. 3563.

194. Bartelt-Hunt, K. S.L., and M.A. Barlaz, *A review of chemical warfare agent simulants for the study of environmental behavior.* Critical Reviews in Environmental Science and Technology, 2008. 38: p. 112-136.

195. EPA.gov, *Revised HPV Robust Summaries for Dimethylmethylphosphonate 201-16026* August 2005: Ardsley, NY, 10502.

196. Singer, B.C., et al., *Indoor Sorption of Surrogates for Sarin and Related Nerve Agents.* Environmental Science & Technology, 2005. 39: p. 3203-3214.

197. Preston, J.M. and V. Starrock, *Partial Vapor Pressures and Activify Coefficients of GB and GD in Aqueous Solution, Report 893, Chemical Defence Section, Protective Sciences Division, Defence Research Establishment.*, 1983: Ottawa, Canada, September. AD-A140644.

198. Lundblad, R.L. and F.M. MacDonald, in *Handbook of Biochemistry and Molecular Biology*2010, CRC Press. p. 747-750.

199. Britton, K.B. and C.L. Grant, *Prediction of Octanol- Water Partition Coefficients of Organophosphonates. Evaluation of Structure-Function Relationships*, 1988, Special Report 88-1 1, U.S. Army Corps of Engineers Cold Regions Research & Engineering Laboratory, Hanover, NH.

200. Gupta, R.C., in *Handbook of Toxicology of Chemical Warfare Agents*2009, Elsevier: Oxford, UK.

201. D.H. Rosenblatt, et al., *Background Chemistry for Chemical Warfare Agents and Decontamination Processes in Support of Delisting Waste Streams at the US. Army 'Dugway Proving Ground, Utah, Environemtal Assessment Division Argonne National Laboratory*, 1996.

202. Sage, G.W. and P.H. Howard, *Environmental Fate Assessments of Chemical Agents HD and VX, CRDEC-CR-034, prepared by Syracuse Research Corporation, Syracuse, NY, for the Chemical Research, Development and Engineering Center, Aberdeen Proving Ground, MD, June. AD-B135352.*, 1989.

203. Bizzigotti, G.O., et al., *Parameters for Evaluation of the Fate, Transport and Environmental Impacts of Chemical Agents in Marine Environments.* Chem. Rev., 2009. 109: p. 236-256.

204. Ault, B.S., et al., J. Phys. Chem. A, 2004. 108: p. 10094.

205. Vishnyakov, A. and A.V. Neimark, J. Phys. Chem. A, 2004. 108: p. 1435.

206. Eaton, G., et al., J. Chem. Soc. Faraday Trans., 1992. 88: p. 3527.

207. Bhatnagar, N., et al., *Direct Calculation of Octanol-Water Partition Coefficients from Adaptive Force Bias Molecular Dynamics Simulations.* J. Chem. Phys., 2011. submitted.

208. Kamath, G., et al., Phys. Chem. Chem. Phys., 2012.

209. Gillett, J.W., *A comprehensive Prebiological Screen for Ecotoxicologic Effects.* Environmental Toxicology and Chemistry, 1983. 2: p. 463-476.

210. Jorgensen, W.L., D.S. Maxwell, and J. TiradoRives, *Development and testing of the OPLS all-atom force field on conformational energetics and properties of organic liquids.* Journal of the American Chemical Society, 1996. 118(45): p. 11225-11236.

211. Cornell, W.D., et al., *A 2nd Generation Force-Field for the Simulation of Proteins, Nucleic-Acids, and Organic-Molecules.* Journal of the American Chemical Society, 1995. 117(19): p. 5179-5197.

212. MacKerell, A.D., et al., *All-atom empirical potential for molecular modeling and dynamics studies of proteins.* Journal of Physical Chemistry B, 1998. 102(18): p. 3586-3616.

213. Oostenbrink, C., et al., *A biomolecular force field based on the free enthalpy of hydration and solvation: The GROMOS force-field parameter sets 53A5 and 53A6.* Journal of Computational Chemistry, 2004. 25(13): p. 1656-1676.

214. Halgren, T.A., *Merck Molecular Force Field. II. MMFF94 van der Waals and Electrostatic Parameters for Intermolecular Interactions.* J. Comput. Chem., 1995. 17: p. 520-552.

215. Yin, D.X. and A.D. Mackerell, *Combined ab initio empirical approach for optimization of Lennard-Jones parameters.* Journal of Computational Chemistry, 1998. 19(3): p. 334-348.

216. Chen, I.J., D.X. Yin, and A.D. MacKerell, *Combined ab initio/empirical approach for optimization of Lennard-Jones parameters for polar-neutral compounds.* Journal of Computational Chemistry, 2002. 23(2): p. 199-213.

217. Xu, Z.T., H.H. Luo, and D.P. Tieleman, *Modifying the OPLS-AA force field to improve hydration free energies for several amino acid side chains using new atomic charges and an off-plane charge model for aromatic residues.* Journal of Computational Chemistry, 2007. 28(3): p. 689-697.

218. Nath, S.K., F.A. Escobedo, and J.J. de Pablo, *On the simulation of vapor-liquid equilibria for alkanes.* Journal of Chemical Physics, 1998. 108(23): p. 9905-9911.

219. Errington, J.R. and A.Z. Panagiotopoulos, *A new intermolecular potential model for the n-alkane homologous series.* Journal of Physical Chemistry B, 1999. 103(30): p. 6314-6322.

220. Ungerer, P., et al., *Optimization of the anisotropic united atoms intermolecular potential for n-alkanes.* Journal of Chemical Physics, 2000. 112(12): p. 5499-5510.

221. Potoff, J.J. and D.A. Bernard-Brunel, *Mie Potentials for Phase Equilibria Calculations: Application to Alkanes and Perfluoroalkanes.* Journal of Physical Chemistry B, 2009. 113(44): p. 14725-14731.

222. Kamath, G., N. Lubna, and J.J. Potoff, *Effect of partial charge parametrization on the fluid phase behavior of hydrogen sulfide.* Journal of Chemical Physics, 2005. 123(12).

223. Ketko, M.H., G. Kamath, and J.J. Potoff, *Development of an Optimized Intermolecular Potential for Sulfur Dioxide.* Journal of Physical Chemistry B, 2011. 115(17): p. 4949-4954.

224. Potoff, J.J. and J.I. Siepmann, *Vapor-liquid equilibria of mixtures containing alkanes, carbon dioxide, and nitrogen.* Aiche Journal, 2001. 47(7): p. 1676-1682.

225. Kamath, G., G. Georgiev, and J.J. Potoff, *Molecular modeling of phase behavior and microstructure of acetone-chloroform-methanol binary mixtures.* Journal of Physical Chemistry B, 2005. 109(41): p. 19463-19473.

226. Wang, J.M., et al., *Development and testing of a general amber force field.* Journal of Computational Chemistry, 2004. 25(9): p. 1157-1174.

227. Vanommeslaeghe, K., et al., *CHARMM General Force Field: A Force Field for Drug-Like Molecules Compatible with the CHARMM All-Atom Additive Biological Force Fields.* Journal of Computational Chemistry, 2010. 31(4): p. 671-690.

228. Berger, O., O. Edholm, and F. Jahnig, *Molecular dynamics simulations of a fluid bilayer of dipalmitoylphosphatidylcholine at full hydration, constant pressure, and constant temperature.* Biophysical Journal, 1997. 72(5): p. 2002-2013.

229. Chiu, S.W., et al., *Incorporation of Surface-Tension into Molecular-Dynamics Simulation of an Interface - a Fluid-Phase Lipid Bilayer-Membrane.* Biophysical Journal, 1995. 69(4): p. 1230-1245.

230. Chiu, S.W., et al., *An Improved United Atom Force Field for Simulation of Mixed Lipid Bilayers.* Journal of Physical Chemistry B, 2009. 113(9): p. 2748-2763.

231. Poger, D., W.F. Van Gunsteren, and A.E. Mark, *A New Force Field for Simulating Phosphatidylcholine Bilayers.* Journal of Computational Chemistry, 2010. 31(6): p. 1117-1125.

232. Kukol, A., *Lipid Models for United-Atom Molecular Dynamics Simulations of Proteins.* Journal of Chemical Theory and Computation, 2009. 5(3): p. 615-626.

233. Zhao, W., et al., *Atomic-scale structure and electrostatics of anionic palmitoyloleoylphosphatidylglycerol lipid bilayers with Na+ counterions.* Biophysical Journal, 2007. 92(4): p. 1114-1124.

234. Cieplak, P., et al., *Application of the Multimolecule and Multiconformational Resp Methodology to Biopolymers - Charge Derivation for DNA, Rna, and Proteins.* Journal of Computational Chemistry, 1995. 16(11): p. 1357-1377.

235. Jojart, B. and T.A. Martinek, *Performance of the general amber force field in modeling aqueous POPC membrane bilayers.* Journal of Computational Chemistry, 2007. 28(12): p. 2051-2058.

236. Skjevik, A.A., et al., *LIPID11: A Modular Framework for Lipid Simulations Using Amber.* Journal of Physical Chemistry B, 2012. 116(36): p. 11124-11136.

237. Dickson, C.J., et al., *GAFFlipid: a General Amber Force Field for the accurate molecular dynamics simulation of phospholipid.* Soft Matter, 2012. 8(37): p. 9617-9627.

238. Feller, S.E., R.M. Venable, and R.W. Pastor, *Computer simulation of a DPPC phospholipid bilayer: Structural changes as a function of molecular surface area.* Langmuir, 1997. 13(24): p. 6555-6561.

239. Husslein, T., et al., *Constant pressure and temperature molecular-dynamics simulation of the hydrated diphytanolphosphatidylcholine lipid bilayer.* Journal of Chemical Physics, 1998. 109(7): p. 2826-2832.

240. Klauda, J.B., et al., *Update of the CHARMM All-Atom Additive Force Field for Lipids: Validation on Six Lipid Types.* Journal of Physical Chemistry B, 2010. 114(23): p. 7830-7843.

241. Feller, S.E. and R.W. Pastor, *Constant surface tension simulations of lipid bilayers: The sensitivity of surface areas and compressibilities.* Journal of Chemical Physics, 1999. 111(3): p. 1281-1287.

242. Feller, S.E. and A.D. MacKerell, *An improved empirical potential energy function for molecular simulations of phospholipids.* Journal of Physical Chemistry B, 2000. 104(31): p. 7510-7515.

243. Jensen, M.O., O.G. Mouritsen, and G.H. Peters, *Simulations of a membrane-anchored peptide: Structure, dynamics, and influence on bilayer properties.* Biophysical Journal, 2004. 86(6): p. 3556-3575.

244. Sonne, J., et al., *Reparameterization of all-atom dipalmitoylphosphatidylcholine lipid parameters enables simulation of fluid bilayers at zero tension.* Biophysical Journal, 2007. 92(12): p. 4157-4167.

245. Jambeck, J.P.M. and A.P. Lyubartsev, *Derivation and Systematic Validation of a Refined All-Atom Force Field for Phosphatidylcholine Lipids.* Journal of Physical Chemistry B, 2012. 116(10): p. 3164-3179.

246. Jambeck, J.P.M. and A.P. Lyubartsev, *An Extension and Further Validation of an All-Atomistic Force Field for Biological Membranes.* Journal of Chemical Theory and Computation, 2012. 8(8): p. 2938-2948.

247. Lubna, N., et al., *Transferable potentials for phase equilibria. 8. United-atom description for thiols, sulfides, disulfides, and thiophene.* Journal of Physical Chemistry B, 2005. 109(50): p. 24100-24107.

248. Martin, M.G. and J.I. Siepmann, *Novel configurational-bias Monte Carlo method for branched molecules. Transferable potentials for phase equilibria. 2. United-atom description of branched alkanes.* Journal of Physical Chemistry B, 1999. 103(21): p. 4508-4517.

249. Sokkalingam, N., et al., *Extension of the Transferable Potentials for Phase Equilibria Force Field to Dimethylmethyl Phosphonate, Sarin, and Soman.* Journal of Physical Chemistry B, 2009. 113(30): p. 10292-10297.

250. Rai, N. and J.I. Siepmann, *Transferable potentials for phase equilibria. 9. explicit hydrogen description of benzene and five-membered and six-membered heterocyclic aromatic compounds.* Journal of Physical Chemistry B, 2007. 111(36): p. 10790-10799.

251. Taylor, J., et al., *Validation of all-atom phosphatidylcholine lipid force fields in the tensionless NPT ensemble.* Biochimica Et Biophysica Acta-Biomembranes, 2009. 1788(3): p. 638-649.

252. Cordomi, A., O. Edholm, and J.J. Perez, *Effect of Force Field Parameters on Sodium and Potassium Ion Binding to Dipalmitoyl Phosphatidylcholine Bilayers.* Journal of Chemical Theory and Computation, 2009. 5(8): p. 2125-2134.

253. Bockmann, R.A., et al., *Effect of sodium chloride on a lipid bilayer.* Biophysical Journal, 2003. 85(3): p. 1647-1655.

254. Gurtovenko, A.A. and I. Vattulainen, *Effect of NaCl and KCl on phosphatidylcholine and phosphatidylethanolamine lipid membranes: Insight from atomic-scale simulations for understanding salt-induced effects in the plasma membrane.* Journal of Physical Chemistry B, 2008. 112(7): p. 1953-1962.

255. Anezo, C., et al., *Methodological issues in lipid bilayer simulations.* Journal of Physical Chemistry B, 2003. 107(35): p. 9424-9433.

256. Nagle, J.F. and S. Tristram-Nagle, *Structure of lipid bilayers.* Biochimica Et Biophysica Acta-Reviews on Biomembranes, 2000. 1469(3): p. 159-195.

257. Costigan, S.C., P.J. Booth, and R.H. Templer, *Estimations of lipid bilayer geometry in fluid lamellar phases.* Biochimica Et Biophysica Acta-Biomembranes, 2000. 1468(1-2): p. 41-54.

258. Petrache, H.I., et al., *Structure and fluctuations of charged phosphatidylserine bilayers in the absence of salt.* Biophysical Journal, 2004. 86(3): p. 1574-1586.

259. Poger, D. and A.E. Mark, *Lipid Bilayers: The Effect of Force Field on Ordering and Dynamics.* Journal of Chemical Theory and Computation, 2012. 8(11): p. 4807-4817.

260. Poger, D. and A.E. Mark, *On the Validation of Molecular Dynamics Simulations of Saturated and cis-Monounsaturated Phosphatidylcholine Lipid Bilayers: A Comparison with Experiment.* Journal of Chemical Theory and Computation, 2010. 6(1): p. 325-336.

261. Jambeck, J.P.M. and A.P. Lyubartsev, *Another Piece of the Membrane Puzzle: Extending Slipids Further.* Journal of Chemical Theory and Computation, 2013. 9(1): p. 774-784.

262. Pan, J.J., et al., *Molecular structures of fluid phase phosphatidylglycerol bilayers as determined by small angle neutron and X-ray scattering.* Biochimica Et Biophysica Acta-Biomembranes, 2012. 1818(9): p. 2135-2148.

263. Henin, J., W. Shinoda, and M.L. Klein, *Models for Phosphatidylglycerol Lipids Put to a Structural Test.* Journal of Physical Chemistry B, 2009. 113(19): p. 6958-6963.

264. Sun, W.J., et al., *Order and Disorder in Fully Hydrated Unoriented Bilayers of Gel Phase Dipalmitoylphosphatidylcholine.* Physical Review E, 1994. 49(5): p. 4665-4676.

265. Tristram-Nagle, S., et al., *Structure of gel phase DMPC determined by X-ray diffraction.* Biophysical Journal, 2002. 83(6): p. 3324-3335.

266. Kucerka, N., J. Katsaras, and J.F. Nagle, *Comparing Membrane Simulations to Scattering Experiments: Introducing the SIMtoEXP Software.* Journal of Membrane Biology, 2010. 235(1): p. 43-50.

267. Petrache, H.I., S.W. Dodd, and M.F. Brown, *Area per lipid and acyl length distributions in fluid phosphatidylcholines determined by H-2 NMR spectroscopy*. Biophysical Journal, 2000. 79(6): p. 3172-3192.

268. Seelig, A. and J. Seelig, *Dynamic Structure of Fatty Acyl Chains in a Phospholipid Bilayer Measured by Deuterium Magnetic-Resonance.* Biochemistry, 1974. 13(23): p. 4839-4845.

269. Kucerka, N., et al., *Lipid bilayer structure determined by the simultaneous analysis of neutron and x-ray scattering data.* Biophysical Journal, 2008. 95(5): p. 2356-2367.

270. Vermeer, L.S., et al., *Acyl chain order parameter profiles in phospholipid bilayers: computation from molecular dynamics simulations and comparison with H-2 NMR experiments.* European Biophysics Journal with Biophysics Letters, 2007. 36(8): p. 919-931.

271. Ulmschneider, J.P. and M.B. Ulmschneider, *United Atom Lipid Parameters for Combination with the Optimized Potentials for Liquid Simulations All-Atom Force Field.* Journal of Chemical Theory and Computation, 2009. 5(7): p. 1803-1813.

272. Perly, B., I.C.P. Smith, and H.C. Jarrell, *Effects of the Replacement of a Double-Bond by a Cyclopropane Ring in Phosphatidylethanolamines - a H-2 Nmr-Study of Phase-Transitions and Molecular-Organization.* Biochemistry, 1985. 24(4): p. 1055-1063.

273. Siu, S.W.I., et al., *Biomolecular simulations of membranes: Physical properties from different force fields.* Journal of Chemical Physics, 2008. 128(12).

274. Klauda, J.B., et al., *Simulation-based methods for interpreting X-ray data from lipid bilayers.* Biophysical Journal, 2006. 90(8): p. 2796-2807.

275. Benz, R.W., et al., *Experimental validation of molecular dynamics simulations of lipid bilayers: A new approach.* Biophysical Journal, 2005. 88(2): p. 805-817.

276. Kucerka, N., et al., *Structure of fully hydrated fluid phase DMPC and DLPC lipid bilayers using X-ray scattering from oriented multilamellar arrays and from unilamellar vesicles.* Biophysical Journal, 2005. 88(4): p. 2626-2637.

277. Sabatini, B.L. and W.G. Regehr, *Timing of neurotransmission at fast synapses in the mammalian brain.* Nature, 1996. 384(6605): p. 170-172.

278. Llinas, R., I.Z. Steinberg, and K. Walton, *Relationship between Presynaptic Calcium Current and Postsynaptic Potential in Squid Giant Synapse.* Biophysical Journal, 1981. 33(3): p. 323-351.

279. Heidelberger, R., et al., *Calcium-Dependence of the Rate of Exocytosis in a Synaptic Terminal.* Nature, 1994. 371(6497): p. 513-515.

280. Chapman, E.R., *How does synaptotagmin trigger neurotransmitter release?* Annual Review of Biochemistry, 2008. 77: p. 615-641.

281. Rizo, J., X.C. Chen, and D. Arac, *Unraveling the mechanisms of synaptotagmin and SNARE function in neurotransmitter release (vol 31, pg 339, 2006).* Trends in Cell Biology, 2006. 16(11): p. 549-550.

282. Jackson, M.B. and E.R. Chapman, *Fusion pores and fusion machines in Ca(2+)-triggered exocytosis.* Annual Review of Biophysics and Biomolecular Structure, 2006. 35: p. 135-160.

283. Jahn, R. and R.H. Scheller, *SNAREs - engines for membrane fusion.* Nature Reviews Molecular Cell Biology, 2006. 7(9): p. 631-643.

284. Perin, M.S., et al., *Phospholipid Binding by a Synaptic Vesicle Protein Homologous to the Regulatory Region of Protein Kinase-C.* Nature, 1990. 345(6272): p. 260-263.

285. Perin, M.S., et al., *Domain-Structure of Synaptotagmin (P65).* Journal of Biological Chemistry, 1991. 266(1): p. 623-629.

286. Sutton, R.B., et al., *Structure of the First C-2 Domain of Synaptotagmin .1. A Novel Ca2+/Phospholipid-Binding Fold.* Cell, 1995. 80(6): p. 929-938.

287. Shao, X.G., et al., *Solution structures of the Ca2+-free and Ca2+-bound C(2)A domain of synaptotagmin I: Does Ca2+ induce a conformational change?* Biochemistry, 1998. 37(46): p. 16106-16115.

288. Fernandez, I., et al., *Three-dimensional structure of the synaptotagmin 1 C2B-domain: Synaptotagmin 1 as a phospholipid binding machine.* Neuron, 2001. 32(6): p. 1057-1069.

289. Shao, X.G., et al., *Bipartite Ca2+-binding motif in C-2 domains of synaptotagmin and protein kinase C.* Science, 1996. 273(5272): p. 248-251.

290. Ubach, J., et al., *Ca2+ binding to synaptotagmin: how many Ca2+ ions bind to the tip of a C-2-domain?* Embo Journal, 1998. 17(14): p. 3921-3930.

291. Davis, A.F., et al., *Kinetics of synaptotagmin responses to Ca2+ and assembly with the core SNARE complex onto membranes.* Neuron, 1999. 24(2): p. 363-376.

292. Gerona, R.R.L., et al., *The C terminus of SNAP25 is essential for Ca2+-dependent binding of synaptotagmin to SNARE complexes.* Journal of Biological Chemistry, 2000. 275(9): p. 6328-6336.

293. Earles, C.A., et al., *The tandem C2 domains of synaptotagmin contain redundant Ca2+ binding sites that cooperate to engage t-SNAREs and trigger exocytosis.* Journal of Cell Biology, 2001. 154(6): p. 1117-1123.

294. Bai, J.H., et al., *Fusion pore dynamics are regulated by synaptotagmin center dot t-SNARE interactions.* Neuron, 2004. 41(6): p. 929-942.

295. Bhalla, A., et al., *Ca2+-synaptotagmin directly regulates t-SNARE function during reconstituted membrane fusion.* Nature Structural & Molecular Biology, 2006. 13(4): p. 323-330.

296. Bai, J.H., P. Wang, and E.R. Chapman, *C2A activates a cryptic Ca(2+)-triggered membrane penetration activity within the C2B domain of synaptotagmin I.* Proc Natl Acad Sci U S A, 2002. 99(3): p. 1665-1670.

297. Herrick, D.Z., et al., *Position of synaptotagmin I at the membrane interface: Cooperative interactions of tandem C2 domains.* Biochemistry, 2006. 45(32): p. 9668-9674.

298. Murray, D. and B. Honig, *Electrostatic control of the membrane targeting of C2 domains.* Molecular Cell, 2002. 9(1): p. 145-154.

299. Zhang, X.Y., J. Rizo, and T.C. Sudhof, *Mechanism of phospholipid binding by the C(2)A-domain of synaptotagmin I.* Biochemistry, 1998. 37(36): p. 12395-12403.

300. Martens, S., M.M. Kozlov, and H.T. McMahon, *How synaptotagmin promotes membrane fusion.* Science, 2007. 316(5828): p. 1205-1208.

301. Arac, D., et al., *Close membrane-membrane proximity induced by Ca2+-dependent multivalent binding of synaptotagmin-1 to phospholipids.* Nature Structural & Molecular Biology, 2006. 13(3): p. 209-217.

302. Stein, A., et al., *Synaptotagmin activates membrane fusion through a Ca2+-dependent trans interaction with phospholipids.* Nature Structural & Molecular Biology, 2007. 14(10): p. 904-911.

303. Baker, N.A., et al., *Electrostatics of nanosystems: Application to microtubules and the ribosome.* Proc Natl Acad Sci U S A, 2001. 98(18): p. 10037-10041.

304. Cuezzo, M.G. and I. Fernandez, *A new species of the land gastropod genus Solaropsis Beck, 1837 (Helicoidea : Camaenidae) from Bolivia.* Veliger, 2001. 44(3): p. 315-324.

305. Foloppe, N. and A.D. MacKerell, *All-atom empirical force field for nucleic acids: I. Parameter optimization based on small molecule and condensed phase macromolecular target data.* Journal of Computational Chemistry, 2000. 21(2): p. 86-104.

306. Martyna, G.J., D.J. Tobias, and M.L. Klein, *Constant-Pressure Molecular-Dynamics Algorithms.* Journal of Chemical Physics, 1994. 101(5): p. 4177-4189.

307. Darve, E., D. Rodriguez-Gomez, and A. Pohorille, *Adaptive biasing force method for scalar and vector free energy calculations.* Journal of Chemical Physics, 2008. 128(14).

308. Brose, N., et al., *Synaptotagmin - a Calcium Sensor on the Synaptic Vesicle Surface.* Science, 1992. 256(5059): p. 1021-1025.

309. Dolinsky, T.J., et al., *PDB2PQR: expanding and upgrading automated preparation of biomolecular structures for molecular simulations*. Nucleic Acids Research, 2007. 35: p. W522-W525.

310. Dolinsky, T.J., et al., *PDB2PQR: an automated pipeline for the setup of Poisson-Boltzmann electrostatics calculations*. Nucleic Acids Research, 2004. 32: p. W665-W667.

311. Cho, W.J., A. Jeremic, and B.P. Jena, *Size of supramolecular SNARE complex: Membrane-directed self-assembly*. Journal of the American Chemical Society, 2005. 127(29): p. 10156-10157.

ABSTRACT

HOW ATOMIC LEVEL INTERACTIONS DRIVE MEMBRANE FUSION: INSIGHTS FROM MOLECULAR DYNAMICS SIMULATIONS

by

NAVENDU BHATNAGAR

May 2013

Advisor: Dr. Jeffrey Potoff

Major: Chemical Engineering

Degree: Doctor of Philosophy

This project is focused on identifying the role of key players in the membrane fusion process at the atomic level with the use of molecular dynamics simulations. Membrane fusion of apposed bilayers is one of the most fundamental and frequently occurring biological phenomena in living organisms. It is an essential step in several cellular processes such as neuronal exocytosis, sperm fusion with oocytes and intracellular fusion of organelles to name a few. Membrane fusion is a frequent process in a living organism but is still not fully understood at the atomic level in terms of the role of various factors that play a crucial part in completion of membrane fusion. Two major factors that have been identified and studied experimentally are the protein Synaptotagmin and SNAREs. In addition, Ca^{2+} is known to play a crucial role in this process, however the exact mechanism of action is still unknown.

Prime objective of this study is to understand these interactions and the role of Ca2 + in the process at the atomic level by carrying out molecular dynamics simulations. One of the primary calculations to perform is potential of mean force (PMF) between SYT and bilayer to analyze the effect of Ca^{2+} on their relative affinities.

1–octanol–water partition coefficient (log K_{ow}) of a solute is a key parameter used in the prediction of a wide variety of complex phenomena such as drug availability and bioaccumulation potential of trace contaminants. Adaptive biasing force method is applied to calculate 1-octanol partition coefficients of n-alkanes and extended to other complex systems like ionic liquids, energetic materials and chemical warfare agents.

Molecular dynamics simulations show that both domains of SYT-1, C2A and C2B, once calcium bound, insert into the lipid bilayer composed of anionic phospholipids. In contrast, no insertion is observed when the domains do not have bound calcium or when the bilayer is not charged negative. Electrostatic interactions play an important role in this insertion process. Effect of calcium binding to the C2A and C2B domain on the overall electrostatics of the protein was studied by generating the ESP maps. Negative potential on the Calcium binding pocket transforms into positive potential once calcium is attached to those sites. Interaction of this positive potential surface with the negatively charged bilayer acts as a driving force for protein insertion into the bilayer.

In addition, adaptive biasing force method has emerged as a powerful tool for prediction of 1-octanol water partition coefficients and is successfully implemented and optimized for n-alkanes and extended to the systems of ionic liquids, energetic materials and chemical warfare agents for which 1-octanol water partition coefficient is either not known or is difficult to measure via experimental methods.

AUTOBIOGRAPHICAL STATMENT

Navendu Bhatnagar was born in Meerut, India on October 20, 1981 and spent his childhood in the city of industrial city of Kashipur located in the hilly regions of northern India. He attended and graduated from Maria Assumpta Convent High School in the year 1997. He attended Kurukshetra University from 1999 to 2003 and graduated with a Bachelors of Technology (B. Tech.) degree in chemical engineering.

The author later joined the leading multinational pharmaceutical manufacturing company, Ranbaxy Laboratories Limited as a Project Manager in the department of Technology transfer and was involved in scale up of novel active pharmaceutical ingredients (API) from 2003-2006.

In 2006, the author moved to United States of America to pursue higher studies and enrolled in the M.S course with major in chemical engineering. Later in 2007, he enrolled in Ph.D. program and joined Potoff Research Lab as a graduate research assistant and started the research career in the field of computational modeling. The author is focused on getting an industry based research job where he can use his knowledge of chemical engineering fundamentals and computational research for betterment of society.